CUKUROVA UNIVERSITY
INSTITUTE OF NATURAL AND APPLIED SCIENCE

PhD THESIS

Volkan ALTUNAL

DEVELOPMENT OF BeO CERAMIC OSL DOSIMETERS: THEIR SYNTHESIS, SINTERING AND LUMINESCENCE STUDIES

DEPARTMENT OF PHYSICS

ADANA-2022

ÇUKUROVA ÜNİVERSİTESİ
FEN BİLİMLERİ ENSTİTÜSÜ

DEVELOPMENT OF BeO CERAMIC OSL DOSIMETERS: THEIR SYNTHESIS, SINTERING AND LUMINESCENCE STUDIES

Volkan ALTUNAL

DOKTORA TEZİ

FİZİK ANABİLİM DALI

Bu Tez …/…/2022 Tarihinde Aşağıdaki Jüri Üyeleri Tarafından Oybirliği/Oyçokluğu ile Kabul Edilmiştir.

……	…….	……..
Prof. Dr. Ahmet EKİCİBİL	Prof. Dr. Kasım KURT	Prof. Dr. Tunç TÜKEN
DANIŞMAN	ÜYE	ÜYE
…….	…….	
Prof. Dr. Faruk KARADAĞ	Doç. Dr. Eren ŞAHİNER	
ÜYE	ÜYE	

Bu Tez Enstitümüz Fizik Anabilim Dalında hazırlanmıştır.
Kod No:

Prof. Dr. Sadık DİNÇER
Enstitü Müdürü

To my family...

ABSTRACT

PH.D. THESIS

DEVELOPMENT OF BeO CERAMIC OSL DOSIMETERS: THEIR SYNTHESIS, SINTERING AND LUMINESCENCE STUDIES

Volkan ALTUNAL

CUKUROVA UNIVERSITY
INSTITUTE OF NATURAL AND APPLIED SCIENCES
DEPARTMENT OF PHYSICS

Supervisor : Prof. Dr. Ahmet EKİCİBİL
Year: 2022; Page: 345
Jury : Prof. Dr. Ahmet EKİCİBİL
: Prof. Dr. Kasım KURT
: Prof. Dr. Tunç TÜKEN
: Prof. Dr. Faruk KARADAĞ
: Assoc. Prof. Dr. Eren ŞAHİNER

The main purpose of this study is to synthesize the novel optically stimulated luminescence (OSL) materials based on BeO synthesized using Sol-Gel and Co-precipitation methods. Structural, morphological and thermal characterizations of newly developed BeO-based ceramics were done with XRD, SEM-EDS, FTIR, and TGA techniques. To enhance TL and OSL characteristics of BeO ceramics, appropriate calcination and sintering condition were determined for two synthesis methods. The effect of metal and lanthanide dopant elements on luminescence and dosimetric characteristics of BeO ceramics was studied in detail. Furthermore, the obtained luminescence emissions were examined by RL, OSL and TL techniques. Dosimetric characteristics of newly developed samples in this thesis were tested by performing reusability, dose- and energy-responses, dark storage fading experiments. With the step annealing, TL after OSL and TT-OSL studies, the origin of the OSL signals and correlation between TL and OSL signals of all the samples were determined. Photo-transferred OSL was also studied and further discussions on luminescence mechanism in doped BeO ceramics were done. Moreover, thermal quenching energies of BeO ceramics were evaluated using two different techniques (read temp and TOSL). Kinetic parameters of some newly developed BeO-based ceramics were examined in detail.

Key words: Optically Stimulated Luminescence, Thermoluminescence, Radioluminescence, Berilyum Oksit (BeO), Radiation Dosimetry, Radiation Energy Storage, Sol-gel synthesis, Co-precipitation synthesis

ÖZ

DOKTORA TEZİ

BeO SERAMİK OSL DOZİMETRELERİNİN GELİŞTİRİLMESİ: SENTEZİ, SİNTERLENMESİ VE LÜMİNESANS ÇALIŞMALARI

Volkan ALTUNAL

ÇUKUROVA ÜNİVERSİTESİ
FEN BİLİMLERİ ENSTİTÜSÜ
FİZİK ANABİLİM DALI

Danışman : Prof. Dr. Ahmet EKİCİBİL
Yıl: 2022; Sayfa: 345
Jüri : Prof. Dr. Ahmet EKİCİBİL
: Prof. Dr. Kasım KURT
: Prof. Dr. Tunç TÜKEN
: Prof. Dr. Faruk KARADAĞ
: Doç. Dr. Eren ŞAHİNER

Bu çalışmanın temel amacı, Sol-Gel ve çökeltme yöntemleri kullanılarak sentezlenen BeO tabanlı yeni optik olarak uyarılmış lüminesans (OSL) materyallerini sentezlemektir. Yeni geliştirilen BeO tabanlı seramiklerin yapısal, morfolojik ve termal karakterizasyonları XRD, SEM-EDS, FTIR ve TGA teknikleri ile yapılmıştır. BeO seramiklerinin TL ve OSL özelliklerini geliştirmek için iki sentez yöntemi için uygun kalsinasyon ve sinterleme koşulları belirlendi. Metal ve lantanit katkılı elementlerin BeO seramiklerinin lüminesans ve dozimetrik özelliklerine etkisi detaylı olarak incelenmiştir. Ayrıca elde edilen lüminesans emisyonları RL, OSL ve TL teknikleri ile incelenmiştir. Bu tezde yeni geliştirilen örneklerin dozimetrik özellikleri, yeniden kullanılabilirlik, doz ve enerji yanıtları, karanlıkta depolama sönümleme deneyleri yapılarak test edilmiştir. Adım tavlama, OSL sonrası TL ve TT-OSL çalışmaları ile tüm numunelerin OSL sinyallerinin kaynağı ve TL ile OSL sinyalleri arasındaki ilişki belirlenmiştir. Fototransfer OSL de incelenmiştir ve katkılı BeO seramiklerinin lüminesans mekanizması hakkında daha fazla tartışma yapılmıştır. Ayrıca, BeO seramiklerinin termal söndürme enerjileri, iki farklı teknik (sıcaklıkta okuma ve TOSL) kullanılarak değerlendirildi. Yeni geliştirilen bazı BeO tabanlı seramiklerin kinetik parametreleri detaylı olarak incelenmiştir.

Anahtar Kelime: Optik Uyarılmış Lüminesans, Termolüminesans, Radyolüminesans, Berilyum Oksit (BeO), Radyasyon Dozimetrisi, Radyasyon Enerjisi Depolama, Sol-jel sentezi, çöktürme sentezi

EXTENDED ABSTRACT

This thesis aims to determine the source of Thermoluminescence (TL) and Optically Excited Luminescence (OSL) emissions of BeO ceramics by different synthesis processes of the material and doping of metal and lanthanide elements, to develop BeO ceramics for dosimetric purposes and obtain high-sensitive controllable luminescence.

In this study, pure and doped BeO ceramic dosimeters were synthesized using Sol-Gel and Precipitation synthesis methods, and BeO ceramic pellets were prepared using BeO nano-powders. The sintering studies of the obtained ceramic pellets were studied in detail.

Effect of synthesis, calcination and sintering methods on the morphological and structural properties of produced undoped and doped BeO ceramics X-ray diffraction (XRD), Fourier transform infrared spectroscopy (FT-IR), Differential scanning calorimetry and Thermogravimetric analysis (DSC-TGA), and Scanning Characterization analyses such as electron microscopy (SEM) methods were performed.

Synthesis, calcination and sintering processes of undoped and doped BeO materials and the relationship between luminescence properties were studied using Radioluminescence (RL), TL and OSL techniques. All dosimetric experiments of materials to be produced, such as annealing and preheating conditions, thermal stability, cascade annealing, repeatability, radiation dose and radiation energy response, and dark fading properties, kinetic parameters were performed and studied in depth using a well-known automated Risø TL/OSL DA-20 model reader. The Riso reader has a beta source of $^{90}Sr/^{90}Y$. For OSL readings, optical stimulation was provided with the help of blue LEDs ($\lambda p \sim 470$ nm) inside the device, and a UV-permeable Hoya U-340 filter was used in front of the photomultiplier tube window. For TL measurements, a Schott BG-39 filter with visible region transmittance was used.

One of the most important steps in the production of BeO material by sol-gel and precipitation methods is the sintering process. The sintering process is optimized to ensure good crystallization of the BeO material formed after synthesis, the particles bonding to each other after pellet preparation, and minimizing the voids on the surface. By choosing the most suitable sintering temperature value of 1600 °C for BeO, 2, 4, 6, 12, 18- and 24-hour sintering processes were carried out for sol-gel and precipitation methods. BeO ceramics obtained after sintering were exposed to 0.5 Gy beta dose and TL and OSL measurements were made. Considering the TL and OSL curves, it was observed that the sintering time was not a variable depending on the synthesis method, and a 2-hour sintering condition at 1600 °C was suitable for both methods.

In this study, the role of the calcination process (temperature and time), which is another important step in the production of BeO material by sol-gel and precipitation methods, on the phase formation, morphology, grain growth behavior and luminescence properties of microparticles was investigated. In the RL spectra of BeO ceramics produced by both synthesis methods, it was observed that there was a characteristic emission peak between 200 and 500 nm, as well as a broad emission peak between 700 and 800 nm due to anion defects. To obtain a promising BeO dosimeter with highly sensitive TL and OSL signals for OSL dosimetry, suitable calcination conditions were determined for the precipitation and sol-gel methods at 900 and 1000 °C for 4 hours, respectively.

The effects of Al^{+3} and Ca^{+2} ions on the luminescence process were observed by dosimetric comparison of the undoped BeO, BeO:$Al_{1\%}$, BeO:$Ca_{1\%}$ and BeO:$Al_{1\%}$,$Ca_{0.1\%}$ ceramic pellets synthesized by the sol-gel method. Wide emission peaks at 230 nm (~5.4 eV) and 300 nm (~4.1 eV) were observed in the RL emission analyses of BeO, BeO:$Al_{1\%}$, BeO:$Ca_{1\%}$ and BeO:$Al_{1\%}$,$Ca_{0.1\%}$ ceramic pellets. TL peaks contributing to OSL signals for ceramics have been studied in depth. Thermal quenching experiments of OSL signals were performed and quenching energies were calculated to be between about 0.5 eV and about 0.7 eV.

The applicability, dose-response, reusability and dark fading of OSL signals were investigated comparatively for pellets produced for dosimetric purposes. In the dose-response experiment of BeO, BeO:$Al_{1\%}$, BeO:$Ca_{1\%}$ and BeO:$Al_{1\%}$,$Ca_{0.1\%}$ ceramics, it was observed that the samples had a linear dose-response between 0.1 and 100 Gy and the minimum detectable dose values were calculated as 0.9 mGy, 4 mGy, 0.5 mGy and 0.5 mGy for each group of pellets, respectively. Very good reusability was observed in the samples, with a maximum deviation of 2% of the OSL signals over ten experimental cycles. Results from BeO:$Al_{1\%}$,$Ca_{0.1\%}$ ceramics have been reported to be useful for OSL dosimetry, especially in medical applications..

The luminescence properties of metal-doped BeO optical ceramics, which were synthesized efficiently by the precipitation method, were also investigated. BeO nanophosphors were doped separately with metal elements at different doping concentrations (0.1%, 0.5, 1 and 5%): Al, Ca, Mg, Na, Li, K, B, Si, Zn, Sr, In and Cu. The formation of the hexagonal wurtzite phase of BeO was confirmed by XRD data and SEM images showed that BeO ceramics exhibit different surface morphologies and have a narrow size distribution. Similar broad UV emission bands between 200 nm and 450 nm were observed in the RL emission analyzes of single metal-doped BeO ceramics. While Al, Na, K, B and Zn dopant elements increase the sensitivity of TL peaks responsible for traps located up to 300 °C, Ca, Mg, K, B and In dopant elements have significantly increased the intensities of TL peaks located between high temperature 300 and 650 °C. In addition, Na, Li, K and Cu doping elements led to increases of 47%, 37%, 18% and 28%, respectively, in the OSL signal intensity of the undoped BeO material. To investigate the feasibility of using the studied BeO materials, dose-response, reusability and short-term fading in the dark were investigated by TL and OSL methods of promising ceramic dosimeters.

In this thesis, the luminescence properties of lanthanide-doped BeO ceramics, which were successfully synthesized by precipitation method, were also

investigated. For the doping of BeO ceramics, lanthanides with +3 valence: (Ln^{3+}) Eu^{3+}, Ce^{3+}, Nd^{3+}, Yb^{3+}, Er^{3+}, Gd^{3+}, Tb^{3+}, Tm^{3+}, Sm^{3+}, Pr^{3+} and Dy^{3+}, and auxiliary doping element Na+ alkali metal ion are selected, RL, TL and OSL techniques have been characterized. The lanthanides presented as additives not only affected the luminescence centres but also changed the luminescence mechanisms. OSL emission bands were found to be located between ~250 and ~390 nm. The results showed that the inclusion of suitable Ln^{3+} and alkali metal ion additives and their optimum concentration significantly increased the luminescence signals of pure BeO. The studied ceramics of BeO:$Na_{5\%}$,$Ce_{0.01\%}$,$Er_{0.01\%}$, BeO:$Na_{5\%}$,$Ce_{0.005\%}$,$Tb_{0.05\%}$, and BeO:$Na_{5\%}$,$Ce_{0.01\%}$,$Dy_{0.01\%}$ are extremely sensitive have been proposed as controllable luminescence dosimeters. The sensitivity range of these samples is such that they are most likely to be used in clinical therapy dosimetry rather than health physics.

In addition, in this study, it was found that the OSL signals of BeO:Na,Dy,Er and BeO:Na,Tb,Gd ceramic dosimeters developed by the precipitation method individually have high sensitivity, dose linearity, low fading properties, reusability and thermal stable OSL signals. With these features, these dosimeters are suitable for personal and medical dosimetry applications.

Except for chemical, structural and thermoluminescence (TL) properties, no studies based on OSL properties of synthesized BeO nanopowders or prepared BeO pellets have been reported in the literature so far. Synthesis, doping, calcination, sintering and luminescence studies will shed light on the existing literature for the widespread use and development of this material in dosimetry in the future.

PREFACE

This dissertation is submitted as the fulfillment of the requirement for the PhD degree in Physics, at the Cukurova University (CU). The PhD research work was carried out at the Thermoluminescence (TL) and Optical Stimulated Luminescence (OSL) Dosimeters Laboratory at CU from October 2017 to June 2022. This project was started to be managed by Prof. Dr Zehra YEGINGIL and in the last days of the project, it was taken over by Prof. Dr Ahmet EKICIBIL.

ACKNOWLEDGEMENTS

I am deeply grateful to my Ph.D. unofficial supervisor, Prof. Dr. Zehra YEĞİNGİL, for allowing me to do my Ph.D., and for her incredible friendly support, guidance, encouragement and patience throughout my Ph.D. Her critical contributions have consistently guided me, not only in producing results but also in writing this thesis. I would like to express my endless gratitude to her for her incredible influence on this thesis and the opportunities she provided me in my process of becoming a successful academician.

In the last period of my thesis work, as my supervisor, I would like to express my gratitude to Prof. Dr. Ahmet EKICIBIL for his invaluable help, guidance, encouragement and patience.

I would like to thank the Council of Higher Education (YÖK) for the financial support under the 100/2000 YÖK Ph.D. Scholarship project. I want to thank a lot to the Research Funding Projects Unit and its members at the Çukurova University for their support of this Ph.D. thesis under the project numbers FDK-2018-10190. I am also grateful to all staff of the Institute of Natural and Applied Sciences for their valuable friendship and their support. I would like to thank the North Atlantic Treaty Organization (NATO) in the frame of the NATO Science for Peace and Security (SPS) Program under the project number SfP 1984649 and SPS MYP G5647.

I would like to thank my colleagues Assoc. Prof. Dr. Adnan ÖZDEMIR and Dr. Veysi GUCKAN in TL/OSL Luminescence Dosimetry and Medical Physics Group for their incredible friendly support at every stage of this thesis. My friends, who always keep their doors open to discussions and practical applications, have always supported me whenever I faced a problem and/or needed direction. I would also like to thank Ph.D. student Wafaa ABUSAID.

I would like to extend my sincerest thanks to Prof. Dr. Kasım KURT from the Physics Department of Mersin University, Prof. Dr. Faruk KARADAG from

Physics Department of Cukurova University, Prof. Dr. Tunç TUKEN from the Department of Chemistry of Cukurova University for sparing time for me and helping to shape my thesis with their valuable comments and guidance. I would also like to deeply thank Prof. Dr. Enver BULUR from the Physics Department of Middle East Technical University, for sharing his valuable discussions while getting started with my thesis.

I would like to thank all the staff of Cukurova University Central Research Laboratory for their attention to analysis, their kind approach to me and for providing priorities and assistance that has accelerated my work. I would also like to thank Ph.D. student Tayfun ÇAVDAR from the Physics Department of Mersin University for his help in radioluminescence measurements, his patience, and his kind behavior towards me.

I would like to thank Dr. Mayank JAIN from the Department of Physics, RISØ National Laboratory at the Technical University of DENMARK, who opened the doors of his laboratory to me within the scope of the NATO project work for allowing me to use all the possibilities of RisØ. I am also grateful to Prof. Dr. Sergii UBIZSKII from the semiconductor Electronics Department, Lviv Polytechnic National University, for multiple times lab opening doors and fluorescence spectrometry analysis.

Last but not least, I feel honored to express my feeling of indebtedness to my grandmother Yüksel ALTUNAL, my father Hakan ALTUNAL, my mother Şengül ALTUNAL, my brother Arslan ALTUNAL, my sister Melisa ALTUNAL ERKOÇ and her husband Ahmet ERKOÇ for their endless love, patience, financial and spiritual support at every stage of my life, and I would like to express my apologies for not spending as much time with them during the period of this study. Finally, I would like to thank my dear wife Melisa ASLANHAN ALTUNAL for the patience she has shown me and for her kind behavior and love support at every stage of this process, and I want her to know that I am grateful to my angel.

CONTENTS **PAGE**

LIST OF TABLES **SAYFA**

LIST OF FIGURES **SAYFA**

LIST OF PUBLICATIONS

The results of the present thesis have been presented in national and international conferences, and also have been published in international peer-reviewed scientific journals. Following is a list of them:

- **Patent related to the current thesis:**

Patent Number: US20210261861A1

Patent name: Doped BeO Compounds for Optically Stimulated Luminescence (OSL) and Thermoluminescence (TL) Radiation Dosimetry

Cozen Ref.: 6107-221P (425549) Patent

Inventors: Zehra Yegingil, Enver Bulur, **Volkan Altunal**, Yan Yu, Veysi Guckan, Adam Dicker

- **Publications in SCI index Journals concerning the present thesis:**

1. **Altunal, V.**, Guckan, V., Ozdemir, A., Zydhachevskyy, Y., Lawrence, Y., Yu, Y., & Yegingil, Z. (2022). Three newly developed BeO-based OSL dosimeters. ***Journal of Luminescence***, 241, 118528. (https://doi.org/10.1016/j.jlumin.2021.118528).
2. **Altunal, V.**, Guckan, V., Ozdemir, A, Ekicibil, A., Karadag, F, Yegingil, I, Yegingil, Z. (2021). A systematic study on luminescence characterization of lanthanide-doped BeO ceramic dosimeters. ***Journal of Alloys and Compounds***, 876, 160105, (https://doi.org/10.1016/j.jallcom.2021.160105).
3. **Altunal, V.**, Guckan, V., Ozdemir, A., Kurt, K., Ekicibil, A., Yegingil, Z. (2020). Investigation of luminescence properties of BeO ceramics doped with metals for medical dosimetry. ***Optical Materials***, 108, 110436, (https://doi.org/10.1016/j.optmat.2020.110436).

4. **Altunal, V.**, Guckan, V., Ozdemir, A.**,** Yegingil, Z. (2020). A Calcination Study on BeO Ceramics for Radiation Dosimetry. ***Materials Research Bulletin***, 110921, (https://doi.org/10.1016/j.materresbull.2020.110921).
5. **Altunal, V.**, Guckan, V., Yu, Y., Dicker, A., Yegingil, Z. (2020), "A newly developed OSL dosimeter based on beryllium oxide: BeO:Na,Dy,Er" ***Journal of Luminescence***, 222, 117140, (https://doi.org/10.1016/j.jlumin.2020.117140).
6. **Altunal, V.**, Guckan, V., Ozdemir, A., Yegingil, Z. (2020), "Radiation dosimeter utilizing optically stimulated luminescence of BeO: Na, Tb, Gd ceramics" ***Journal of Alloys and Compounds***, 817, 152809, (https://doi.org/10.1016/j.jallcom.2019.152809).
7. **Altunal, V.**, Guckan, V., Ozdemir, A.**,** Sotelo, A., Yegingil, Z., (2019), "Effect of sintering temperature on dosimetric properties of BeO ceramic pellets synthesized using precipitation method", ***Nuclear Instruments and Methods in Physics Research Section B: Beam Interactions with Materials and Atoms***, 441, 46-55 (https://doi.org/10.1016/j.nimb.2018.12.036).
8. **Altunal, V.**, Guckan, V., **Ozdemir, A**., Can, N., Yegingil, Z., (2019), "Luminescence characteristics of Al-and Ca-doped BeO obtained via a sol-gel method", ***Journal of Physics and Chemistry of Solids, 131***, 230-242 (https://doi.org/10.1016/j.jpcs.2019.04.003).

- **Publications in national scientific journals concerning current thesis:**

1. **Altunal, V.**, Güçkan, V., Özdemir, A., & Yegingil, Z. (2019). The Effect of Calcination Conditions on Luminescence Efficiency of BeO Ceramics Synthesized Using Co-Precipitation Method. Journal of Investigations on Engineering and Technology, 2(2), 40-44.

- **Oral presentations in International Conferences concerning present thesis:**

1. **V. Altunal**, V. Guckan, A. Ozdemir, W. Abusaid, A. Ekicibil, F. Karadag, Z. Yegingil, (2021). "Luminescence Characterization of BeO:Na5%,Ce0.01%,Er0.01% Ceramic" 6th International Conference on Oxide Materials for Electronic Engineering – Fabrication, Properties and Application (OMEE-2021) September28- October 2, 2021, Lviv, UKRAINE.
2. **V. Altunal**, A. Ozdemir, V. Guckan, Z. Yegingil., (2019). "A Study of BeO Luminophosphores Synthesized with Different Calcination Conditions", 6th International Conference on Materials Science and Nanotechnology for Next Generation (MSNG2019), October 16-18, 2019, Niğde, TURKEY.
3. **V. Altunal,** V. Guckan, A. Ozdemir, E. Bulur and Z. Yegingil," Systematic development of an OSL dosimeter based on BeO", 5th Internatıonal conference on materials science and nanotechnology for next generation (MSNG2018), 04-06 October 2018, NEVŞEHİR/Cappadocia/TURKEY.
4. **V. Altunal**, V. Guckan, A. Ozdemir, E. Bulur and Z. Yegingil, "OSL from BeO:Al,Ca ceramics synthesized using sol-gel method", 11th International Conference on Luminescence and ESR Dosimetry, 5-7 September 2018, Gaziantep University, Gaziantep, TURKEY.
5. **V. Altunal**, V. Guckan, A. Ozdemir, T. Depci, N. Nur, K. Kurt, Z. Yegingil, "Effect of Sintering Temperature on Dosimetric Properties of BeO Ceramic Pellets Synthesized Using Precipitation Method", International Conference on Oxide Materials for Electronic Engineering – fabrication, properties and application, May 29 – June 2, 2017, Lviv, UKRANIE.

LIST OF ABBREVIATIONS

TL : Thermoluminescence; TSL: Thermally stimulated luminescence
OSL : Optically stimulated luminescence
CW-OSL : Continuous-wave OSL
LM-OSL : Linearly-modulated OSL
POSL : Pulsed-OSL
XRD : X-ray diffraction
SEM : Scanning electron microscope
FT-IR : Fourier-transform infrared
EDS : Energy dispersive spectroscopy
RL : Radioluminescence
UV : Ultraviolet
VIS : Visible
IR : Infrared
PMT : Photomultiplier Tube
HR : Heating Rate
RT : Room Temperature
β : Heating rate ($°C.s^{-1}$ or $K.s^{-1}$)
τ : Lifetime (s)
T : Temperature (°C)
I_0 : Initial density at time t=0
eV : Electron volt
LC : Luminescent centers
R : Recombination centers
E : Activation energy (eV)
E_f : Fermi energy level
b : Kinetic order

s : Frequency factor

Gy : Gray

k : Boltzmann constant, $k = 8.6173303(50) \times 10^5$ eV.K^{-1}

^{90}Sr : Strontium-90

^{90}Y : Yttrium-90

a.u. : Arbitrary unit

TLD : Thermoluminescence dosimeter

TLD-100 : LiF:Mg,Ti (magnesium and titanium doped lithium fluoride)

Φ : Optical stimulation density

σ : Photo-ionization cross section

E_0 : Stimulation threshold

λ : Wavelength

α : Absorption coefficient

I : Light intensity

p : Probability

FWHM : Full width at half maximum

T_m : The temperature corresponding to the peak temperature of the TL curve

FGT : Fraction glow technique

μ : Micro (10^{-6} m length unit)

MDD : Minimum detectable dose

1. INTRODUCTION AND OVERVİEW

1.1. Motivation and Purpose

Ionizing radiation, which is defined as a wave or particle-like radiation that carries enough energy to cause the ionization of the atoms of matter (i.e., the removal of electrons from atoms or molecules), constitutes an important part of today's human activities and needs. Radioactive material sources and radiation generators are widely used in various industrial sectors such as the nuclear industry for heat and electricity generation, the healthcare industry for medical diagnosis and treatment applications, the research and education industry. The widespread use of radiation increases the need for dosimeters used in measurement and evaluation processes to protect and monitor people working with radiation, the public, and the environment from unwanted or planned radiation irradiation. Luminescent materials have been a widespread subject over the past three decades. The importance of luminescent materials is not associated with only the fact that these materials widen our understanding of luminescence characteristics of crystals down to nanometer size, but also the fact that they present a prominent potential for wide applications in technology thanks to their unique properties.

Thermoluminescence (TL) dosimeters are widely used in the measurement of ionizing radiation resulting from exposure to X-rays, gamma rays, beta particles, alpha particles, and neutrons. The TL process has two stages: a) the generation of free electrons and holes by ionizing radiation exposure, and then the capture of these charge carriers at lattice defects (traps, ie energy levels) b) discharge of trapped charges by heating up to a specified temperature at a controlled rate; followed by radiative electron-hole recombination resulting in TL. Integration of the emitted luminescence intensity can be used in determining the radiation dose. In practice, such dosimeters typically require an expensive reader system and information about the radiation dose can only be read once.

The phenomenological principles of optically stimulated luminescence (OSL) and TL are the same. The emitted luminescence signal in TL is obtained by heating the sample previously exposed to ionizing radiation, while the emitted luminescence signal in OSL is obtained by excitation of the sample optically at a wavelength greater than the emission wavelength; In both cases, the signal emitted by the material is measured by a highly sensitive device, usually a photomultiplier. Compared to TL dosimeters, OSL dosimeters have features such as reusability, multiple reading procedures, and the possibility of local (point) stimulation, providing them with ease of use. The use of OSL is a promising way of meeting all dosimetric requirements for a luminescent phosphor.

Luminescence of dosimetric materials is controlled using appropriate dopant ions generally transition metal or rare-earth metal ions as the luminescent centers. Such dosimeters should have features of high sensitivity to radiation, light-sensitive trapped charges, low-fading at room temperature, insensitivity to external influences such as humidity or mechanical stress, and possibly easy and fast readouts. Besides, features such as soft tissue equivalency for Z_{eff} value, minimum size, or cost may be important for the commercialization of the product. Since the first OSL measurement on quartz and feldspar using an argon-ion laser in a retrospective dosimetry application (Huntley et al., 1985), the use of OSL in radiation dosimetry has been still restricted due to the lack of the number of commercially available luminescent materials e.g., Al_2O_3:C from Landauer Inc. and Thermalox 995 BeO from Materion Inc. (Akselrod et al., 1998; Jahn et al., 2013). This has encouraged researchers to satisfy the demand to develop new OSL materials for dosimetry applications. Recently, parallel to this demand, the OSL technique is being developed and has found use in several dosimetry applications, including personal, environmental, medical, and retrospective dosimetry. The earlier reports have described the OSL properties of several important materials that can be used as synthetic OSL dosimeters: Al_2O_3:C (Akselrod et al., 1990; Akselrod et al., 1998; Bøtter-Jensen, 1997; McKeever et al., 1999), halides (Allen

et al., 1990; Chernov et al., 2001; J. Thomsen et al., 2002; Nanto et al., 1993a; Nanto et al., 1993b), sulfides (Rao et al., 1984), and oxides (Huston et al., 2001; Kortov et al., 1993b; Rhyner et al., 1970).

One of the most important and versatile luminescent materials is BeO which is a binary oxide semiconductor that possesses the wurtzite structure with a hexagonal crystal structure and possesses a direct bandgap of 10.6 eV. BeO has recently attracted interest due to its outstanding physical and chemical properties, such as high thermal conductivity, high melting material, excellent thermal shock resistance, and high chemical stability. In addition to its superior physical and chemical properties, BeO is an attractive material for specifically passive dosimetry. BeO Thermalox 995 OSL material from Materion Ceramics is a widely used commercial dosimeter in research and has been described in the literature (Jahn et al., 2014; Jahn et al., 2013). BeO Thermalox 995 chips contain many transition metal impurities such as Si, Mg, Fe, Al, B, and Ca (Bøtter-Jensen et al., 2003; Vij et al., 1997). As these elements are not specifically doped to the material for dosimetric purposes, understanding and controlling the luminescence characteristics of the material are complicated. Therefore, it attracts researchers to produce new BeO-based materials with appropriate dopants to improve the luminescence properties of BeO ceramic material and achieve controllable luminescence.

The purpose of my Ph.D. research is to understand and investigate the nature of defects in BeO, to determine how the luminescence mechanism occurred, and to test if the intra-defect emissions originated from the synthesis techniques, conditions and dopant elements can be successfully exploited for dosimetric application. As a student of Physics, I have always been interested in the idea of finding and developing something new. This Ph.D. allowed me to produce and develop new dosimetric materials that show new optical properties; Therefore, not only in dosimetric or optical studies but also in materials science, I am also motivated to carry out interdisciplinary research.

1.2. Luminescence

Luminescence is the result of the radiative emission process from transitions of electrons from a high energy level to a lower energy level in solids. Furthermore, luminescence is also called cold light, which is described as the emission of non-thermal radiation by solid after energy is absorbed as depicted in Figure 1.1.

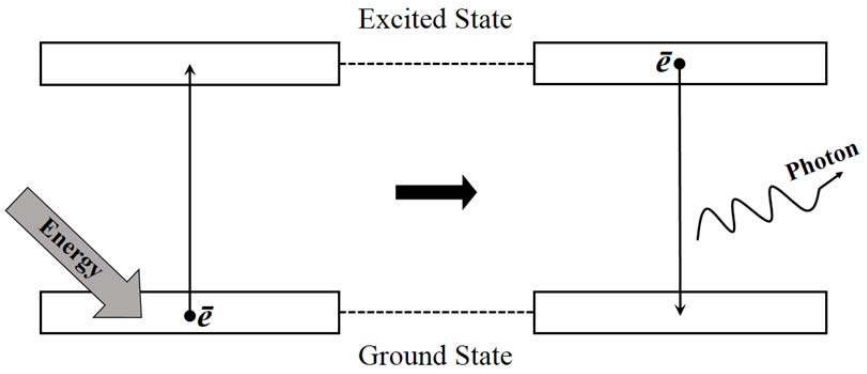

Figure 1.1. General representation of luminescence phenomenon

By using various sources, excitation energy for the electronic transition from low energy level to a high energy level and the resultant relaxation process can be created. Luminescence types can be named by using these sources. For example, photoluminescence using light without irradiation, thermoluminescence using thermal treatment, cathodoluminescence using electrons, ionoluminescence using ions, electroluminescence using an electric field, sonoluminescence using a sound field, lyoluminescence using dissolving after irradiation, mechanoluminescence using a mechanical effect and chemiluminescence or bioluminescence using chemical or biochemical treatments (McKeever, 1988). Additionally, TL and OSL are separated from the processes mentioned above through stimulation. If thermal treatment for stimulation is chosen, the luminescence is called TL. Aside from this, if the photons is used to stimulate

irradiated materials, it is called OSL since the stimulation is generally observed at visible wavelengths.

By considering the recombination processes, luminescence can be classified in two categories, fluorescence and phosphorescence, which depend on the degree of the excited electron spin states for the transition of an electron from the excited state to the ground state in solid. Fluorescence is the luminescence emission originating from the allowed process where the promotion of an electron from a ground state to an excited state is spin preserved (e.g., the direction of the spin of the promoted electron does not change and there exist still two paired electrons with opposite spin direction). On the other hand, if the spin direction of the promoted electron is reversed, there exist two independent electrons of the same spin in different orbitals and it is a forbidden process called phosphorescence. The processes mentioned below are shown in Figure 1.2 by considering a structure that has energy levels such as ground state (S_0), excited states (S_1 and S_2) and vibrational energy levels. Fluorescence can be described as the emission of light as a result of the direct return of an electron from S_1 to S_0. Before this transition, internal conversions between the excited states and vibrational relaxations between the levels of S_0, S_1 and S_2 can occur to transport the electron to the S_1 state. This process is called internal conversion and generally occurs within 10^{-12} s or less. Since fluorescence lifetimes are typically near 10^{-8} s, internal conversion is generally complete prior to emission (Lakowicz, 2013).

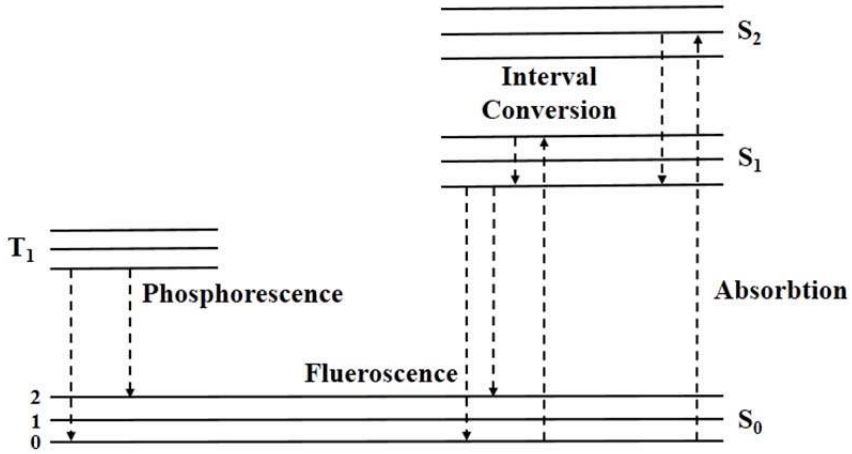

Figure 1.2. Excitation and emission from the transitions between excited states, S_1 and S_2, and ground state energy level, S_0 for the fluorescence process and the phosphorescence process (Redrawing of Figure from (Lakowicz, 2013))

If the electron first passes on a spin conversion into a triplet state (T_1), it's known as a metastable state. After a time delay, it reverts to the ground state level. The time delay between excitation and emission is longer than that of fluorescence making the process to be known as phosphorescence (Chen et al., 1997).

When the topic of phosphorescence reaches the band theory of solids, electronic transitions among the localized states moving as metastable trapping levels and the delocalized bands turn out to be the fundamental process for OSL. The major idea for the examination of OSL occurs from the definition of phosphorescence.

1.2.1. Thermoluminescence (TL)

Since the early 1950s, the TL technique has been used in the field of dosimetry in radiation dose measurements (Daniel et al., 1953). The technique has followed in archeology (dating) in the early 1960s (Aitken, 1985; Mejdahl, 1969), and in the field of geology since the 1980s (Wintle et al., 1980). The TL process is a light emission emitted by the material by heating the radiation energy absorbed

by the imperfections and impurities in the crystal of an insulating or semiconductor material at a linear heating rate. Light emitted from the material during linear heating is recorded as a curve with one or more peaks as a function of temperature. The curve recorded against the temperature is called "TL glow curve". It will be briefly referred to as "TL curve" in the thesis. The typical TL glow curve were illustrated in Figure 1.3. The shapes of TL curves and intensities and positions of peaks vary depending on the trap energy levels and trap parameters of the "trap" responsible for the TL signals.

The TL process basically consists of two stages:

i. Exposure to ionizing radiation: Electrons in the crystal's valence band, which are exposed to ionizing radiation, reach the conduction band by leaving a hole behind the valence band with the radiation energy they absorb. Electrons that tend to return to a steady state are caught in "traps" through defects in the forbidden energy range within the crystal.
ii. Stimulation: Stimulation of trapped electrons by linear heating to crystal. Following the stimulation process, the electrons are freed from the traps and merge with holes in the recombination centers and TL emission is observed.

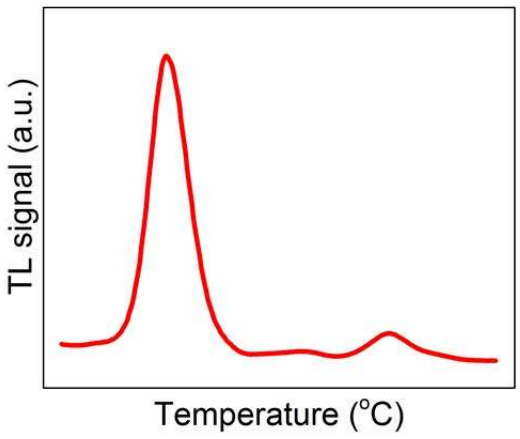

Figure 1.3. Typical TL glow curve

1.2.2. Optically Stimulated Luminescence (OSL)

Optically Stimulated Luminescence (OSL) is the temporary luminescence monitored during illumination of some crystalline materials (insulators and semi-conductors) that were beforehand excited by ionizing radiation. The excitation puts the crystal in a metastable state, characterized by electrons and holes separately trapped at defects in the crystal lattice (Yukihara et al., 2011). After the stimulation, these electrons and holes are released from these trapping centers and OSL occurs with electron/hole recombination and excitation of luminescence centers.

This process mentioned above is illustrated in Figure 1.4, which demonstrates the basic use of OSL in the detection and measurement of ionizing radiation.

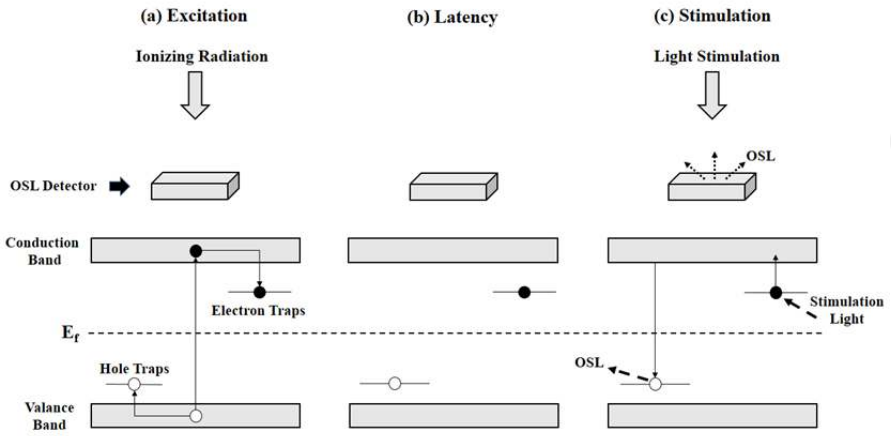

Figure 1.4. The basic concept and processes in the OSL creation: (a) excitation of the OSL detector and occurrence of free electrons (●) and holes (○); (b) latency process with a metastable condition of electrons and holes trapped (c) light stimulation, causing recombination and emission of photons (OSL). The upper half demonstrates the correlation among the detector, ionizing radiation field and stimulation light; the lower half demonstrates the band diagram for the detector with possible energy levels and suitable electronic transitions occurring during each stage (Redrawing of Figure 2.1 from (Yukihara and McKeever, 2011).)

In Figure 1.4a, the detector is excited by ionizing radiation. The energy transferred by ionizing radiation: electrons move to the conduction band, where they can be free and then holes are left behind electrons, they can also be free in the valance band. The electron/hole creation process is illustrated in Figure 1.4a by the upward arrow connecting these bands. There is a possibility that these free electrons and holes may become trapped in some energy levels which are indicated by short horizontal lines in between the valance and conduction bands.

After excitation with ionizing radiation, there is a latency process characterized by a metastable condition of electrons and holes trapped (Figure 1.4b). If the potential wells (e.g. the trapping centers) are deep enough, then the thermally stimulated escape possibility of the trapped charges is insignificant at room temperature. This comparatively stable concentration of trapped charges is associated with the energy transferred during the excitation process, that is, to the absorbed dose of radiation; it indicates concealed information about the radiation field.

The information stored about the radiation field in the detector, as an energy, can be interpreted by using light (Figure 1.4c). In the illustration, a stimulation light of wavelength λ_{stim} forces the electron to move to the conduction band. When the electron is in the conduction band, it is free to pass throughout the crystal and can possibly reach the trapped hole. The electron/hole recombination process creates a defect in the excited state, which relaxes to the ground state by the emission of a photon of wavelength λ_{OSL}.

OSL process associated with the interaction and vibrating of the electrons can be figured out by considering the configurational coordinate model represented in Figure 1.5. It demonstrates the potential energy levels of the luminescent center as a function of the interval among the impurity atom and the first nearest neighbor.

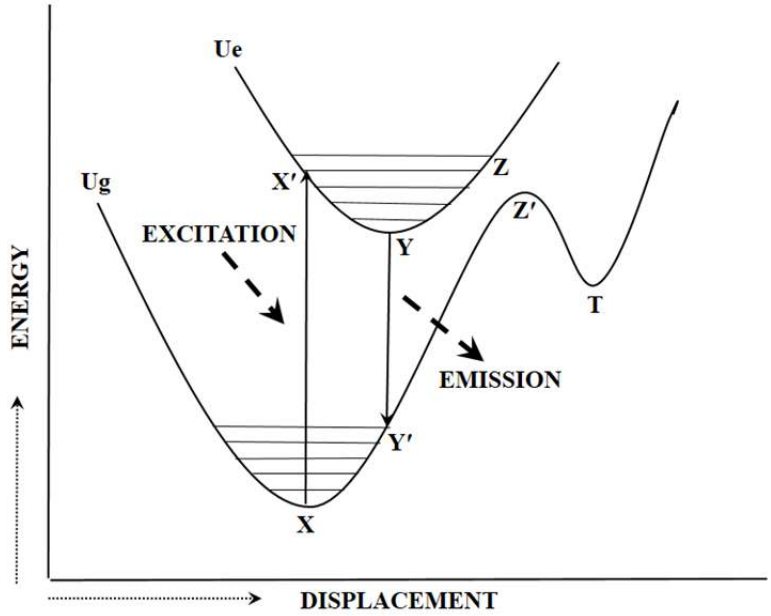

Figure 1.5. Configurational coordinate model of an impurity atom in a crystal (Redrawing of Figure 7 from (Vij, 2012).)

Ionizing radiation can transfer energy to an electron in the ground state (X) and this electron by absorbing this energy can be promoted to a higher energy level (X'). After this transition, some of the energy is lost as heat and the relaxing to zero level of excited state Y occurs. Then, a radiative transition YY' may occur by emitting light and follow by a non-radiative transition Y'X. On the other hand, if the transition ZZ' may happen, the excited electron can also be trapped at T which is the potential trap center. If this state is a deep trap enough, the electron can only be stimulated with stimulation (either light or heat). Upon stimulation, the electron can be promoted to the Z level. Through the YY' transition, luminescence has occurred and this process is briefly called OSL (Vij, 2012).

There are three ways that optical stimulation can be done according to the aim of the investigation:

- If the stimulation light intensity is kept constant, it is named Continuous-Wave OSL (CW-OSL).
- If the stimulation light intensity is increased (or modulated) linearly, it is named Linearly Modulated OSL (LM-OSL).
- If the stimulation source is pulsed and the information of OSL is read between the pulses, it is named Pulsed OSL (POSL).

A schematic representation of the three main OSL stimulation modes is illustrated in Figure 1.6.

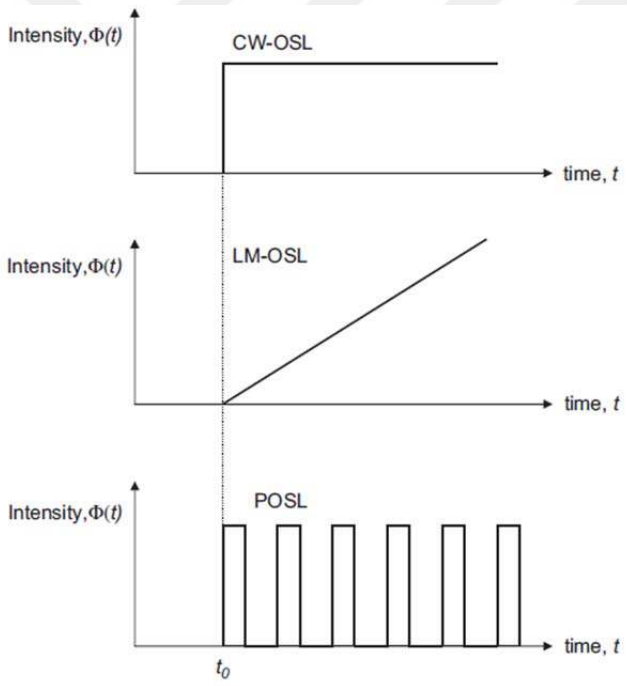

Figure 1.6. Schematic representation of the three main OSL stimulation modes, namely: CW-OSL, LM-OSL and POSL (Akselrod et al., 2006).

Continuous-Wave OSL (CW-OSL)

In the CW-OSL method, the intensity of stimulation light is kept constant during the measurement. Therefore, the separation of stimulation light and the emitted light is essential. This is obtained merely by using the combination of optical stimulation in a suitable wavelength range and detection filters providing convenience for measurement. As a result, the OSL traps in some energy levels can be examined and the emissions of OSL can be observed in this method. A typical decay curve of the OSL signal obtained from this stimulation method was illustrated in Figure 1.7.

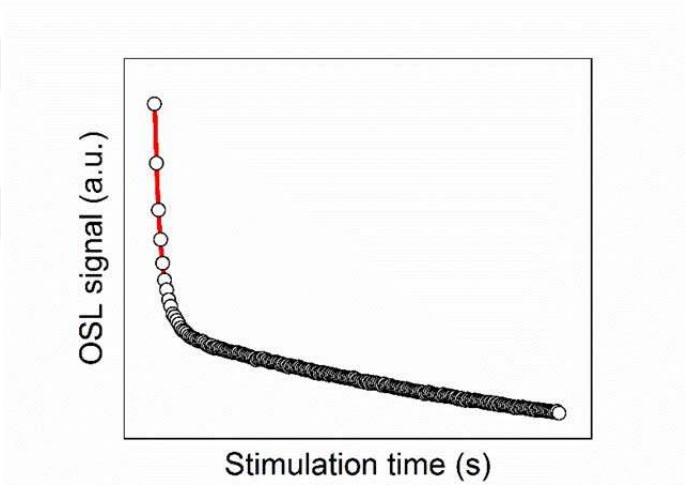

Figure 1.7. A typical OSL curve representing the emission light intensity against stimulation time.

1.3. Models and Rate Equations

The OSL process can be expressed mathematically as a combination of a number of non-linear series and coupled rate equations which are compelling. During optical stimulation, to achieve an analytic expression for the alteration of the OSL intensity with time and to demonstrate the relation of the OSL signal with the absorbed dose, several simplifying assumptions are required. Therefore, previous models which were used to comprehend the structure of the material are

now additionally applied to the experimental results to comprehend the OSL characteristics of the investigated material. Each of these models comprises transitions of electrons towards the conduction band in order to reach the trapping centers which have trapped holes. The first and simplest model is the one-trap/one-center model which is illustrated in Figure 1.8.

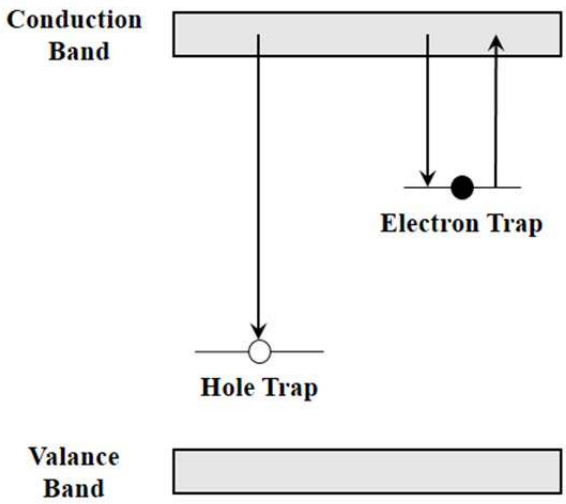

Figure 1.8. The one-trap/one-center model.

This model accepted that there is one type of electron trap and hole trap in the crystal. After the electrons are promoted with the rate of stimulation p (in units of s^{-1}) from the traps to the conduction band, they recombine with the trapped holes by leaving the conduction band and OSL emission occurs, or they are re-trapped in the electron trap. To define this system mathematically, the neutrality of charge can be written as:

$$n_c + n = m_v + m \tag{1.1}$$

where n_c, and m_v, are the concentrations of electrons which are situated in the conduction band and holes, in the valance band, respectively. Additionally, n and m are electron and hole traps, respectively. At the end of the irradiation period, considering the presence of thermal stability such that n_c and m_v are accepted e as zero, then at the start of optical stimulation, we can write that $n_0 = m_0$where the subscripts "0" mean at time $t = 0$.

During optical stimulation of the electrons from the traps, transitions to the valance band do not occur. Hence, the charge neutrality condition becomes $n_c + n = m$, from which the rate of change of the various concentrations can be written as follows:

$$(dn_c)/dt = -dn/dt + dm/dt \tag{1.2}$$

The terms on the right can be written clearly as:

$$dn/dt = np - n_c\, C(N - n) \tag{1.3}$$

And

$$dm/dt = n_c\, C_m\, m = n_c/\tau \tag{1.4}$$

Where p is the rate of stimulation (in units of s^{-1}) of electrons from the trap and is associated with the incident photon flux Γ and the photoionization cross-section σ by

$$p = \Gamma\sigma \tag{1.5}$$

The other terms in Eqs. ((1.3) and ((1.4) comprise C, the retrapping probability (in units of $m^{-3}s^{-1}$); C_m, the recombination probability (also in units of $m^{-3}s^{-1}$); N, the total available concentration of electron traps (in m^{-3}); and $\tau = 1/C_m m$, the free electron recombination lifetime (in s). By using the assumptions of quasi-equilibrium ($(dn\_c)/dt \ll dn/dt, dm/dt$ and $n_c \ll n, m$) and insignificant re-trapping ($n_c C(N-m) \ll np, n_c C_m$) we have

$$I_{OSL} = -dm/dt = -dn/dt = np \tag{1.6}$$

the solution of which is

$$I_{OSL} = n_0\, pexp(-tp) = I_0\, exp(-\frac{t}{\tau_d}) \tag{1.7}$$

where, n_0 and I_0 are the concentration of trapped electrons and the luminescence intensity at time $t = 0$, respectively and $\tau_d = 1/p$ is the decay constant. According to the simplest model, it is figured out from this equation that the decay curve of OSL has a simple exponential form, and finally, OSL becomes zero since all the traps are depleted (McKeever et al., 1997). However, the experimental OSL decay curves in general are not a simple exponential form. Because these curves may contain a considerable re-trapping process or various trap types which have photo-ionization cross-sections. For this reason, Chen and McKeever (1997) have represented that in the form of considerable re-trapping, the intensity of OSL is written as:

$$I_{OSL} = dm/dt = -dn/dt = np - n_c\,(N-n)C \tag{1.8}$$

For a particular form of $N \gg n, C/C_m = R$ and $R \gg n/(N-n)$, second order function results and so

$$I_{OSL} = (n^2\, p)/NR = dm/dt = -dn/dt \tag{1.9}$$

re-writing

$$dn/n^2 = -p/NR\, dt \tag{1.10}$$

After integration, this solution is converted:

$$I_{OSL} = I_0\, (1 - (n_0\, pt)/NR)^{-2} \tag{1.11}$$

where $I_0 = (n_0^2\, p)/NR$. For the further general form, where $I = (n^b p)/NR$, the decay curve of OSL is described by

$$\left(\frac{I_{OSL}}{I_o}\right)^{\frac{1-b}{b}} = \left(1 - \frac{n_0 pt}{NR}\right) \tag{1.12}$$

or

$$I_{OSL} = I_0 \left(1 - \frac{n_0 pt}{NR}\right)^{-\frac{b}{1-b}} \tag{1.13}$$

Considering the presence of two optically active traps (n_1 and n_2 concentrations and p_1 and p_2 rates of stimulation), it is straightforward to indicate that (Chen and McKeever, 1997; McKeever and Chen, 1997):

$$dm/dt = -(dn_1)/dt - (dn_2)/dt \tag{1.14}$$

and that

$$\begin{aligned} I_{OSL} &= n_{10} p_1 \exp(-t p_1) + n_{20} p_2 \exp(-t p_2) \\ &= I_{10} \exp(-\frac{t}{\tau_1}) + I_{20} \exp(-\frac{t}{\tau_2}) \end{aligned} \tag{1.15}$$

If we consider the usage of the superposition law and without interaction among electron and hole traps, this equation can also be expended to more than two optically traps, each depleting at the rate of their characteristics during stimulation.

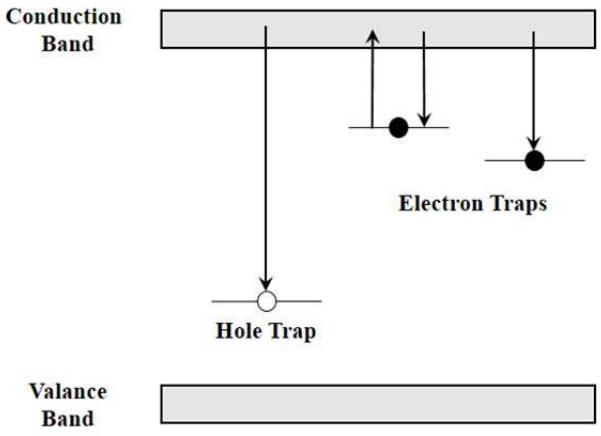

Figure 1.9. Two electron traps and one trap model, only one of which is optically active.

As seen in Figure 1.9, the first electron trap which is the shallow one is optically active and the other one which is a deeper trap is not active. Since the intensity of OSL is affected by an inactive trap, it is inevitable to rewrite that:

$$I_{OSL} = n_{10} p_1 \exp(-t p_1) - dn_2/dt \tag{1.16}$$

from where

$$(dn_2)/dt = n_c\,(N_2 - n_2) C_2 \tag{1.17}$$

Here, N_2, n_2 and C_2 are the concentration of available traps, concentration of filled traps, and trapping probability, respectively. As understood from the equation,

since a deep trap added to the first model, the intensity of OSL is reduced and the decay is not anymore exponential.

Considering that the other trap is a shallow trap, thermally quasi-stable at the temperature which was carried out the readouts of OSL, Eq. ((1.17) turns into,

$$dn_2/dt = n_c\,(N_2 - n_2)C_2 - n_2 f \tag{1.18}$$

where f is the rate of thermal stimulation from the trap and this term is defined mathematically by the Arrhenius equation:

$$f = s\exp(-\frac{E}{kT}) \tag{1.19}$$

where E, s and k are thermal activation energy, frequency factor and the Boltzmann's constant, respectively. Now, to describe the intensity of OSL we have:

$$\begin{aligned} I_{OSL} &= n_{10} p \exp(-t/\tau_d) - n_2 s \exp(-\frac{E}{kT}) \\ &\quad - n_c\,(N_2 - n_2)C_2 \end{aligned} \tag{1.20}$$

The last two terms on the right-hand side in Eq. ((1.20) are associated to make a long-lived, temperature-dependent ingredient to the OSL decay. The form of this ingredient is a preliminary increase, subsequently a decrease at longer times. In comparison with the first term depending on the relative size of this ingredient, the overall OSL decay curve may show an initial increase, subsequently a decrease. The relative size of the two ingredients also interconnects with the excitation rate p such that at low values of p, the temperature-dependent ingredient may be meaningful.

In addition to mentioned above models, there is also another model which includes two recombination centers as radiative and non-radiative. This model is illustrated in Figure 1.10.

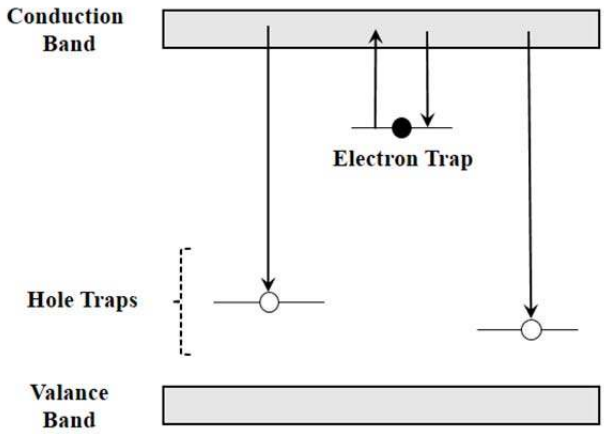

Figure 1.10. An electron trap and two recombination centers model.

In such a case, after irradiation, the total trapped electron concentration n is given by:

$$n = m_1 + m_2 \tag{1.21}$$

where, m_1 and m_2 are the concentrations of trapped holes in the different recombination centers. In this case, the intensity of OSL is written as:

$$I_{OSL} = n_0 p exp(-\frac{t}{\tau_d}) - dm_2/dt \tag{1.22}$$

Again, it is adapted from this equation that the intensity of OSL is reduced by the existence of an extra recombination center which is a non-radiative, optically inactive and deep electron trap. Quasi-equilibrium $dn_c/dt \approx 0$ give rise to:

$$m_1 \approx m_{10}\exp(-tn_c C_{m1}) \tag{1.23}$$

And

$$m_2 \approx m_{20}\exp(-tn_c C_{m2}) \tag{1.24}$$

where C_{m1} and C_{m2} are the probabilities of recombination at the two centers and the relative size of the recombination centers is time-dependent and so:

$$m_1/m_2 \approx m_{10}/m_{20} \exp(-tn_c (C_{m1} - C_{m2})) \tag{1.25}$$

In this situation that $C_{m1} \approx C_{m2}$, the ratio keeps approximately constant and the decay curve of OSL remains approximately exponential according to:

$$I_{OSL} = 1/K\, n_0\, pexp(-tp) \tag{1.26}$$

where K is a constant given by $K = m_1 + m_2/m_1$. If the Eq. ((1.20) is compared with the Eq. ((1.7), it is seen that, out as expected, the previous case gives a lower OSL signal (by a factor $1/K$) (Chen and McKeever, 1997; McKeever and Chen, 1997).

The models shown until now are for very special cases only. Because real materials can include all of the electron trap and recombination center types together. Hence, the decay curves of OSL obtained from these materials are overmuch complex. However, this difficult problem can be resolved by interpreting the results of measurements and using the basic information of these models.

1.4. TL and OSL Dosimetry

Dosimetry is the technique of measuring and calculating how much radiation a material or living tissue is exposed to directly or indirectly. Dosimeters

are dose monitoring devices used to determine the radiation dose exposed. The process of determining the presence and degree of ionizing radiation, radioactive contamination is called monitoring. It is mandatory to have a field dosimeter fixed at certain points in order to detect the amount of radiation exposure at various points in areas where ionizing radiation is used. Field monitoring dosimeters are used to ensure that adequate protection measures are taken against radiation exposure to both staff and other people. OSL and TL dosimeters are used extensively for the same dosimetric applications as personal, environmental, medical, and retrospective dosimetry.

In personal dosimetry applications, the primary goal is to measure the amount of radiation that personnel working in radiation-related jobs are exposed to during routine applications. Nuclear reactor workers, radiotherapy technicians in hospitals, and workers dealing with nuclear waste are examples of this group. Here, the purpose of measuring the radiation dose is to try to keep the radiation dose to which this personnel is exposed below predetermined limits. These limits are set based on agencies such as the International Commission on Radiological Protection (ICRP). In addition to this routine dose determination practice, the measurement of the amount of radiation exposure as a result of radioactive accidents is also included in this field. The main purpose of all these applications is to keep the total amount of radiation each individual is exposed to below the maximum allowable dose value determined by the ICRP (McKeever et al., 1995; Yukihara and McKeever, 2011).

In recent years, science, health, industry, and political circles have started to pay more attention to this issue with the increasing responses of societies to environmental disasters caused by man-made radiation sources. As a result of the daily escaping of gaseous radionuclides, the disposal of low-level wastes, the use of nuclear fuels, nuclear power plant accidents, and some activities carried out by the nuclear energy industry, concerns about the possible environmental damages of these studies have started to arise in a wide audience of the world. As a result, the

continuous measurement of environmental radiation dose has become an important issue for industrialized countries. For this reason, the use of TLDs and OSLDs in measuring environmental radiation is important (McKeever et al., 1995; Yukihara and McKeever, 2011). There is no tissue equivalence in environmental dosimetry. However, low exposure levels require a long reading time. Thus, the dosimeters must remain stable for long periods and maintain their high sensitivity.

The recent increase in spaceflight has led to an increased interest in space dosimetry, a sub-branch of environmental dosimetry. The biggest reason for this interest is to want to determine the radiation dose that astronauts are exposed to as a result of their exposure to harmful radiation. Also, electronic devices are another reason to be exposed to radiation for a long time. Because these devices cause systemic problems when exposed to radiation for a long time (McKeever et al., 1995; Yukihara and McKeever, 2011). The source of space radiation is galactic cosmic rays and heavily charged particles from solar winds, whose main component is mostly high-energy photons. To calculate the effect of high-energy radiations, TLDs have recently been used in many flights (McKeever et al., 1995; Yukihara and McKeever, 2011).

Recently, small-sized TLD and OSLD materials have begun to be widely used in diagnosis and treatment. These dosimeters are frequently used to calculate the amount of ionizing radiation they are exposed to by placing them on the patient's body during diagnosis and/or treatment. Exposed to radiation, TLD is then taken from the patient and measured. In this way, physicists can calculate the actual amount of dose reaching critical internal organs and thus obtain information that can guide the treatment (McKeever et al., 1995; Yukihara and McKeever, 2011). It is very difficult to perform such an application with other types of radiation dosimeters. People are exposed to clinical radiation in two areas; the first is diagnostic radiology (eg they are exposed to X-rays during mammography, dentistry, and general diagnostic films), the second is radiotherapy (different types of first-level cancer therapies). The dose obtained by the use of clinical dosimeters

in this field must be the tissue equivalent dose. For clinical use, dosimeters are expected to be able to measure dose in vivo with high precision and with a linear dose-response and to be as small as possible.

2. LITERATURE REVIEW

Powder crystal raw materials are generally used for the preparation of oxide-based materials (glasses and ceramics). While ceramics are conventionally prepared by solid-state reactions of powders and the high temperature of a granular agglomerate, glasses are generally produced with a melting process. Recent research and development activities have highlighted the importance of chemical synthesis methods, which are performed especially using organic precursors, in the processing and production of ceramics (Boch et al., 2010; Carter et al., 2007). The sol-gel method is used commercially in many applications, such as producing dense ceramics. This synthesis method provides to perform reactions at relatively low temperatures, creating very fine powders, and producing compositions not possible by the solid-state technique (Carter and Norton, 2007; Rane et al., 2018). Another commercial method for producing dense ceramics is the co-precipitation technique. The method offers simple and rapid preparation, easy control of particle size and composition, various possibilities to modify the particle surface state and overall homogeneity, low temperature, etc (Rane et al., 2018). Although sol-gel processing and co-precipitation powder synthesis are widely used, one major disadvantage of these two methods is that the ultra-fine particles of the gel-like precursors undergo severe agglomeration during drying (Li et al., 2000; Rane et al., 2018). This clumping can lead to batch reproducibility problems. This problem can only be solved during the powder processing of the material. Undoubtedly, one of the most important stages during ceramic powder processing is the calcination process which refers to the general heat treatment stage used to synthesize or prepare ceramic powders before dispersing or shaping. The objects of calcination are usually to drive off water, drive off carbon dioxide, sulfur dioxide, or other volatile constituents, and oxidize a part of the whole of the substance. Since the product of most powder synthesis processes is a precursor to the designed material, the phase composition, particle size and aggregation of ceramic powders are

mainly determined during the calcination and sintering process. In the literature, it has been reported that the calcination and sintering process generally affects phase formation (Anderson et al., 1967; Bomlai et al., 2007; Ngamjarurojana et al., 2006; Yeh et al., 2017), surface morphology and sinterability (Simpraditpan et al., 2013; Wang et al., 2010, 2011), and various physical properties of the ceramic materials (Bohlender et al., 2019; Guckan et al., 2020; Sagar et al., 2020; Xie et al., 2018).

The thermoluminescence (TL) and optically stimulated luminescence (OSL) techniques are generally used in dosimetric applications. The luminescence process usually begins with the exposure of semiconductor or insulator materials to ionizing radiation. Absorbed energy creates electrons and holes that can move freely in the crystal, and these charge carriers are trapped in crystal defects. The trapped electrons and holes are in a semi-stable state. Electrons and holes that escape from traps with heat or light stimulation are recombined in the luminescence centers. This recombination process allows us to observe TL and OSL emissions. Thus, indirect information about radiation can be obtained from luminescent materials. Such materials have been widely applied in lighting, display, radiation dosimeters, etc. areas. But, with the advancing technology, many traditional phosphors could not meet the requirements of existing luminescent applications. The limited number of dosimeters (e.g., Al_2O_3:C from Landauer Inc. and Thermalox 995 BeO from Materion Inc.), which are widely used in radiation dosimetry applications, has led researchers to focus their studies on improving luminescence properties of traditional phosphors and preparing new luminescent materials in recent years (Rivera, 2011). In this sense, the different preparation methods and properties of various TL and OSL materials have been investigated to date and it has been observed that metal oxides doped with suitable activators form a promising TL or OSL phosphorus class (Akselrod et al., 1998; Altunal et al., 2019a; Altunal et al., 2019b; Altunal et al., 2018; Nakamura et al., 2017; Oliveira et al., 2016; Singh et al., 2012). For TL and OSL personal and medical dosimetry applications, one of the most important properties of luminescence materials is to

be tissue equivalent (Z_{eff} ~7.5) and hence, it is important to improve luminescence properties of tissue-equivalent materials.

For personal dosimetry applications, BeO is one of the commonly used dosimeters due to its low effective atomic number (Z_{eff} = 7.13), which is very close to that of biological tissues (Z_{eff} = 7.42). Although BeO was previously proposed as thermoluminescence (TL) dosimeter that could be an alternative to most commonly used TLD-100 dosimeters in medical physics applications, BeO's toxicity in powder form and the photosensitivity of TL signals revealed difficulties in using the material in TL applications (Horowitz, 1984; McKeever, 1988; McKeever et al., 1995). This light sensitivity of the TL signals of BeO also encouraged researchers to use the material as an optically stimulated luminescence (OSL) dosimeter (Rhyner and Miller, 1970). After BeO (Thermalox 995 chip) was studied using the continuous OSL technique in detail by Bulur and Goksu (Bulur et al., 1998), the material became popular for OSL dosimetry among researchers. As a result of these studies, a commercial OSL dosimetry system based on BeO ceramics was produced for personal/clinical dosimetry (Jahn et al., 2013; Sommer et al., 2006; Sommer et al., 2008, 2011).

Particularly for radiation dosimetry, Thermalox 995 ceramic offers some advantages compared with other luminescent materials, such as relatively low cost, insensitivity to humidity, resistance to mechanical shock, high sensitivity to ionizing radiation, linear dose-response over six orders of magnitude (from approximately 5 μGy to approximately 5 Gy) (Yukihara, 2011), low fading of less than 1% within 6 months (Sommer et al., 2007), the absence of low-temperature peaks, and moderate energy dependence (Vij and Singh, 1997). Therefore, Thermalox 995 is an attractive candidate material for radiation dosimetry. However, drawbacks to its use include BeO emitting a small amount of tribothermoluminescence and its characteristic light-stimulated fading. BeO is highly toxic in powder form but is completely harmless in the form of sintered pellets and chips (Vij and Singh, 1997). Thermalox 995 detectors as a sintered

ceramic of 99.5% BeO with major impurities of Si, Mg, Fe, Al, B, and Ca are currently used in OSL dosimetry (Bøtter-Jensen et al., 2003; McKeever et al., 1995; Vij and Singh, 1997) and are widely used worldwide.

Although there is a considerable amount of literature on the use of BeO as Thermalox 995 ceramic chips, there has been few luminescence studies of undoped and doped BeO have been reported in the literature. Scarpa (1970) investigated the dosimetric use of BeO discs produced by Consolidated Beryllium Ltd. (Milford Haven, United Kingdom). The main impurity levels for BeO discs were 0.4% for slip-cast and hot-pressed BeO, the contaminants being Si, Na, F, S, and C. Yamashita et al. (1974) studied TL properties of Li-and Na-activated BeO samples and pointed out that they are reliable thermoluminescent phosphors. Kortov et al. (1993b) synthesized optically transparent high-density BeO ceramics to investigate their possible applications in TL and/or ESR dosimetry. It was reported that the BeO ceramics simultaneously doped with Li and Nd gave the best results, with little tendency to sputter and having no pyroelectrical effects during heating or cooling. Additionally, a preliminary study of mixed BeO:TiO_2 ceramic for application in thermally stimulated exoelectron emission and TL dosimetry was reported by the same group of researchers, showing high electrical conductivity of the material (Kortov et al., 1993a). Although the OSL and TL mechanisms of BeO ceramics were not fully understood, it was suggested by (Kortov et al., 1996) that Al sites in BeO act as the recombination centers.

Considering the sintering process of BeO, in the literature, Yamashita et al. (1974) synthesized BeO doped with (Li, Na, Si, Ge, B, and Al) for TLD using Solid State Synthesis Method sintered at 1500 °C. The dose and energy response, emission spectrums and TL fading properties of BeO doped with Li or Na were reported to be acceptable. TL and ESR characteristics of two types BeO transparent ceramics were studied by Kortov et al. (1993b) using 1200 and 1600 °C sintering temperatures. They reported that the optically transparent high-density BeO ceramics, simultaneously doped with Li and Nd gave the best results. Additionally,

TL properties were studied both by Ogorodnikov et al. (1996) for BeO single crystals doped with B or Li impurities in different concentrations and by Kortov and Milman (1996) for the transparent BeO doped with Li. Transparent BeO ceramics doped with a number of impurities, which were prepared by hot pressing at a temperature not higher than 1250 °C and a pressure of 30 MPa, were offered for ionizing radiation dosimetry as an alternative dosimetric material by Kiiko (2004). He also suggested it being used in laser technology as a material for the fabrication of dielectric resonant tubes, waveguides, and dielectric non-transmitting mirrors. Recently, Wang et al. (2010) synthesized BeO nanoparticles using polyacrylamide gel route and determined the most appropriate sintering temperature as 1600 °C. Zahedifar et al. (2011) studied the usability of nanomaterial BeO doped with Mg synthesized with the sol-gel method, for TL dosimetry. Altunal et al. (2018) synthesized undoped BeO nano-phosphor using the sol-gel method and the BeO pellets prepared from nanopowders sintered at 1100 °C. The OSL signals of these BeO pellets were reported to be nearly linear in the dose range from 0.1 to 100 Gy; thermally stable up to 150 °C; fade about 11 % in about a week of dark storage and dominated by fast decay component.

The available experimental results on BeO, in the literature, however, provided luminescence data mostly over Thermalox 995 either using TL or OSL and usually investigated significant experimental results for its interpretation. To the best of my knowledge, a complete study of synthesized BeO material by TL and OSL has not yet been undertaken deeply. This thesis attempt to bridge this gap by reporting experimental measurements of the TL and OSL characterizations, sintering and calcination conditions, the dopants dependence for BeO.

3. MATERIAL AND METHODS

3.1. Beryllium Oxide (BeO)

Beryllium oxide (BeO) is a white crystalline oxide. It occurs in nature as the mineral “Bromellite”. Historically, beryllium oxide was called glucina or glucinium oxide. It is a high melting material (m.p. 2550 °C) with a remarkably high thermal conductivity ($\lambda_{100\ °C}$ = 210 W/mK), excellent thermal shock resistance and high chemical stability with breaking strength comparable to that of α-Al_2O_3. Unfortunately, the industrial production of BeO is more expensive than that of α-Al_2O_3; moreover, there is no broad use for BeO as its abrasive dust is highly toxic. Besides these, its high electrical resistivity (> 1013 Ω·cm), hardness (1250 kg/mm^2), high transparency over a wide spectral range (121-7000 nm), a low thermal neutron cross-section (10 mb), made it useful as a material of heat sink, thermal shock resistance (refractory ware), high-efficiency moderator and reflector in the electronic and nuclear industry. BeO is a binary oxide semiconductor that possesses the wurtzite structure with a hexagonal crystal structure and possesses a direct bandgap of 10.6 eV (Hazen et al., 1986; Sabine et al., 1969; Watanabe et al., 2010).

Beryllium oxide can be prepared by calcining beryllium carbonate, drying the hydroxide, or igniting the metal with oxygen gas, or it can be obtained by combustion processes followed by the preparation of sulfate salt and some aqueous solution.

3.2. Structural Characterization Techniques

Within the scope of this thesis, X-Ray Diffractometer (XRD), Scanning Electron Microscope (SEM), Energy Dispersive X-Ray (EDS), Thermogravimetric Analyzes (TGA), Fourier Transform IR Spectra (FT-IR), and Raman Spectroscopy analyzes were carried out to investigate the crystal structures and morphological

properties of BeO-based undoped and doped materials produced by different synthesis methods and to confirm our products.

3.2.1. X-Ray Diffractometer (XRD)

X-ray Diffraction (XRD) is based on the diffraction of X-rays in a characteristic pattern, depending on the unique atomic arrangement of each crystal phase. With XRD analysis, qualitative and quantitative investigations of rocks, crystalline materials, and thin films can be made. In this thesis, XRD patterns were obtained using a PANalytical Empyrean XRD diffractometer with Cu-Kα (the generator voltage of 60 kV, the current of 40 mA) by scanning from 10° to 90° (2θ) with 0.02° (2θ) steps. The XRD patterns were compared with the reference data by the International Centre for Diffraction Data (ICDD).

3.2.2. Scanning Electron Microscope (SEM)

A scanning electron microscope is a type of electron microscope that obtains images by scanning the sample surface with a focused beam of electrons. Electrons interact with atoms in the sample to produce different signals that contain information about the topography and composition on the sample surface. In this thesis, to investigate the surface morphologies, particle sizes and distributions, of the newly produced ceramics, the SEM analyzes were carried out by Zeiss, Supra 55 at room temperature. The SEM micrographs were taken at different direct magnification and a high voltage of 20 kV.

3.2.3. Energy Dispersive X-Ray (EDS)

The sample surface evaluated by SEM Analysis can also be analyzed using Energy Dispersive Spectroscopy (EDS) to identify specific elements that make up the sample surface. X-rays are also emitted from the surface of the sample, which carries a unique energy signature unique to the elements present in the sample. These X-rays are detected with the EDS detector to give basic information about

the sample. The EDS provides data on the chemical composition of the sample and provides additional data on the properties observed in the SEM micrographs. In this thesis, EDS analyzes were performed by the Zeiss, Supra 55 at room temperature to investigate elemental impurities formed during synthesis and existing dopant ions in the structure.

3.2.4. Thermogravimetric Analyses (TGA)

Thermogravimetric Analysis (TGA) is a technique in which the mass of a sample is monitored as a function of temperature (thermal) or time (equilibrium) under a controlled temperature program in a controlled atmosphere. TGA consists of a sample pan supported by a delicate balance. This pan is located in an oven and is heated or cooled during the experiment. The mass of the sample is monitored during the experiment. The sample purge gas controls the sample environment. This gas can be inert or a reactive gas that flows over the sample and exits an exhaust. TGA is a common analysis method in the chemical and pharmaceutical industries. It is applied to polymers, foods, pharmaceuticals and many other materials. In this thesis, to determine the calcination temperature of the precursors, the TG3+ model Mettler Toledo thermogravimetric (TGA) system was used. Measurements were conducted from ambient temperature to 1200°C, at a heating rate of 20°C/min in an air atmosphere.

3.2.5. Fourier Transform IR Spectra (FT-IR)

Fourier Transform Infrared Spectroscopy (FTIR) is a type of vibrational spectroscopy. FTIR is a chemical analytical method that measures the number of waves against the infrared intensity of light using the mathematical Fourier transform method. The infrared region of the electromagnetic light array is between 14000 cm^{-1} and 10 cm^{-1} and includes near-wavelength infrared (NIR; 4000 ~ 14000 cm^{-1}), medium-wavelength infrared (MIR; 400 ~ 4000 cm^{-1}) and far wavelength infrared (FIR; 4 ~ 400 cm^{-1}) consists of three main regions. IR rays are absorbed by

the vibrational movements of the molecule. In mathematical Fourier transform spectroscopy, the luminous intensity is taken as a function of time. Fast and high-resolution spectra can be obtained without the need to scan each length separately. With this method, molecular bond characterization is performed; functional groups in the structure of solid, liquid, gaseous, or solution organic compounds, whether the two compounds are the same, the state of the bonds in the structure, the binding sites and whether the structure is aromatic or aliphatic can be determined. In this study, an FTIR spectrometer (Thermo Scientific, NicoletiS10) was used to determine the vibrational bonds in the mid-IR region (spectral range between 550 and 4000 cm^{-1}).

3.2.6. Raman Spectroscopy

Raman spectroscopy, like FTIR, is a molecular spectroscopic technique that uses the interaction of light with matter to gain important information about the structure or properties of a substance. The information provided by Raman spectroscopy originates from a light scattering process while infrared spectroscopy relies on the absorption of light. Raman spectroscopy provides insights into intramolecular and intermolecular vibrations and can provide a broader understanding of a reaction. Both Raman and FTIR spectroscopy provide the spectral property of a molecule's specific vibrations ("molecular fingerprint") and are valuable for identifying a substance, but Raman spectroscopy provides additional information about sub-frequency modes and vibrations, providing important data for crystal structure and molecular structure. In this thesis, the Raman spectra of undoped and Ln^{3+} doped BeO ceramics were done using a Raman spectrophotometer (Renishaw in Via Qontor) with 532 nm laser as excitation wavelength.

3.3. Radioluminescence (RL) System

Some of the electrons and holes produced by ionization could result in radiative recombination in one of the two ways:

I. instantaneous recombination at the recombination center after the production and during irradiation to cause a radioluminescence (RL) or scintillation without getting trapped; and
II. recombination via metastable states where some of the charge carriers are trapped and can remain trapped for long periods until sufficiently stimulated (TL or OSL).

Since RL is produced continuously during irradiation, information about a radiation dose rate could be obtained in real-time. In this study, a homemade RL system (in Mersin University) equipped with a highly sensitive spectrometer QE Pro, Ocean Optics, and Hamamatsu FFT-CCD detector was used to provide knowledge about the locations and overview of luminescence bands of undoped and doped BeO dosimeters. The excitation system was developed by a Moxtek mini x-rays device and a high sensitive Ocean Optics spectrometer. Mini x-ray device has 4-40 kV voltage for accelerating electrons from tungsten cathode to silver anode. The flamed current varied between 0 - 0.1 mA. The x-ray excitation energies are ~ 22 keV (Ag- Kα) and 25 keV (Ag- Kβ) possessing 0.056 and 0.049 nm wavelengths, respectively from the silver anode. The spectroscopic wavelength range was between 185-1100 nm with a 5 ms integration time. The optical resolution was around 1 nm. The quantum efficiency of this spectrometer is about 90 %.

3.4. TL and OSL Readout System

A DA-20 model Risø TL/OSL reader system was used for the TL and OSL measurements. The samples were irradiated using a ^{90}Sr-^{90}Y beta particle source

(2.27 MeV maximum energy, 6.689 Gy/min dose rate). TL and OSL emissions in the UV region were detected using a Hoya U-340 filter placed in front of the bialkali photomultiplier tube (PMT) unit. In OSL readouts, samples were firstly irradiated with a certain beta dose and preheated to a pre-determined target temperature for eliminating the signals that come from the shallow traps. 470 nm Blue LEDs were used for the light stimulation in continuous wave OSL mode (CW-OSL mode). TL readouts were conducted by heating the previously irradiated samples to 650 °C without any preheating. In all the TL measurements, the heating rate was 3 °C/s. Before TL/OSL comparison measurements of undoped and doped BeO ceramics, each sample was individually calibrated according to a reference dose of 0.5 Gy for better identification of variations in responses in the same batch. All the experimental data reported in this thesis is presented after the corrections made using calibration factors. To increase the reliability of the luminescent experiments, both the fresh pellets and used pellets were measured after annealing at 650 °C for 10 min.

On the other hand, part of this thesis was carried out using the DA-20 Model TL/OSL reader with DASH (detection and stimulation head) and an ANDOR brand spectrometer connected to this system located at the Risø campus of the Denmark Technical University. The system is a multifunctional developed system that provides the opportunity to obtain the TL emission spectrum simultaneously with increasing temperature, as well as providing temperature-dependent RL signals and time-resolved OSL signals.

3.5. Fluorolog-3

TL and OSL emission spectra were measured using a Horiba Jobin-Yvon Fluorolog-3 spectrofluorometer with a 450 W continuous xenon lamp for excitation and optical detection with a Hamamatsu R928P photomultiplier operating in the photon counting mode. TL spectra of previously irradiated samples with 600 Gy beta dose were obtained at stabilized temperatures of 140 °C and 320 °C

temperatures. All the TL emission spectra were corrected by the spectral response of the detection system and the dark signal subtraction. The excitation monochromator was set to 475 nm and the OSL emission spectra of the previously irradiated samples with 300 Gy beta dose were recorded by scanning from 240 to 420 nm in 3 nm increments using 0.1 s integration time. The slits of excitation and emission were selected as 5 nm and 9.5 nm, respectively. A 450 nm long-pass filter for excitation and a UFS-1 short-pass filter was used. The excitation time was 60 s. All the OSL emission spectra presented here were previously corrected by the spectral response of the system. To reduce the effect of change over time, all spectra were recorded as quickly as possible, and each was averaged after 3 consecutive scans.

3.6. Synthesis Methods

Natural minerals generally do not exhibit luminescent properties with high TL/OSL sensitivity. Therefore, synthetic dosimetric materials are being developed using synthesis methods. It can be said that synthesizing ceramic compounds is quite difficult since crystal forms are required to obtain sensitive luminescent materials.

Some of the methods used in the production of synthetic dosimeters in the literature are presented below:

- Co-precipitation method
- Sol-gel method
- Solution combustion synthesis
- Hydrothermal synthesis
- Solid-state synthesis
- Solution assisted solid-state
- Microwave-assisted solid-state method

All of the mentioned methods can provide advantages or disadvantages according to the application area of the developed material. In this thesis, Co-precipitation and Sol-Gel methods, which are superior to other production methods, were used considering the ease of application and the uniformity of the obtained materials.

In synthetic dosimeter synthesis studies, some parameters that should be considered to produce materials with high sensitivity TL/OSL signal and superior dosimetric properties are listed below:

- Crystal lattice of the main material
- Synthesis method
- Calcination condition (The heat treatment required for the formation of the target material)
- Sintering condition (required heat treatment for the best crystallization of the target material)
- Radius of dopant ions (ionic radii)

Particularly, the concentration percentage of the additive ion is very important. Because the concentration of a dopant ion chosen for the purpose carries the TL and OSL signals of the parent material to the maximum value up to a certain value. After this critical value, the TL/OSL signal decreases and this decrease is called concentration quenching. In other words, dumping occurs in luminescence depending on the concentration ratio. This damping may be due to the contribution of dopant ions, which contain high energy levels, to the structure, increasing the probability of the non-radiative transition of electrons. Another damping mechanism is the possibility of quenching the luminescence in the lattice of the base material with high concentration or the occurrence of emission phases outside the measurement spectral regions. In the synthesis studies of undoped and doped BeO materials carried out in this thesis, the above-mentioned sensitive

mechanisms were handled experimentally and theoretically, and the best possible and reliable materials were developed.

3.6.1. Co-precipitation Synthesis Method

In this method, a solution of the precursor reactants is mixed with dopants in an acid solution. Once the precipitate has the desired compound, the sample is centrifuged and washed repeatedly. The precipitate is treated at high temperature, then cooled to room temperature and dried in an inert atmosphere. Thereafter, the temperature is raised to a higher temperature, holding for a time. Subsequently, the sample is moved slowly toward a zone of lower temperature to crystallize, then the sample is removed from the furnace by cooling rapidly to room temperature. Finally, the product is pulverized and sieved, selecting powder with desired grain size (Zumdahl et al., 2012). This method has been used by some authors for synthesizing diverse materials such as alkaline earth sulfides (Rao, 1986), metallic oxides (Azorín-Vega et al., 2007), strontium aluminate (Chang et al., 2006), calcium phosphate, lithium fluoride, or calcium sulfate.

3.6.2. Sol-gel Synthesis Method

The sol-gel process is an efficient method that uses the same type of reactions among the precursors as the other methods, followed by condensation to yield a polymeric network. Just as the sol or gel is applied to the substrate and then submitted to a thermal treatment to remove undesired organic matter (Brinker et al., 2013). This method is very good for obtaining aluminates, oxides, nitrides, phosphates and sulfides.

4. RESULTS AND DISCUSSIONS

4.1. Determination of Appropriate Sintering Temperature of BeO

In this study, we synthesized the BeO polycrystalline powder material using the precipitation method and used cold molding to shape it in pellets. All the pellets employed in luminescence measurements were sintered at 1200, 1400 and 1600 °C, for 4h for comparison studies. Structural, morphological and luminescent properties were investigated. The first objective of this work is to take advantage of the gain in OSL efficiency that is to be expected from the use of high (1600 °C) sintering temperatures. Another objective is to determine whether there exist changes in the relative OSL response, reusability and fading characteristics due to the sintering temperature-dependent variations in synthesized BeO or not.

4.1.1. Material Synthesis

BeO powders were synthesized using the precipitation synthesis route. In this method, polyethyleneimine solution (Sigma-Aldrich, analytical standard, 50 % (w/v) in H_2O) for polymerization and ammonium hydroxide solution (NH_4OH) (Sigma-Aldrich, ACS reagent, 28.0-30.0% NH_3 basis) as an initiator of the precipitate were used. As the precursor reactant, beryllium sulfate tetra-hydrate ($BeSO_4 \cdot 4H_2O$) (Aldrich, 99.99% trace metals basis) was used. A general experimental procedure of this method is as follows.

Firstly, beryllium sulfate was mixed with distilled water using a magnetic stirrer and waited until it completely dissolved. On the other hand, a certain amount of polyethyleneimine solution was dissolved in distilled water by stirring until it becomes completely transparent and was added to beryllium sulfate solution under vigorous stirring. Afterward, a sufficient amount of ammonia was slowly added to the mixed solution by controlling pH until a white precipitate formation was observed. The precipitate was dried on the heater. In order to burn formed organics and obtain BeO powder, the dried sample was calcined, using an ash furnace

(Nabertherm, model P330), at 800 °C with a 5 °C/min heating rate for 4 hours in an oxygen atmosphere.

A problem for BeO material is it's being toxic in powder form and cause severe lung disease when inhaled. However, in ceramic disc form, BeO is harmless for human health. In this work, BeO samples were studied in pellet forms having more settled OSL signals and providing also easy handling. A similar experimental procedure was presented by Guckan et al. (2017) for $CaSO_4$ pellets. The appropriate amount of powder material and pressure were determined through various measurements as 25 mg and 250 kg-force/cm^2, for 1 min, respectively. The BeO pellets with the density of 1.03 g/cm^3 were prepared in the form of disks with 6.15 mm in diameter and 0.82 mm in thickness, using a cold hydraulic press to avoid high temperatures and without using any binding material during production (Carver, model 3853-9). In order to impart strength and integrity, prepared pellets were sintered, using a box furnace (Thermoscientific, model Lindberg/Blue M™), at three different temperatures (1200, 1400 and 1600 °C, for 4h) in an oxygen atmosphere. After 1200, 1400, 1600 °C sintering processes, the shrinkage led to BeO pellets with 5.86, 5.71, and 5.03 mm diameter and 0.67, 0.66, and 0.54 mm thickness, respectively. As a result of shrinkage regarding sintering, the mass loss and the density increase were also observed in the studied BeO pellets. The masses were measured at 23.5, 23.5 and 23 mg for the indicated sintering temperatures. The evaluated density values of 1.30, 1.41 and 2.14 g/cm^3 are lower than that of the solid-state density of BeO (3.05 g/cm^3) and commercially used Thermalox (2.85 g/cm^3). Although the main reason is not known at the moment, the density difference may possibly originate due to the amount of material used, the applied pressure and the sintering temperatures in the material production stage.

4.1.2. Characterization of BeO

After sintering BeO pellets at three different temperatures (1200, 1400 and 1600 °C, for 4h), XRD analyses of the BeO pellets were performed to investigate

the role of the sintering temperature on the crystal structure of BeO. Figure 4.1 shows the phase identification of BeO pellets sintered for 4 hours, as a function of sintering temperature, using the XRD pattern. Analysis of the XRD data showed that all of the reflections are assigned to BeO phase with hexagonal structure. The patterns of BeO pellet samples match very well with (ICDD) PDF card no 98-016-3468. The cell parameters of the polycrystalline materials were calculated as follows: a=b=2.705 Å and c=4.394 Å for all the sintering temperatures. By the comparison of the characteristic XRD patterns, it was found that the crystallinity of the sintered BeO pellets was clearly improved with increasing sintering temperature. From XRD curves, the sharp higher intensity peaks with broad FWHM values were observed. Whereas, the lower intensity XRD peaks appeared with lower FWHM values. The sharpened diffraction peaks show that the intensity of diffraction increased with increasing sintering temperature, which means that the BeO grains have grown and the size of the crystallites is very fine (Wang et al., 2011). Regarding the grain sizes of the synthesized BeO pellets, it was clarified that there is a positive effect of higher sintering temperature on OSL characteristics which will be discussed in Section 0.

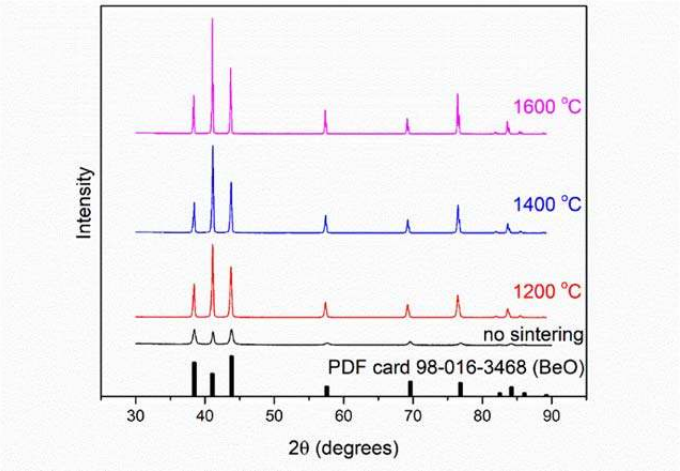

Figure 4.1. XRD patterns of BeO pellets sintered at three different temperatures with that of the reference Pdf Card and no sintered BeO pellet.

The morphology of BeO pellets sintered at 1200, 1400 and 1600 °C was investigated through SEM to figure out the particle's shapes and sizes. It is clear that different sintering temperatures would create differences in the surface morphology of BeO. Sintering is known as the phenomenon of heat transfer to material which leads to the reduction of the specific surface area of powder material in a porous structure. Through this way it causes the growth of the particle contact points, thereby causing the pore shape to change and the pore volume to shrink. Sintering briefly begins with forming of necks between particles contacting each other. Figure 4.2 shows SEM images of BeO pellets at various sintering temperatures. As it is seen in the images, it can be concluded that BeO particles sintered at 1200 °C just began to form necks and still maintain the porous structure at this temperature (see Figure 4.2a). When the sintering temperature was 1400 °C, besides the existence of the porous structure, the distribution of local neck-forming structures is increased inside the material (see Figure 4.2b). With the sintering process at 1600 °C, BeO is formed as a well crystalline material and particles in the material appeared to be as smoother, and bonded, producing a nonporous structure (see Figure 4.2c).

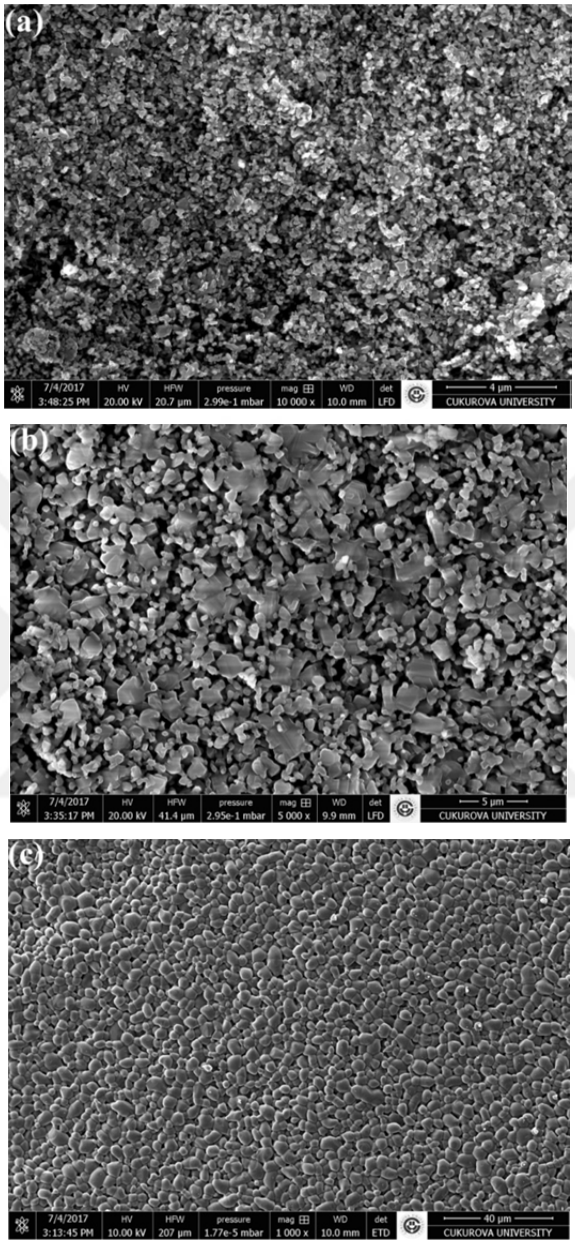

Figure 4.2. SEM images of BeO pellets sintered at three different temperatures; a) 1200 °C, b) 1400 °C, c) 1600 °C for 4h.

As it is also seen in the SEM images (see Figure 4.2), regularly formed repeated particle shapes and their narrow size distribution were observed in the samples. While the grain sizes were detected as around 100 nm (data not shown) for BeO pellets sintered at 1200 °C, for that of 1400 °C they changed due to forming necks between the particles in some regions of the crystalline surface. On the other hand, the grain size detected for BeO pellet sintered at 1600 °C is between 1- 5 μm (data not shown). It was clearly understood that the grains of BeO samples were grown with increasing sintering temperature. Furthermore, these results are consistent with the literature. Wang et al. (2011) reported that the increase in the average grain size of the studied BeO material was associated with the increasing calcination temperature.

On the other hand, the decreasing size of the BeO pellets themselves presented in Section 0, with increasing sintering temperature is due to the dimensional (or volumetric) shrinkage which causes the density increase in the molded powders (or pellets) by sintering.

4.1.3. TL and OSL Signals

In this work, we investigated the TL and OSL luminescence signals obtained from BeO pellets irradiated with 0.1 Gy beta dose. We carried out the TL and OSL measurements by firstly preheating BeO pellets at 110 °C for 60 s to eliminate unstable signals originating from shallow traps. Figure 4.3 shows the analyzed OSL decay curves of the samples sintered at 1200, 1400 and 1600 °C, during blue light stimulation for 200 s at room temperature.

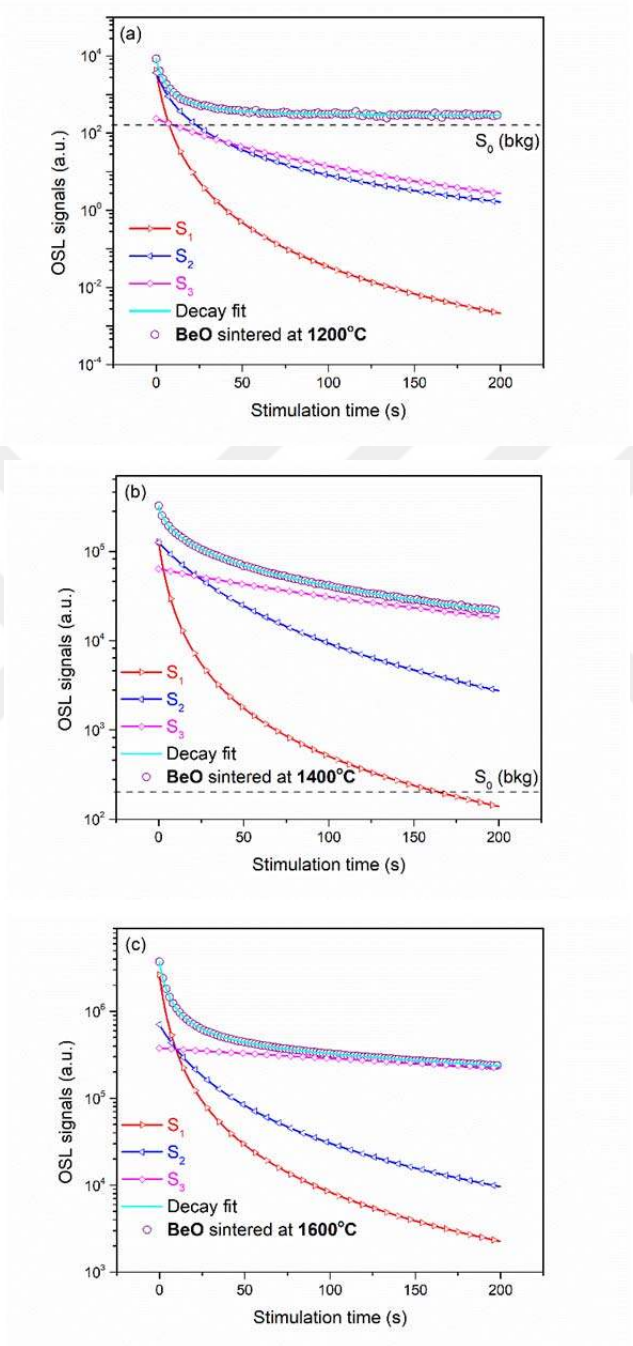

Figure 4.3. OSL signals with decay components of BeO pellets sintered at three different temperatures.

As is seen in Figure 4.3, all of the measured OSL decay curves were fitted to the resultant of three decaying functions of time using linear integration. In a previous study, Chen and McKeever (1997) have given a detailed discussion of this demonstration for the general order kinetic features of phosphorescence decay. This fitting technique was also used for prompt isothermal decay curves of MgB_4O_7:Dy,Na by Kitis et al. (2016). The model equation for these fittings can be written as

$$y = S_0(bkg) + S_1 + S_2 + S_3 + \cdots \tag{4.1}$$

$$I(t) = bkg + I_1\left[1 + (b_1 - 1)\frac{t}{\tau_1}\right]^{-\frac{b_1}{b_1-1}} + I_2\left[1 + (b_2 - 1)\frac{t}{\tau_2}\right]^{-\frac{b_2}{b_2-1}} + I_3\left[1 + (b_3 - 1)\frac{t}{\tau_3}\right]^{-\frac{b_3}{b_3-1}} + \cdots$$

where S_1, S_2 and S_3 are the general-order decay functions presenting the fast, the medium and the slow decay components of the OSL signal, respectively; bkg represents a background value of the signal; t is the stimulation time; $I(t)$ is the intensity of the OSL signals as a function of time; $I_{1,2,3}$, $\tau_{1,2,3}$ and $b_{1,2,3}$ are the amplitudes, the decay times and kinetic orders of the individual components, respectively. From the published curve fitting equation (see Eq. (4.1), $I_{1,2,3}$ amplitudes, $\tau_{1,2,3}$ decay times, $b_{1,2,3}$ kinetic orders and bkg values were determined and presented in Table 4.1 for BeO pellets. During these evaluations, the perfection of fitting curves was checked using the figure of merit (FOM) (Balian et al., 1977), and FOM values were found on trials for both two and three components for the comparison (see Table 4.1). In this work, due to the estimated FOM values, it was considered that the best curve fitting can be evaluated with the

three components. It was statistically performed that when the three components and bkg were used the FOM values were 1.25, 0.62 and 0.34 % for 1200, 1400 and 1600 ºC, respectively. It should be noted that the curve fitting using the three decay functions can only be accepted as an oversimplification of the real situation (the traps and transitions involved in the OSL production) and may not be enough to discover the charge trafficking.

Table 4.1. $\tau_{1,2,3}$ decay times and $b_{1,2,3}$ kinetic orders of the fitted OSL decay curves using two and three components with the figure of merit values for BeO pellets sintered at 1200, 1400 and 1600 °C.

	S_1 (fast component)			***S_2 (medium component)***			***S_3 (slow component)***				
	I_1 (count)	τ_1(s)	b_1	I_2 (count)	τ_2(s)	b_2	I_3 (count)	τ_3(s)	b_3	*bkg* (count)	*FOM* (%)
Using two components											
BeO (1200 °C)	4.2E+03	1.9	1.20	3.9E+03	8.2	2.05	-	-	-	2.86E+02	2.87
BeO (1400 °C)	1.6E+05	8.4	2.03	1.5E+05	82.2	2.04	-	-	-	9.54E+03	0.83
BeO (1600 °C)	3.0E+06	7.0	2.05	4.5E+05	119.9	2.05	-	-	-	1.77E+05	0.85
Using three components											
BeO (1200 °C)	4.2E+03	2.0	1.31	3.6E+03	6.2	1.69	2.4E+02	32.2	1.35	2.87E+02	1.25
BeO (1400 °C)	1.3E+05	6.6	2.05	1.3E+05	36.5	1.71	6.4E+04	233.7	2.03	2.86E+02	0.62
BeO (1600 °C)	2.6E+06	5.8	2.05	7.0E+05	26.2	2.04	3.8E+05	460.1	1.27	2.89E+02	0.34

The maximum OSL signal intensities of the BeO pellets increased with the increasing sintering temperature (see Figure 4.3). It demonstrates that the better crystal structure and morphology may affect the OSL signals positively and the material becomes optically superior with increasing particle size.

On the other hand, typical TL glow curves and the effect of OSL measurements (200 s OSL stimulation with blue LEDs) on TL glow curves of the BeO pellets were also investigated to determine optically active peaks of TL glow curves. In this work, all TL glow curves were recorded after being irradiated with a 0.1 Gy beta dose. Figure 4.4 shows TL and TL after OSL curves (residual TL) of BeO pellets.

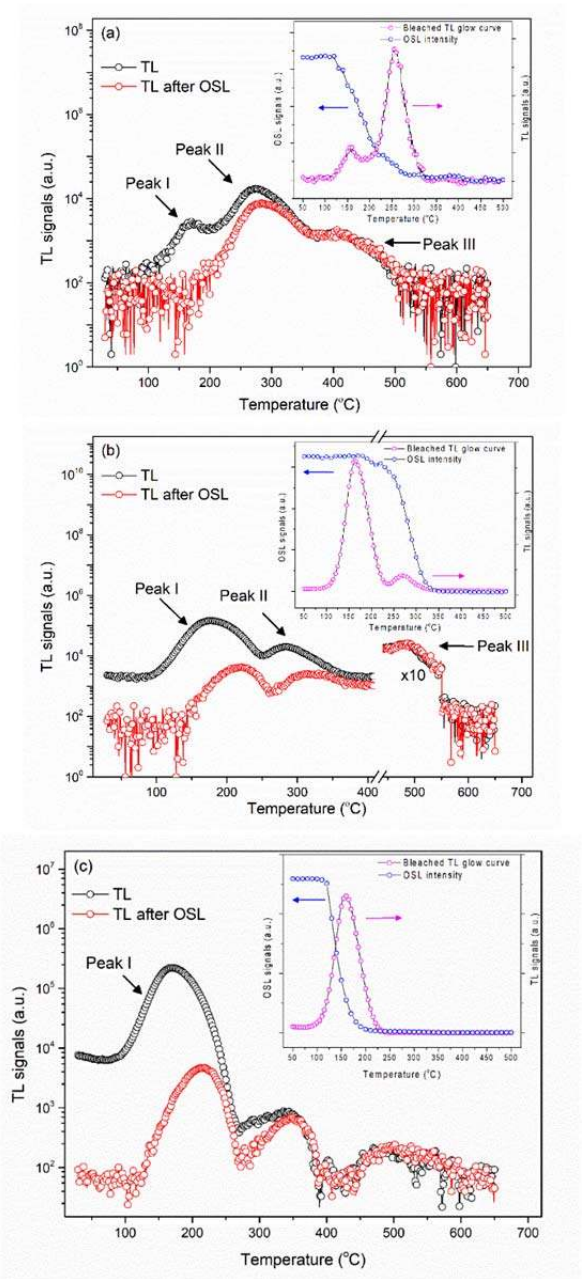

Figure 4.4. Direct TL glow curves and TL curves after OSL measurements, after irradiation with 0.1 Gy. Inset figure: Integrated OSL signals of BeO pellets as a function of preheating temperatures compared to the TL curve of the material obtained by subtracting TL and TL after OSL curves as a function of readout temperature.

As it is seen in Figure 4.4a, the TL glow curve of a BeO pellet (sintered at 1200 °C) showed three peaks located at 170, 275 and 395 °C. In the TL glow curve obtained after blue light stimulation, the first and second peaks were affected, whereas the third peak was not affected by the light exposure. In order to investigate whether this result suggests the source of the OSL signal might be associated with the 170 and 275 °C TL peaks or not, preheating study (thermal stability) experiment was performed in the temperature range from 50 to 500 °C with 5 °C increments. For this purpose, the samples were repeatedly heated to a preheat temperature after irradiation with 0.1 Gy, and the remaining OSL signals were measured each time. Following the OSL measurements, the samples were depleted using TL measurements (up to 650 °C). Changing intensity of OSL signals against the preheating temperatures was illustrated together with the bleached TL glow curve (obtained subtracting the residual TL glow curve from the TL glow curve) in the inset of Figure 4.4a. In this figure, the OSL signals were observed very stable up to 120 °C and started to decrease after this temperature. The OSL signal decrease correlates with the emptying of the 170 °C TL peak after the OSL stimulation. After the complete discharging of the TL traps responsible for the 275 °C TL peak, the OSL signals reach the zero level. It shows that the source of the OSL signals is perhaps associated with both the 170 °C and 275 °C bleached TL peaks and the OSL, most probably, employ the same recombination centers as the 170 °C and 275 °C bleached TL peaks.

The TL glow curve of a BeO pellet sintered at 1400 °C showed three peaks located at 175 °C, 275 °C and 475 °C (see Figure 4.4b). In the TL glow curve obtained after the optical stimulation of 200 s, the first and second peaks were affected, but the third peak was not affected by light exposure. In order to investigate the correlation between the source of the OSL signals and 175 °C and 275 °C peaks of the bleached TL glow curve, the preheating experiment described above was carried out. The intensities of OSL signals against the preheating temperatures were illustrated together with the bleached TL glow curve in the inset

of Figure 4.4b. Unlike the sample sintered at 1200 °C, the preheating studies for the samples sintered at 1400 °C, showed that after the complete discharging of the traps responsible for the 175 °C TL peak, the OSL signals had almost the same values during this process. The OSL signal was observed very stable and started to decrease only after preheating at 250 °C. Additionally, after the complete discharging of the TL traps responsible for the 275 °C TL peak, the OSL signals reached almost zero level. This suggests that the origin of the OSL signals might be associated with only the 275 °C TL peak. It is not clear whether the OSL and TL signals occurred from the same trap or not. But, it is also possible that the 275 °C TL peak is not due to a single trap distribution but an integration of overlapping traps. On the other hand, it is possible to say that even if the 175 °C TL peak has high light sensitivity, it did not contribute to the OSL signals and the optically extracted charges from the 175 °C trap may make some non-radiative transitions or the luminescence emission may not be at the transmittance range of the detection filter (340 ± 40 nm). Similar results for the commercial BeO chips were reported by Bulur and Goksu (1998).

Figure 4.4c shows that a TL glow curve (in logarithmic scale) of a BeO pellet sintered at 1600 °C reveals four peaks located at 170 °C, ~350 °C, ~490 °C and ~560 °C in the TL glow curve. After the OSL stimulation, the first peak located at 170 °C was affected by the OSL measurement (see Figure 4.4c). Hence, the origin of the OSL signals can be associated with the 170 °C TL peak. In order to investigate whether this peak is responsible for OSL or not, preheating measurements were also carried out and intensities of OSL signals against the preheating temperatures were depicted together with the bleached TL glow curve for this sample in the inset of Figure 4.4c. It can be seen in the figure that the decrease in OSL signals starts around 120 °C and ends around 200 °C. It shows that the source of the OSL signal can be assumed as indeed associated with the 170 °C TL peak, and the OSL signals may occur from the same recombination centers with the 170 °C TL peak.

4.1.4. X-ray Luminescence Spectra

The dominant luminescence in BeO is caused by the radiative annihilation of self-trapped excitons. When the temperature is higher than room temperature, luminescence is characterized by the 4.9 eV emission band with the full width half maximum > 1 eV. It is obvious that this emission band is placed far from the spectral range of maximum sensitivity of conventional photomultiplier tubes (PMT). On the other hand, it is known that the F-type centers in BeO single crystals show bright luminescence at 3-4 eV, so the observed luminescence spectrum is an integration of these two emission bands (3-4 eV & 4.9 eV) (Ogorodnikov et al., 1997). Figure 4.5 shows the X-ray luminescence spectra of the sintered BeO samples at 1200, 1400 and 1600 °C which were determined using a CCD spectrometer with a resolution of 1 nm at room temperature.

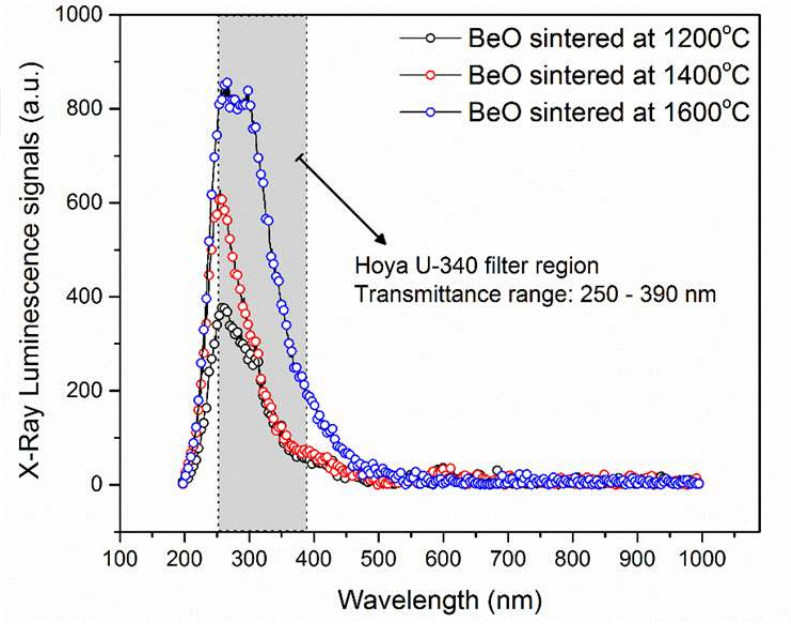

Figure 4.5. XL spectra of BeO pellets sintered at three different temperatures, 1200, 1400 and 1600 °C with a resolution of 1 nm at room temperature

The increasing sintering temperature of the BeO pellets enhanced the XL emission several times. The pellets sintered at 1200 and 1400 °C revealed the same narrow band emission from 200 to 350 nm with the same peak maximum and different emission intensities at 250 nm. The emission spectrum of the BeO pellet sintered at 1600 C was characterized by a wide band from 200 to 450 nm with two appearing emissions peaking at 250 and 325 nm due to the splitting of the states (between 6.2 and 2.7 eV corresponding to between 200 and 450 nm). The obtained emission is at the transmittance range of the Hoya U-340 filter which was used in all OSL and TL measurements in this study. However, even the used transmittance range was very convenient, the 3-4 eV emission band was recorded but the 4.9 eV band was not, because it is located at the upper limit of spectral sensitivity (Hoya U-340 filter). X-ray luminescence spectrum may be caused by excitons produced during X-ray irradiation. Even in this case, the XL emission band will not be observed during the OSL stimulation. Similar results were reported by Yukihara (2011). It should be noted that OSL counts obtained during the measurements are relative i.e. “uncorrected OSL counts” since the emission of 4.9 eV is not observed and more detailed studies related to the measurability of the entire luminescence band of BeO are necessary for this field.

4.1.5. Effect of Reading Temperature

Temperature dependence of an OSL signal is one of the most important sources providing the required information for understanding the luminescence mechanism of the material. In many materials, including BeO, a reduction in luminescence efficiency with temperatures higher than room temperature is observed and is called thermal quenching which increases the probability of non-radiative decays of the luminescence centers from the excited to the ground states (Bøtter-Jensen et al., 2003). The temperature dependence of the OSL signal can be expressed by a function of the type

$$I_{OSL}(T) = \eta(T) I_{OSL} = \frac{I_{OSL}}{1 + C exp(-E_Q/kT)} \quad (4.2)$$

where I_{OSL} is OSL signal, $\eta(T)$ is luminescence efficiency as a function of temperature; C is a constant, E_Q is the thermal activation energy for the non-radiative process; k is the Boltzmann constant and T is the absolute temperature (Bøtter-Jensen et al., 2003). In order to investigate the presence of thermal quenching, the effect of readout temperature on the OSL signal intensity was checked. After irradiating the BeO pellets sintered at 1200, 1400 and 1600 °C with 0.1 Gy beta dose and preheating the samples at 110 °C for 60 s, OSL signals were recorded with 200 s blue light stimulation at various readout temperatures from 50 °C to 110 °C with 5 °C increments. After each reading, the samples were deleted by TL readout up to 650 °C and the samples were irradiated again with the same dose (see Figure 4.6).

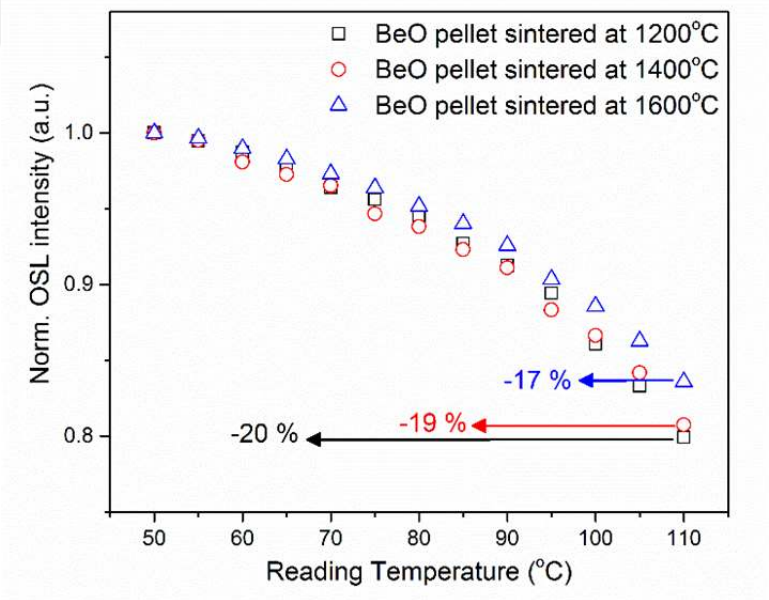

Figure 4.6. Normalized OSL intensities of 0.1 Gy irradiated and preheated (110 °C, 60s) BeO pellets at various readout temperatures.

It can be clearly seen from Figure 4.6 that the decrease of OSL signal intensity with increasing readout temperature implies a considerable amount of thermal quenching. The luminescence outputs obtained at 110 °C were reduced to nearly 20 % of the level obtained at 50 °C for the samples sintered at 1200, 1400 and 1600 °C. A similar thermal quenching effect is also predicted by Bulur and Goksu (1998) using the OSL measurements for Thermalox 995 to describe the effect of reading temperatures on OSL.

Another method to determine the thermal quenching effect caused by increasing readout temperature is to subtract the TL curve from the TL curve obtained with OSL stimulation (the so-called TOSL curve) (Duller et al., 1993). Here we obtained the TOSL curves for BeO pellets sintered at 1200, 1400 and 1600 °C. We performed 0.1 s pulsed stimulation with a 0.9 s time interval between the pulses. For each case with and without stimulation, the TL glow curves were obtained by heating the samples up to 425 °C at a heating rate of 3 °C /s. In Figure 4.7, the TOSL curves from BeO samples sintered at 1200, 1400 and 1600 °C were given together with both the TL curves and TL curves obtained with OSL stimulation.

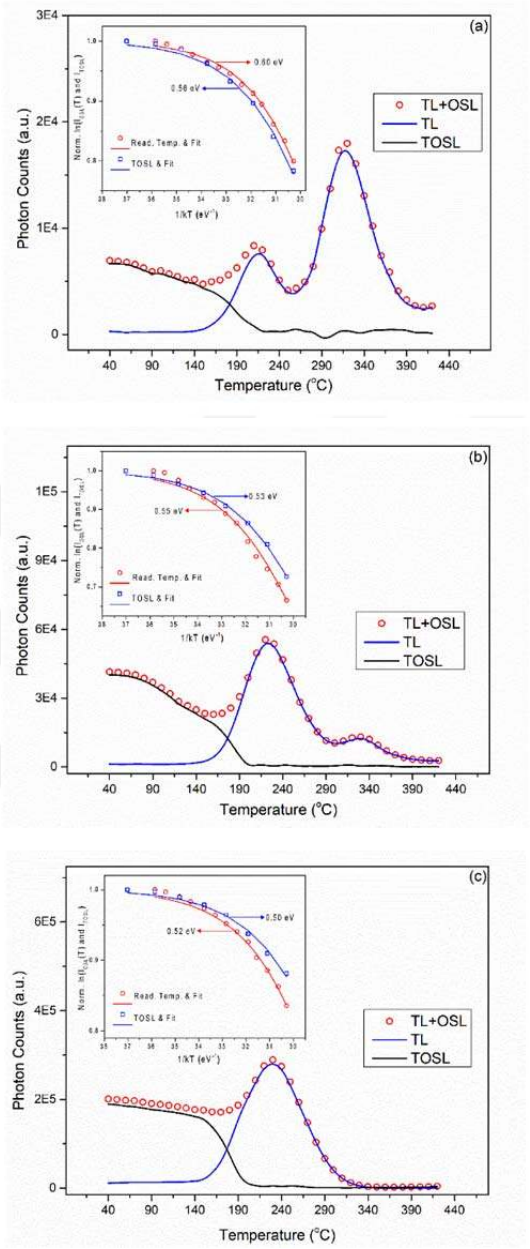

Figure 4.7. The TOSL curves obtained by subtracting the TL curves from the TL curves obtained with optical stimulation for the BeO samples sintered at a) 1200 °C, b) 1400 °C and c) 1600 °C. Inset figures: graphs of the natural logarithms of the OSL signals vs 1/kT obtained both from the TOSL curves and the various reading temperatures.

Thermal efficiency curves were depicted by plotting the natural logarithms of the OSL intensities obtained at various readout temperatures from Figure 4.6, versus the reciprocal of the readout temperatures, for each sintering temperature (see in the insets of Figure 4.7). Similarly, the natural logarithms of OSL intensities obtained from the initial parts of the TOSL curves and plotted against 1/kT are given in the insets of Figure 4.7, too, for each sintering temperature. Fitting the obtained data to Eq. (4.2, the quenching energies (E_Q) were found as 0.61, 0.55 and 0.53 eV for the samples sintered at 1200, 1400 and 1600 °C, respectively. On the other hand, when the method of TOSL was used, the quenching energies (E_Q) were determined as 0.57, 0.54 and 0.51 eV, for the samples sintered at the given temperatures, respectively (see Table 4.2).

Table 4.2. Thermal quenching parameters, E_Q and C values, of BeO pellets sintered at 1200, 1400 and 1600 °C.

Methods	***BeO (1200 °C)***		***BeO (1400 °C)***		***BeO (1600 °C)***	
	E_Q (eV)	C (a.u.)	E_Q (eV)	C (a.u.)	E_Q (eV)	C (a.u.)
Reading Temp	0.61	3 x 10^7	0.55	1 x 10^7	0.53	2 x 10^6
TOSL	0.57	8 x 10^6	0.54	5 x 10^6	0.51	7 x 10^5

No large spread of quenching energy values in E_Q estimated in the experiments arises from different sintering temperatures. In these two methods, the obtained E_Q values of BeO ceramic pellets are slightly higher than previously presented values of 0.48 and 0.52 eV in a CW-OSL study (Bulur and Goksu, 1998), similar to the E_Q values found as between 0.55 and 0.59 eV in an LM-OSL study (Bulur et al., 2010), similar to the E_Q value of 0.56 eV found in the lifetime measurements (P-OSL) (Yukihara, 2011), for BeO Thermalox ceramics. Recently,

E_Q values were determined as between 0.54-0.66 eV and 0.74-0.86 eV using U-340 filter for 2nd and 3rd TL peaks of the BeO Thermalox ceramic samples, respectively (Aşlar et al., 2017). The differences in the indicated E_Q values may be due to the sensitive temperature dependence of the BeO samples measured by different devices with different experimental accuracy.

4.1.6. Dose-Response of OSL signals

Dose-response behavior due to the OSL signals from the BeO pellets sintered at 1200, 1400 and 1600 °C, were investigated in the beta dose range between 0.1 Gy and 50 Gy. The exposure doses to the material were 0.1, 0.2, 0.5, 1, 2, 5, 10, 20 and 50 Gy. The OSL signals were obtained from the three BeO pellets for each dose value after preheating the samples at 110 °C for 60 s.

The plots of linearly fitted curves for the normalized integrated OSL signals (the sum of the counts obtained from 0 to 200 s) as a function of the radiation doses were given in Figure 4.8 for BeO pellets sintered at different temperatures. From the linear fit, the slope values were found to be 0.995, 0.994 and 1.002 for the BeO pellets sintered at 1200, 1400 and 1600 °C, respectively. Fitting parameters for each group of BeO pellets were presented in the inset table of Figure 4.8. As it was evaluated from the obtained slope values, the dose-response of this material sintered at different temperatures can be accepted as linear for the sintering temperatures of 1200, 1400 °C and 1600 °C.

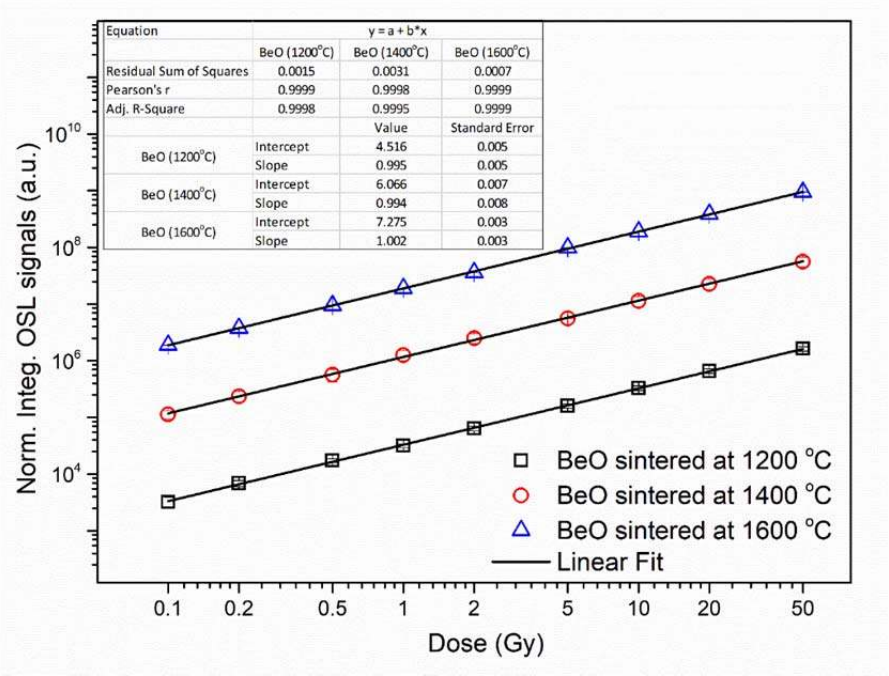

Figure 4.8. Dose-response curves of BeO pellets for different sintering temperatures. Each data point is the mean value of integrated OSL signals from the samples and the standard deviation of the means is represented by the error bars (not visible for some samples due to the error margin being too small).

For the present experimental conditions and for the present BeO pellets, the minimum detectable dose (MDD) values were estimated using the following equation:

$$MDD(Gy) = \frac{3\sigma\ (counts)}{Integrated\ CW-OSL\ signal\ per\ unit\ dose\ (counts\ \cdot G} \quad (4.3$$

where σ is the standard deviation in background counts integrated for time, 3σ implies MDD evaluated with 99.73% confidence level. An Integrated CW-OSL signal for time is obtained by subtracting the integrated background counts for the

same time from the area under the CW-OSL curve (Rawat et al., 2014). Using Equation (4.3, the MDD values were evaluated as 77, 18 and 0.1 mGy for BeO pellets sintered at 1200, 1400 and 1600 °C, respectively. It should be noted that these MDD values are considered only as an estimated order of magnitude because we do not perform sufficient measurements in the low dose range due to being the radiation source not precisely calibrated.

4.1.7. Reusability of OSL signals

The OSL measurements must be reusable for the dosimetric applications, i.e., the OSL signals must give the same response when it is re-measured under the same experimental procedures. In order to investigate the reusability, the OSL signals were obtained from the three annealed BeO pellets after preheating the samples at 110 °C for 60 s for 0.2 Gy beta dose. Residual OSL signals at each readout were deleted by performing TL readout (up to 650 °C) to prepare samples for the next measurement. The same type of measurement was repeated 10 times. In Figure 4.9, the normalized integrated OSL signals were plotted versus the number of the experimental cycles for the samples. OSL signals indicated very good reusability over 10 cycles. The maximum deviation of each integrated OSL output from that of the first readout was determined as 3.1 %, 4.3 % and 1.5 % for the BeO pellets sintered at 1200, 1400 and 1600 °C, respectively.

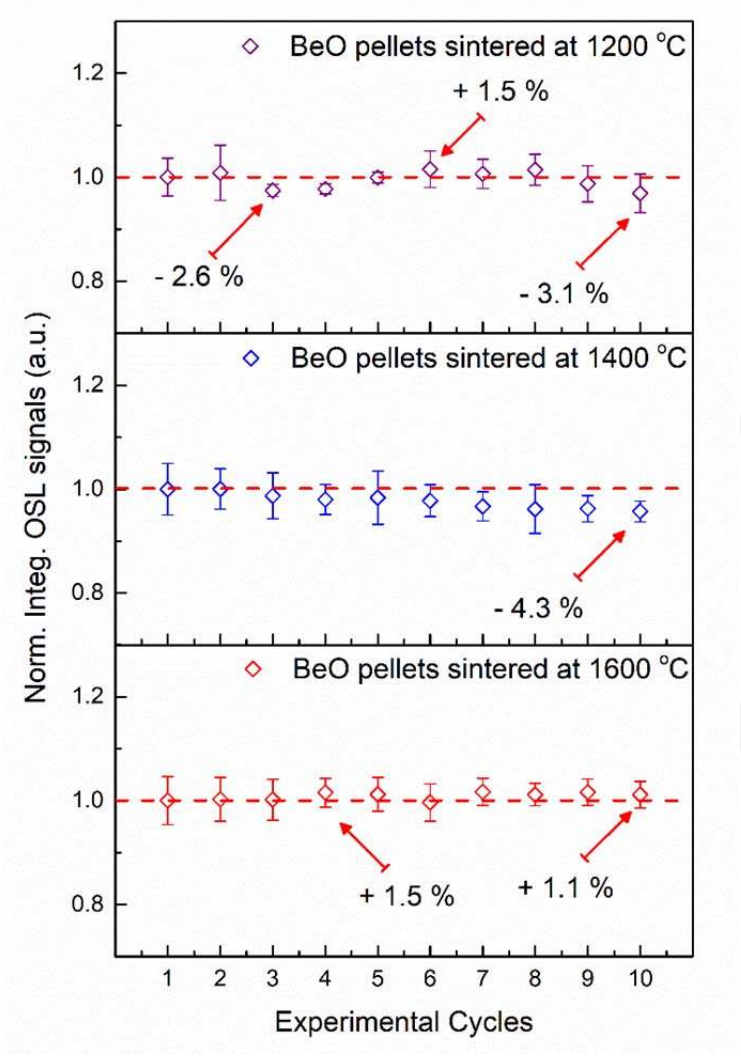

Figure 4.9. Reusability features of integrated OSL signals from BeO pellets irradiated with 0.2 Gy beta dose for different sintering temperatures. At each cycle the integrated OSL signals are the average of three BeO pellets and error bars are lying within 1 σ standard deviations of the mean.

4.1.8. Short Time Dark Storage of OSL signals

Luminescence signals of reliable dosimetric materials are expected not to fade upon storage after exposure. In order to investigate the fading characteristics of BeO pellets sintered at 1200, 1400 and 1600 °C, after irradiation with 1 Gy beta dose, the pellets were kept in dark at room temperature. The decay of the absorbed dose was observed for various storage times up to 24 h. The reductions in integrated OSL outputs obtained at room temperature following 110 °C for 60 s preheating for each 200 s OSL blue light stimulation, as a function of short storage time up to 24 hours was given for all BeO pellets in Figure 4.10. Here, we obtained the first readouts after half an hour following the radiation exposure. After the 24 h in which the shallow traps are responsible for the observed fading of the material, the deviations of the total OSL signals from the first readout values were found as -15.3 % and -2.5 % for the 1200 and 1400 °C sintering temperatures, respectively. No fading with respect to the first readout value was observed for the samples sintered at 1600 °C.

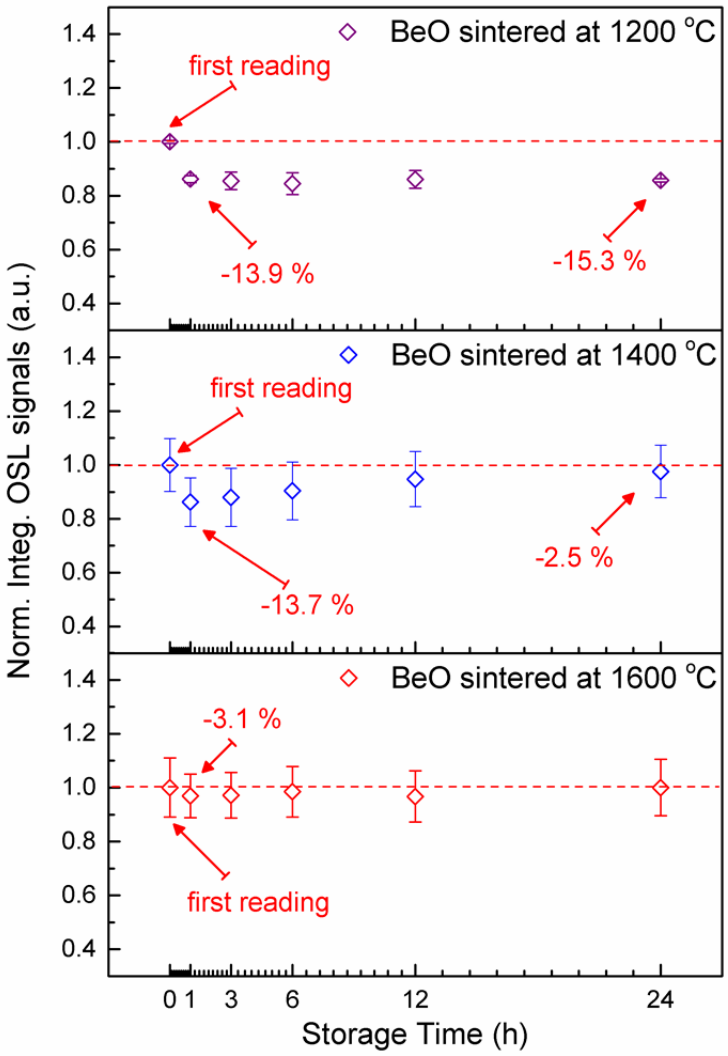

Figure 4.10. Decay of integrated OSL signals as a function of short storage time up to 24 h from BeO pellets for different sintering temperatures. The first readouts were recorded after half an hour following the radiation exposure with 1 Gy beta dose and preheating at 110 °C for 60 s. At each storage time, the integrated OSL signals are the average of three BeO pellets and error bars are lying within 1 σ standard deviations of the mean.

4.1.9. Discussion

Determination of appropriate sintering conditions study was done on BeO pellets prepared using the precipitation method and sintered at 1200, 1400 and 1600 °C. The variation of the structural, morphological and relevant dosimetric and luminescent properties of the BeO pellets was investigated as a function of the sintering temperatures.

The structural and morphological investigations revealed that the pellets have a polycrystalline wurtzite structure with a hexagonal crystal structure. With increasing sintering temperature, the crystallinity improved, the FWHM decreased and the grain size of the BeO pellets increased. The average grain size was observed between the range (1 - 5) μm for the BeO pellets sintered at 1600 °C (data not shown). It was demonstrated that increasing sintering temperatures with better crystallinity created higher OSL intensity (even without doping) at least up to 1600 °C upon optical stimulation (470 nm). Not only the maximum OSL intensity but also the total OSL (area under the OSL curve) from BeO pellets were increased with increasing sintering temperature. It appeared that the OSL signals from the BeO pellets sintered at 1200, 1400 and 1600 °C were not simple decay curves to be explained using the simple trap models. For this reason, we assumed that the luminescence processes involved are obeying the general order kinetics. With curve fitting techniques employing decaying functions, the OSL decay curves were analyzed and shown that the OSL signals can be best described using three components and background for each sintering temperature.

We evaluated the bleached TL curves (obtained subtracting residual TL glow curve from the direct TL glow curves) and step-annealing curves of BeO samples for each sintering temperature to observe the contribution to the OSL signals. The step-annealing curves of BeO samples sintered at 1200 °C showed that the source of the OSL signals is associated with both the 170 °C and 275 °C bleached TL peaks and the OSL employs the same recombination centers as the 170 °C and 275 °C bleached TL peaks. For the BeO pellets sintered at 1400 °C, we

suggested that the origin of the OSL signals might be associated with only the 275 °C TL peak. It is not clear whether the OSL and TL signals occurred from the same trap or not. But, it is also possible that the 275 °C TL peak is not due to a single trap distribution but an integration of overlapping traps. On the other hand, it is possible to say that even the 175 °C TL peak did not contribute to the OSL signals and the optically extracted charges from the 175 °C trap may make some non-radiative transitions or the luminescence emission may not be at the transmittance range of the detection filter (340 ± 40 nm). For the samples sintered at 1600 °C, the source of the OSL signal might be associated with the 170 °C TL peak, and the OSL signals probably occur from the same recombination centers with the 170 °C TL peak.

We compared the X-ray luminescence spectra of BeO pellets sintered at three different temperatures at 1200, 1400 and 1600 °C. The XL spectrum of the sample sintered at 1600 °C has a broad peak located between 200 and 450 nm with two peak maximums at 250 and 300 nm (between 6.2 and 2.7 eV) with different amplitudes from the other emissions of the samples sintered at 1200 and 1400 °C.

When we used the reading temperature method, the quenching energies were calculated as 0.61, 0.55 and 0.53 eV for the samples sintered at 1200, 1400 and 1600 °C, respectively. On the other hand, when the method of TOSL was used, the quenching energies were determined as 0.57, 0.54 and 0.51 eV, for the samples sintered at the given temperatures, respectively. Because the quenching energy values evaluated using the given two methods for the BeO pellets sintered at different temperatures don't have much difference between each other, it might be concluded that the thermal quenching characteristic of the BeO phosphor is the material's intrinsic characteristic and might not be associated with the sintering temperature.

The general characteristics of BeO pellets sintered at 1600 °C for use in dosimetry can be summarized as follows: *i)* Very high sensitivity to beta irradiation with a minimum detectable dose value of 8 μGy by calculating the whole OSL

signal *ii)* Wide range of linear response for beta dose exposures from 0.1 to 50 Gy *iii)* Very good reusability with the deviation of 1 % from the first cycle of ten repeated exposure and readout measurements *iv)* Almost no fading after delivering 1 Gy beta dose after 24 h at room temperature in dark.

4.2. Determination of Appropriate Calcination Conditions of BeO

In this study, undoped BeO nanoparticles were synthesized by using the co-precipitation and sol-gel methods. For a better sintering process of this nanostructure ceramic and achieving a promising OSL dosimeter with high luminescent efficiency, the role of calcination temperature and duration on nanograins' phase formation, morphology, grain-growth behavior, and luminescence characteristics were examined. The samples evaluated in this study were first calcined at 800, 900, 1000, 1100 and 1200 °C for 4h and then calcined for 2, 4, 6, 8, 10 and 24 h at a constant temperature of 900 and 1000 °C for the co-precipitation and sol-gel methods, respectively. OSL decay components and the lifetimes of each component were discussed in detail.

4.2.1. Material Synthesis

BeO samples were synthesized in two synthesis methods: co-precipitation and sol-gel. In the co-precipitation method, polyethyleneimine (Analytical standard, 50 % (w/v) in H_2O, Sigma-Aldrich) and ammonium hydroxide (NH_4OH) (ACS reagent, 28.0-30.0% NH3 basis, Sigma-Aldrich) solutions for polymerization and as an initiator of the precipitate were used, respectively. In the sol-gel method, ethylene glycol ($C_2H_6O_2$, 99.8% purity, Sigma-Aldrich) solution as a solvent and citric acid ($C_6H_8O_7$, 99.5% purity, Sigma-Aldrich) salts as a reactant, were used. In order to obtain BeO phosphors, the typical process of BeO synthesis begins using beryllium sulfate tetrahydrate ($Be(SO_4)x4H_2O$, %99.9, Sigma-Aldrich) salts as precursor reactants in two methods. Deionized water was prepared using the New Human Power ultra-purification system (Human Corporation, Korea) and used

throughout the synthesis. The general synthesis process has been performed earlier for the co-precipitation method (Altunal et al., 2019b; Altunal et al., 2020c) and the sol-gel method (Altunal et al., 2019a; Altunal et al., 2018) as reported by Altunal et al. In this study, while the calcination temperatures were selected as 800, 900, 1000, 1100 and 1200 °C, the duration times were 2, 4, 6, 8, 10 and 24 hours. After the calcination process, BeO samples were prepared in pellet form by using pure BeO powders for easy handling and to obtain stable luminescent signals from the surfaces of BeO. Here, for the preparation of pellets, the applied pressure was 500 kg force/cm^2 and the duration time was 1 min. Finally, the prepared BeO pellets were sintered to stabilize trap structures and achieve a uniform crystal structure at 1600 °C, for 4 h. In this study, thermal, structural and morphological analyses were performed by using BeO powders calcinated at different temperatures and durations, while luminescent characterizations were carried out using sintered BeO pellets. The number of the samples and their corresponding notations and preparation conditions were presented in Table 4.3.

.

Table 4.3. Sample numbers with their corresponding notations and preparation conditions

No.	**Synthesis method**	**Calcination temperatures** (°C)	**Calcination duration** (h)
P1.	Co-precipitation	800	4
P2.	Co-precipitation	900	4
P3.	Co-precipitation	1000	4
P4.	Co-precipitation	1100	4
P5.	Co-precipitation	1200	4
P6.	Co-precipitation	900	2
P7.	Co-precipitation	900	6
P8.	Co-precipitation	900	8
P9.	Co-precipitation	900	10
P10.	Co-precipitation	900	24
S1.	Sol-Gel	800	4
S2.	Sol-Gel	900	4
S3.	Sol-Gel	1000	4
S4.	Sol-Gel	1100	4
S5.	Sol-Gel	1200	4
S6.	Sol-Gel	1000	2
S7.	Sol-Gel	1000	6
S8.	Sol-Gel	1000	8
S9.	Sol-Gel	1000	10
S10.	Sol-Gel	1000	24

4.2.2. Characterization Results

In order to determine the calcination temperature of the precursors, the TG3+ model Mettler Toledo thermogravimetric (TGA) system was used. Measurements were conducted from ambient temperature to 1200°C, at a heating rate of 20°C/min in an air atmosphere. Crystallographic phases of BeO ceramic pellets were determined by using XRD patterns which were obtained using Rigaku SmartLab Diffractometer with Cu-Kα (40 kV, 30 mA) from 20° to 80° (2θ) with 0.02° (2θ) increments. Phase identification was carried out using the International Center for Diffraction Data (ICDD) PDF card 98-016-3468. For investigation of the surface morphology and grain sizes of the materials synthesized via two methods, the SEM micrographs were taken by using FE-SEM, Zeiss, Supra 55 with the spectral slit width of 1.5 nm at room temperature. The micrographs presented here were taken at 1000x and 5000x direct magnifications, 20 kV, and a spot size of 2.5. Using SEM micrographs, the sizes and the shapes of grains, as well as the number of grains can be obtained.

4.2.2.1. Thermal Decomposition of Precursors

In order to characterize decomposition and crystallization during ceramic powder processing and to determine optimum calcination temperatures, TG analyses were conducted by heating the samples from ambient temperature up to 1200 °C with a 20 °C/min heating rate. Figure 4.11 shows the TG curves of the beryllium sulfate salt, dried-gel precursor obtained as a result of sol-gel synthesis and precipitate precursor obtained as a result of co-precipitation synthesis. Here, when the precipitate precursor was semi-aqueous, the gel precursor had a very sticky formation before the thermal analysis was completely dried at 200 °C for 1 h and called dried-gel precursor.

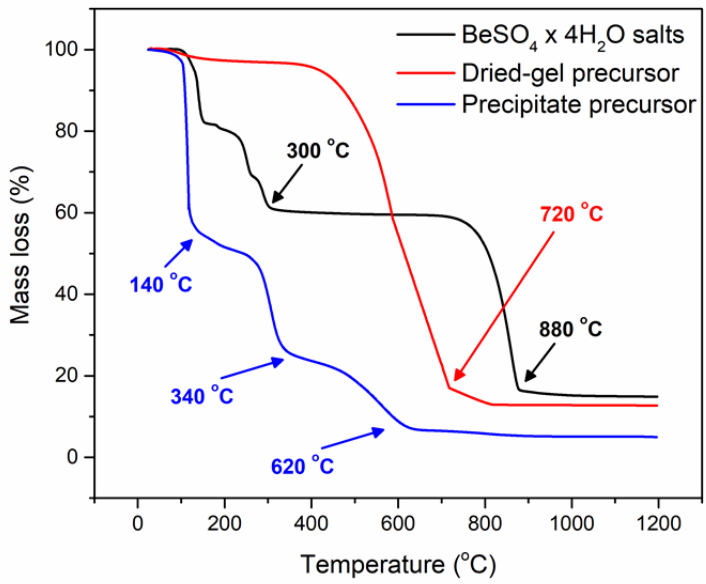

Figure 4.11. TG curves at a heating rate of 20 °C/min for the beryllium sulfate salt, dried-gel precursor and precipitate precursor.

As can be seen from the curve for $BeSO_4x4H_2O$ in Figure 4.11, beryllium salt has a multiple decomposition process, completed at 880 °C. Approximately 49 % of mass loss observed at temperatures below 300 °C was attributed to the removal of planar and crystalline water in the structure. The fact that the mass does not vary between 300 and 700 °C indicates that salt exists stable in this temperature region in the case of BeSO4. The reason for the sharp decline between 700 and 880 °C indicates that $BeSO_4$ decomposes in this range. Almost no change was observed in the TG curve after 880 °C. This indicates that the beryllium salts decompose after 880 °C to form the BeO structure (Wang et al., 2010). The total mass loss which occurred from ambient temperature to 880 °C was determined by 83.5 %. On the other hand, the red curve for the dried-gel precursor containing beryllium sulfate has two decaying parts, fast and slow. While the fast decaying part begins with the carbon being burned away from the structure and the decomposition of $BeSO_4$ salts, it ends at 720 °C with the formation of BeO (Purgato et al., 2010).

The mass loss which occurred from ambient temperature to 720 °C was determined by 83.2 %. After 5 % mass loss in the slow decaying part from 720 to 800 °C, mass loss up to 1200 °C was observed almost stable and total mass loss was determined as 87.3 %. The curve for the precipitate precursor solution containing water, beryllium sulfate, polyethyleneimine, and ammonia is more complex than the other TG curves. The mass loss areas were observed at 140 °C, 340 °C, and 620 °C, respectively. The first mass loss of approximately 44 % at the range of room temperature to 340 °C could be attributed to the absorbed solvent evaporation and the removal of planar and crystalline water in the structure. A mass loss of 92.3% occurs from ambient temperature up to 620 °C, which results from the dehydration (below 340 °C) and decomposition of the beryllium sulfate, degradation of polyethyleneimine organic polymer on the surface of nanoparticles, etc. (between 340 and 620 °C) (Arabi et al., 2016). As a result, it was observed that the dried-gel precursor obtained in the sol-gel method started to form BeO after 720 °C, however, the precipitate precursor obtained in the co-precipitation method produced BeO form after 620 °C. For this reason, suitable calcination temperature for both methods was selected as 800 °C or higher temperatures at which the loss of mass relatively ends. The reason for the calcination temperature to drop to lower temperatures than the conventional methods (see Figure 4.11) may be an expansion of the surface area of the salts and a decrease in the activation energy as a result of the formation of smaller units with the help of polymers, in both methods (Wang et al., 2010).

4.2.2.2. Phase Analysis of BeO powders

XRD analysis was performed to investigate the phases of BeO nano-powders synthesized using the co-precipitation and sol-gel methods after calcination treatments. Figure 4.12 shows the XRD patterns of BeO nano-powders calcinated at 800, 900, 1000, 1100, 1200 °C for 4 h. It can be seen from the figure that there are three highly sensitive Bragg reflections regarding (100), (002), and (101) orientations which are identities of BeO nano-particles. The patterns are assigned to the BeO phase with hexagonal structure and well-matched with the ICDD card no. 98-16-3468. As is seen in Figure 4.12, some peaks due to impurity phases can be observed at smaller angles of P1 and S2. In addition, halo peaks resulting from amorphous phases in the structure were observed in XRD patterns of P1, S1 and S2 samples. In the co-precipitation method, XRD peaks begin to sharpen after 900 °C, whereas in the sol-gel method, similar behavior was observed after 1000 °C. The intensities of the peaks are clearly affected by the calcination temperature, and it was observed that peak intensity increased with increasing calcination temperature, which means that the BeO grains have grown and the crystallites have been improved.

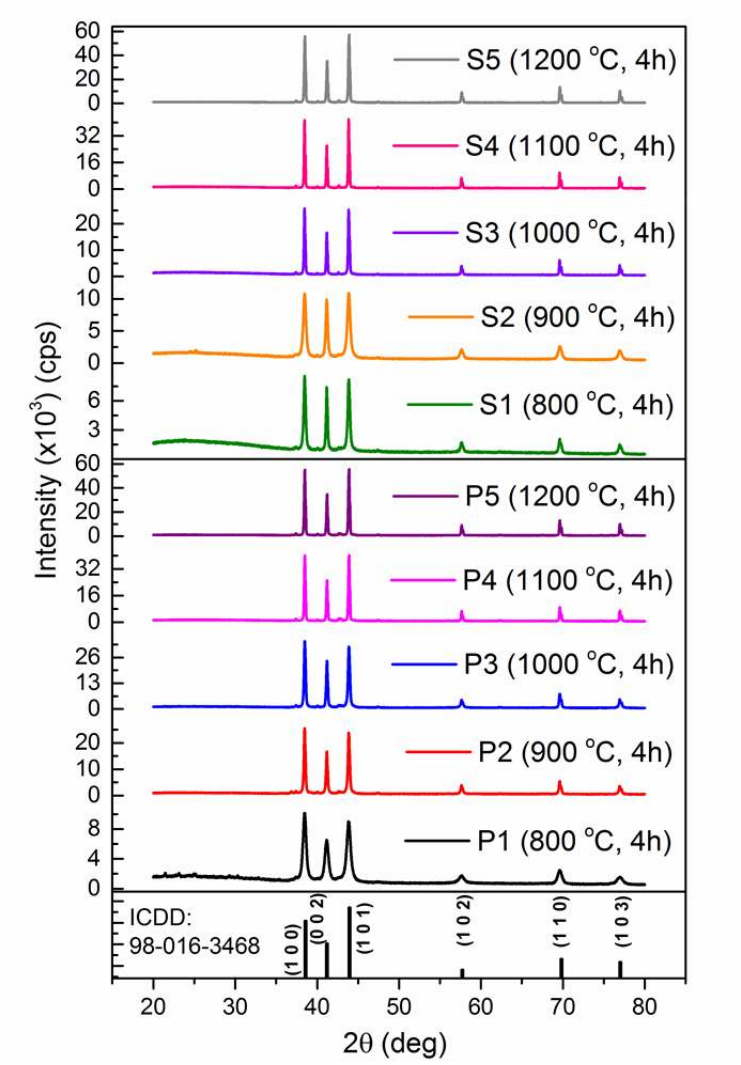

Figure 4.12. XRD patterns of BeO powders synthesized by co-precipitation (P series) and sol-gel (S series) methods calcining at different temperatures.

On the other hand, the effect of calcination durations on the phases of BeO nano-powders was also investigated for 2, 6, 8, 10, and 24 h. Figure 4.13 shows the XRD patterns obtained from the calcined BeO nano-powders at different durations. Similar to the XRD peak behavior of BeO nanoparticles obtained with different

calcination temperatures, it is seen that the peak intensities increased and the peaks sharpened with increasing calcination time. The results for the phase and crystallinity of BeO nanoparticles are in good agreement with the reported studies in the literature with different calcination conditions (Norazlina et al., 2013; Wang et al., 2010, 2011).

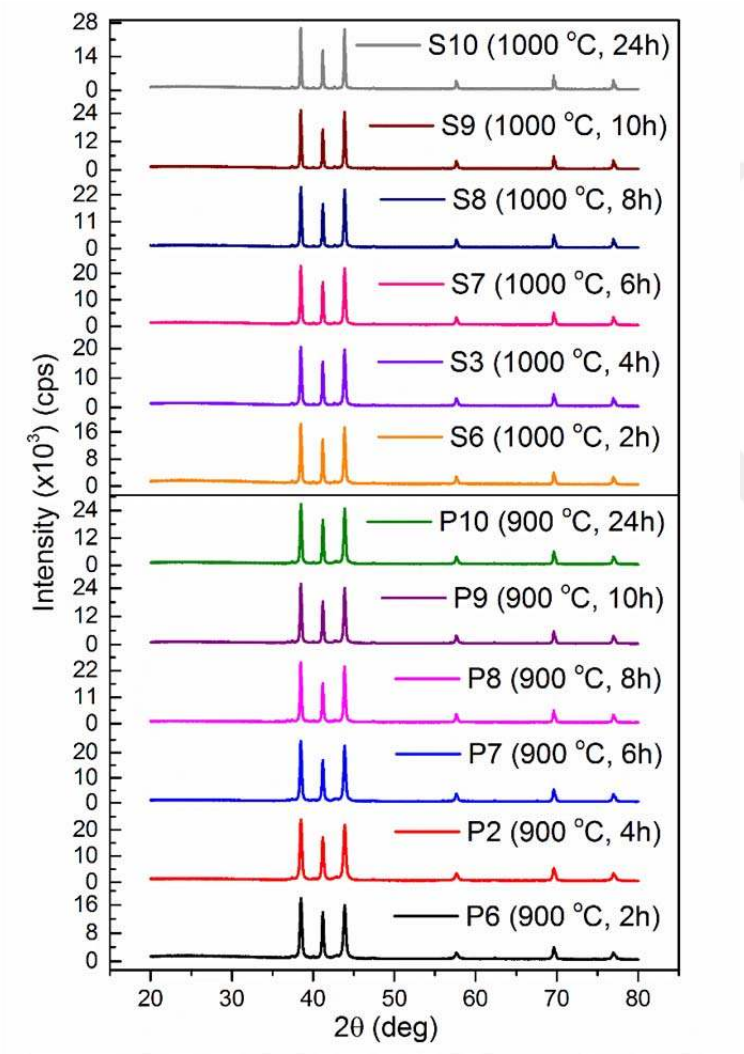

Figure 4.13. XRD patterns of BeO nano-powders calcinated at 900 °C (co-precipitation, P series), 1000 °C (sol-gel, S series) for varying calcination durations.

From the XRD data, all observed peak positions for BeO nano-powders for different calcination conditions in two synthesis methods are summarized in Table 4.4. As can be seen from table, the peak positions slightly shifted to the right and left with varying calcination conditions. This means that the lattice parameters and the defect concentration in the structure have changed. In the co-precipitation method, it can be said that the (100) and (101) oriented peaks shift to the right with increasing calcination temperature and time, and the concentration of defect in the structure increases (Norazlina et al., 2013). But according to microstrain calculations (to be discussed later), defect concentration decreases. On the other hand, in the sol-gel method, it is an indication that the (100) and (101) oriented peaks almost have no shift except the 1200 °C of calcination temperature state and the concentration of defects in the structure does not change. As a result, it can be suggested that the BeO nanoparticles synthesized by the sol-gel method produce fewer defects as they grow at the preferred orientation with increasing temperature and time (Norazlina et al., 2013).

Table 4.4. Diffraction peak positions (2θ), (100), (002) and (101) for BeO nano-powders synthesized by the co-precipitation (P series) and the sol-gel (S series) methods at different calcination conditions

Calcination Temperature (800, 900, 1000, 1100 and 1200 °C for 4 h)										
hkl	P1	P2	P3	P4	P5	S1	S2	S3	S4	S5
(100)	38.44°	38.46°	38.48°	38.49°	38.49°	38.47°	38.45°	38.47°	38.47°	38.51°
(002)	41.15°	41.18°	41.20°	41.21°	41.21°	41.16°	41.16°	41.17°	41.17°	41.22°
(101)	43.81°	43.85°	43.86°	43.89°	43.89°	43.84°	43.85°	43.85°	43.85°	43.89°
Calcination Time (900 °C (co-precipitation) and 1000 °C (sol-gel) for 2, 6, 8, 10, 24 h)										
hkl	P6	P7	P8	P9	P10	S6	S7	S8	S9	S10
(100)	38.46°	38.47°	38.47°	38.48°	38.49°	38.47°	38.48°	38.48°	38.48°	38.47°
(002)	41.17°	41.18°	41.18°	41.18°	41.20°	41.18°	41.18°	41.20°	41.18°	41.17°
(101)	43.86°	43.86°	43.85°	43.86°	43.88°	43.85°	43.86°	43.86°	43.85°	43.85°

Additionally, the average crystallite sizes of BeO nano-powders were calculated by the Debye-Scherrer formula (Klug et al., 1974);

$$D_{hkl} = K\lambda/(\beta_{hkl}cos\theta) \quad (4.4)$$

where D is the crystallite size (nm), hkl are the Miller indices of the planes being analyzed, K is a numerical factor frequently referred to as the crystallite-shape factor (K is typically 0.9 and a good approximation of cubic structure and (h00) line, but many theoretical calculations of the constant have been made (Dopita et al., 2013; Lele et al., 1966; Lngford et al., 1978), λ is the wavelength (λ = 0.15418 nm), θ is Bragg angle of the diffraction, and β is full width half maximum (FWHM) in radian. The calculated crystallite sizes for three highly sensitive peaks regarding (100), (002), and (101) orientations are given in Table 4.5.

The sharpening of diffraction peaks is related to the particle sizes and strains. Thus, sharpened diffraction peaks show larger crystallite sizes, while decreasing strain values indicate low defect concentration in the structure. In both methods, the particle sizes of BeO nano-powders increased significantly as the calcination

temperature and duration increased (see Table 4.5). Particularly, the observed particle sizes of BeO samples calcined at 1200 degrees are higher than that of other processing temperatures and times. The crystallite sizes of the BeO powders were mostly smaller than 50 nm and an increase in crystallite size of the BeO powders with the increase of calcination temperature and duration was observed, i.e. the higher the calcination temperature and duration, the larger the crystallite size of the BeO nanocrystals formed. In addition to the crystallite size, the strain (ε) values were evaluated by the following equation (Norazlina et al., 2013):

$$\varepsilon = \beta cos\theta/4 \tag{4.5}$$

where β is FWHM and θ is half of the diffraction angle. The evaluated strain values are presented in Table 4.5. It is seen from the table that strain values significantly decreased with increasing calcination temperature. This means that BeO nano-particles had fewer defects by the calcination treatments. Although there is no significant decrease in strain values with increasing calcination time, BeO nano-particles produced in both methods have lower strain values in 4 h by comparing that of 2, 6, 8, 10, and 24 h of calcination processes. This indicates that the BeO crystals produced during the 4 h calcination period have relatively fewer defects as they grow in preferred orientations. Another parameter is the dislocation density (δ) that influences many of the properties of materials (Theivasanthi et al., 2011). The dislocation densities in BeO nano-particles were determined using an equation:

$$\delta = 1/D^2 \tag{4.6}$$

where D is the crystallite size of the BeO nano-particles. Dislocation density values calculated using Equation (4.6) are presented in Table 4.5. As seen in table, the increasing calcination temperature and time and the dislocation density in the

structure decreased and the stress in the structure created by the calcination process led to the growth of the BeO nano-particles in the preferential orientations. As a result of the phase analyzes, it was found that the crystallinity, defect structures and physical properties of the BeO nanoparticles depended strongly on the calcination temperature and duration.

Table 4.5. Structural parameter of BeO nano-particles synthesized by the co-precipitation (P series) and the sol-gel (S series) methods at different calcination conditions

	FWHM, β (°)			**Crystallite size, D (nm)**			**Micro strain, ε x 10^{-2}**			**Dislocation density, δ (10^{20})**		
	(100)	(002)	(101)	(100)	(002)	(101)	(100)	(002)	(101)	(100)	(002)	(101)
P1	0.45	0.50	0.54	19.35	17.70	16.62	10.59	11.73	12.49	5.17	5.65	6.02
P2	0.22	0.22	0.25	39.11	40.29	36.10	5.21	5.15	5.75	2.56	2.48	2.77
P3	0.22	0.21	0.25	39.91	41.85	35.17	5.09	4.96	5.90	2.51	2.39	2.84
P4	0.17	0.17	0.19	50.85	52.89	48.35	3.99	3.92	4.29	1.97	1.89	2.07
P5	0.16	0.15	0.18	54.89	57.82	49.04	3.70	3.59	4.23	1.82	1.73	2.04
P6	0.29	0.24	0.33	30.77	36.20	27.46	6.63	5.73	7.56	3.25	2.76	3.64
P7	0.25	0.24	0.28	35.52	36.58	32.01	5.78	5.67	6.48	2.82	2.73	3.12
P8	0.24	0.22	0.27	36.85	40.29	33.29	5.53	5.15	6.23	2.71	2.48	3.00
P9	0.23	0.22	0.26	37.97	40.85	34.70	5.35	5.08	5.98	2.63	2.45	2.88
P10	0.22	0.21	0.25	39.91	41.68	36.10	5.08	4.98	5.75	2.51	2.40	2.77
S1	0.39	0.27	0.41	22.75	33.30	22.01	8.95	6.23	9.43	4.40	3.00	4.54
S2	0.28	0.22	0.30	31.35	40.42	29.55	6.52	5.13	7.02	3.19	2.47	3.38
S3	0.18	0.19	0.20	49.17	47.61	44.40	4.14	4.36	4.67	2.03	2.10	2.25
S4	0.16	0.16	0.18	54.27	54.20	49.81	3.75	3.83	4.17	1.84	1.85	2.01
S5	0.13	0.12	0.13	66.78	73.30	71.31	3.02	2.83	2.91	1.50	1.36	1.40
S6	0.22	0.20	0.24	39.15	43.27	36.57	5.20	4.80	5.67	2.55	2.31	2.73
S7	0.22	0.20	0.25	39.39	43.38	36.15	5.16	4.78	5.74	2.54	2.31	2.77
S8	0.22	0.20	0.24	40.45	44.69	37.19	5.01	4.64	5.58	2.47	2.24	2.69
S9	0.20	0.19	0.22	44.28	45.57	40.82	4.59	4.55	5.08	2.26	2.19	2.45
S10	0.18	0.19	0.20	47.21	47.62	44.40	4.14	4.36	4.67	2.12	2.10	2.25

4.2.2.3. Morphological Analysis of BeO powders

SEM analyses were carried out to investigate the effect of calcination conditions on grain size and morphology of the calcinated BeO powders and the sintered pellets. SEM micrographs corresponding to powders samples which were calcinated at 800, 900, 1000, 1100, 1200 °C for 4 h in two synthesis methods, co-precipitation, and sol-gel, are given in Figure 4.14 and Figure 4.15, respectively. According to the SEM micrographs of the calcinated powders shown in Figure 4.14 and Figure 4.15, different surface morphologies for the two synthesis methods were observed with varying calcination temperatures. The micrographs of the samples show that the particle sizes and shape begin to appear as the calcination temperature increases. Moreover, as the calcination temperature increases, particle boundaries become increasingly evident with increasing particle sizes, and particle shapes become more orderly. While it can be said that clustering and homogeneous structures started to be observed with 900 °C of calcination temperature for BeO powders produced with the co-precipitation method (see the SEM micrograph of sample P2. in Figure 4.14), the regular situation starts with 1000 °C for BeO powders produced with the sol-gel method (see the SEM micrograph of sample S3. in Figure 4.15). BeO particles produced by the sol-gel method have a more uniform distribution, as opposed to the strong agglomeration of samples produced by the co-precipitate method since the open structure of the gelatinous condition consisting of the precursor material in the sol-gel process allows the beryllium crystal to freely aggregate (Kim et al., 2008; Rajaeiyan et al., 2013). On the other hand, SEM images of BeO pellets sintered at 1600 °C for 4h prepared from BeO nano-powders obtained after varying calcination temperatures were taken for both synthesis methods, and presented in Figure 4.14 for the co-precipitation method and in Figure 4.15 for the sol-gel method. In the SEM images of BeO pellets, it can be seen that the particles with decreasing specific surface areas in the hollow structure were well-bonded to each other by increasing contact points through the sintering process. BeO pellets prepared from the nano-particles with homogeneous

structures started to be obtained by calcination processes of 900 °C in the co-precipitation method and 1000 °C in the sol-gel method have created a smoother and non-porous surface after sintering treatment. The grain sizes were found between 2 and 70 μm in both methods (see Figure 4.14 and Figure 4.15). The calcination process has significant effects on phase crystallization, phase transformation, crystal size and, consequently, the surface area.

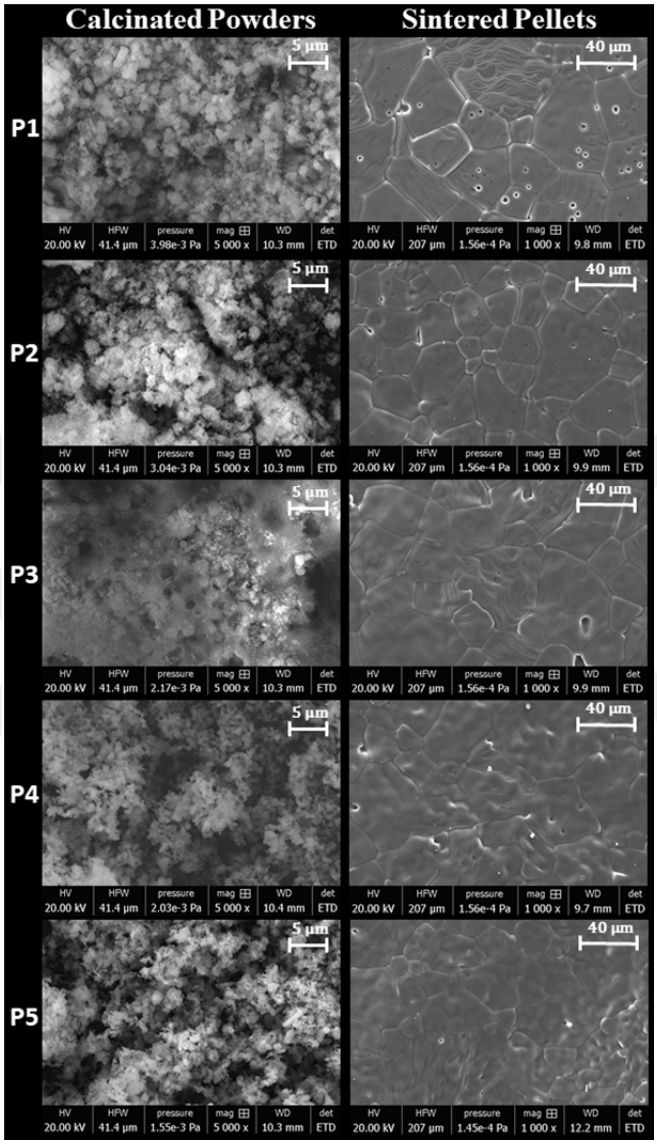

Figure 4.14. SEM micrographs of BeO nano-powder and pellet samples. BeO nano-powders synthesized by co-precipitation (P series) method calcining at 800 °C (P1), 900 °C (P2), 1000 °C (P2), 1100 °C (P3), 1200 °C (P5) for 4 h. BeO pellets were sintered at 1600 °C for 4 h after calcination treatments.

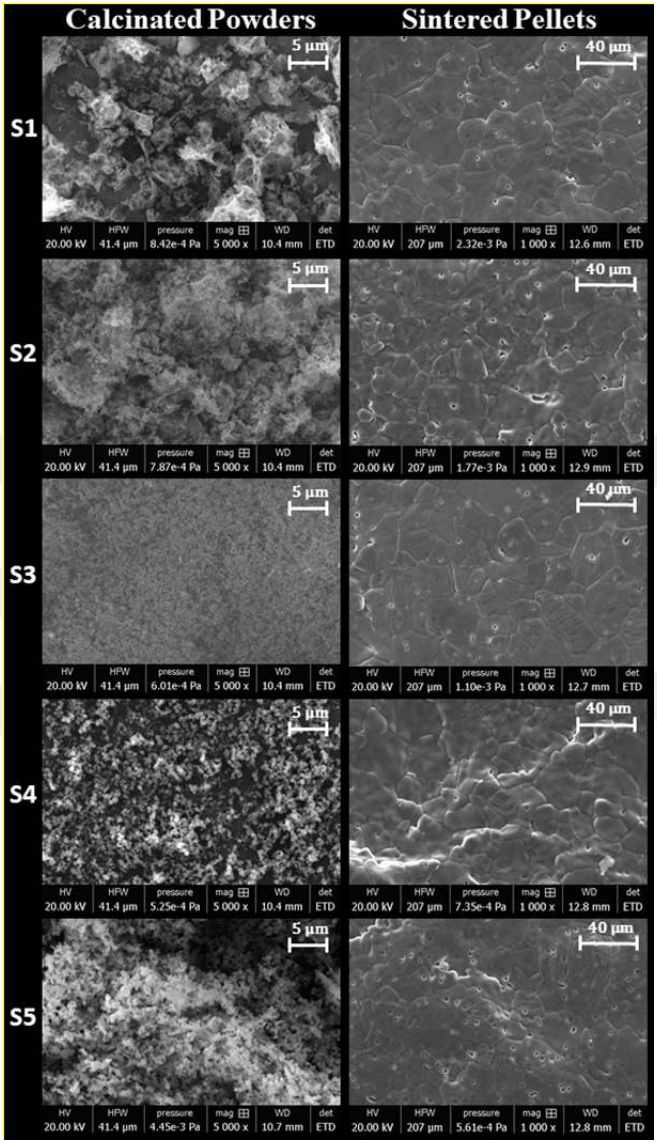

Figure 4.15. SEM micrographs of BeO nano-powder and pellet samples. BeO nano-powders synthesized by Sol-gel (S series) method calcining at 800 °C (S1), 900 °C (S2), 1000 °C (S3), 1100 °C (S4), 1200 °C (S5) for 4 h. BeO pellets were sintered at 1600 °C for 4 h after calcination treatments.

However, the effects of calcination time on the morphologies of BeO powder and pellet samples were also studied, since a number of substances that disappear from the structure during calcination may also cause significant changes in the properties of the final product. Figure 4.16 and Figure 4.17 show the SEM micrographs of BeO powders calcinated at 900 °C (co-precipitation synthesis), 1000 °C (sol-gel synthesis) for varying calcination duration (2, 8, 24 h) and BeO pellets sintered at 1600 °C, 4h prepared from BeO nano-powders obtained after mentioned calcination duration, respectively. While the particle sizes of BeO nano-powders increased significantly with increasing calcination time, it can be concluded that a minimum of 4 h of calcination duration is needed to obtain homogeneous structures for both methods. In both methods, the surfaces of BeO ceramics calcined in 24 hours were found very different from the surfaces of ceramics that were calcined in 4 h. It can be concluded that the 8 h calcination condition can be a transition process from a relatively regular surface morphology to a more irregular structure.

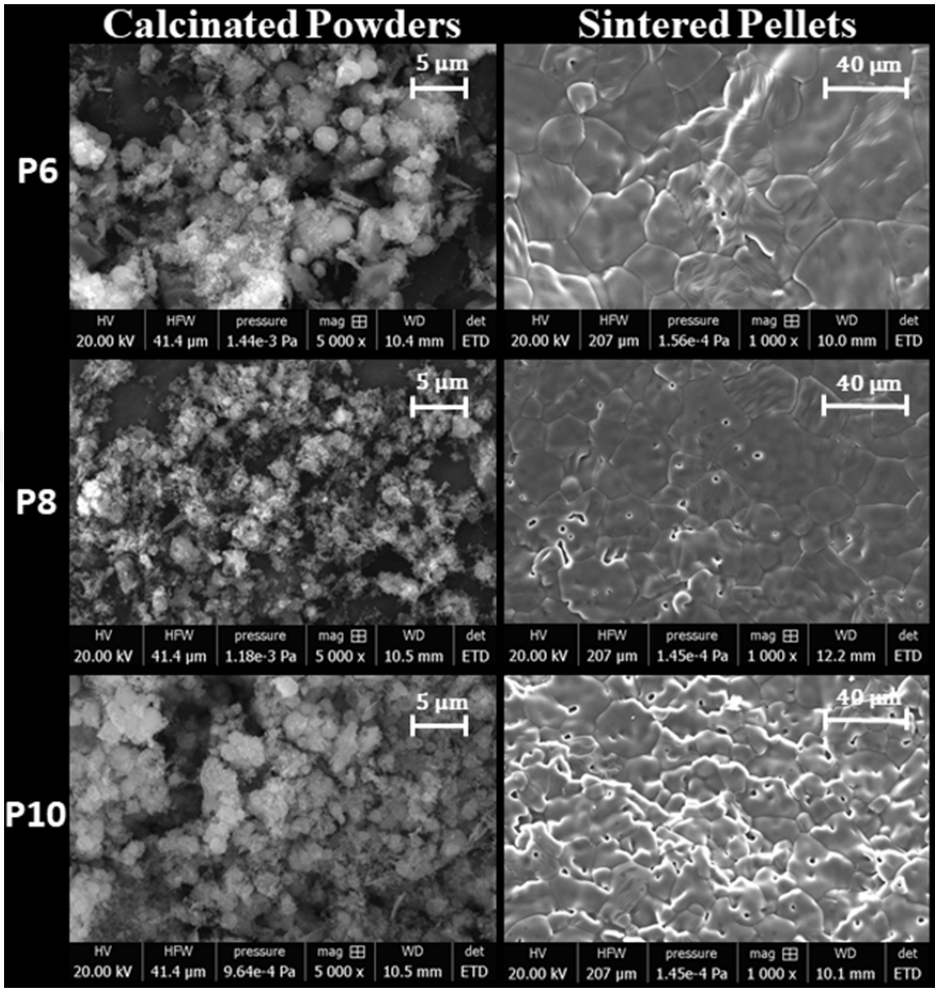

Figure 4.16. SEM micrographs of BeO powder and pellet samples. BeO nano-powders were calcinated at 900 °C (co-precipitation, P series), for varying calcination duration, 2 h (P6), 8 h (P8), 24 h (P10).

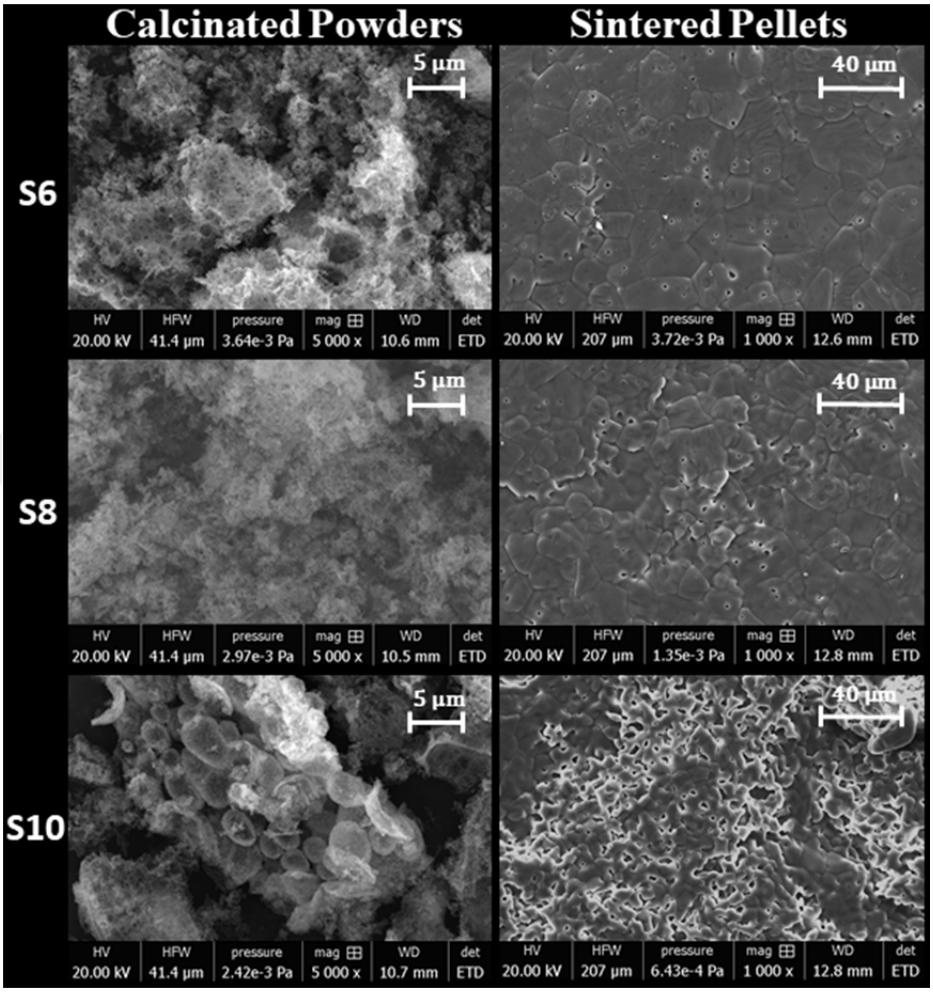

Figure 4.17. SEM micrographs of BeO nano-powder and pellet samples. BeO nano-powders were calcinated at 1000 °C (sol-gel, S series) for varying calcination duration, 2 h (S6), 8 h (S8), 24 h (S10).

4.2.3. Luminescence Results

After the thermal analysis of precursors, all the BeO nano-powders were prepared in pellet form. Then, all the BeO pellets were sintered at the pre-determined sintering condition, 1600 °C for 4 h (Altunal et al., 2019a; Altunal et al., 2019b; Altunal et al., 2020c; Altunal et al., 2018). Luminescence measurements were carried out to understand the effect of calcination procedures applied before

sintering on luminescence signals rather than revealing the inherent dosimetric identity of the material.

4.2.3.1. RL Emissions of BeO Pellets

The RL spectra of BeO pellets produced under different calcination conditions and using two different methods were studied between 200 and 1000 nm to obtain initial information about the positions and general appearance of RL bands. All the studied RL spectra showed a similar broad emission peak located between 200 and 450 nm with a maximum of 230 nm. Figure 4.18 shows the typical RL spectra of BeO pellets synthesized using co-precipitation and sol-gel methods, calcinated at 900 °C and 1000 °C for 4h, respectively. The observed dominant radioluminescence emission is associated with the radiative annihilations of self-trapped excitons in BeO during x-ray irradiations (Altunal et al., 2019a; Altunal et al., 2019b; Ogorodnikov and Kruzhalov, 1997; Ogorodnikov et al., 1995). In the literature, BeO has two characteristic luminescence bands between 300 and 400 nm, and 250 nm. Even if we assume that RL emission bands and OSL emission bands correlate, only luminescence from 300-400 nm can be measured, since the luminescence signals from the 250 nm luminescence band will not be in the transmittance range of the photomultiplier tube and Hoya U-340 filter used in OSL measurements (Altunal et al., 2019a; Altunal et al., 2019b; Altunal et al., 2020c). On the other hand, as an unexpected result for BeO pellets, a low sensitive peak located between 670 and 850 nm was observed for two synthesis methods. This observed emission is associated with the oxygen defects in BeO that may act as anion defects in the structure. It is known that such anion defects occurring during synthesis in the structure may show large emissions at high wavelengths in RL measurements (Tavernier et al., 2006). Oxygen vacancies in the structure may have been formed since the hydroxyl groups contained in the gel- and precipitate-precursors before calcination in the sol-gel and co-precipitation methods could not be removed by an aging process which should last longer under normal conditions (Jones, 1990).

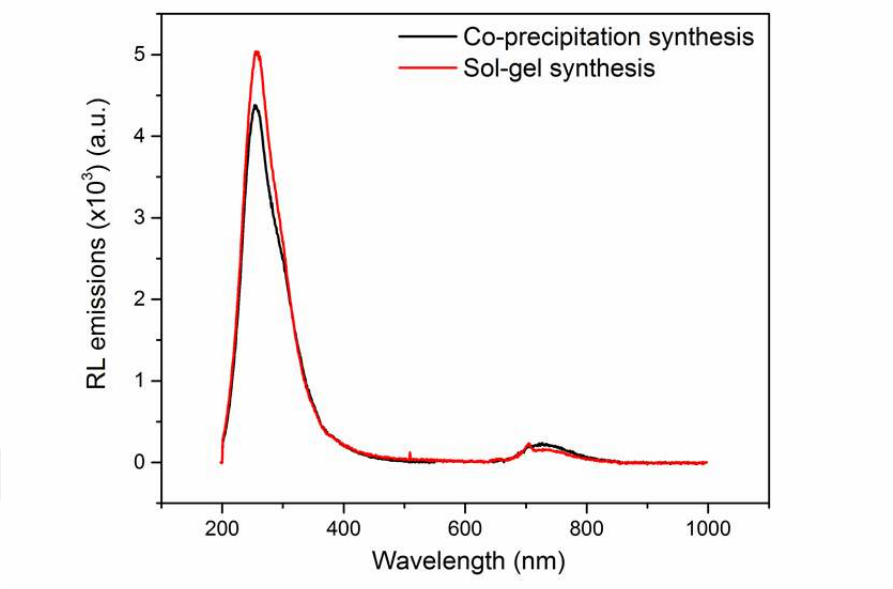

Figure 4.18. RL spectra of the sintered BeO ceramic pellets calcinated at 900 °C (P2, co-precipitation), 1000 °C (S3, sol-gel) for 4h.

The effects of calcination conditions on RL emission intensities of BeO pellets were also investigated. Figure 4.19 shows the integrated RL emission signals obtained from the BeO pellets which were calcinated at different calcination conditions in co-precipitation and sol-gel synthesis. In Figure 4.19a, the maximum integrated RL emission signals were obtained from the BeO pellets calcinated at 900 °C for co-precipitation synthesis and 1000 °C for sol-gel synthesis. Additionally, in both methods, the integrated RL emission signals of BeO pellets increased when the calcination duration is 4 h (see Figure 4.19b). It was observed that there was a decrease in RL signals with increasing calcination durations. The maximum reduction in RL signals is 2 hours for the co-precipitation method and 24 hours for the sol-gel method.

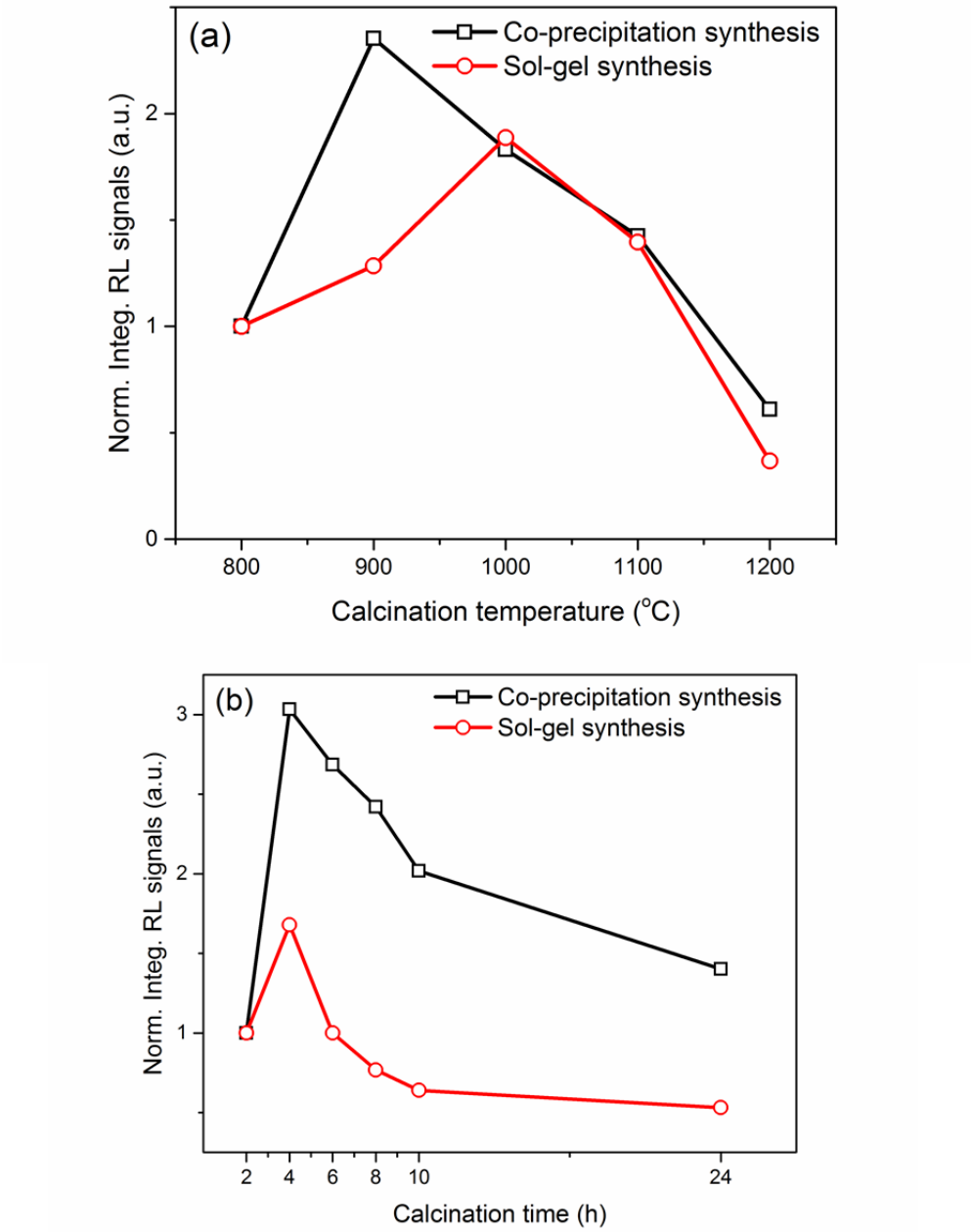

Figure 4.19. Integrated RL signals of BeO pellets synthesized by co-precipitation and sol-gel methods calcining (a) at 800 °C, 900 °C, 1000 °C, 1100 °C and 1200 °C for 4 h; (b) at 900 °C (co-precipitation), 1000 °C (sol-gel) for varying calcination durations, 2, 4, 6, 8, 10, 24 h.

4.2.3.2. TL Signals of BeO pellets

To see the effect of calcination conditions and synthesis methods on TL characteristics of BeO pellets, TL measurements were carried out by heating the pellets irradiated with 0.5 Gy dose, from room temperature up to 650 °C with a 3 °C/s heating rate without preheating procedure. Figure 4.20 shows the typical TL glow curves of BeO pellets produced using co-precipitation and sol-gel synthesis and calcinated at 900 °C and 1000 °C for 4h, respectively. At the first view, it was observed that TL signals of BeO pellets prepared by the co-precipitation method are more sensitive than TL signals produced by the sol-gel method and TL glow curves in both methods have a high precision peak at 170 °C and a shoulder peak around 250 °C (see Figure 4.20a). To view better the luminescence signals located in deep traps, TL glow curves were plotted on the logarithmic scale and presented in Figure 4.20b. It was observed that TL glow curves obtained with both methods have six similar trap regions. Investigations on the luminescence properties of BeO reveal three main TL peaks at ∼75 °C, ∼200 °C and ∼340 °C having their exact positions depending on the heating rate used to record the TL curve (Bulur and Goksu, 1998). High-temperature glow peaks at 530 and 630 °C were also observed in ‘‘Thermalox 995’’ (Hobzova, 1980). Additionally, the results are compatible with BeO dosimeters prepared in different forms. TL glow curve of the Nuclear Quality BeO disk showed almost the same behavior as that of the S series BeO pellets (Scarpa, 1970). Similar to TL glow curves of P series BeO pellets, TL glow peaks at 180 °C were observed from the BeO:Li (0.5 mol %) and BeO:Na (0.5 mol %) phosphors (Yamashita et al., 1974). Furthermore, the results are also in good agreement with the reported TL characteristics of BeO pellets synthesized by using co-precipitation (Altunal et al., 2019b; Altunal et al., 2020c) and sol-gel (Altunal et al., 2019a) methods.

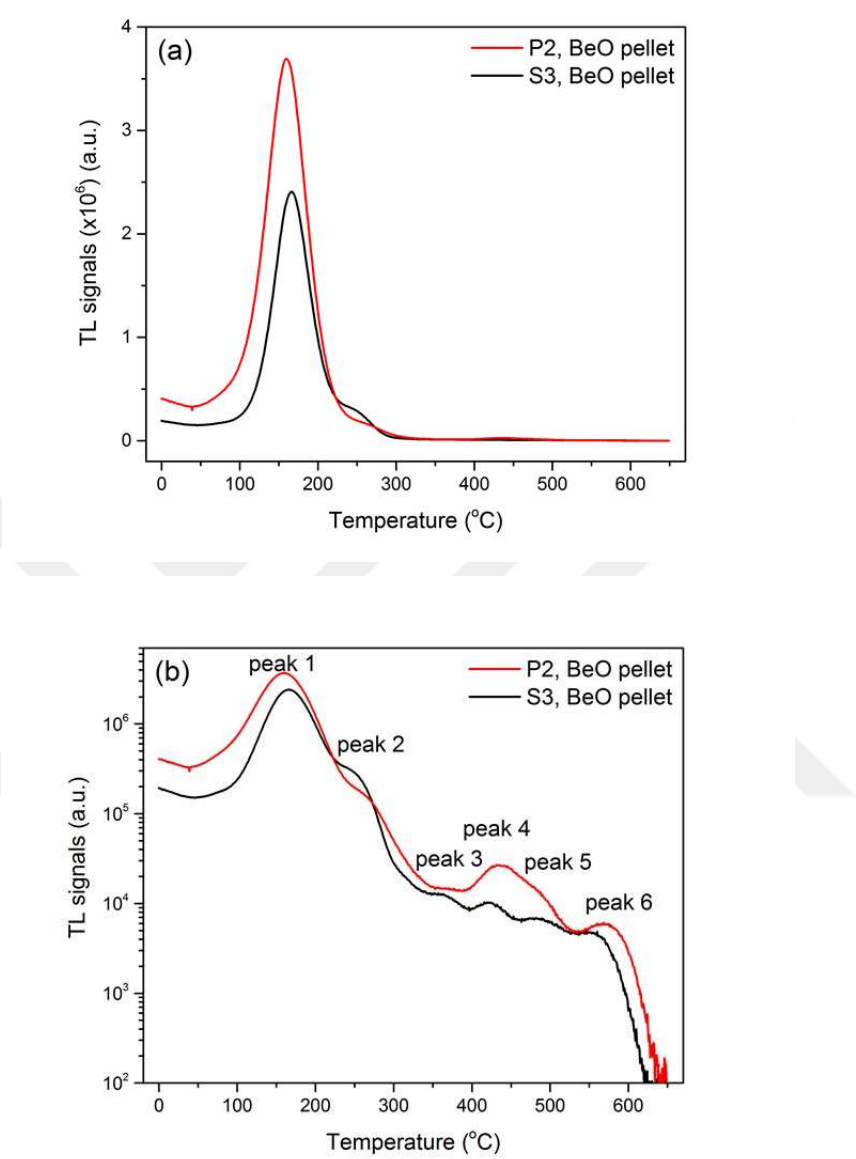

Figure 4.20. (a) TL glow curves of the sintered BeO ceramic pellets calcinated at 900 °C (*P2, co-precipitation*), 1000 °C (*S3, sol-gel*) for 4h, (b) TL low curves for better viewing in logarithmic-scale.

The effects of calcination conditions on the intensity of TL signals of BeO pellets were investigated by the integrated TL signals for each calcination condition presented in Figure 4.21. Maximum luminescent efficiencies were obtained for the calcination temperatures of 900 and 1000 °C in the co-precipitation and sol-gel methods, respectively. Afterward, the samples were kept at determined temperatures for 2, 4, 6, 8, 10 and 24 h (see Figure 4.21b). In thermal treatments, although TL efficiencies didn't change significantly when the temperature was changed from 2 to 24 h, it could be suggested that the highest TL signals were observed at 900 and 1000 °C calcination temperatures for 4 h, for the co-precipitation and sol-gel methods, respectively.

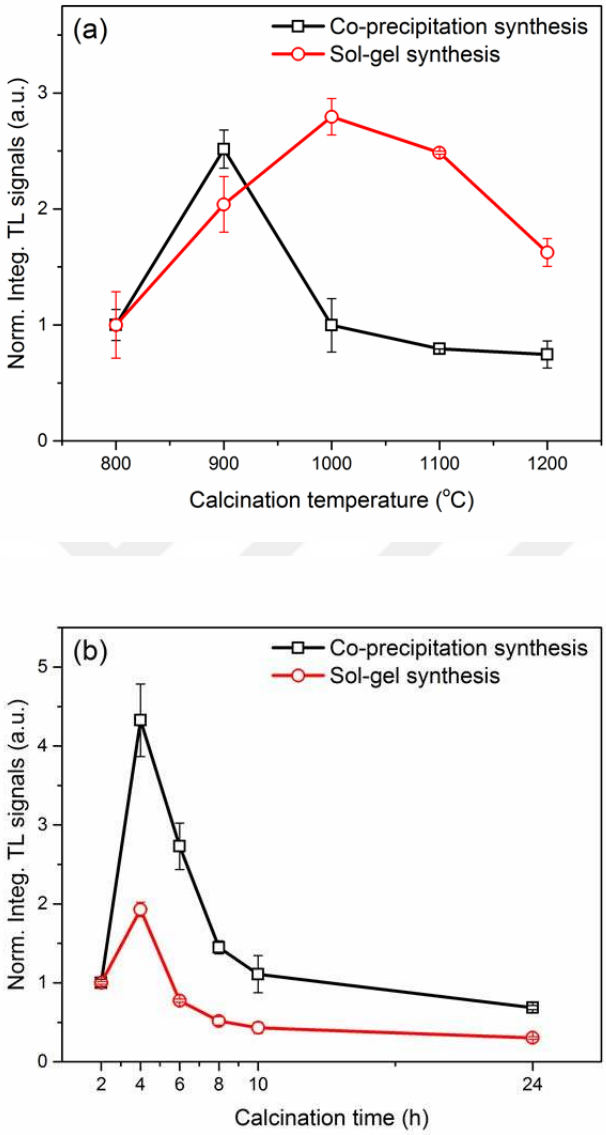

Figure 4.21. Integrated TL signals of BeO pellets synthesized by co-precipitation and sol-gel methods calcining (a) at 800, 900, 1000, 1100 and 1200 °C for 4 h; (b) at 900 °C (co-precipitation), 1000 °C (sol-gel) for varying calcination duration, 2, 4, 6, 8, 10, 24 h.

4.2.3.3. OSL Signals of BeO pellets

The typical OSL decay curves of BeO pellets, which were synthesized by co-precipitation and sol-gel methods calcining at 900 °C (co-precipitation), 1000 °C (sol-gel) for 4 h, recorded after 0.5 Gy beta dose are shown in Figure 4.22a-b, respectively. OSL signals were recorded during 1000 s of blue-light stimulation after preheating at 110 °C for 60 s. As can be seen from Figure 4.22, both OSL decay curves obtained in the two methods have two components: fast and slow decaying components. The OSL signals reach zero levels after at least 1000 s (data not shown). The OSL sensitivities of BeO pellets are sufficient and usable for dosimetry applications. Considering that the signals of the produced BeO pellets vary from the synthesized batch to batch, the fresh samples from the same batch were used in each experiment to increase the reliability of the experiments under laboratory conditions.

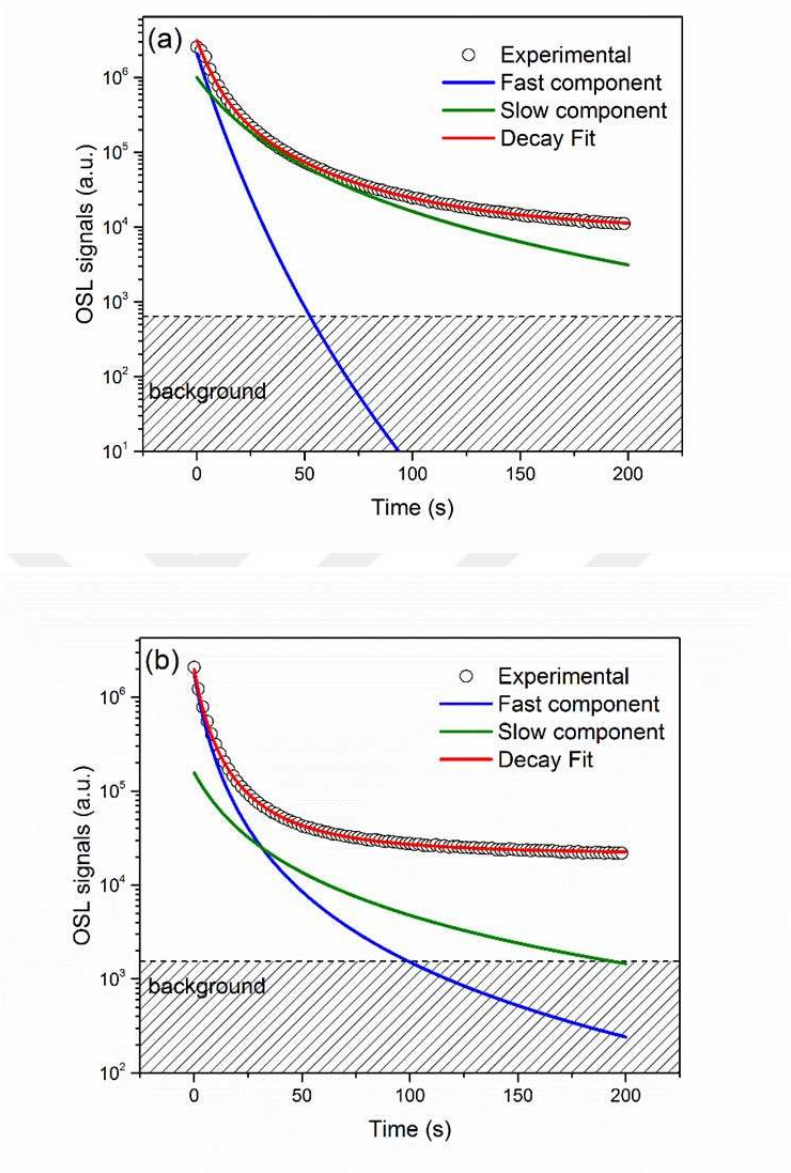

Figure 4.22. The OSL decay curves and the resultant components from the curve fitting of the sintered BeO ceramic pellets calcinated (a) at 900 °C (*P2, co-precipitation*); (b) 1000 °C (*S3, sol-gel*); for 4h.

The analysis of the OSL decay curve and observing the behavior of its components are very important starting points for recognizing a product in OSL dosimetry. The OSL decay curves of BeO pellets, which were synthesized by co-precipitation and sol-gel methods calcining at different calcination temperatures and durations, were analyzed by fitting to the linear integration of the two-time decaying functions and presented in Figure 4.22. The fitting technique was conducted by using the general kinetic approach of the luminescence decay curves. This technique was also used in the literature for phosphorescence decay (Chen and McKeever, 1997), OSL decay curves of undoped and doped BeO pellets (Altunal et al., 2019a; Altunal et al., 2019b; Altunal et al., 2020c), OSL curve from doped-Al_2O_3 (Reddy et al., 2018). The equation for the used fitting can be written as:

$$y = S_0(background) + S_1(fast\ component) + S_2(slow\ component) \tag{4.7}$$

$$I(t) = background + I_1\left[1 + (b_1 - 1)\frac{t}{\tau_1}\right]^{-\frac{b_1}{b_1-1}} + I_2\left[1 + (b_2 - 1)\frac{t}{\tau_2}\right]^{-\frac{b_2}{b_2-1}} + \cdots$$

where S_1 and S_2 are the general-order decay functions presenting the fast and the slow decay components of the OSL signal, respectively. In Equation (4.7). t is the stimulation time; $I(t)$ is the intensity of the OSL signals as a function of time; $I_{1,2}$, $\tau_{1,2}$ and $b_{1,2}$ are the amplitudes, the decay times and kinetic orders of the individual components, respectively. $I_{1,2}$, $\tau_{1,2}$ and $b_{1,2}$ values were determined using Equation (4.7) and presented in Table 4.6. In addition to these evaluated values, the FOM values were also calculated to test the goodness of the fitting process (Balian and Eddy, 1977) and presented in Table 4.6. FOM values decreased significantly with increasing calcination temperature and time and it was observed that the fitting process improved. In the co-precipitation method, the b values of the fast

component showed general order kinetic behavior by having values between 1.47 and 1.76 except for the P2 sample (i.e., calcined at 900 °C). While τ_1 lifetime values of the fast components decreased with increasing temperature, lifetime, τ_2 values of the slow components increased significantly when the temperature increased. Additionally, in the sol-gel method, the b values of the fast component of the OSL decay curves vary from 1.05 first-order kinetic behavior to 2.05 second-order kinetic behavior with increasing calcination temperature and time. τ_1 lifetime values of the fast components increased with increasing temperature and lifetime, τ_2 values of the slow components increased only with increasing temperature. Similar OSL decay curve behaviors were observed and fitting parameter values, ($\tau_{1,2}$ and $b_{1,2}$) were found in the previous studies for the undoped and doped BeO pellets (Altunal et al., 2019a; Altunal et al., 2019b; Altunal et al., 2020c). In this study, the OSL curves of BeO pellets produced by different methods under different calcination conditions could be explained with two-time decaying functions. For Thermalox BeO chips, this number was three-time decaying functions (Bulur and Goksu, 1998). It should be noted that this OSL decay curve fitting to such a function is only an oversimplified approximation of the real situation. Studies based on the numerical solutions of the charge trafficking equations are necessary to understand more about the traps and transitions involved in OSL production.

Table 4.6. $\tau_{1,2}$ decay times, $b_{1,2}$ kinetic orders and FOM values of the curve fittings using two components for BeO pellets synthesized via the co-precipitation and sol-gel methods.

No.	***S1 (fast component)***			***S2 (medium component)***				
	I_1 (count)	τ_1(s)	b_1(a.u.)	I_2 (count)	τ_2(s)	b_2(a.u.)	*bkg* (count)	*FOM* (%)
P1.	7.5E+05	10.30	1.67	6.0E+05	4.05	1.05	5.16E+03	2.42
P2.	2.2E+06	5.14	1.08	1.0E+06	16.70	1.52	8.22E+03	2.34
P3.	7.9E+05	4.68	1.63	2.3E+04	516.41	2.05	1.68E+04	0.31
P4.	1.2E+06	4.74	1.68	2.0E+04	1006.37	2.05	6.41E+03	0.37
P5.	1.1E+06	5.47	1.76	1.7E+04	1011.23	2.05	7.05E+03	0.36
P6.	6.2E+05	5.56	1.64	7.9E+03	592.73	2.05	6.23E+03	0.59
P7.	1.7E+06	5.85	1.75	9.8E+03	269.00	2.05	1.60E+04	0.29
P8.	9.7E+05	4.64	1.60	5.8E+04	551.29	1.06	9.44E+03	0.30
P9.	5.7E+05	4.34	1.51	9.6E+04	497.57	1.05	8.83E+03	0.24
P10.	3.6E+05	4.17	1.47	8.5E+04	662.29	1.53	6.63E+03	0.21
S1.	4.00E+05	3.58	1.05	1.00E+05	20.95	2.05	2.86E+04	2.01
S2.	1.18E+06	4.33	1.39	1.56E+05	21.04	2.05	2.01E+04	0.69
S3.	1.86E+06	4.78	1.55	1.59E+05	20.91	2.05	2.08E+04	0.55
S4.	1.90E+06	5.70	1.77	2.15E+04	1109.25	2.05	6.82E+03	0.23
S5.	1.23E+06	5.05	1.75	2.46E+04	867.07	2.05	6.49E+03	0.32
S6.	7.22E+05	7.42	2.02	3.11E+04	373.46	1.91	4.98E+03	0.30
S7.	3.83E+05	8.52	2.05	6.79E+04	143.06	2.05	6.46E+03	0.30
S8.	3.35E+05	8.66	2.05	7.59E+04	151.40	2.05	7.30E+03	0.28
S9.	2.73E+05	7.94	2.05	9.71E+04	168.97	1.87	7.10E+03	0.24
S10.	1.64E+05	9.15	2.05	8.01E+04	154.41	1.96	4.97E+03	0.26

On the other hand, to investigate the calcination effects on OSL efficiencies of BeO pellets, the integrated OSL signal intensities for each calcination condition were presented in Figure 4.23. As can be seen from Figure 4.23, similar to the changes in the integrated TL signals mentioned above, the maximum OSL efficiencies were obtained at 900 and 1000 °C for co-precipitation and sol-gel methods, respectively. It can be concluded that the employment of appropriate calcination conditions in co-precipitation and sol-gel synthesis of BeO is a good starting procedure to achieve a promising OSL dosimeter with high luminescent efficiency.

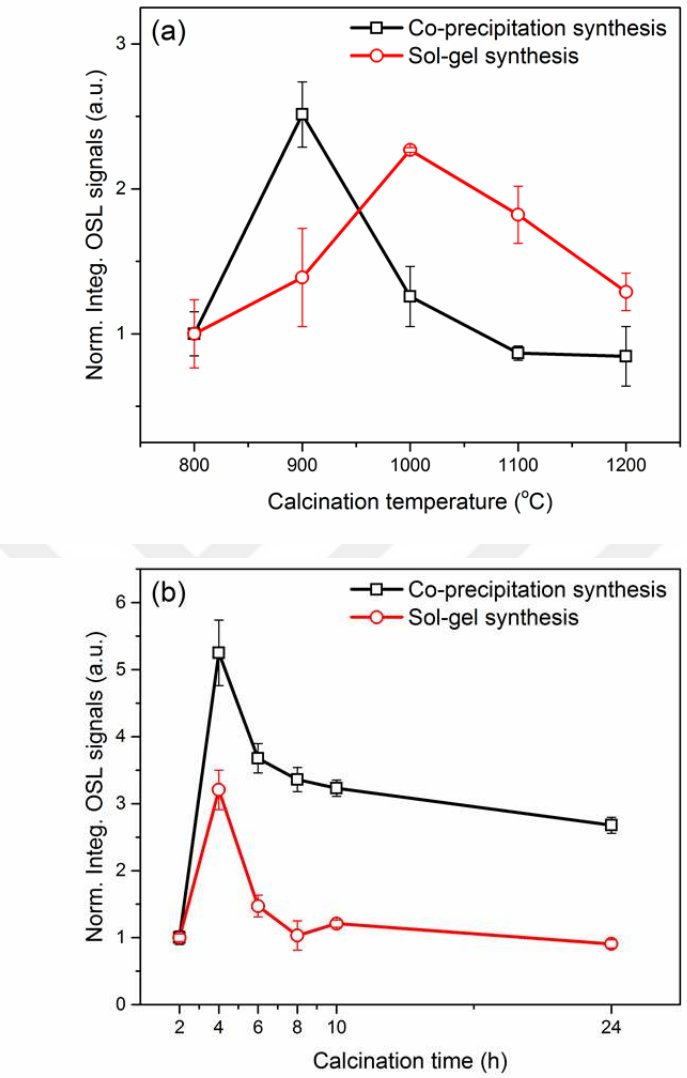

Figure 4.23. Integrated TL signals of BeO pellets synthesized by co-precipitation and sol-gel methods calcining (a) at 800, 900, 1000, 1100 and 1200 °C for 4 h (b) at 900 °C (co-precipitation), 1000 °C (sol-gel) for varying calcination durations, 2, 4, 6, 8, 10, 24 h.

4.2.3.4. Dose Linearities of BeO pellets

Knowing the range in which the dose-response is linear is extremely important in determining the area of application. For this purpose, the dose linearities of the OSL signals from BeO pellets synthesized by co-precipitation and sol-gel methods under different calcination conditions were studied in the dose range between 0.1 Gy (the minimum applicable dose value of TL/OSL readout system) and 20 Gy. Firstly, BeO pellets, namely P1, P2, P4, P6, P8, S1, S3, S5, S6, S8, were irradiated with 0.1, 0.2, 0.5, 1, 2, 5, 10, and 20 Gy beta test doses in repeated experimental cycles. Then, samples were preheated at 100 °C, 10 s. After OSL readouts were performed using 200 s blue light stimulations, residual signals were deleted by heating the samples to 650 °C via TL readout. Figure 4.24 shows plots of the normalized (according to the readout after exposure with 0.1 Gy) and integrated OSL signals (the total OSL signal counts from 0 to 200 s) against the absorbed dose. With the linear fitting, evaluated fit parameters such as slope, intercept, etc. were presented for each synthesis method in the inset tables of Figure 4.24a and Figure 4.24b. From the linear fittings and considering the slope values of the samples produced by the co-precipitation method, only P2 had a linear dose-response with the slope value of 1.00265, while of the samples produced by the sol-gel method, only S3 had a linear dose-response curve with the slope value of 1.00366. Moreover, in the slope values obtained, all samples with a relatively low crystalline structure and luminescence sensitivity exhibited sub-linear (slope value < 1) properties. In the literature, similar linear dose-response behavior has been reported for the BeO sample in different forms (Altunal et al., 2019a; Altunal et al., 2019b; Altunal et al., 2020c; Altunal et al., 2020e; Altunal et al., 2018; Sommer and Henniger, 2006).

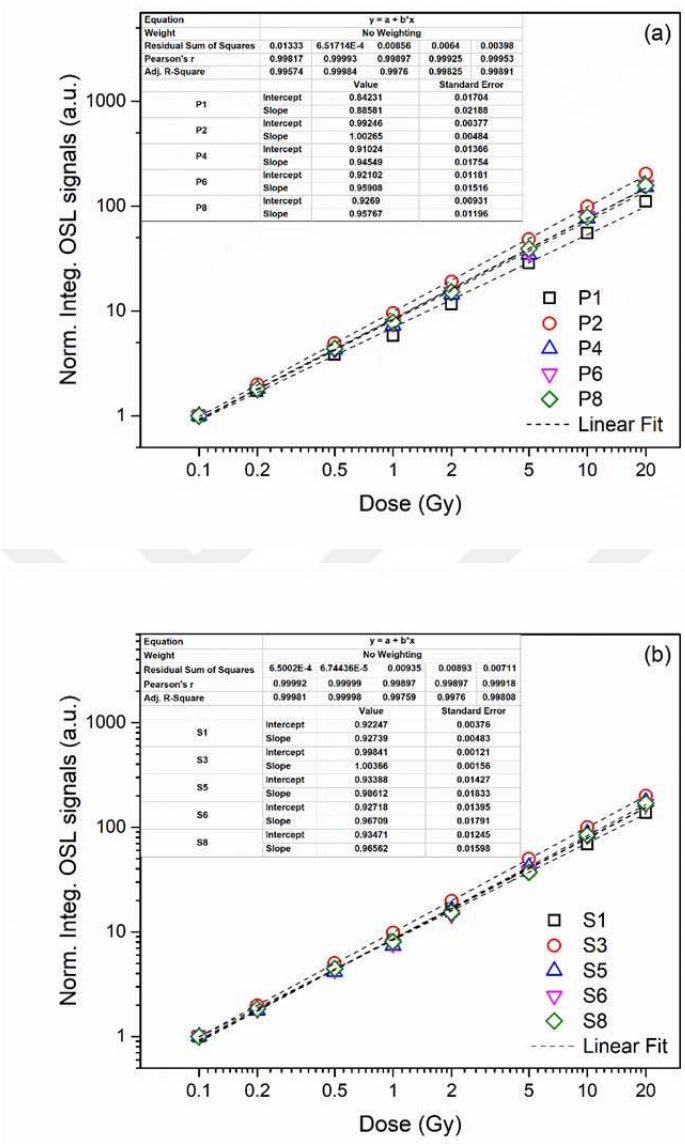

Figure 4.24. Dose-response curves in the dose range between 0.1 and 20 Gy of the OSL signals from BeO pellets synthesized (a) with precipitation method; (b) with the sol-gel method. Inset: Linear fitting parameters was obtained by equation of y = a + bx, where refers to y = log(I), x = log(D), a is intercept, b is slope, (I) represents Integrated OSL signals, and D is dose value.

4.2.3.5. Short-time Fading of BeO pellets

The fact that the number of trapped charges is stable at room temperature, is a desirable feature for all dosimetry applications. To investigate whether the charge population in traps is stable, the fading properties of BeO pellets, produced by co-precipitation and sol-gel synthesis methods under different calcination conditions, after irradiation with a 0.5 Gy beta dose were tested by keeping the samples in the dark at room temperature. The fading property of the pellets was investigated for different time intervals for 1 day. The first reading began half an hour after irradiation. Figure 4.25 shows the stability of the OSL signals integrated (the total OSL signal counts from 0 to 200 s) and normalized (according to 1st readout obtained after half an hour) against the storage time. As is seen from Figure 4.25a, after the 24 h in which the shallow traps are responsible for the observed fading of the BeO pellets synthesized with the co-precipitation method, the deviations of the total OSL signals from the first readout values were found as −12%, −6%, −14%, −16% and −18% for the P1, P2, P4, P6 and P8 samples, respectively. Similarly, for the BeO pellets synthesized via the sol-gel method, the decreases in the integrated OSL signals of the S1, S3, S5, S6 and S8 samples at the end of 24 h were observed as 13%, 5%,12%,14% and 16%, respectively. These results are consistent with the results of various BeO ceramic forms previously studied (Altunal et al., 2019a; Altunal et al., 2019b; Altunal et al., 2020c; Altunal et al., 2020e; Altunal et al., 2018; Sommer and Henniger, 2006). As a result, the short time fading could become a problem for very fast readings. In environmental and personal dosimetry this could only play a tangential role. But in medicine, it may be important. For these cases a short, for example, 10 s preheat at 100 °C might be useful. It should be noted that long-term fading experiments should be carried out to better understand the effect of calcination on the fading property of BeO. In future studies, the fading feature could be investigated by applying various preheating conditions to this experiment.

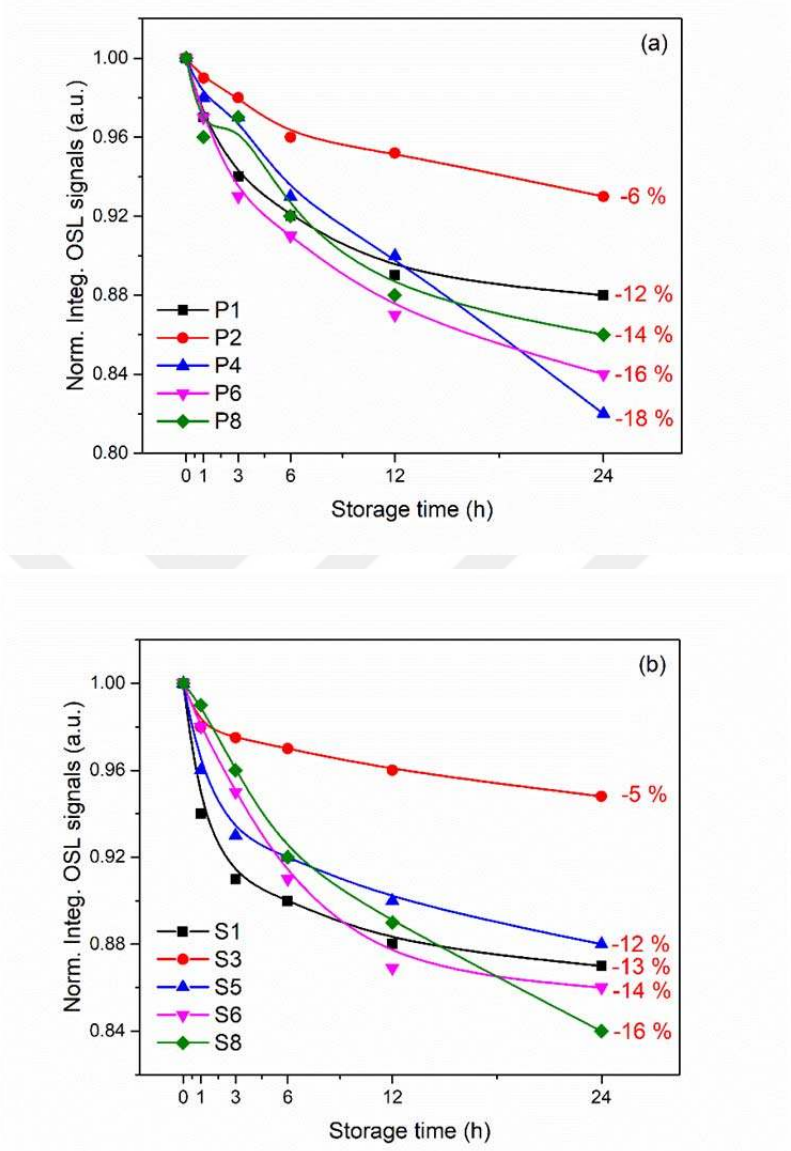

Figure 4.25. Stability of the OSL signals over one day period of storage at room temperature following a 0.5 Gy β radiation. Each data point represents the integrated (the total OSL signal counts from 0 to 200 s) and normalized (according to 1st readout obtained after half an hour) OSL signals from BeO pellets synthesized (a) with precipitation method (b) with the sol-gel method.

4.2.4. Discussion

The results for BeO pellets presented here must be discussed from the point of view of the underlying calcination mechanism, and the practical point of view for applications in radiation dosimetry. Calcination is considered as the process of heating and purification of solids to a high temperature to remove volatiles, oxidize a part of the mass or render them friable. It has significant effects on phase crystallization, phase transformation, crystal size and the surface area, consequently, the sinterability of the material. In this work, the results showed that the luminescence efficiency of the BeO material produced by co-precipitation and sol-gel methods significantly increase under favorable calcination conditions. TGA (thermogravimetric analysis) data, indicated that BeO which is hydrated at room temperature, becomes anhydrous at 620 and 720 °C for co-precipitation and sol-gel methods, respectively and releasing water molecules possibly damage the crystal lattice which gets restored at higher calcination temperatures. The water molecules released almost at 800 °C possibly displace Be ions from its lattice site causing a reduction in luminescence efficiency (Lakshmanan, 2012). In both methods, calcination at relatively higher-temperature possibly restores the Be ions in their original lattice sites and hence restores the luminescence sensitivity. In this study, the main reason to have an increase in luminescence intensities at appropriate calcination temperatures and times might be because of the formation of a lattice with appropriate phase structure and crystallinity, which improve the physical properties of the material. The BeO nanoparticles bonded together by high-temperature sintering have had a better surface morphology than the other samples; hence, the luminescence signals from the surfaces of opaque ceramic BeO pellets, which have less porousness on their surface, will have increased luminescence significantly.

From the practical point of view for applications in radiation dosimetry, OSL signals and decay components are very important to determine the behavior of the luminescence of the dosimeter during stimulation. It is clearly seen that the

luminescence efficiencies of the materials are increased under the calcination conditions of 900 °C and 1000 °C, 4h, for co-precipitation and sol-gel methods, respectively. However, the behaviors of all these total luminescent signal curves are the same. It might suggest that the sources of all the luminescence signals for BeO pellets are the same, i.e., TL and OSL signals are also fed from similar luminescence bands like RL signals mentioned in Section 0. The results of the OSL fitting by using two decaying functions showed that the lifetimes, $\tau_{1,2}$ values, were strongly affected by calcination conditions

Increasing calcination temperature decreased the lifetime values of the fast component in the precipitation method, while an increase in lifetime values of that in the sol-gel method. It means that the precipitation method creates much shallower trap levels when compared to the sol-gel method. In Table 4, the long decay times are due to deeper trap levels, while the high initial intensity of OSL signals is due to the density of shallow trap levels. Considering the multi-readability, i.e., the ability to be read several times without significant depletion of the signal intensity feature of OSL dosimeters, a longer lifetime may be a desirable feature and OSL signals with longer lifetimes could be obtained by applying different calcination conditions. Additionally, P2 and S3 samples synthesized with appropriate calcination conditions determined in both methods have proven to be superior in dosimetric applications with their linear dose responses from 0.1 Gy to 20 Gy and acceptable short-time fading properties (-6% for P2, -5% for S3) as well as structural and luminescence characteristics.

4.3. Determination of Appropriate Sintering Durations of BeO

In this study, the effect of sintering durations on luminescence signals of BeO was also studied. Luminescence signals of BeO samples which were produced by co-precipitation and sol-gel methods were examined in TL and OSL techniques.

4.3.1. Material Synthesis

BeO samples were synthesized in two synthesis methods: co-precipitation and sol-gel. In the co-precipitation method, polyethyleneimine (Analytical standard, 50 % (w/v) in H_2O, Sigma-Aldrich) and ammonium hydroxide (NH_4OH) (ACS reagent, 28.0-30.0% NH3 basis, Sigma-Aldrich) solutions for polymerization and as an initiator of the precipitate were used, respectively. In the sol-gel method, ethylene glycol ($C_2H_6O_2$, 99.8% purity, Sigma-Aldrich) solution as a solvent and citric acid ($C_6H_8O_7$, 99.5% purity, Sigma-Aldrich) salts as a reactant, were used. To obtain BeO phosphors, the typical process of BeO synthesis begins using beryllium sulfate tetrahydrate ($Be(SO_4)x4H_2O$, %99.9, Sigma-Aldrich) salts as precursor reactant in two methods. Deionized water was prepared using the New Human Power ultra-purification system (Human Corporation, Korea) and used throughout the synthesis. The precipitation synthesis route was presented in detail in Section 0. In the sol-gel synthesis process, undoped BeO solution was prepared by mixing stoichiometric amounts of beryllium sulfate powder and ethylene glycol solution on a hot plate with continuous magnetic stirring at 80 °C for 1 h. Once the undoped BeO solutions became transparent after 1 h magnetic stirring at 80 °C, citric acid salt was added into these mixtures under vigorous stirring. The hot plate temperature was raised to 300 °C while stirring until the translucent gel was occurred and became darker in about an hour. The obtained gel was fired in an ash furnace (Nabartherm, model P330) at 500 °C for 1 h forming a black and soft porous spongy material. To burn formed organics and obtain BeO powder, the resultant gel precursor was grounded in an agate mortar and calcined at 800 °C for 4 h in an oxygen atmosphere. The opaque white color materials were obtained and again powdered in an agate mortar. In this work, considering both the health risk of BeO and the difficulty in handling the material in powder form, samples were studied in pellet forms. The pellets were prepared by synthesized undoped/doped BeO nanopowders without adding any binding material and using a cold hydraulic press (Carver, model 3853-9) with evacuable pellet dies. The 25 mg nanopowder

materials were pressed at the pressure of 25 MPa (250 kg-force/cm^2) for 1 min into a pellet of 6 mm in diameter and 0.8 mm in thickness. To impart strength and integrity and to obtain more settled OSL signals, prepared pellets were sintered using a box furnace (Thermoscientific, model Lindberg/Blue M™) at 1600 °C for 1, 2, 3, 4, 5, 8, 12, 18 and 24 h in an oxygen atmosphere.

4.3.2. TL and OSL Signals

To determine the time parameter of the sintering condition of the BeO material, the materials prepared as pellets after the calcination process were sintered separately at 1600 °C at different durations (1, 2, 3, 4, 5, 8, 12, 18, 24 h). OSL decay curves and TL glow curves were recorded after 0.5 Gy beta dose and 10 s preheating condition at 120 °C. While blue light of 200 s was used for OSL stimulation, TL glow curves were recorded by heating the materials to 650 °C using a heating rate of 3 °C/s. In Figure 4.26, TL signals of BeO samples obtained for sintering duration of 2, 4, 8, 12, 18, and 24 h are presented for two synthesis methods.

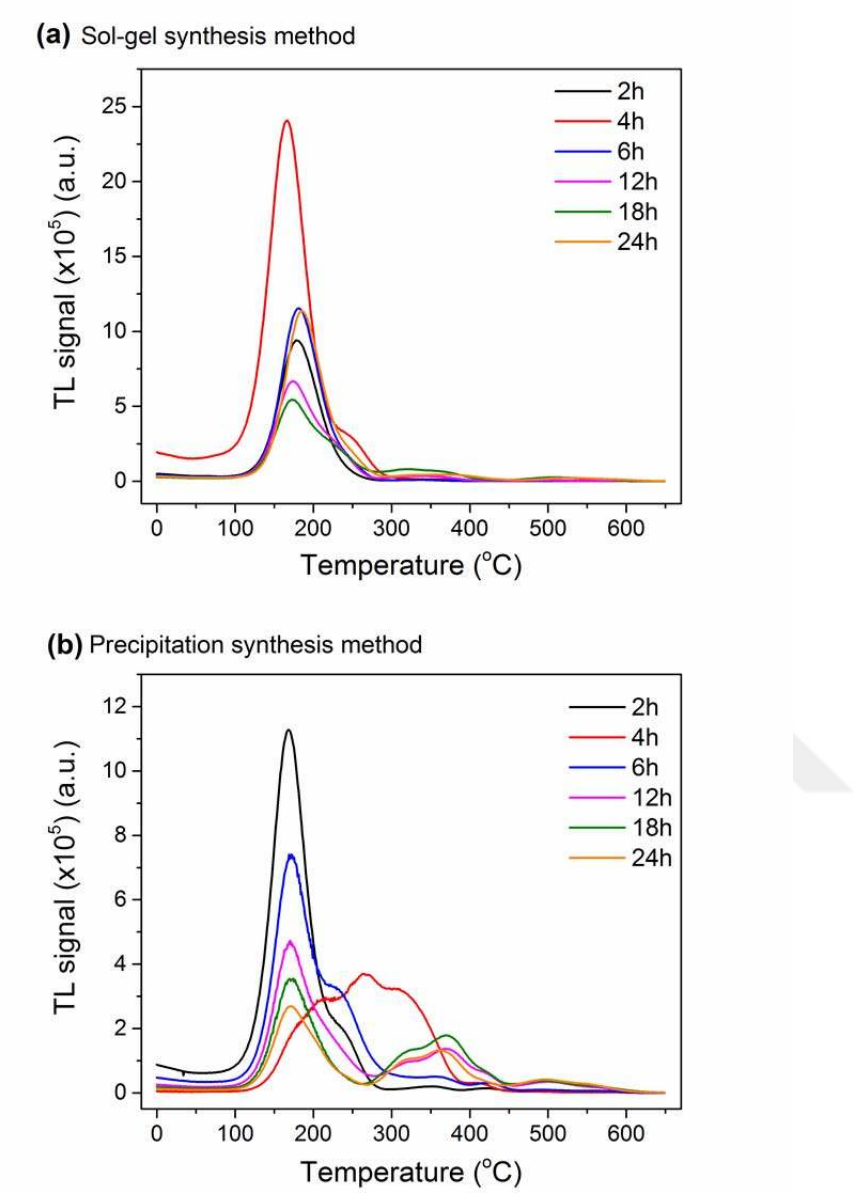

Figure 4.26. TL glow curves of BeO samples obtained for sintering duration of 2, 4, 8, 12, 18, and 24 h in two synthesis methods; (a) Sol-Gel synthesis method, (b) Precipitation synthesis method

As can be seen in Figure 4.26, the TL glow curve appearance of BeO has changed with the increase of sintering time, and accordingly, it can be said that the trap structures are significantly affected by the sintering duration. While no major differences are observed in TL glow curves in short-term sintering, it can be said that electron densities shift towards relatively deep traps in samples with long-term sintering conditions. Moreover, in the precipitation synthesis method, an unexpected TL behavior was obtained from the 4 h sintered BeO samples. This was the first time to meet such a TL glow curve for BeO ceramics produced by the precipitation synthesis method (it will be discussed later).

On the other hand, OSL decay curves were also studied, and obtained for sintering duration of 2, 4, 8, 12, 18, and 24 h were presented for two synthesis methods in Figure 4.27.

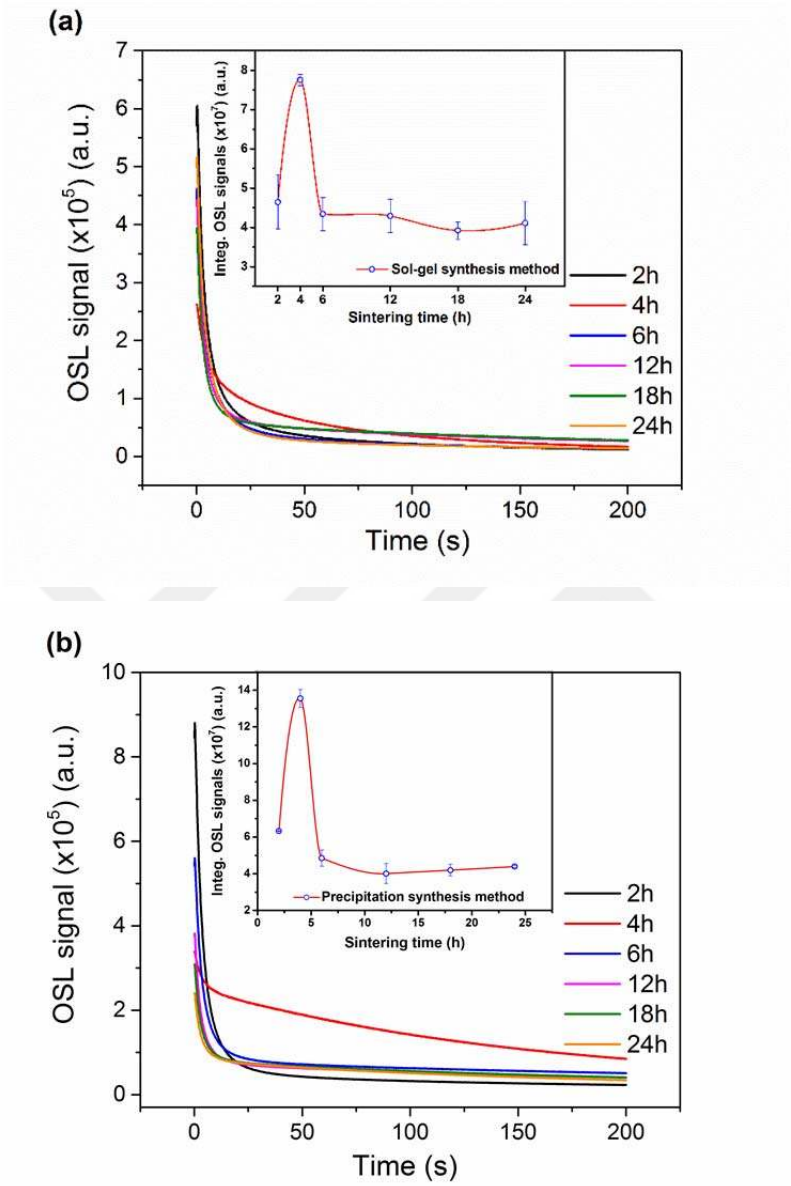

Figure 4.27. OSL glow curves of BeO samples obtained for sintering duration of 2, 4, 8, 12, 18, and 24 h in two synthesis methods; (a) Sol-Gel synthesis method, (b) Precipitation synthesis method

As is seen from Figure 4.27, while the most appropriate sintering duration was determined at 4 h for the sol-gel method, it can be difficult to decide the appropriate sintering duration for precipitation method. To confirm and determine the appropriate sintering duration in the precipitation method, TL and OSL signals of BeO samples obtained for sintering duration of 1, 2, 3, 4, and 5 h were presented in Figure 4.28. As is seen from Figure 4.28, the optimum sintering time was determined as 2 hours, since the material exhibited a higher OSL sensitivity despite the relatively low TL signals.

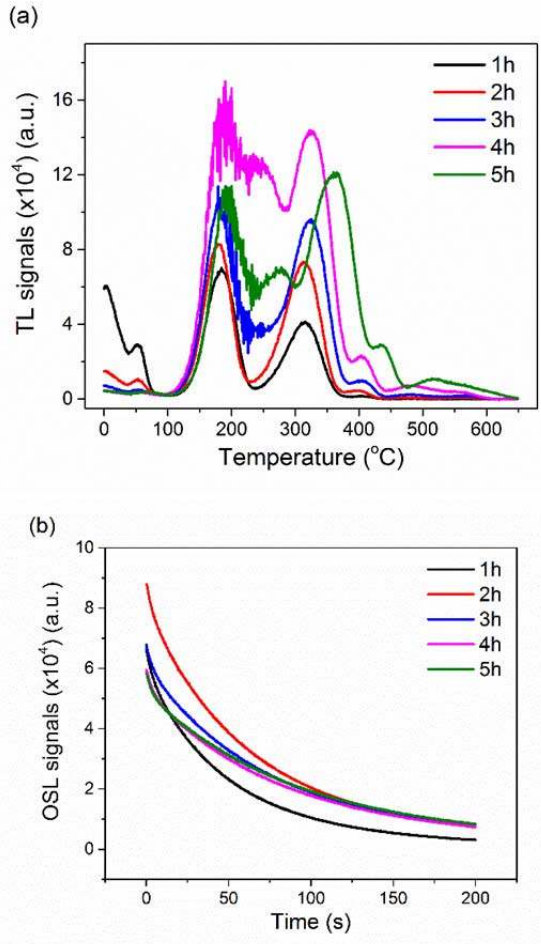

Figure 4.28. (a) TL and (b) OSL signals of BeO samples obtained for sintering duration of 1, 2, 3, 4, and 5 h

At the end of this complementary study, the most suitable conditions were determined for the production methods used in this thesis, sol-gel and co-precipitation synthesis methods, and the conditions mentioned so far were used during the preparation of the samples unless otherwise stated.

4.4. Al-and Ca-Doped BeO Pellets Obtained via a Sol-Gel Method

In the present study, we synthesized BeO, BeO:$Al_{1\%}$, BeO:$Ca_{1\%}$, and BeO:$Al_{1\%}$,$Ca_{0.1\%}$ pellets using the sol-gel method, and the synthesized samples were analyzed by X-ray diffraction (XRD), scanning electron microscopy (SEM), and Fourier transform IR (FTIR) spectroscopy to understand the structural formation, surface morphology, and vibrational modes. We also investigated their OSL characteristics to demonstrate the potential of these samples and their suitability for OSL dosimetry. The correlation between TL and OSL signals was examined by thermal stability experiments. Thermal quenching energies were evaluated with the effect of reading temperature on the OSL signals and the temperature-dependent optically stimulated luminescence (TOSL) curves. The dosimetric characteristics, such as dose-response, minimum detectable dose (MDD), reusability, and short-term dark storage fading, were investigated by the continuous wave OSL (CW-OSL) technique. We believe that this study is an important step toward enhancing our understanding of the mechanism of BeO ceramics.

4.4.1. Synthesis and Sample Preparation

In this study, BeO nanopowders were synthesized via the sol-gel synthesis method of the precursor beryllium sulfate tetra-hydrate ($BeSO_4 \cdot 4H_2O$, >99.0%, Sigma-Aldrich) in the desired stoichiometric ratios along with citric acid ($C_6H_8O_7$, 99.5%, Sigma-Aldrich) salts as reactants and ethylene glycol ($C_2H_6O_2$, 99.8 %, Sigma-Aldrich) as solvent. The undoped BeO master solution was prepared by mixing stoichiometric amounts of beryllium sulfate powder and ethylene glycol

solution on a hot plate with continuous magnetic stirring at 80 °C for 1 h. Doped BeO samples were prepared in the same procedure by adding dopants to the master solution at the beginning of the preparation. In this work, as dopants, aluminum nitrate nonahydrate 1% M ($Al(NO_3)_3 \cdot 9H_2O$, ACS reagent, ≥98%, Sigma-Aldrich) salt with 1% M, calcium nitrate ($Ca(NO_3)_2 \cdot 4H_2O$, ≥99.0%, Sigma-Aldrich) salt with 1% M or a combination of them (1% M of Aluminum, 0.1% M of Calcium) were used. Once the undoped and/or doped BeO solutions became transparent after 1 h magnetic stirring at 80 °C, citric acid salt was added into these mixtures under vigorous stirring. The hot plate temperature was raised to 300 °C while stirring until the translucent gel was occurred and became darker in about an hour. The obtained gel was fired in an ash furnace (Nabartherm, model P330) at 500 °C for 1 h forming a black and soft porous spongy material. To burn formed organics and obtain BeO, BeO:$Al_{1\%}$, BeO:$Ca_{1\%}$ and BeO:$Al_{1\%}$,$Ca_{0.1\%}$ powder, the resultant gel precursor was grounded in an agate mortar and calcined at 800 °C for 4 h in an oxygen atmosphere. The opaque white color materials were obtained and again powdered in an agate mortar. In this work, considering both the health risk of BeO and the difficulty in handling the material in powder form, samples were studied in pellet forms. The pellets were prepared by synthesized undoped/doped BeO nanopowders without adding any binding material and using a cold hydraulic press (Carver, model 3853-9) with evacuable pellet dies. The 25 mg nanopowder materials were pressed at the pressure of 25 MPa (250 kg-force/cm^2) for 1 min into a pellet of 6 mm in diameter and 0.8 mm in thickness. To impart strength and integrity and to obtain more settled OSL signals, prepared pellets were sintered using a box furnace (Thermoscientific, model Lindberg/Blue M™) at 1600 °C for 4h in an oxygen atmosphere (Altunal et al., 2019b). As a consequence of the shrinkage of the ceramic pellets during sintering, we observed the diameter and thickness reduction. After the sintering, the pellets were measured as 5 mm in diameter and 0.5 mm in thickness. The masses of the pellets were taken as approximately 23 mg. The densities of the pellets were calculated as around 2.1

g/cm^3. The evaluated density value of the pellets was found to be lower than that of the solid-state density of BeO (3.05 g/cm3) and commercially used Thermalox (2.85 g/cm3) given in the literature. During the synthesis and preparation process of the BeO samples, personal protective equipment was used in our laboratory.

4.4.2. Structural Characterization

Synthesized BeO, BeO:$Al_{1\%}$, BeO:$Ca_{1\%}$, and BeO:$Al_{1\%}$,$Ca_{0.1\%}$ pellets were characterized by XRD, SEM, and FTIR spectroscopy. X-ray measurements were conducted with Cu Kα radiation (40 kV, 30 mA) for the identification of crystallographic phases. Patterns were taken from 5° to 90° (2θ) with a step size of 0.02°. The divergence slit and the incident and length-limiting slit were 0.66° and 10 mm, respectively. To investigate the surface morphology and the particle size of the synthesized materials, SEM was performed at room temperature. FTIR was used to determine the vibrational bonds in the mid-IR region (spectral range between 550 and 4000 cm^{-1}).

4.4.2.1. X-Ray Diffractions

To identify the phase composition, the crystal structure of the BeO and the role of dopants on the BeO, XRD diffraction patterns of BeO, BeO:$Al_{1\%}$, BeO:$Ca_{1\%}$ and BeO:$Al_{1\%}$,$Ca_{0.1\%}$ pellets were recorded. As illustrated in Figure 4.29, X-ray diffractions obtained for all samples are assigned to the BeO phase with a hexagonal structure. The diffraction positions and relative intensities of the BeO pellet samples are found well-matched with ICDD-PDF-card no 98-016-3468. By the comparison of the characteristic XRD patterns, it was found that the crystallinity of the undoped BeO pellets was almost the same as the doped BeO pellets. The observed diffraction peaks indicate that the crystallite sizes of the samples are very fine. The average crystallite sizes were estimated by the Debye-Scherer Equation (4.4). The crystallite sizes of the samples were found to be 37 ± 2, 41 ± 3, 56 ± 2 and 45 ± 2 nm, respectively.

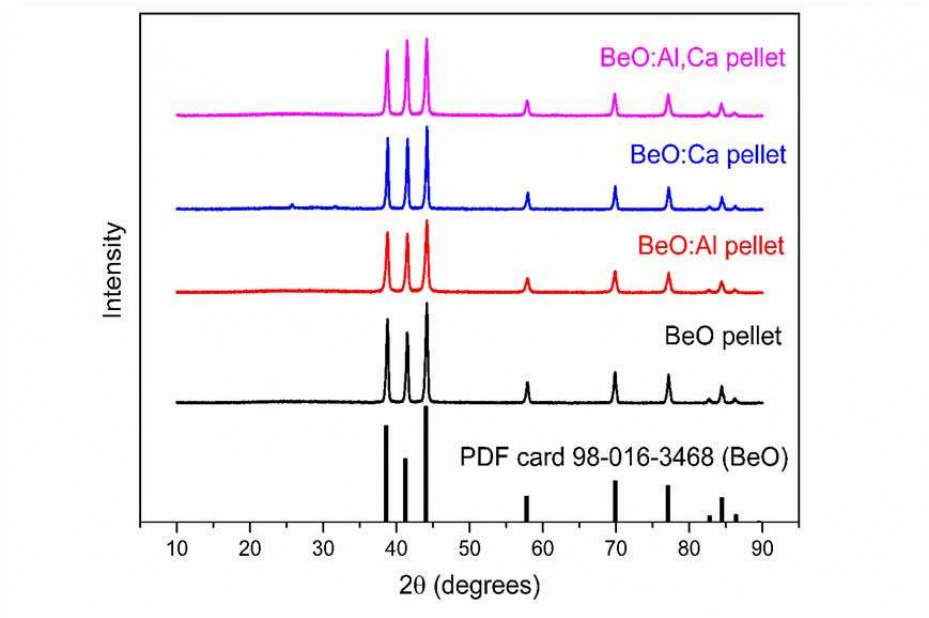

Figure 4.29. XRD patterns of BeO, BeO:Al, BeO:Ca, BeO:Al,Ca pellets and BeO phase ICDD PDF card no 98-016-3468. All the obtained patterns of the studied pellets were taken from 5° to 90° 2θ with a step size of 0.02° 2θ and matched very well with the hexagonal structure of the BeO phase.

4.4.2.2. SEM Pictures

The morphologies of the BeO, BeO:$Al_{1\%}$, BeO:$Ca_{1\%}$ and BeO:$Al_{1\%}$,$Ca_{0.1\%}$ ceramic pellets sintered at 1600 °C were investigated through SEM pictures to figure out the shapes and sizes of the particles. Different dopants would create differences in the surface morphology of BeO. Figure 4.30 shows SEM images of the produced pellets. For the undoped BeO (see Figure 4.30a), a non-homogeneous distribution of the particles was observed and some areas of the surface of the material displayed as rod-like structures that could be the result of the pressure applied during pellet preparation, and the adhesion of grains during the sintering process. In our previous BeO study (Altunal et al., 2018), the same surface morphology did not take place on the SEM images of sintered BeO pellets at 1100 °C sintering temperature. In Figure 4.30b, it is seen that a structure with a more

homogeneous and narrow size distribution (30 – 50 nm) emerged with Al doping. As regards BeO doped with Ca (see Figure 4.30c), we suggest that a structure with relatively well-formed, large and small particles was formed with growing the dimensions of the rod-like structures shown in Figure 4.30a. When the BeO was doped with Al and Ca, regularly shaped hexagonal particles were observed in the phosphor structure (see Figure 4.30d). It can be concluded from the SEM pictures that the particle sizes of the studied pellets are in nanometer scale and agrees with that evaluated by X-ray line broadening.

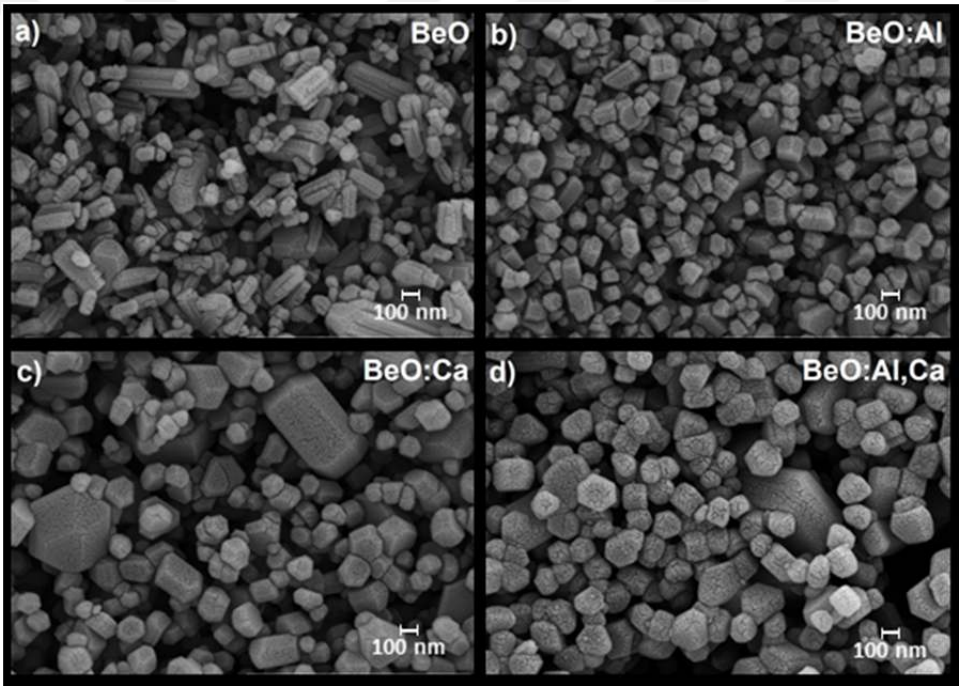

Figure 4.30. SEM images of the pellet samples for BeO (a), BeO:Al (b), BeO:Ca (c) and BeO:Al,Ca pellets (d) at room temperature. Magnification is 50,000 for each SEM picture.

4.4.2.3. FT-IR Analyzes

To observe the vibrational modes of functional groups of the produced phases, FTIR analyzes of the materials were performed. Figure 4.31 demonstrates

the IR spectra of BeO, BeO:$Al_{1\%}$, BeO:$Ca_{1\%}$ and BeO:$Al_{1\%}$,$Ca_{0.1\%}$ pellets. When the assignment vibrations of different doping groups were examined, it was observed that their IR bands were consistent with each other. From the IR spectra, the sharp decaying behavior at about 675 cm^{-1} can be assigned to the Be-O vibration in the BeO crystal and the other raising peak at about 1500 cm^{-1} contains the new product bands discussed here as well the BeO_2 anti-symmetric stretching absorption. Besides, FT-IR results reveal that there is no change in the band positions of the material due to the doping which agrees with those from the XRD measurements. In addition, no peak between 3400 and 3600 cm^{-1} indicating the presence of water molecules (O-H stretching mode of hydroxyl groups) was found. One may say that undoped and doped BeO pellets were successfully produced and are not hygroscopic which affects the behavior of luminescence signals negatively.

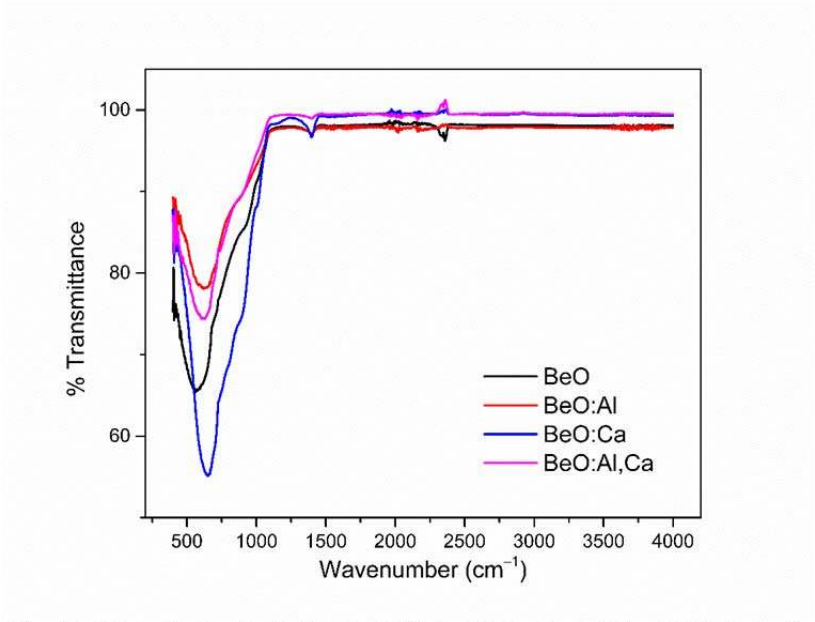

Figure 4.31. FT-IR spectra of BeO, BeO:Al, BeO:Ca and BeO:Al,Ca pellets

4.4.3. Luminescence Results

The TL and OSL measurements were conducted with a Risø TL/OSL reader (model DA-20) coupled to a photomultiplier tube with a bialkali photocathode (Electron Tubes, 9235QA) for the detection of luminescence signals, and blue LEDs (λ_{photon} ~ 470 nm, full width at half maximum approximately 30 nm) were used for stimulation. The $^{90}Sr/^{90}Y$ radiation source emits β particles with a maximum energy of 2.27 MeV, and the dose rate was approximately 6.689 Gy/min. CW-OSL stimulation mode was used at a power density of approximately 80 mW/cm. To prevent scattered stimulation light from reaching the photomultiplier tube, a detection filter (Hoya U-340 UV bandpass filter with 7.5 mm thickness; transmittance range from 250 to 390 nm, maximum at 340 nm) located in front of the photomultiplier tube was used. TL measurements were performed by our heating the sample from room temperature to 650 °C at a rate of 2 °C/s in a nitrogen atmosphere. After each TL and OSL measurement, background readouts were performed in the same conditions, and the data, which were to be used in experimental calculations, were obtained by our subtracting the background counts.

The X-ray luminescence (XL) spectra were obtained with a homemade XL system equipped with an Ocean Optics QE Pro high-sensitivity spectrometer for low-light-level applications. In XL measurements, an *f*/2 collimator was used in front of the fiber-optic cable throughout the CCD detector and samples were irradiated by a mini X-ray tube operated at 4–40 kV to stimulate the pellets. The samples were excited with a voltage of approximately 20 kV.

4.4.3.1. TL and OSL signals

The TL and OSL signals were obtained from the ceramic pellets irradiated with 0.2 Gy beta dose. The measurements were performed by preheating the pellets at 110 °C for 60 s to eliminate unstable signals originating from shallow traps. Figure 4.32 shows the TL glow curves of BeO, BeO:$Al_{1\%}$, BeO:$Ca_{1\%}$ and

BeO:$Al_{1\%}$,$Ca_{0.1\%}$ pellets. The insets in Figure 4.32, in logarithmic scale, were depicted to reveal the relatively low-intensity TL peaks at the high-temperature region. From the data in Figure 4.32a, it is apparent the TL glow curve of a BeO pellet presented four peaks located at 80, 200, 370 and 520 °C. The TL glow curve of a BeO:Al pellet was represented by three peaks located at 200, 350 and 500 °C (see Figure 4.32b). The TL glow curve obtained from a BeO:Ca pellet was characterized by four peaks located at the same peak temperature regions of BeO pellet as shown in Figure 4.32c. On the other hand, in Figure 4.32d, TL glow curve of BeO:Al,Ca showed three peaks like BeO:Al located at 200, 350 and 500 °C. We speculate that Ca in BeO:Al,Ca may act as a co-dopant because the addition of Ca does not change the TL peak temperatures and hence does not create new energy levels in the bandgap of BeO:Al,Ca when compared with BeO:Al.

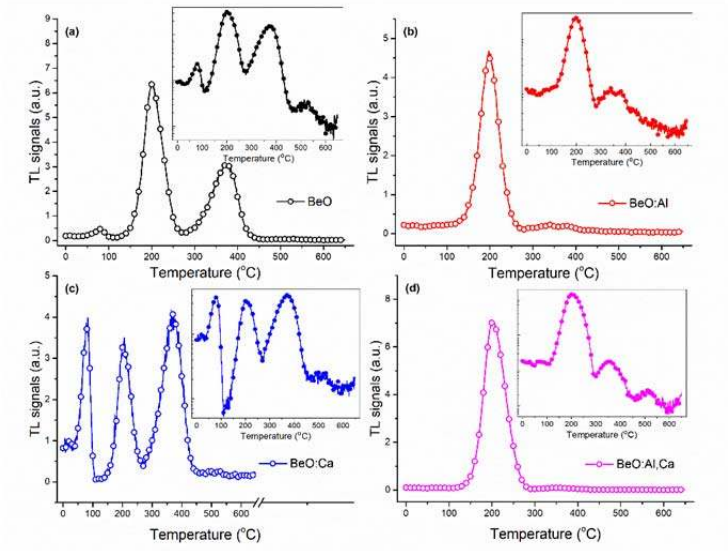

Figure 4.32. TL glow curves of BeO (a), BeO:Al (b), BeO:Ca (c) and BeO:Al,Ca pellets (d). TL readouts were performed heating the previously irradiated samples (0.2 Gy) from room temperature (RT) to 650 °C with the heating rate (HR) of 2 °C/s. Insets: TL signals in log scale only for better viewing of invisible high-temperature peaks due to TL intensity.

The characterization of the OSL decay curves is an essential starting point to understand how the luminescence production mechanism takes place. Following the irradiation with 0.2 Gy β dose, OSL decay curves of the BeO, BeO:$Al_{1\%}$, BeO:$Ca_{1\%}$ and BeO:$Al_{1\%}$,$Ca_{0.1\%}$ pellets rely on blue-light stimulation and are presented in Figure 4.33.

As is seen in Figure 4.33, the OSL decay curves were best fitted to the three decaying functions of time and a background component. The fitting technique used in this study was previously used by the researchers on various luminescent materials. Firstly, Chen and McKeever defined the model for general order kinetic features of a phosphorescence decay for MgO (Chen and McKeever, 1997). This fitting technique was also used for prompt isothermal decay curves of MgB_4O_7:Dy,Na by Kitis et al. (Kitis et al., 2016). The model equation for these fittings was given before as Equation (4.7). $I_{1,2,3}$ amplitudes, $\tau_{1,2,3}$ decay times and $b_{1,2,3}$ kinetic orders were determined from the curve fitting and presented for the pellets in Table 4.7. Additionally, the perfection of fitting curves was tested using the figure of merits (FOM) (Balian and Eddy, 1977), and FOM values were found as around < 2% (see Table 4.7). Firstly, in the FOM calculations, it was assumed that the OSL decay signals are fitting to the two components. The greater FOM values were obtained when compared with the computed FOM values by fitting to the three components. The FOM values by fitting the OSL signal to the three components were calculated as 0.64, 1.11, 1.49 and 0.57 % for BeO, BeO:$Al_{1\%}$, BeO:$Ca_{1\%}$ and BeO:$Al_{1\%}$,$Ca_{0.1\%}$ pellets, respectively. It should be noted that the curve fitting using three decay functions must be considered as an approximation showing mathematical consistency rather than a proof of the existence of separate physical mechanisms (traps), and hence more detailed studies on this are evidently necessary.

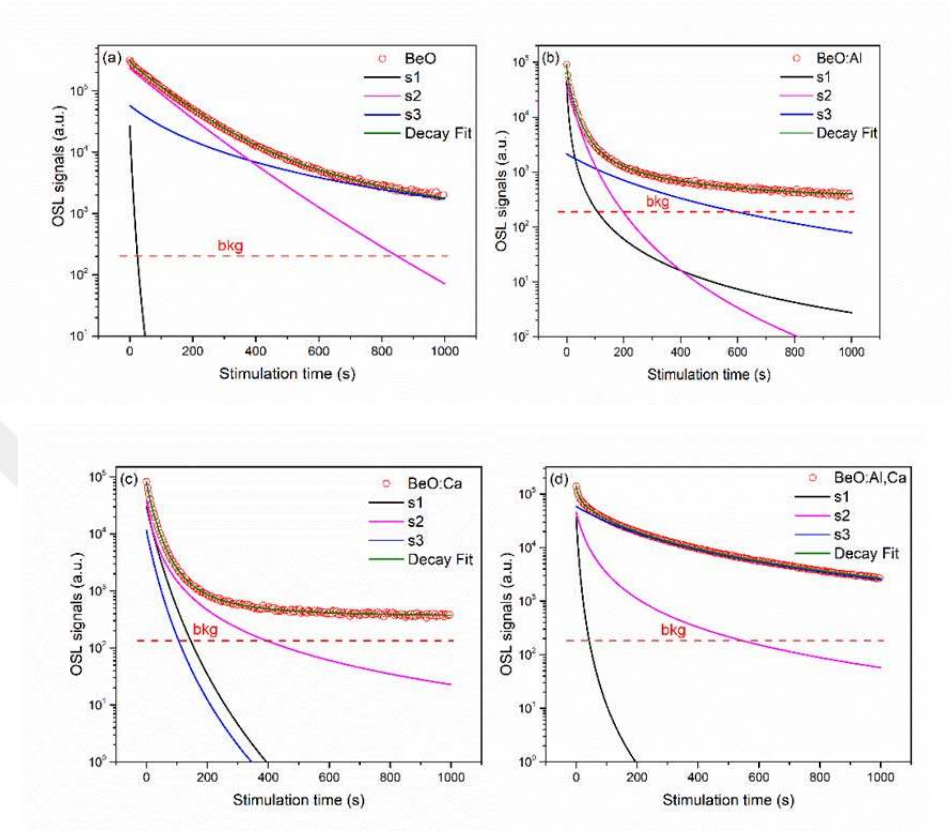

Figure 4.33. OSL decay curves of BeO (a), BeO:Al (b), BeO:Ca (c) and BeO:Al,Ca pellets (d). The presented curves were obtained from the samples irradiated with 0.2 Gy β dose. OSL signals were recorded during 1000 s blue light stimulation after preheating at 110 °C for 60 s. bkg represents a background value of the signal.

Table 4.7. $\tau_{1,2,3}$ decay times, $b_{1,2,3}$ kinetic orders and FOM values of the curve fittings using two and three components

	S_1 (fast component)			***S_2 (medium component)***			***S_3 (slow component)***				
	I_1 (count)	τ_1(s)	b_1	I_2 (count)	τ_2(s)	b_2	I_3 (count)	τ_3(s)	b_3	*bkg*	*FOM* (%)
Using two components											
BeO	3.16E+04	4.35	2.04	2.91E+05	114.30	1.14	-	-	-	1614.5	1.71
BeO:Al	1.90E+04	3.27	2.05	7.26E+04	24.02	1.98	-	-	-	406.18	2.36
BeO:Ca	3.90E+04	21.2	1.12	4.32E+04	23.56	1.96	-	-	-	345.75	1.55
BeO:Al,Ca	6.83E+04	19.7	2.05	6.39E+04	246.13	2.05			-	187.92	1.81
Using three components											
BeO	2.76E+04	4.54	1.29	2.38E+05	105.92	1.05	5.40E+04	219.19	2.05	192.35	0.64
BeO:Al	4.24E+04	7.57	2.05	4.61E+04	23.66	1.28	2.13E+03	242.71	1.68	316.91	1.11
BeO:Ca	3.03E+04	21.4	1.14	1.14E+04	19.60	1.18	4.03E+04	23.90	2.02	353.42	1.49
BeO:Al,Ca	3.70E+04	5.17	1.33	4.58E+04	37.02	1.99	5.86E+04	262.84	2.05	95.71	0.57

Considering the change in decay times of undoped samples by adding Al and Ca ions, one may conclude that the doping of BeO host matrix material with Al and Ca ions cause the decay times (slow-medium-fast components) to change. Here, the long decay times may be due to the higher trap densities of deeper traps. Similar explanations were presented for the lifetimes of phosphorescence decays based on $SrAl_4O_7$ green nanophosphors (Singh et al., 2016a; Singh et al., 2016b).

4.4.3.2. RL Emissions

In this work, X-ray luminescence spectra from BeO, BeO:$Al_{1\%}$, BeO:$Ca_{1\%}$ and BeO:$Al_{1\%}$,$Ca_{0.1\%}$ pellets were recorded at room temperature with a resolution of 1 nm and presented in Figure 4.34. This is a good starting point for the analysis of the luminescence spectra of X-ray excitation because it exhibits the general view and the positions of the luminescence bands.

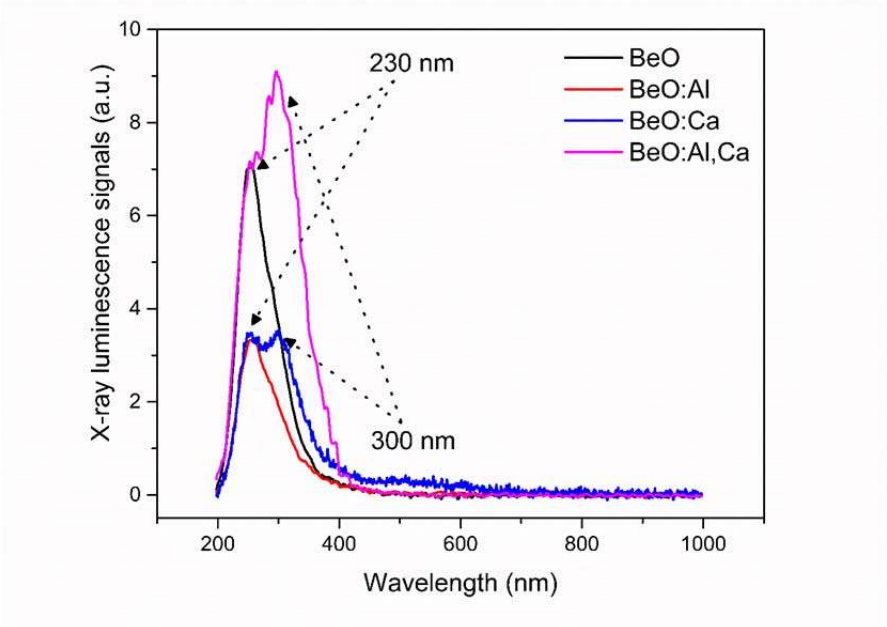

Figure 4.34. X-ray Luminescence spectra from the BeO, BeO:Al, BeO:Ca and BeO:Al,Ca pellets

As is seen from Figure 4.34, the XL spectra of BeO and BeO:Al pellets showed the same broad peak located between 200 and ~400 nm with a peak maximum at 230 nm (at photon energies of ~5.4 eV)). The recent vision attributes these bands to the radiative annihilation of self-trapped excitons (STE) of two kinds: namely STE1 and STE2. According to earlier works suggested by Ogorodnikov et al. the UV band at 3.5-5.5 eV is due to the BeO host emission (Ogorodnikov and Kruzhalov, 1997; Ogorodnikov et al., 1995). The hole components of both STE's are in the form of the O^- ion-type small radius polarons differentiated in the directions of Be-O bonds. As is seen from Figure 4.34, the broad luminescence bands peaked at ~5.4 eV are induced by the radiative decay of two different STEs, which are distinguished based on their valance hole configuration within BeO unit cell (Ivanov et al., 1994). The observed luminescence band located at 5.4 eV is consistent with that observed by Ogorodnikov et al. (Ogorodnikov and Kruzhalov, 1997; Ogorodnikov et al., 1995).

After doping with Ca, the same broad emission spectrum was observed for BeO:Ca and BeO:Al,Ca pellets. Noticeably, there are two dominant peaks in this spectrum: the first one at ~5.4 eV (230 nm wavelength) and the other peak at a photon energy of ~4.1 eV (300 nm wavelength). We revealed that the two-peak emission was closely associated with the energy transfer taking place between Ca activators located at two different crystallographic sites in the BeO (for BeO:Ca) and BeO:Al (for BeO:Al,Ca) structures. Considering the emission band of BeO pellets, one may make inferences that while Al additive does not change the spectra, Ca additive causes the emission regions of the spectra to shift to the higher wavelength. In addition to the UV signal emission, a weak red emission at ~600-615 nm was surprisingly observed from the BeO:Ca pellet. Although there is no water peak in FT-IR spectrum, this emission could be interpreted as hydroxyl groups that are present in solid samples stored in ambient conditions and may be potentially active luminescence emitters (Garcia-Guinea et al., 2018). In this study, the obtained emission spectrum from the pellets is at the transmittance range of the Hoya U-340 filter used in all OSL and TL measurements. Since the used range was very convenient, the ~3-4 eV emission band of BeO OSL emission was successfully recorded. The OSL emission spectrum is considerably different than the XL emission spectrum. It may be considered that the excitons produced during X-ray irradiation cause the X-ray luminescence spectrum. For this reason, the XL emission band will not be observed during the OSL stimulation. The reported OSL emission band has a peak at 280 nm and the main TL emission band at 335 nm (McKeever et al., 1995; Yukihara, 2011).

4.4.3.3. Effect of OSL Measurements on TL Signals

To investigate optically active parts of TL glow curves from BeO, BeO:$Al_{1\%}$, BeO:$Ca_{1\%}$ and BeO:$Al_{1\%}$,$Ca_{0.1\%}$ ceramic pellets, the TL glow curve (direct TL) and the TL glow curve obtained after OSL measurement (residual TL) were recorded up to 650 °C at a heating rate of 2 °C/s, after being irradiated with

0.2 Gy beta dose. Figure 4.35 shows direct TL, residual TL and bleached TL glow curves for each pellet. Bleached TL curves were obtained by subtracting the residual TL from the direct TL. The bleached TL curve for each studied sample represents the optically active parts of the TL glow curves. As is seen from Figure 4.35a, the 1^{st}, 2^{nd}, 3^{rd} peaks of the TL glow curve of BeO pellets were affected by optical stimulation whereas the 4^{th} peak was not. This effect of light exposure on TL glow curve provides us to say that the source of the OSL signal might be associated with the 80, 200 and 370 °C TL peaks. Considering residual TL curve for BeO:Al pellets, 1^{st} and 2^{nd} peaks were affected from OSL measurements, whereas 3^{rd} peak was not (see Figure 4.35b). This also may provide us to interpret that the origin of the OSL signals for BeO:Al can be associated with the 200 and 350 °C TL peaks. Similar to BeO, for BeO:Ca pellets, it is seen from Figure 4.35c that 1^{st}, 2^{nd}, 3^{rd} peaks were affected but the 4^{th} peak was not, after the light exposure. We can reach the same result for BeO:Ca with that of BeO; the origin of the OSL signals might be related to the TL peaks located at 80, 200 and 370 °C. On the other hand, it was observed that all peaks were affected by light stimulation and there was a correlation between all the TL peaks and the OSL signals when the residual TL of BeO:Al,Ca was examined (see Figure 4.35d).

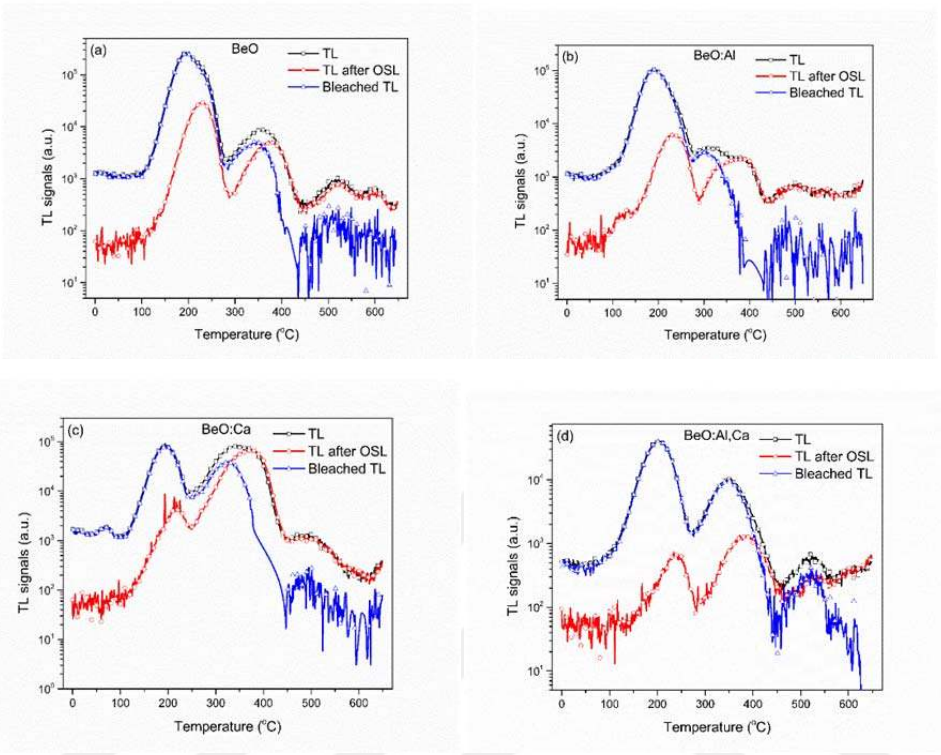

Figure 4.35. TL glow curves (direct TL), TL glow curves (residual TL) obtained after OSL measurements (optical stimulation of 200 s) and Bleached TL curves from the 0.2 Gy irradiated pellets for BeO (a), BeO:Al (b), BeO:Ca (c) and BeO:Al,Ca (d). Bleached TL curves were obtained by subtracting residual TL from the direct TL for each sample. The heating rate of TL readouts was 2 °C/s.

4.4.3.4. Step Annealing Experiments

To investigate the correlation between these affected TL peaks and the source of the OSL signals for the studied pellets, the step-annealing experiments (thermal-stability experiments) were performed in the temperature range from 50 to 570 °C with 10 °C increments, 5 °C/s heating rates. For this purpose, the pellets were repeatedly heated to an annealing temperature after irradiation with 0.2 Gy, and the remaining OSL signals were recorded using 200 s blue-light stimulation each time. The samples were depleted using TL measurements (up to 650 °C)

following the OSL measurements. The changing of the integrated OSL signals (the sum of the counts obtained from 0 to 200 s) against the annealing temperatures were illustrated together with the bleached TL curves for each pellet in Figure 4.36.

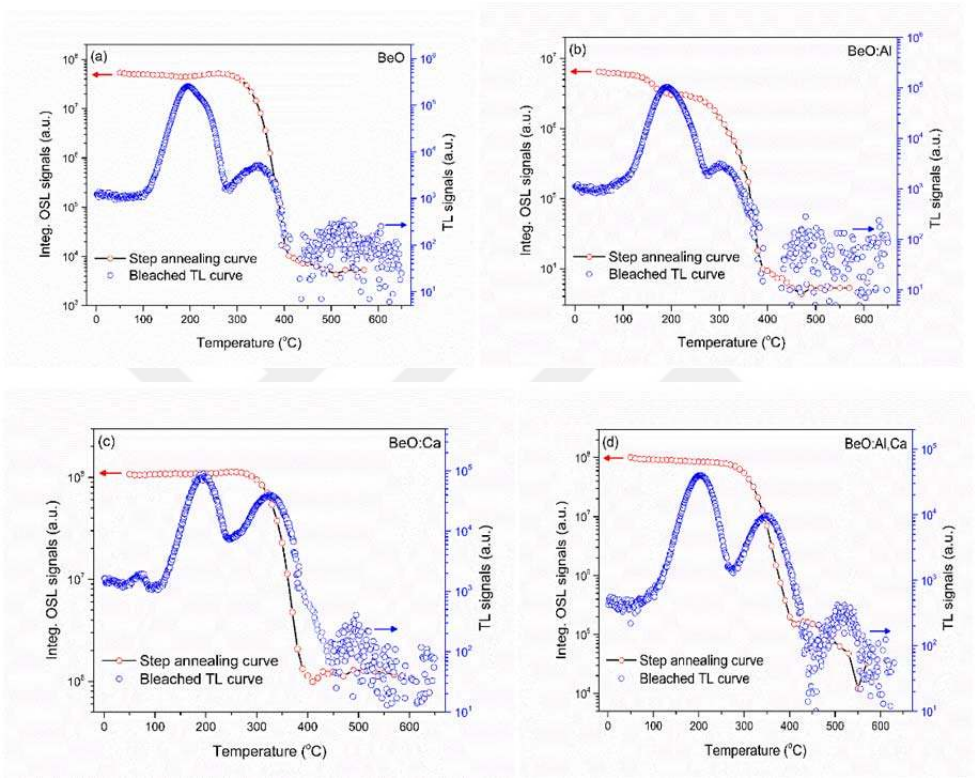

Figure 4.36. Step annealing curves of OSL signals from 0.2 Gy irradiated pellets for BeO (a), BeO:Al (b), BeO:Ca (c) and BeO:Al,Ca pellets (d) with bleached TL curves. After the OSL measurement in each step, residual signals were depleted by performing TL readout from RT up to 650 °C for 2 °C/s of HR. The arrows indicate the related axes.

For BeO pellets, the OSL signals were very stable up to 300 °C and started to decrease after this temperature (see Figure 4.36a). The decrease of OSL signals can be associated with the emptying of the 370 °C TL peak after the light exposure. After the complete discharging of the TL traps responsible for the 370 °C TL peak, the OSL signals reach the background level. As a result, for the BeO pellets, one

may say that the OSL, most probably, employ the same recombination centers as the 370 °C TL peak. Similar results were presented for commercially available Thermalox995 BeO chips by Bulur and Goksu (Bulur and Goksu, 1998). For BeO:Al pellets, it is seen from the step-annealing curve in Figure 4.36b, the first decrease in OSL signals started after an annealing temperature of 150 °C. The decrease in OSL signals correlates with the emptying of the 200 °C TL peak after the OSL stimulation. After the first decrease in the step-annealing curve, the OSL signals were very stable up to 260 °C and started to the second decrease after this temperature. Following the complete discharging of the TL traps responsible for the 350 °C TL peak, the OSL signals reach the zero level. It shows that the source of the OSL signals is perhaps associated with both the 200 and 350 °C TL peaks and the OSL, most probably, employ the same recombination centers as the 200 and 350 °C TL peaks. Similar results were obtained for 1100 °C sintered BeO pellets synthesized using the sol-gel method by Altunal et al. (Altunal et al., 2018). In Figure 4.36c, considering the step-annealing curve of BeO:Ca pellets, OSL signals were found as very stable with the increasing annealing temperature up to 300 °C and started to decrease after this temperature similar to BeO pellets. The decay of the OSL signals with the annealing temperature infers a possible association of 370 °C TL peak with the OSL signal observed. The OSL signals may occur from the same recombination centers with the 370 °C TL peak. Finally, as is seen from the step-annealing and bleached TL curves of BeO:Al,Ca pellets in Figure 4.36d, the OSL signal decreased after the annealing temperature of 300 °C might be associated with only the 350 °C TL peak. It may not be concluded whether the OSL and TL signals occurred from the same trap or not. On the other hand, it can be interpreted that 200 °C TL peak has high light sensitivity but does not contribute to the OSL signals of BeO:Al,Ca pellets. The extracted charges from 200 °C traps by optical stimulation may make some non-radiative transitions or luminescence emission may occur out of the detection band of the used filter (Hoya U-340). Further studies are necessary to collect more evidence about this.

4.4.3.5. Thermal Quenching of the OSL Signals

In many materials, thermal quenching is observed with the reduction in luminescence intensity at temperatures higher than room temperature. To investigate the presence of thermal quenching which gives information about the increase in the probability of non-radiative transitions from the excited to the ground state of the luminescence centers (the Mott-Seitz model) (Bøtter-Jensen et al., 2003), the study of the temperature dependence of OSL signals from the studied ceramic pellets were checked after the irradiation with 1 Gy beta dose and preheating at 110 °C for 60 s. The temperature dependence of the OSL signal can be expressed by Equation (4.2. In this work, OSL signals were obtained with the 200 s blue-light stimulation at various reading temperatures ranging from 50 to 130 °C with 5 °C increments (see Figure 4.37). After each OSL measurement, residual luminescent signals were deleted by performing TL readouts up to 650 °C and the samples were irradiated again with the same dose for the next measurement.

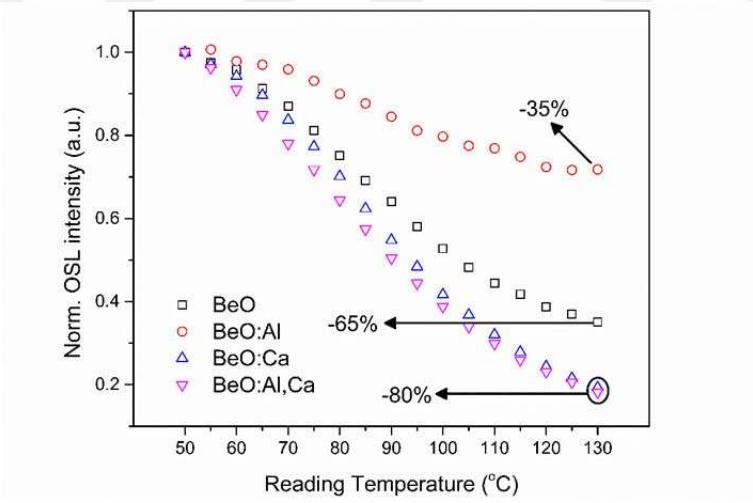

Figure 4.37. Normalized OSL intensities of the BeO, BeO:Al, BeO:Ca and BeO:Al,Ca ceramic pellets at various reading temperatures after the irradiation with 1 Gy beta dose and preheating the samples at 110 °C for 60 s. Residual signals were deleted by performing TL readout (from RT to 650 °C, 5 °C/s of HR) for each step.

As is seen from Figure 4.37, the reduction in luminescence intensity with increasing readout temperature demonstrates the presence of strong thermal quenching. The integrated OSL signals obtained at 130 °C decreased by ~35 % for BeO:Al, ~65 % for BeO, ~80 % for both the BeO:Ca and BeO:Al,Ca pellets when compared with that of OSL signals obtained at 50 °C for the same samples. As a result, when BeO doped with Al, the loss in OSL signals obtained at increasing readout temperatures, decreased concerning the host material. But, when Ca ions were used as a dopant together with and without Al, it was observed that Ca ions caused the strong thermal quenching in OSL signals when the OSL signal was obtained at 130 °C compared with that of obtained at 50 °C.

TOSL curves can be used as an alternative method to get information about the thermal quenching mechanism. A TOSL curve indicates the temperature dependence of the OSL signal which is obtained by subtracting the TL curve from the TL curve obtained with OSL stimulation. This technique was reported in the literature for feldspars (Duller and Bøtter-Jensen, 1993), aluminum oxide (Markey et al., 1996) and BeO chips (Thermalox995) (Bulur and Goksu, 1998). Here we used 0.1 s pulsed stimulation with 0.9 s time interval between the pulses while TL readout. The signals measured during the light stimulations are the combinations of the OSL as a function of temperature and the TL (i.e. TL+OSL). The measurements performed during the time interval between the pulses give the TL signals (TL). The difference between the TL+OSL and TL curves gives the TOSL curve providing information about the temperature dependence of the OSL process. Figure 4.38 shows TL+OSL, TL and TOSL curves for the BeO, BeO:$Al_{1\%}$, BeO:$Ca_{1\%}$ and BeO:$Al_{1\%}$,$Ca_{0.1\%}$ pellets with TL readout up to 650 °C at a rate of 5 °C/s having blue-light stimulation at the same period.

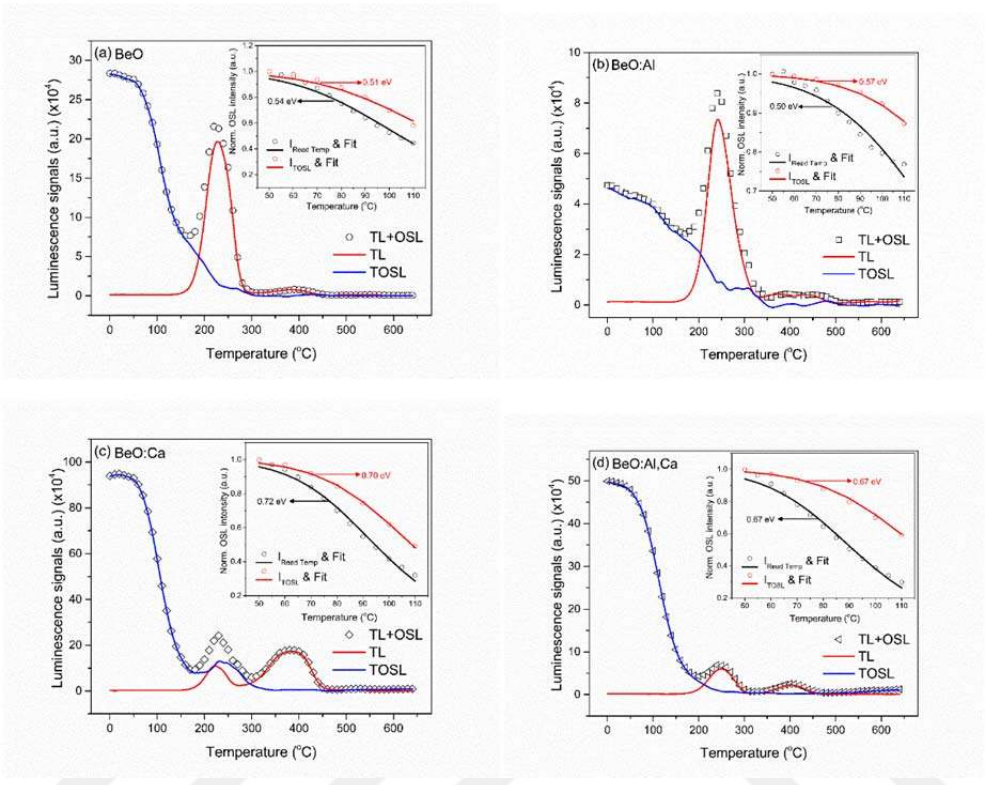

Figure 4.38. The TOSL curves from 1 Gy irradiated pellets for BeO (a), BeO:Al (b), BeO:Ca (c) and BeO:Al,Ca (d). TOSL curves obtained by subtracting the TL curves from the TL curves obtained with optical stimulation for each studied pellet. Insets: calculation of the thermal quenching energy using the signal intensities of TOSL curves and OSL signals obtained at various readout temperatures ranging from 50 °C to 110 °C. The arrows indicate the related axes.

In Figure 4.38, from the TOSL curves of BeO and BeO:Al,Ca pellets, the OSL outputs sharply decreased up to 150 °C, beyond which slow reductions were observed up to 230 °C. After this temperature, the OSL outputs reached zero level. It can be inferred that the first sharp decrease may be associated with the strong thermal quenching and the second decrease (relatively slower one) may be responsible for emptying the dosimetric traps. Considering the TOSL curve of the Al-doped BeO pellet in Figure 4.38b, it can be interpreted that the decrease in OSL

outputs up to 150 °C originated from thermal quenching followed by both the dosimetric traps being emptied with the stimulation and reaching the OSL outputs to the zero level. In Figure 4.38c, TOSL curve of BeO:Ca exhibited similar behavior with that of BeO and BeO:Al,Ca pellets up to 150 °C. After this temperature, the OSL outputs increased up to 250 °C. Following the next decrease up to 300 °C, the OSL outputs reached zero level. As a result, it can be suggested that the increase in TOSL signals between the temperature region from 150 to 250 °C may be due to the transitions of the electrons from the deep traps to the shallow traps (i.e. phototransfer to 200 °C TL peak from 370 °C TL peak which is responsible for OSL signals as mentioned above). This statement is only an assumption on PTTL for understanding the mechanism of luminescence from BeO:Ca pellet, more detailed PTTL studies of the material should be performed to prove whether this assumption is true or not.

The thermal quenching energies of the materials were evaluated using the data collected in OSL readouts (see Figure 4.37) and by fitting them into Equation (3). We also used the reduction data in the initial parts of TOSL curves to evaluate the thermal quenching energies (see Figure 4.38). The obtained data were fitted to the curve. The fitting curves and the estimated E_Q values using both methods were presented for each pellet in the graphs of the insets of Figure 4.38, which plot the OSL signal intensity as a function of temperature. The perfection of the fitting curves in two methods was tested using the figure of merits (FOM) (Balian and Eddy, 1977), and the obtained FOM values, which is a sign of agreement between experimental and theoretical data, were presented together with the E_Q and C values of both methods, in Table 4.8.

Table 4.8. Thermal quenching parameters, E_Q and C values, of BeO pellets with the related FOM values

	Reading Temperature			***TOSL***		
	E_Q (eV)	C (a.u.)	FOM(%)	E_Q (eV)	C (a.u.)	FOM(%)
BeO	0.54	1.56E+07	1.38	0.51	3.51E+06	0.49
BeO:Al	0.50	1.54E+06	0.49	0.57	4.55E+06	0.01
BeO:Ca	0.72	7.42E+09	0.70	0.70	1.80E+09	0.08
BeO:Al,Ca	0.67	2.05E+09	1.02	0.67	4.83E+08	0.15

4.4.3.6. Dose-Response and Minimum Detectable Dose Values

The behavior of the OSL signals from BeO, BeO:$Al_{1\%}$, BeO:$Ca_{1\%}$ and BeO:$Al_{1\%}$,$Ca_{0.1\%}$ ceramic pellets were investigated in the beta dose range between 0.1 Gy and 100 Gy. The materials were given 0.1, 0.2, 0.5, 1, 2, 5, 10, 20, 50 and 100 Gy beta doses. Three irradiated samples were preheated from room temperature up to 110 °C for 60 s before the OSL measurements. Following the OSL measurements of the materials, residual signals were depleted by TL readout (up to 650 °C). The plots of integrated OSL signals (the sum of the counts obtained from 0 to 200 s) against the absorbed beta dose were presented in Figure 4.39. It is seen from the figure that the dose-response behaviors of the pellets are linear in the dose range between 0.1 and 100 Gy. The slope values were found to be 1.03, 1.06, 1.03 and 1.02, from the linear fitting of dose-response curves for BeO, BeO:$Al_{1\%}$, BeO:$Ca_{1\%}$ and BeO:$Al_{1\%}$,$Ca_{0.1\%}$ pellets, respectively. Similar results were presented in a previous study for BeO ceramic pellets synthesized using the sol-gel technique at a sintering temperature of 1100 °C by Altunal et al. (Altunal et al., 2018).

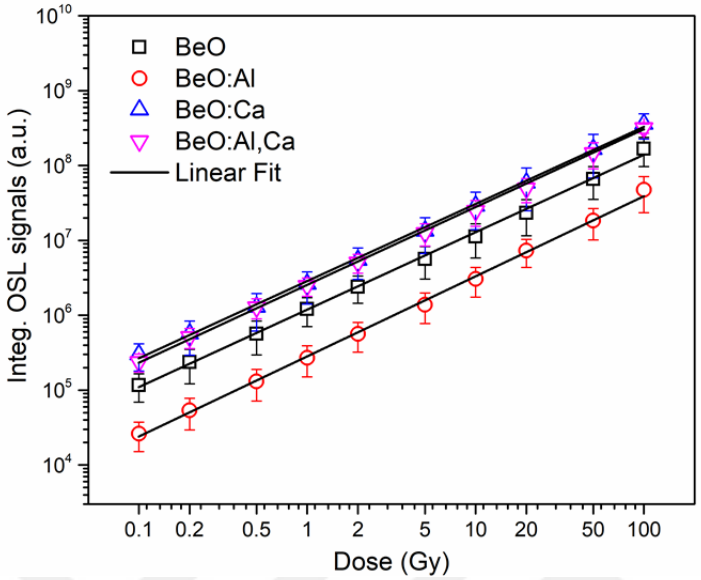

Figure 4.39. The integrated OSL signals of BeO, BeO:Al, BeO:Ca and BeO:Al,Ca ceramic pellets with various radiation doses from 0.1 to 100 Gy. BeO pellets were stimulated with 200 s blue light after preheating (up to 110 °C with 5 °C/s of HR).

In addition to the radiation dose linearity, the minimum detectable dose (MDD) values of the pellets were estimated as dose considering three times the experimental standard deviation of the background signal from the unirradiated sample and the total OSL signal from the sample irradiated with a minimum applicable dose of the readout system. MDD in CW-OSL mode can be expressed by Equation (4.3) (Rawat et al., 2014). The MDD values of BeO, BeO:$Al_{1\%}$, BeO:$Ca_{1\%}$ and BeO:$Al_{1\%}$,$Ca_{0.1\%}$ pellets were estimated as ~0.9, ~4, ~0.5 and ~0.5 mGy, respectively. Here, we did not perform sufficient measurements in the low dose range due to using the radiation source not being precisely calibrated, so it must be noted that these MDD values are as an estimated order of magnitude.

4.4.3.7. Reusability of the OSL Signals

The OSL dosimeters are expected to be reusable in dosimetric applications, i.e., the OSL signal is expected to exhibit the same response following the same exposures under carefully controlled laboratory conditions. The reusability properties of three BeO, BeO:$Al_{1\%}$, BeO:$Ca_{1\%}$ and BeO:$Al_{1\%}$,$Ca_{0.1\%}$ pellets irradiated at a dose of 0.2 Gy were investigated measuring OSL signals after the preheating process at 110 °C for 60 s. Following each OSL readout, the residual OSL signals were deleted by TL readout (up to 650 °C). The identical measurements were repeated 10 times. In Figure 4.40, the normalized integrated OSL signal intensities versus the experimental cycles were illustrated. As can be seen from the figure, OSL signals of all the samples matched well with each other and showed very good reusability over ten cycles. The deviation from the first readout value was determined as a maximum ~2%.

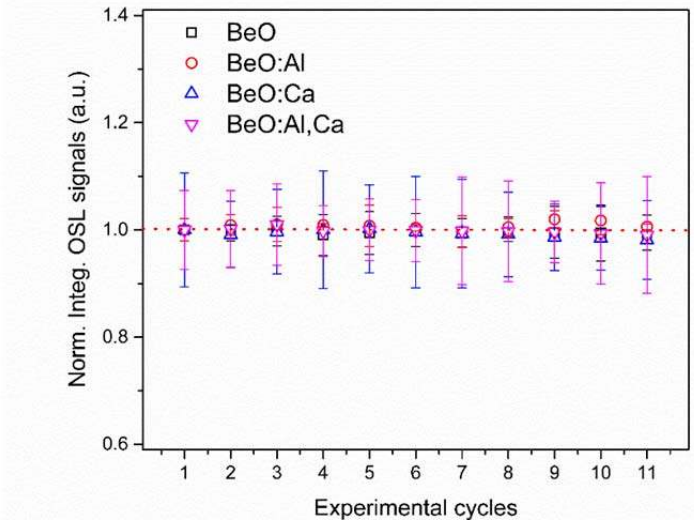

Figure 4.40. The reusability properties of OSL signal of BeO, BeO:Al, BeO:Ca and BeO:Al,Ca ceramic pellets. Each sample was irradiated with 0.2 Gy beta test dose and OSL signals were recorded for 200 s after preheating at 110 °C for 60 s. The residual signals were deleted by a TL reading up to 650 °C with 5 °C/s of HR after each OSL measurement.

4.4.3.8. Dark Storage Fading

The fading characteristics of BeO, BeO:$Al_{1\%}$, BeO:$Ca_{1\%}$ and BeO:$Al_{1\%}$,$Ca_{0.1\%}$ pellets were checked by keeping three samples from each group in dark at room temperature after irradiation with 0.2 Gy beta dose. The fading of the samples was investigated for various time intervals during one month; starting after half an hour from the exposure (see Figure 4.41).

No significant decrease was observed in the 72 hour storage period for the signals of the BeO, BeO:Al,Ca. The decrease of the integrated OSL signals was ~5% at the end of 72 h (see Figure 4.41a). On the other hand, for BeO:Al pellets, the decrease of integrated OSL signal was observed as ~9% at the end of 24 h and ~12% at the end of 72 h. When considering the OSL signals of BeO:Ca pellets, an increase of ~21% was observed in the first 1 hour storage period after the first readout and this increase was reduced to the initial readout value after 24 hours. At the end of 72 h, the decrease of the integrated OSL signal was observed as ~20% (see Figure 4.41a). While the initial fall of the OSL signals from the BeO, BeO:Al and BeO:Al,Ca at the end of the 24 h be considered as a result of the escaping of electrons from the shallow traps at room temperature (Guckan et al., 2017; Ozdemir et al., 2018; Yukihara et al., 2017), the unexpected increase of the OSL signals from the BeO:Ca pellets with storage time during 72 h period could be related with the tunneling of escaped electrons from the shallow traps to deep traps at room temperature (Nambi, 1977; Ozdemir et al., 2016).

In Figure 4.41b, the integrated OSL signals from each group of pellets were presented against a storage time of 1 month. As is seen from Figure 4.41b, the OSL signals from the BeO pellets were first observed as very stable up to 1 week and slightly increased (~5%) up to 1 month when compared with the first readout OSL signals. After the decrease in OSL signals from BeO:Al pellets at the end of 72 h, the integrated OSL signals increased ~25% and ~2 in 1 week and 1 month of storage in dark storage, respectively. The integrated OSL signals from BeO:Ca decreased approximately 28% in 1 week when compared with the first integrated

OSL intensity and then increased to ~14% during the following two weeks. At the end of the fourth week, the material decreased to the same level as the first week. On the other hand, as is seen in Figure 4.41b, the BeO:Al,Ca pellets with the residual signals keeping stability exhibited almost no fading at the end of 1 month. As a result, one may say that the separate doping of Al and Ca causes high fading in BeO. When both of the ions Al and Ca are doped together the sample is enabling the improved energy storage property.

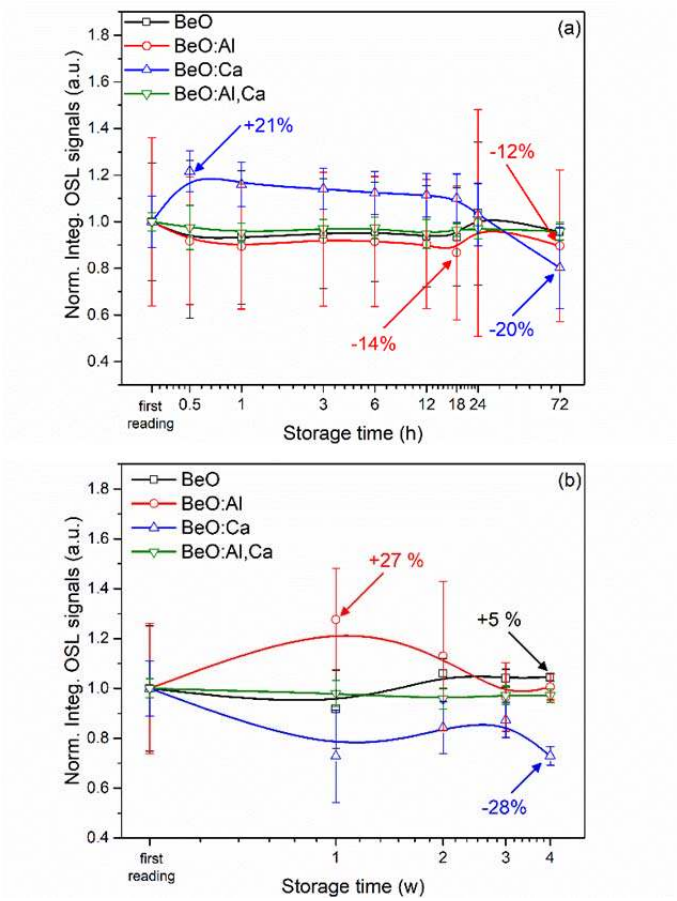

Figure 4.41. The fluctuation in fading of the OSL signals of undoped and doped BeO ceramic pellets as a function of short storage time up to 72 h (a), storage time up to 4 weeks (b) after 0.2 Gy beta dose exposure.

4.4.4. Discussion

To understand the role of Ca and Al ions in the BeO lattice and how the luminescence mechanism takes place, a simplified luminescence process is needed. Al or Ca ions upon introduction into the BeO lattice should create shallow local levels in the forbidden band and actively manifest themselves in recombination processes. For example, doped Al^{2+} would replace Be^{2+} ions sites on the host lattice. The difference of ionic radius between Al^{2+} (0.68 Å) and Be^{2+} (0.59 Å) would decrease the lattice constant, which can lead to lattice deformation in BeO structure. We have a similar pattern for Ca^{2+} ions. Due to the remarkable differences between ionic radius (1.14 Å for Ca^{2+}) and Be^{2+}, the Ca^{2+} ion may wish to locate in crystalline vacancies rather than to substitute for the Be^{2+} ion. Even Ca^{2+} generates an interstitial defect, Ca^{2+} ions in crystalline vacancies would have an effect similar to the structural deformation occurring in the substitutional defects. Regarding the energy, the crystal field energy should get a perturbation when the lattice changes, which would increase luminescence efficiency.

It is possible to say that the luminescence mechanism of doped BeO can be explained more than the luminescence type which assumes a trap and a recombination center. The luminescence process simply begins by exposing the crystal to ionizing radiation and then creating charge carriers, i.e., electrons and holes moving freely inside the crystal. In this study, the heterovalent substitution impurity (Al^{2+}) acts as a hole trap and becomes Al^{3+} during delivering irradiation. On TL/OSL readout, a trapped electron is released from the trapping center, and Al^{2+} ion occurs with recombination of this electron with Al^{3+} ion. Therefore, during TL/OSL readout, Al^{2+} ion plays an important role as a recombination center (Kortov et al., 1993b; Kruzhalov et al., 1996). In this process, Al^{2+} ion is still in an excited state. Luminescence emission occurs with the relaxation of Al^{2+}. This proposed process is summarized in Figure 4.42.

On the other hand, we have met with unexpected TL and XL results for Ca^{2+}. Although the characteristics of the TL glow curves obtained from undoped

and singly doped (with Ca^{2+}) samples did not change, the XL spectra of undoped BeO shifted to higher wavelengths with Ca^{2+} doping. Moreover, adding Ca^{2+} ions (doping) to BeO:Al did not change XL and TL characteristics obtained when compared with BeO:Al. But it enhanced the sensitivity of the luminescent signals, visibly. Here, one possible explanation of this phenomenon is that Ca^{2+} may play a role as a charge compensator. Similar co-dopant behavior has been reported for Li^{+} ion-doped to MgO host material (Oliveira et al., 2016; Yukihara et al., 2013).

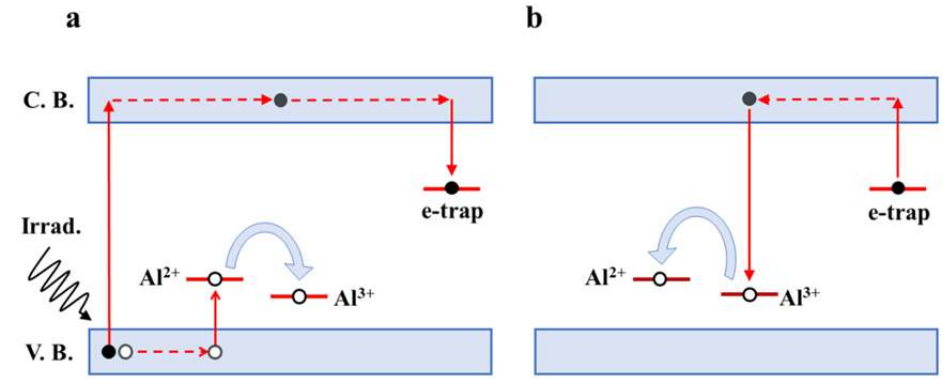

Figure 4.42. Proposed TL/OSL mechanism: (a) During irradiation, charge carriers (electron and holes) are created, and trapped by electron- and hole (Al^{2+})- traps, ($Al^{2+} + h^{+} \rightarrow Al^{3+}$). (b) During TL/OSL readout (thermal or optical stimulation), electrons are released from the trapping center and recombine with Al^{3+} ions, converting them to Al^{2+} in an excited state. Luminescence occurs with the relaxation of these compounds. Electrons and holes are represented by solid and open circles, respectively.

4.5. BeO Ceramics Doped with Metals

In this work, BeO ceramics were successfully doped with some monovalent, divalent, trivalent, and tetravalent metal elements, Al^{3+}, Ca^{2+}, Mg^{2+}, Na^{+}, Li^{+}, K^{+}, B^{3+}, Si^{4+}, Zn^{2+}, Sr^{2+}, In^{3+}, and Cu^{4+} by using the co-precipitation method. The phase formation and surface morphology were characterized by x-ray diffraction (XRD) and scanning electron microscopy (SEM) analyses, respectively. Luminescence characterizations were examined using radioluminescence (RL), TL,

and OSL methods. We investigated the TL and OSL behavior in terms of a possible relation to the different valent metal dopant impurities added in BeO pellets. Furthermore, dosimetric tests were performed using some promising metal-doped BeO samples such as dose-response, reusability, and dark fading properties. This study demonstrated the metal dopant possibilities based on the better intensity of TL and OSL outputs for the development of promising novel BeO dosimetric materials.

4.5.1. Material Synthesis

BeO samples were synthesized using the co-precipitation method. The characteristics of the used precursor reactants (raw materials) were presented in Table 4.9. The co-precipitation method was discussed in previous studies (Altunal et al., 2019b; Altunal et al., 2020b; Altunal et al., 2020c; Altunal et al., 2020d), and the preparation method has been modified in this study to allow better process control. We were first controlled doping various elements: Al, Ca, Mg, Na, Li, K, B, Si, Zn, Sr, In, Cu with 0.1, 0.5, 1, 5 % molar ratios as a nominal composition of the BeO samples. The resultant samples were calcined at 900 °C for 4 h in an oxygen atmosphere to remove the organic formations in the synthesis process and achieve BeO nano-particles. Finally, single-metal doped BeO white powders were achieved and used in pellet form which provides more settled OSL signals. 25 mg BeO ceramic pellets were prepared as discs with, ~3.1 mm in radius and ~0.8 mm in thickness. To provide strength, integrity and avoid the toxicity of BeO in powder form, the obtained pellets were sintered at 1600 °C for 4 h. After the 1600 °C sintering of the pellets, the weight losses were also observed in the studied BeO pellets. The measured weights were ~23.1 ± 0.2 mg. RL, TL and OSL emissions of BeO:$Ca_{5\%}$ samples could not be measured in this study because the pellets adhered to the crucible after sintering at 1600 °C for 4h and could not be recovered. It must be noted that handling BeO ceramics in solid form (chips, rods, discs, etc.) poses no special health risk. Inhalation of airborne beryllium may cause a serious lung disorder in susceptible individuals. We performed safety and environmental efforts

and followed the safe handling practices in our work with BeO. Personal protective equipment such as gloves, dust and gas masks, goggles, etc. were used in the laboratory during the synthesis of this material.

Table 4.9. Characteristics of the precursors (raw materials)

Raw materials	Molecular Formula	Function	Purity	Supplier
Beryllium sulfate tetrahydrate	$BeSO_4 \cdot 4H_2O$	Initial salt	99.90%	Sigma-Aldrich
Polyethyleneimine solution	$(NHCH_2CH_2)_n$	Polymerization	50% (w/v) in H2O	
Ammonium hydroxide	NH_4OH	Initiator of precipitate	28.0-30.0% NH3 basis	
Aluminum nitrate nonahydrate	$Al(NO_3)_3 \cdot 9H_2O$	Dopant	Trace metals basis, 99.997%	
Calcium nitrate tetrahydrate	$Ca(NO_3)_2 \cdot 4H_2O$	Dopant	≥99.0%	
Magnesium nitrate hexahydrate	$Mg(NO_3)_2 \cdot 6H_2O$	Dopant	Trace metals basis, 99.999%	
Lithium nitrate	$LiNO_3$	Dopant	Trace metals basis, 99.99%	
Potassium sulfate	K_2SO_4	Dopant	Reagent Plus®, ≥99.0%	
Boric acid	H_3BO_3	Dopant	ACS reagent, ≥99.5%	
Silicium Standard for ICP	10,000 mg/L Si in nitric acid	Dopant	10′000 mg/L Si in 5% nitric acid (contains HF traces), prepared with high purity Si, HNO3, HF and water	
Zinc nitrate hexahydrate	$Zn(NO_3)_2 \cdot 6H_2O$	Dopant	Purum p.a., crystallized, ≥99.0% (KT)	
Strontium nitrate	$Sr(NO_3)_2$	Dopant	ACS reagent, ≥99.0%	
Indium(III) nitrate hydrate	$In(NO_3)_3 \cdot xH_2O$	Dopant	Trace metals basis, 99.99%	
Copper(II) nitrate hydrate	$Cu(NO_3)_2 \cdot xH_2O$	Dopant	Trace metals basis, 99.999%	

4.5.2. Structural Characterization

Characterization of the single-metal doped BeO pellets was examined by using XRD and SEM analyzes. To obtain an idea about the crystallographic phase formation of the synthesized pellets, XRD analysis was carried out with Cu-Kα (40 kV, 30 mA). The XRD pattern was achieved from 10° to 90° (2θ) with 0.02° (2θ) increments. Phase identification was performed using the International Center for Diffraction Data (ICDD) PDF card 98-006-2733. To characterize the surface morphology and grain sizes of produced pellets, the SEM analyses were done with the spectral slit width of 1.5 nm at room temperature. The micrographs of the single-metal doped BeO ceramic pellets were taken at 10kx direct magnification, 20 kV, and a spot size of 2.5 nm.

4.5.2.1. X-Ray Diffractions

The XRD analyzes of the undoped and metal-doped BeO pellets were performed to investigate the effects of metal doping on the structures and sizes of BeO crystals. The XRD patterns of the samples were presented by comparing them with that of the reference spectrum compiled by the International Centre for Diffraction Data (ICDD) (see Figure 4.43). As is seen from Figure 4.43, the three highly sensitive characteristic Bragg reflections were obtained with (100), (002), and (101) orientations which are identities of BeO nano-particles. All the obtained peaks from the undoped and doped pellets were well-indexed to the main data of the hexagonal BeO phase and reported in the ICDD PDF-card no 98-006-2733. The analysis showed that the samples with different metals doping had the same phase since they were produced under the same synthesis conditions (calcination and sintering processes). Considering the low intensive peaks located at 77° (2θ) and 84° (2θ), split for all samples. The reason for this should be originated from a reduction in symmetry of BeO phases, indicating the difficulties for metal atoms with different ionic radii to be introduced into the BeO crystal structure (Oliveira et al., 2019). It can be suggested that the metal-doped BeO nano-particles have

created many defects, including structural strain since most of the dopants have much larger ionic radii than that of Be and have different charge states. The supporting information "The ionic radii of Be and dopants used" was presented to show the relative difference to Be of all the dopants in Table 4.10. It was also found that the peak intensities of the samples increased with metal doping, which means that the BeO grains have grown and the crystallites have been improved (Altunal et al., 2020b).

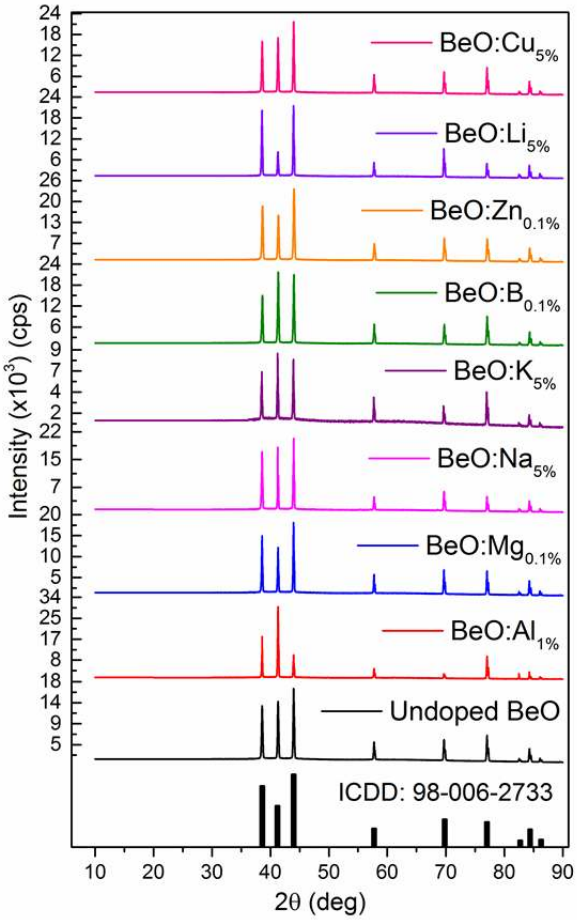

Figure 4.43. The XRD patterns of undoped and single-metal doped BeO pellet samples.

Table 4.10. The ionic radii in Å for coordination number 4 of Be and dopants used in this work

	Charge	Coordination number	Ionic radius (Å)	Relative size difference (%)
Be	2	IV	0.27	-
Al	3	IV	0.39	44.44
Mg	2	IV	0.57	111.11
Na	1	IV	0.99	266.67
Li	1	IV	0.59	118.52
K	1	IV	1.37	407.41
B	3	IV	0.11	-59.26
Si	4	IV	0.26	-3.70
Zn	2	IV	0.60	122.22
In	3	IV	0.62	129.63
Cu	1	IV	0.60	122.22
	2	IV	0.57	111.11

4.5.2.2. SEM Pictures

In our previous studies, it was observed that the surface morphology of undoped BeO changed with dopants and more settled luminescence was obtained from the non-porous surfaces (Altunal et al., 2019a; Altunal et al., 2020c; Altunal et al., 2020e). For this reason, SEM analyzes were conducted to investigate the effect of metal dopants on the morphology and grain size of BeO ceramic material. The SEM micrographs of the samples produced by the co-precipitation method and promising luminescence properties are presented in Figure 4.44. According to the obtained SEM micrographs, it is easily seen that single metal-doped BeO ceramics exhibit different surface morphologies and have a narrow size distribution within themselves (data not shown). While BeO:Al ceramic exhibits rectangular grains grown with different orientations (see Figure 4.44a), more spherical grains were

observed in BeO:B, BeO:Zn, and BeO:Cu ceramics (see Figure 4.44e,f,h). Also, it has been observed in the BeO:Mg, BeO:Na, BeO:K, and BeO:Li ceramic samples (see Figure 4.44b,c,d,g) that grains with larger surfaces appear smoother, bonded to each other with well-defined boundaries, and thereby created non-porous structures. On the other hand, the average grain sizes of BeO:$Al_{1\%}$, BeO:$Mg_{0.1\%}$, BeO:$Na_{5\%}$, BeO:$K_{5\%}$, BeO:$B_{0.1\%}$, BeO:$Zn_{0.1\%}$, BeO:$Li_{5\%}$, and BeO:$Cu_{5\%}$ ceramics were found to be ~ 3, 7, 10, 13, 1, 4, 6, and 5 μm, respectively (data not shown). The grain growth rates for BeO samples containing Mg, Na, K, and Li having less porosity were found to be qualitatively higher than BeO samples containing Al, B, Zn, and Cu.

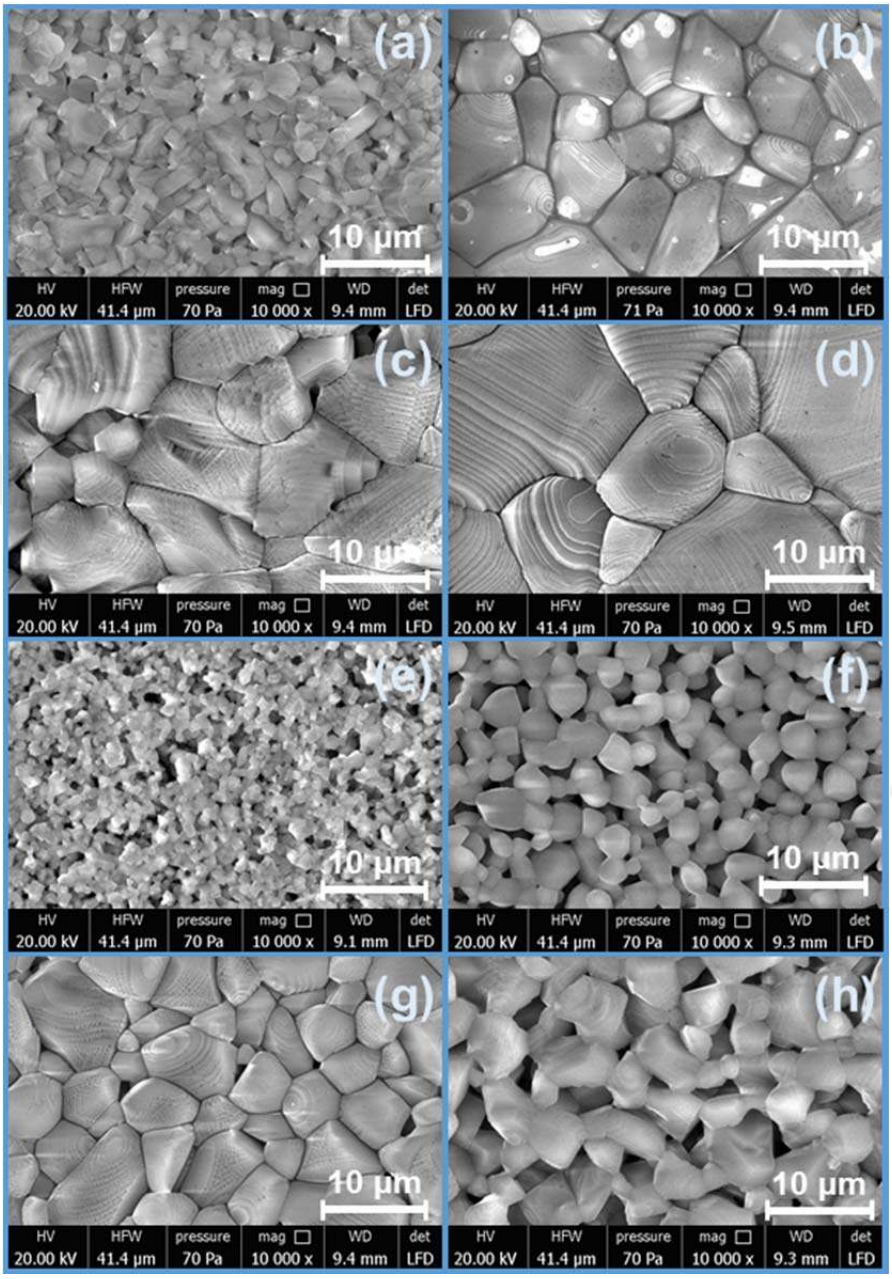

Figure 4.44. SEM micrographs of metal-doped BeO ceramic pellets; **(a)** BeO:$Al_{1\%}$, **(b)** BeO:$Mg_{0.1\%}$, **(c)** BeO:$Na_{5\%}$, **(d)** BeO:$K_{5\%}$, **(e)** BeO:$B_{0.1\%}$, **(f)** BeO:$Zn_{0.1\%}$, **(g)** BeO:$Li_{5\%}$, and **(h)** BeO:$Cu_{5\%}$.

4.5.3. Luminescence Characterizations

Luminescence characterizations of the single metal-doped BeO samples were investigated by using RL, TL and OSL techniques. TL and OSL emissions were filtered using a Hoya U-340 nm filter in front of PMT and detected in the UV region. In OSL readouts, samples were irradiated with 0.5 Gy beta dose and preheated at 100 °C for 10 s. Then, OSL readout was carried out by using blue light stimulation for 200 s in continuous wave OSL mode (CW-OSL mode). TL readouts were carried out by heating the 0.5 Gy irradiated sample to 650 °C with a 3 °C/s heating rate without a preheating procedure. Each sample was individually calibrated with an irradiation dose of 0.5 Gy due to the variations in responses in the same batch. All stated values in this work were given after correction with calibration factors. To increase the reliability of the TL experiments, newly produced/or annealed (at 650 °C for 10 min) pellets having almost the same mass (between 23.1-23.3 mg) were used in each experiment.

RL emissions of the BeO pellets were achieved from a homemade X-ray Luminescence system. The RL emissions were detected by using a CCD detector, while samples were exposed to X-rays with ~20 kV voltage.

4.5.3.1. RL Emissions

Investigation of RL characteristics is a good starting point for knowledge of the positions and general appearance of the luminescence bands. In this work, RL spectra were obtained from the undoped BeO and single metal-doped BeO ceramics with different dopant concentrations (x = 0.1, 0.5, 1, 5%), namely, BeO:$Al_{x\%}$, BeO:$Ca_{x\%}$, BeO:$Mg_{x\%}$, BeO:$Na_{x\%}$, BeO:$Li_{x\%}$, BeO:$K_{x\%}$, BeO:$B_{x\%}$, BeO:$Si_{x\%}$, BeO:$Zn_{x\%}$, BeO:$Sr_{x\%}$, BeO:$In_{x\%}$, and BeO:$Cu_{x\%}$, using a 1 nm resolution at RT and presented in Figure 4.45a-l, respectively. The RL spectra of all BeO ceramic pellets demonstrated the same wide emission peak located between 200 and ~450 nm with the maximum at 250 nm (photon energies of ~4.9 eV) (see Figure 4.45). This dominant luminescence band located at 4.9 eV is observed with

the radiative annihilation of self-trapped excitons emerging with X-ray irradiation (Altunal et al., 2020e; Ogorodnikov et al., 1995). It is known that the luminescence band in BeO is characterized by 3–4 eV (300-400 nm) and 4.9 eV two emission bands (Ogorodnikov and Kruzhalov, 1997). 4.9 eV emission band is not close to the conventional PMT spectral range and Hoya U-340 filter transmittance range. However, even though the transmittance range used was very suitable for the TL and OSL measurements, only a 3-4 eV emission band was observed. In the literature, OSL emission in a Thermalox BeO chip is different from RL emission and the resulting luminescence mechanism can be said to be different (Yukihara, 2011). However, considering the similar behavior between RL and OSL emissions obtained from the undoped BeO pellets produced by the precipitation method (Altunal et al., 2020e), it can be suggested that a similar luminescence process has occurred for both RL and OSL emissions of the single metal-doped BeO ceramics.

On the other hand, although the RL spectra of single metal-doped BeO ceramics were not significantly different than the RL spectrum of the undoped BeO, concentration quenching in luminescence intensities was observed in all produced ceramics. The maximum RL intensities comparing with that of undoped BeO were obtained from the samples of BeO:$Al_{1\%}$, BeO:$Ca_{0.5\%}$, BeO:$Mg_{0.5\%}$, BeO:$Na_{5\%}$, BeO:$Li_{5\%}$, BeO:$K_{5\%}$, BeO:$B_{0.1\%}$, BeO:$Si_{0.5\%}$, BeO:$Zn_{0.5\%}$, BeO:$Sr_{0.5\%}$, BeO:$In_{0.5\%}$, and BeO:$Cu_{5\%}$. To compare the intensities of BeO pellets having approximately the same masses, with different dopants in the given plots (see Figure 4.45), the background signal obtained in every single analysis was recorded and then matched with each other to correct the RL signals used. Additionally, as an unexpected result for the BeO:Mg ceramic pellets, an emission peak with low sensitivity was observed between 650 and ~820 nm with the maximum at 730 nm. This unexpected emission peak is originated from the anion defects in the BeO structure emerging during synthesis (Altunal et al., 2020b). Another unexpected result was encountered through a visible emission located between 400 and 600 nm with a maximum at 500 nm in the RL spectrum of BeO:$Si_{5\%}$ ceramics (see Figure

4.45h). This visible emission peak is associated with the ~2.5 eV emission band of SiO_2 (Liao et al., 1996), which formed in the BeO structure with increasing Si concentration.

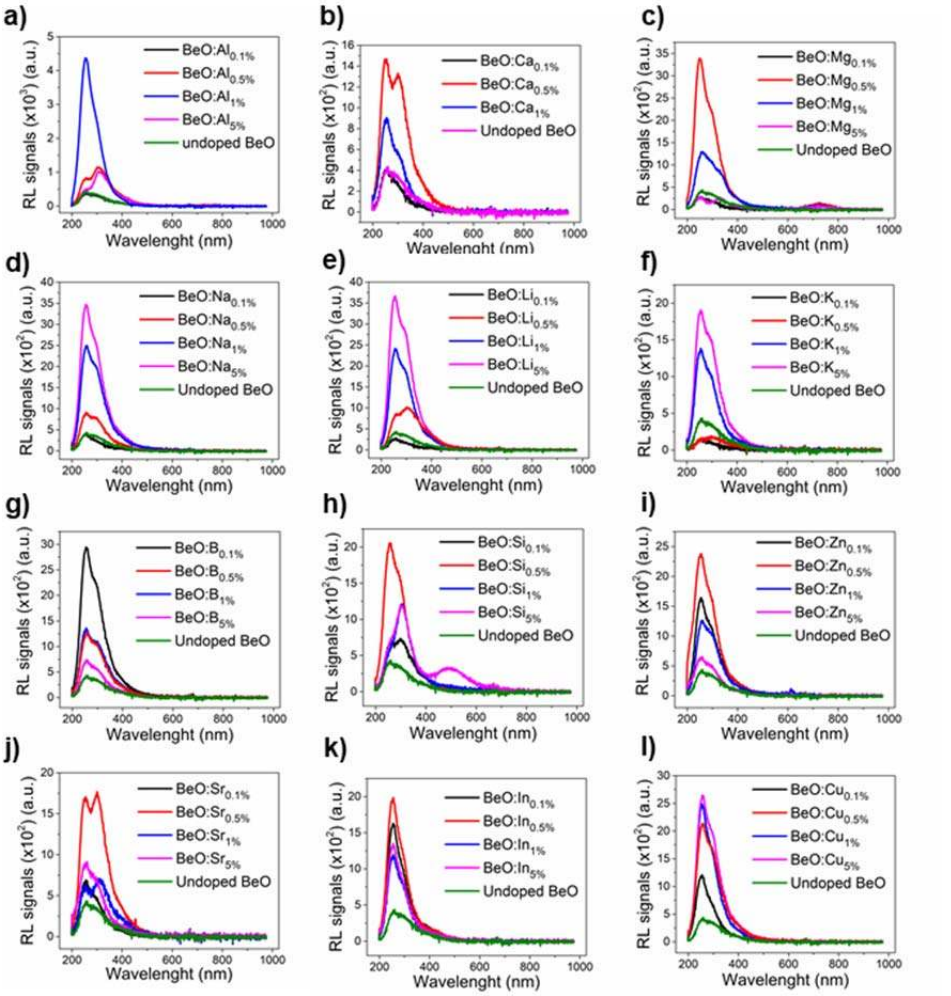

Figure 4.45. RL emissions from single-metal doped BeO samples having different dopant concentrations (x = 0.1, 0.5, 1, 5%) **(a)** BeO:$Al_{x\%}$, **(b)** BeO:$Ca_{x\%}$, **(c)** BeO:$Mg_{x\%}$, **(d)** BeO:$Na_{x\%}$, **(e)** BeO:$Li_{x\%}$, **(f)** BeO:$K_{x\%}$, **(g)** BeO:$B_{x\%}$, **(h)** BeO:$Si_{x\%}$, **(i)** BeO:$Zn_{x\%}$, **(j)** BeO:$Sr_{x\%}$, **(k)** BeO:$In_{x\%}$, and **(l)** BeO:$Cu_{x\%}$.

4.5.3.2. TL Signals

To see the effect of metal doping on TL characteristics of undoped BeO pellets, TL measurements were performed by heating the pellets irradiated with 0.5 Gy dose, from room temperature up to 650 °C with a 3 °C/s heating rate without preheating procedure. Figure 4.46 shows typical TL glow curves of undoped BeO and single-metal doped BeO pellets with different dopant concentrations in the semi-log scale, after 0.5 Gy exposure to beta-rays.

As is seen in Figure 4.46, the variable fractions of the dopant concentrations participated in thermoluminescence, and the TL glow curve of the host material BeO changed. It is the main 170 °C glow peak that is of primary interest to dosimetry because of its sensitivity and stability. All the curves, in Figure 4.46 show 170 °C in varying degrees. A small but distinct peak at 60 °C is also noted. The other peaks are a shoulder peak at around 250 °C, a low sensitive 350 °C peak, and a very high-temperature peak located at 495 °C. Different grown 2nd shoulder peaks in the 400 °C regions occurred in the TL glow curves of BeO:Mg, BeO:K, BeO:Zn, BeO:Sr and BeO:In pellet samples. The reason for this appearance might be described as the 350 °C TL peak which is not associated with a single trap but a combination of overlapping peaks and differences in TL intensities of these overlapping peaks connected to varying electron densities in these traps. Although fundamental research on TL signals of BeO indicates three main trap regions at 75, 200, and 340 °C (vary with heating rates used to record the TL curves) (Bulur and Goksu, 1998), some trap levels were also observed in the high-temperature regions (Hobzova, 1980). The five peaks observed in the TL glow curves of the single-metal doped BeO pellets were found consistent with that of the undoped and doped BeO materials indicated in our previous studies (Altunal et al., 2020b; Altunal et al., 2020c; Altunal et al., 2020e).

From a more specific point of view, Al^{3+}, Na^{+}, K^{+}, B^{3+} and Zn^{2+} dopants enhanced the TL peaks located at 170 °C, 250 °C and 350 °C (see Figure 4.46a,d,f,g,i), whereas Ca^{2+}, Li^{+}, Sr^{2+} and Cu^{4+} ions enhanced only the 495 °C TL

peaks (see Figure 4.46b,e,h,l). Additionally, Ca^{2+}, Li^{+}, Si^{4+}, Sr^{2+} and In^{3+} ions caused a decrease in total TL signals. Because the traps produce the highly sensitive 170 °C peaks, the shoulders at around 250 °C, the low sensitive 350 °C peaks are intrinsic defects of BeO crystal, here the dopant ions may act indirectly to increase or decrease the number of traps giving electrons to the traps or taking them, satisfying the law of the space charge neutrality (will be discussed in 0.) (Yamashita et al., 1974). The TL intensities in deep traps that are responsible for OSL signals were determined by step annealing experiments (Altunal et al., 2019a; Altunal et al., 2019b; Altunal et al., 2020c; Altunal et al., 2020e). In this work, considering these measurements, BeO:$Al_{1\%}$, BeO:$Mg_{0.1\%}$, BeO:$Na_{5\%}$, BeO:$K_{5\%}$, BeO:$B_{0.1\%}$, and BeO:$Zn_{0.1\%}$ were selected as the promising TL samples for dosimetric studies. It must be noted that enhancements of the given TL peaks in Figure 4.46 were evaluated in terms of the comparison of intensity ratios of different TL glow curves.

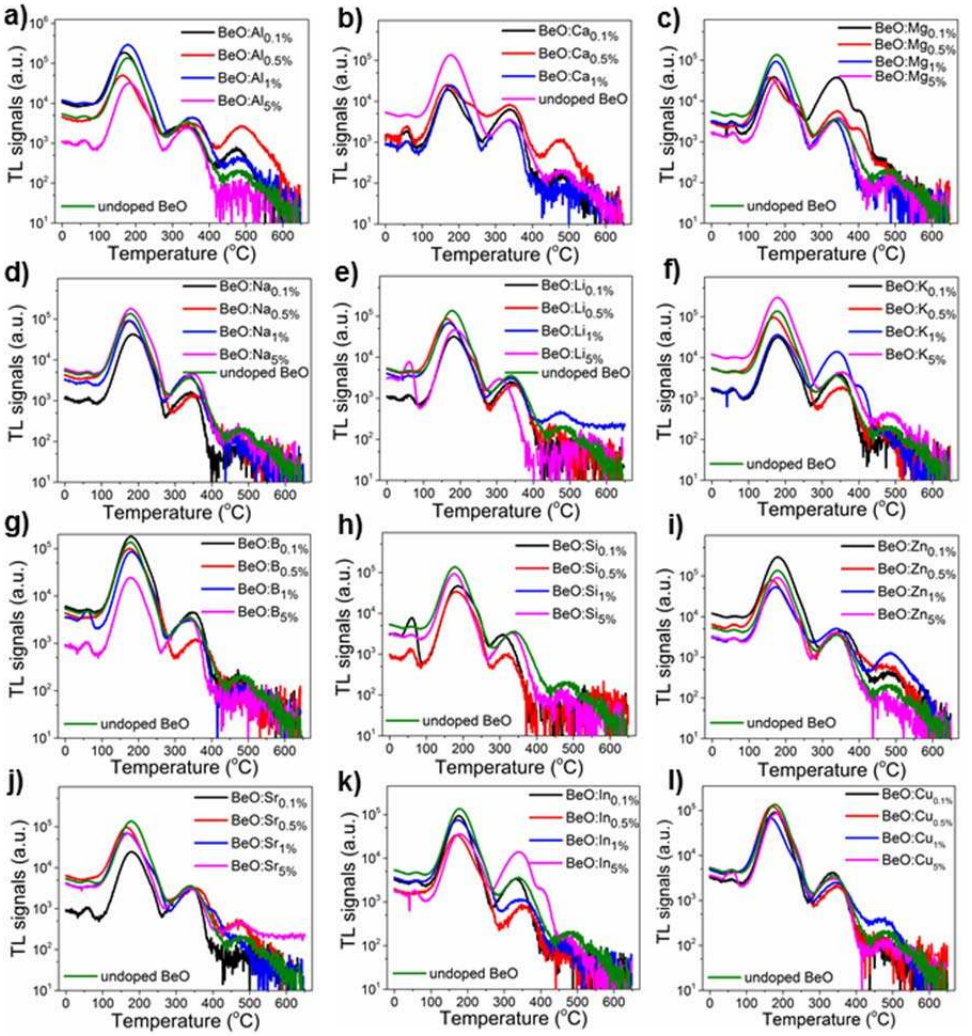

Figure 4.46. TL glow curves from single metal-doped BeO samples having different dopant concentrations (x = 0.1, 0.5, 1, 5%) in semi-log scale for better presentation of low sensitive high temperature peaks; **(a)** BeO:$Al_{x\%}$, **(b)** BeO:$Ca_{x\%}$, **(c)** BeO:$Mg_{x\%}$, **(d)** BeO:$Na_{x\%}$, **(e)** BeO:$Li_{x\%}$, **(f)** BeO:$K_{x\%}$, **(g)** BeO:$B_{x\%}$, **(h)** BeO:$Si_{x\%}$, **(i)** BeO:$Zn_{x\%}$, **(j)** BeO:$Sr_{x\%}$, **(k)** BeO:$In_{x\%}$, and **(l)** BeO:$Cu_{x\%}$. In order to increase the reliability of the experiments under laboratory conditions, newly produced/or annealed (at 650 °C for 10 min) pellets having almost the same mass (between 23.1-23.3 mg) were used in each experiment.

4.5.3.3. OSL Signals

Luminescence characteristics of undoped and single-metal doped BeO pellets were also studied using the OSL technique. OSL measurements were carried out by stimulating the 0.5 Gy irradiated pellets using 200 s continuous blue light. Before the OSL readouts, BeO pellets were preheated at 100 °C for 10 s to erase the signals originating from the shallow traps. Examples of the OSL decay curves from single-metal doped BeO pellets with different dopant concentrations were presented by comparing that of undoped BeO pellets on a semi-log scale in Figure 4.47. As is seen from the figure metal doping strongly affected the OSL signals of BeO pellets (see Figure 4.47a-l). As observed in RL and TL signals, since BeO is a very stable host material, it positively responds only to some dopant types and concentrations. Only Na^{2+}, Li^{+}, K^{+}, and Cu^{4+} (see Figure 4.47d,e,f,l) dopants at a concentration of 5% enhanced the OSL signals of undoped BeO pellets and the luminescence lifetimes were increased by adding only these dopants. The obtained OSL signals from the other single-metal doped BeO pellets were recorded as at least 40 % less than that of undoped samples. Lower concentrations are easier to be incorporated than larger concentrations, and the rule of thumb to allow or not for efficient incorporation is a difference of 15% between the radii of Be and the dopant. It is possible that the bigger dopants (see. Table 4.10 for dopant radii) are mostly concentrated on the surface of the particles and that would affect the luminescence behavior. Also, considering the integrated OSL signals of the single-metal doped BeO pellets (see Figure 4.47d,e,f,l), BeO:$Na_{5\%}$, BeO:$Li_{5\%}$, BeO:$K_{5\%}$, and BeO:$Cu_{5\%}$ showed promising results with increasing the integrated OSL signals (the sum of the data from 0 s up to 200 s) of the undoped BeO pellets by 47%, 37%, 18%, and 28%, respectively. Whereas Al, Ca, Mg, B, Si, Zn, Sr, In dopant elements decreased them almost -80% (see Figure 4.47a,b,c,g,h,i,j,k). In my previous studies, Al- and Ca-doped BeO samples having 1% dopant concentrations decreased not only the OSL signals of undoped BeO synthesized via the sol-gel method, but also some of their dosimetric properties,

such as dose linearity and dark storage of energy (Altunal et al., 2019a). In this study, OSL investigations were focused on materials that show promising results, for example, have OSL signals with high sensitivity and improve the OSL behavior of undoped BeO.

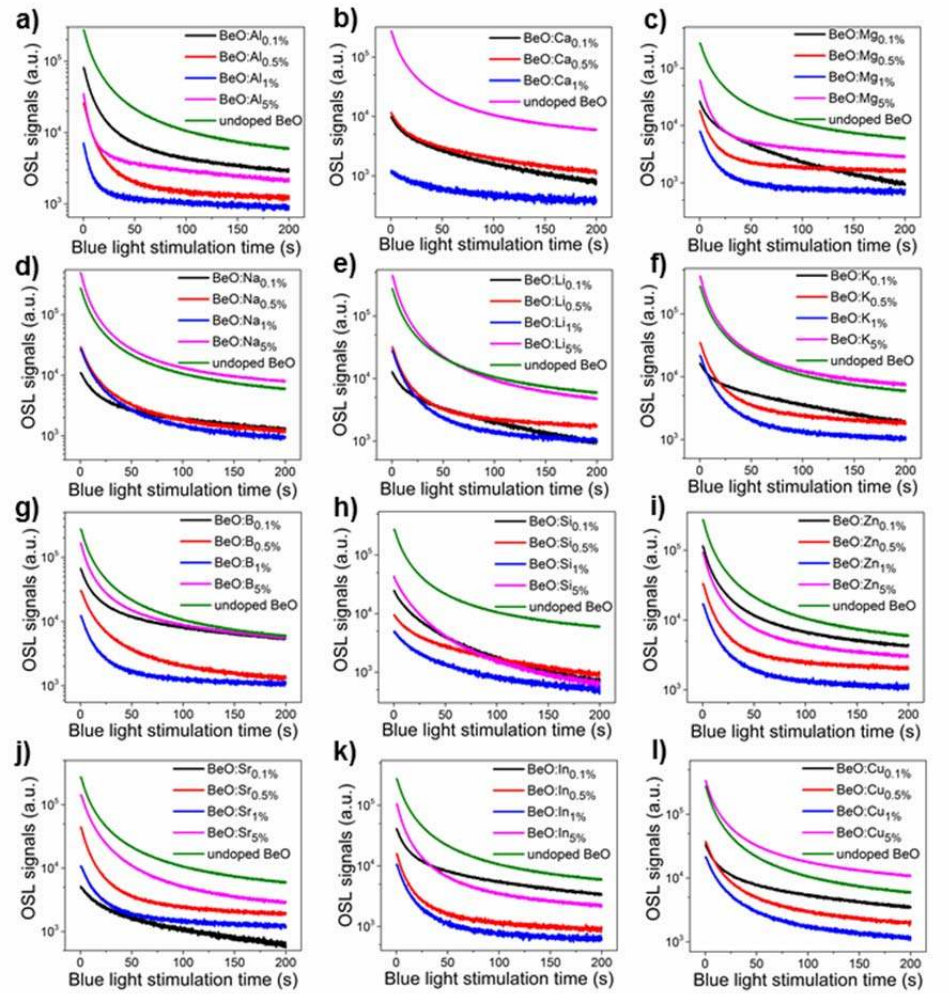

Figure 4.47. OSL decay curves from single-metal doped BeO samples at different dopant concentrations (x = 0.1, 0.5, 1, 5%) in semi-log scale for better viewing fast decaying part of the signals; **(a)** BeO:$Al_{x\%}$, **(b)** BeO:$Ca_{x\%}$, **(c)** BeO:$Mg_{x\%}$, **(d)** BeO:$Na_{x\%}$, **(e)** BeO:$Li_{x\%}$, **(f)** BeO:$K_{x\%}$, **(g)** BeO:$B_{x\%}$, **(h)** BeO:$Si_{x\%}$, **(i)** BeO:$Zn_{x\%}$, **(j)** BeO:$Sr_{x\%}$, **(k)** BeO:$In_{x\%}$, and **(l)** BeO:$Cu_{x\%}$.

4.5.4. Dosimetric Studies

Luminescence signals from the synthesized undoped and single-metal doped BeO ceramic pellets were investigated using two luminescence techniques, TL and OSL. The behavior of luminescence signals under various experimental conditions was studied. To check the luminescence characteristics of the BeO:$Al_{1\%}$, BeO:$Mg_{0.1\%}$, BeO:$Na_{5\%}$, BeO:$K_{5\%}$, BeO:$B_{0.1\%}$, and BeO:$Zn_{0.1\%}$ for TL dosimetry and that of the BeO:$Na_{5\%}$, BeO:$Li_{5\%}$, BeO:$K_{5\%}$, and BeO:$Cu_{5\%}$ for OSL dosimetry, the dose-response, reusability and fading properties of the TL and OSL signals were investigated.

4.5.4.1. Dose-Response Features

Determination of the linear dose range of the dosimeter is one of the sources of information needed in the dosimetric application area. The effect of β-radiation on luminescent signals was checked in the dose range of 0.1 Gy and 10 Gy. Firstly, the materials, namely BeO:$Al_{1\%}$, BeO:$Mg_{0.1\%}$, BeO:$B_{0.1\%}$, BeO:$Zn_{0.1\%}$, BeO:$Na_{5\%}$, BeO:$K_{5\%}$, BeO:$Li_{5\%}$, and BeO:$Cu_{5\%}$ were irradiated with 0.1, 0.2, 0.5, 1, 2, 5, and 10 Gy beta test doses in repeated experimental cycles. In the dose-response experiments for the TL signals, the TL signals were recorded by heating the BeO:$Al_{1\%}$, BeO:$Mg_{0.1\%}$, BeO:$B_{0.1\%}$, BeO:$Zn_{0.1\%}$, BeO:$Na_{5\%}$, and BeO:$K_{5\%}$ pellets from the room temperature up to 650 °C with 3°C/s heating rates. Background signals subtractions were conducted at each cycle and pellets were annealed at 650°C for 10 min to make materials ready for the next cycles. As a result of these measurements, the integrated TL signals were obtained and plotted against the irradiation doses for each group of samples as is seen in Figure 4.48a. With the linear fitting of the experimental data, the slopes were found to be 1.06, 1.06, 1.04, 1.03 and 1.03 for BeO:$Al_{1\%}$, BeO:$Mg_{0.1\%}$, BeO:$B_{0.1\%}$, BeO:$Zn_{0.1\%}$, BeO:$Na_{5\%}$, and BeO:$K_{5\%}$, respectively. According to the obtained slope values, the dose-responses of the BeO:$Al_{1\%}$, BeO:$Mg_{0.1\%}$, BeO:$B_{0.1\%}$, and BeO:$Zn_{0.1\%}$ can be accepted as slightly linear. BeO:$Na_{5\%}$, and BeO:$K_{5\%}$ had linear TL dose-response

characteristics in the dose range 0.1 and 10 Gy. On the other hand, in OSL dose-response experiments, previously irradiated BeO:$Na_{5\%}$, BeO:$Li_{5\%}$, BeO:$K_{5\%}$, and BeO:$Cu_{5\%}$ pellets were preheated at 100 °C for 10 s. After OSL readouts were performed using 200 s blue light stimulations, residual signals were deleted by heating the samples to 650 °C via TL readout. The integrated OSL signals (the sum of the data from 0 s up to 200 s) were illustrated accordingly irradiation doses with linear fit curves (see Figure 4.48b). Considering the slope values which were obtained from the linear fitting, BeO:$Na_{5\%}$ and BeO:$Cu_{5\%}$ pellets exhibited linear dose-response characteristics with slope values of 1.00. While BeO:$K_{5\%}$ pellets had slightly linear dose-response characteristics with 1.07 slope value, BeO:$Li_{5\%}$ pellets had a sublinear property with a slope of 0.92. Similar results for dose-response behaviors were presented in our recent papers for undoped and doped BeO samples synthesized using co-precipitation and sol-gel methods (Altunal et al., 2019a; Altunal et al., 2020b; Altunal et al., 2020c; Altunal et al., 2020e).

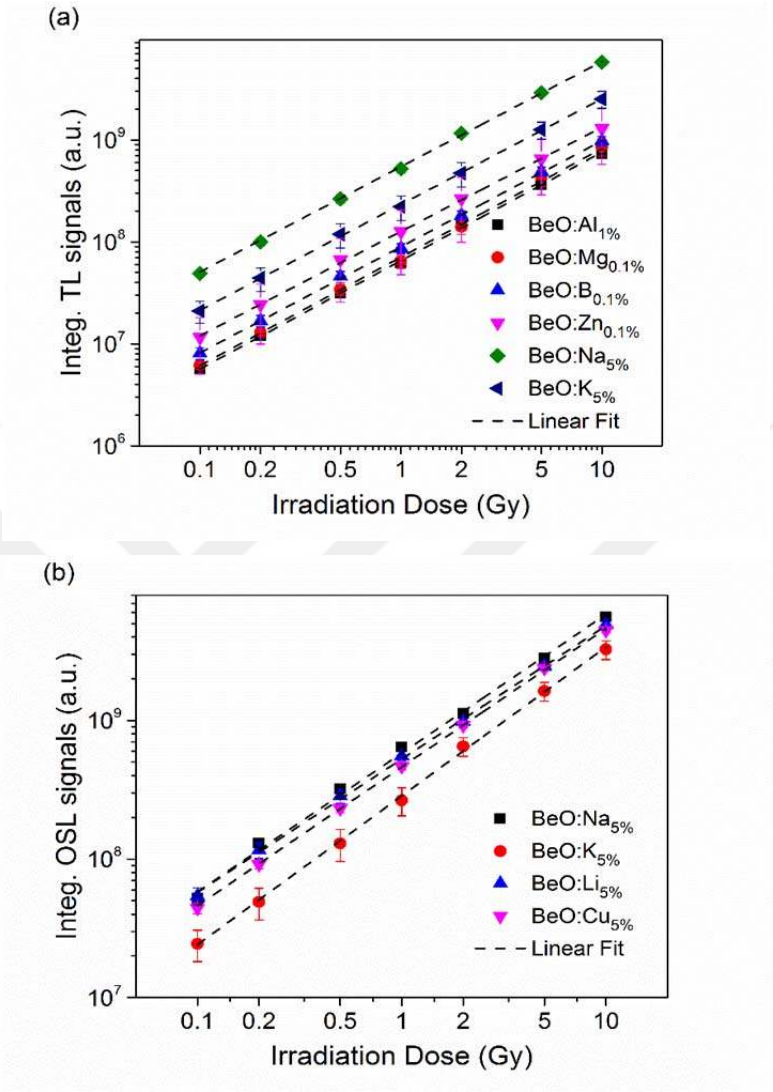

Figure 4.48. Dose-response characteristics of the luminescence signals from the synthesized single-metal doped BeO pellets; **(a)** The integrated TL signals, **(b)** The integrated OSL signals with various radiation doses from 0.1 to 10 Gy. The preheating process was applied only before OSL measurements at 110 °C for 10 s. TL measurements were performed by heating the pellets from room temperature up to 650 °C with a 3 °C/s heating rate, and the OSL signals were obtained by using 200 s blue light stimulations. The error bars represent the experimental standard deviations of mean values obtained from three pellets in each cycle.

4.5.4.2. Reusability Properties

The reusability characteristics were investigated for BeO:$Al_{1\%}$, BeO:$Mg_{0.1\%}$, BeO:$Na_{5\%}$, BeO:$K_{5\%}$, BeO:$B_{0.1\%}$, and BeO:$Zn_{0.1\%}$ using the TL response curves, and BeO:$Na_{5\%}$, BeO:$Li_{5\%}$, BeO:$K_{5\%}$, BeO:$Cu_{5\%}$ pellets by OSL decay signals. The preheating process was applied only before OSL measurements at 110 °C for 10 s. TL measurements were performed by heating the pellets from room temperature up to 650 °C with a 3 °C/s heating rate, the OSL signals were obtained by using 200 s blue light stimulations. After each TL and OSL measurement, the residual signals were deleted by heating the samples to 650 °C via TL readout. Measurement cycles were repeated 10 times under the same conditions and inter-cycle deviations were calculated. In Figure 4.49, the integrated TL and OSL signals were plotted against the experimental cycle numbers. The dosimeters showed a little variation of response. The distribution of TL responses of BeO:$Al_{1\%}$, BeO:$Mg_{0.1\%}$, BeO:$Na_{5\%}$, BeO:$K_{5\%}$, BeO:$B_{0.1\%}$, and BeO:$Zn_{0.1\%}$ pellets that received equal exposures of 0.5 Gy beta radiation is given in Figure 4.49a. Deviations from the first readouts for the samples of BeO:$Al_{1\%}$, BeO:$Mg_{0.1\%}$, BeO:$B_{0.1\%}$, BeO:$Zn_{0.1\%}$, BeO:$Na_{5\%}$ and BeO:$K_{5\%}$ were found as 3.4%, 2.5%, 4.2%, 15%, 4.4%, and 6.7%, respectively. On the other hand, in Figure 4.49b, very good repeatabilities were observed in OSL signals from BeO:$Na_{5\%}$, BeO:$Li_{5\%}$, BeO:$K_{5\%}$, BeO:$Cu_{5\%}$ pellets. Deviations from the first readouts were found as 1.8%, 3.1%, 10.2% and 2.5%, respectively.

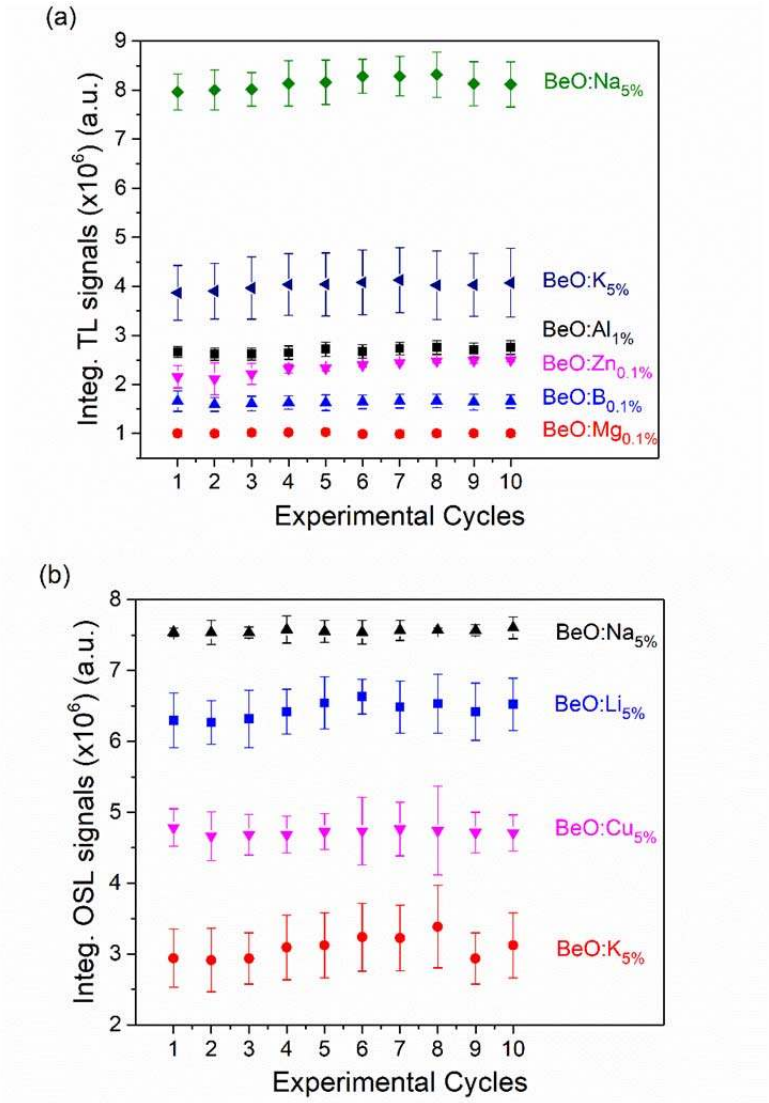

Figure 4.49. Reusability characteristics of luminescence signals from the synthesized single-metal doped BeO pellets; **(a)** The normalized and integrated TL signals, **(b)** The normalized and integrated OSL signals with repeated experimental cycles. TL measurements were performed by heating the pellets from room temperature up to 650 °C with a 3 °C/s heating rate, and the OSL signals were obtained using 200 s blue light stimulations. The error bars represent the experimental standard deviations of mean values obtained from three pellets in each cycle.

4.5.4.3. Short-Time Fading Experiments

The BeO pellets were exposed to 0.2 Gy of beta radiation and stored at room temperature in dark. Different storage time intervals up to 1 week were tested and TL/OSL measurements were performed by starting 30 min after irradiation. The fading of the TL and OSL signals were recorded at room temperature following 120 °C for 60 s preheating. After TL readouts, each sample was annealed at 650 °C for 10 min to make the pellets ready for the next readout procedure. On the other hand, after OSL readouts, residual signals were deleted by TL measurements. The results of investigations on the decay of stored energy in BeO pellets are presented in Figure 4.50. As seen in Figure 4.50a, the decrease in the integrated TL signals of BeO:$Al_{1\%}$, BeO:$Mg_{0.1\%}$, BeO:$B_{0.1\%}$, BeO:$Zn_{0.1\%}$, BeO:$Na_{5\%}$ and BeO:$K_{5\%}$ were about 8%, 3.9%, 4.7%, 10%, 4.9% and 12%, respectively at the end of 24h. One can say that the reason for this first fall is electrons that escape from shallow traps. At the end of 7 days, the deviations from the first readout were found as -5.3%, -8%, -15.3%, -13.1%, -8.1% and -15.3%, respectively. In addition to the TL signal storage measurements, the fading properties of the integrated OSL signals from the synthesized BeO:$Na_{5\%}$, BeO:$Li_{5\%}$, BeO:$K_{5\%}$, and BeO:$Cu_{5\%}$ pellets were also checked and plotted in Figure 4.50b. It can be seen from the figure that the first remarkable decreases in the integrated OSL signals were observed at the end of 12 h storage period. The decrease rates in BeO:$Na_{5\%}$, BeO:$Li_{5\%}$, BeO:$K_{5\%}$, and BeO:$Cu_{5\%}$ were evaluated as 4%, 6.5%, 14% and 4%, respectively. After the initial falls in the OSL signals after 7 days, it was observed that the total OSL signal losses were -7.1%, 9.2%, 19.2%, and 11.1%, respectively. In the literature, the short-term fading of Thermolax 995 BeO chips after 10 h storage was recorded as approx. -6% compared with the 30 min measurement (Sommer et al., 2007). The fading for the same commercial dosimeters was determined as -5% and -8% after 24 h and 1-week storage, respectively in dark (Sommer and Henniger, 2006). The commercial BeO Thermolax 995 ceramic dosimeter has the long-term fading which is negligible (less than 1% over 6 months) (Sommer et al., 2007; Sommer

and Henniger, 2006). In one of our previous works, we found that undoped BeO pellets have almost no fading at the end of 1-month dark storage with similar behaviors for short-term fadings (Altunal et al., 2019a). It may be suggested that long-term fading experiments have to be carried out for a better understanding of the effects of metal doping on fading of BeO. In further studies, less fading can be achieved by co-doping of BeO with some metals or lanthanides that activate deep traps and make them more stable.

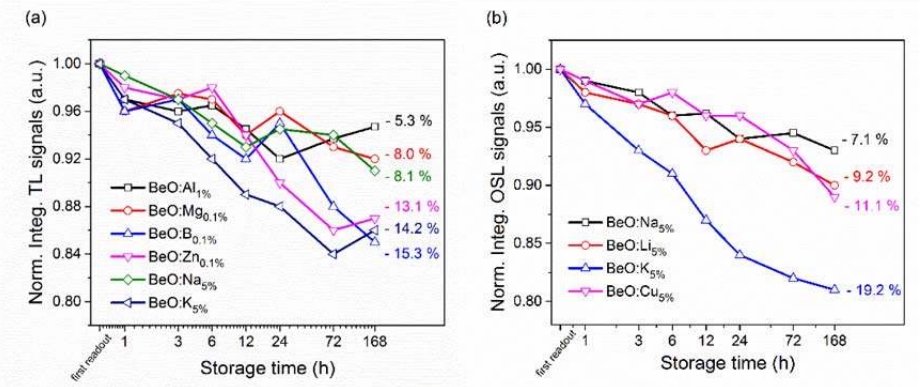

Figure 4.50. Short time fading characteristics of luminescence signals from the synthesized single-metal doped BeO pellets; **(a)** The normalized and integrated TL intensities **(b)** The normalized and integrated OSL signals as a function of short storage time up to 168 h. TL measurements were performed by heating the pellets from room temperature up to 650 °C with a 3 °C/s heating rate, and the OSL signals were obtained by using 200 s blue light stimulations.

4.5.5. Discussion

It is possible to say that different valent metal ions are brought about some local levels in the forbidden band and are actively involved in the luminescence process. Generally, if we consider the difference in ionic radii of doping elements from that of Be^{2+}, it is clear that some lattice distortions affecting luminescence directly or indirectly will occur.

The roles of alkaline-ions, Li^{1+}, Na^{1+}, and K^{1+}, as dopants contributing to luminescent characteristics and dosimetric properties of undoped BeO ceramic

pellets, were discussed elsewhere in the literature (Altunal et al., 2020c; Altunal et al., 2020e; Kortov et al., 1993b; Yamashita et al., 1974). The luminescence processes in BeO:Li, BeO:Na, and BeO:K samples begin with the defect formations of $(Li_{Be})^{-}$, $(Na_{Be})^{-}$, and $(K_{Be})^{-}$ with a negative charge capability as a result of the substitution of these ions with Be^{2+} ions in BeO lattice. As a hypothesis, the assumption that the ideal substitution of Li, Na and Be needs evidence. One can envision, e.g., an interstitial charge-neutralized by OH-. Negative charge $(Li_{Be})^{-}$, $(Na_{Be})^{-}$, and $(K_{Be})^{-}$ defects may compensate for the incorporation of positive effective charge in an intrinsic defect of BeO crystal (Altunal et al., 2020e; Kortov et al., 1993b; Yukihara et al., 2013). The experimental data of RL, TL and OSL signals from the BeO:$Li_{5\%}$, BeO:$Na_{5\%}$, and BeO:$K_{5\%}$ pellets show that Li^{1+}, Na^{1+}, and K^{1+} dopants did not create the new peaks in TL signals and the behavior of the RL and OSL signals has not changed, however, they participate in thermoluminescence with the charge compensation effect.

On the other hand, considering the general theory of defects (Stoneham, 2001), it can be predicted that introducing divalent ions into the BeO host lattice should create some shallow levels which will actively manifest themselves in the recombination processes. With the low-temperature luminescence studies in the literature, it was concluded that introducing of Mg^{2+} and Zn^{2+} into the BeO lattice causes shallow trapping centers contributing to TL signals or participating in the inner defect tunneling recombination (Ogorodnikov et al., 2016; Ogorodnikov et al., 2018). Additionally, our recent paper based on BeO:Ca ceramic pellets (Altunal et al., 2019a) showed that Ca^{2+} in BeO host lattice plays a role as a charge compensator. In this study, we obtained that all the intrinsic TL peaks of undoped BeO were strongly affected by divalent ions. Mg^{2+} doping contributed to the high-temperature TL peaks whereas the doping of Zn^{2+} ions leads to an increase in the intensity of TL signals up to 200 °C. As an interesting result here, although the TL peaks located up to 350 °C regarding the origin of OSL signals in BeO ceramic

pellets (Altunal et al., 2019a; Altunal et al., 2019b; Altunal et al., 2020b) increased with Mg^{2+} and Zn^{2+}, OSL signals considerably decreased with the divalent dopant ions. This means that TL and OSL signals might be originated from different luminescence bands. It must be noted that emission spectra of the TL and OSL have to be studied in detail to obtain more information about the luminescence mechanism.

The luminescence process in trivalent and tetravalent ion-doped BeO can be explained more than the luminescence mechanism that assumes an electron trap and a recombination center. Al^{3+}, B^{3+}, In^{3+}, Si^{4+}, and Cu^{4+} on the somewhat smaller Be^{2+} sites cause lattice distortions. Such distortions that may occur in this way, may stabilize holes from the valence band (Dorenbos et al., 2008). In this work, exposing the crystal with ionizing radiation and then creating charge carriers, i.e., electrons and holes moving freely inside the crystal. The heterovalent/trivalent substitution impurities (Al^{2+}, B^{2+}, In^{2+} / Si^{3+}, Cu^{3+}) may act as hole traps and become trivalent/quadrivalent ions (Al^{3+}, B^{3+}, In^{3+} / Si^{4+}, Cu^{4+}) during delivering irradiation. On TL and OSL readouts, trapped electrons are released from the electron traps during stimulation with heat or light, and Al^{2+}, B^{2+}, In^{2+} / Si^{3+}, Cu^{3+} substitution ions in excited states occur with recombination of the released electrons with Al^{3+}, B^{3+}, In^{3+} / Si^{4+}, Cu^{4+} ions. With the relaxation processes of Al^{2+}, B^{2+}, In^{2+} / Si^{3+}, Cu^{3+} in excited states, observable luminescence emission is achieved (Altunal et al., 2019a; Altunal et al., 2020c; Kortov et al., 1993a; Kortov et al., 1993b). As a result, the main difficulties we encountered in interpreting experimental data are the exact composition and spatial arrangement of the defect centers in BeO and the mechanisms of interaction to be determined.

4.6. BeO Ceramics Doped with Lanthanides

This part of the thesis was particularly done to achieve the enhanced luminescence in BeO ceramic samples by the optimization of the Ln^{3+} dopant concentrations, and application of the passive admixtures (e.g., Na^{+}, Li^{+}, K^{+} co-

doping). We developed alternative BeO oxide phosphors with better efficiency and extended their applications to be used in luminescence dosimetry. In this work, lanthanides (rare-earth elements) Eu^{3+}, Ce^{3+}, Nd^{3+}, Yb^{3+}, Er^{3+}, Gd^{3+}, Tb^{3+}, Tm^{3+}, Sm^{3+}, Sr^{3+}, Pr^{3+}, and Dy^{3+} doped BeO ceramic samples were successfully produced using the co-precipitation method and interpretation of their luminescence mechanisms were proposed. Luminescence characteristics of the Ln^{3+}-doped BeO samples were studied using OSL spectra, radioluminescence (RL), TL, and OSL techniques. Luminescent behaviors were investigated in terms of possible relations to the trivalent lanthanide dopants and alkali metal ion co-dopants added into the BeO host material.

4.6.1. Material Synthesis

BeO ceramics were synthesized and doped using the co-precipitation method. Beryllium sulfate tetrahydrate (99.90%, $BeSO_4 \cdot 4H_2O$), polyethyleneimine solution ($(NHCH_2CH_2)_n$, 50% (w/v) in H_2O), and ammonium hydroxide (28.0-30.0% NH_3 basis, NH_4OH) precursor reactants were used for initial salt, polymerization, and initiator of the precipitate, respectively. All raw dopant materials (Na^+, Li^+, K^+, and Ln^{3+} (Eu^{3+}, Ce^{3+}, Nd^{3+}, Yb^{3+}, Er^{3+}, Gd^{3+}, Tb^{3+}, Tm^{3+}, Sm^{3+}, Sr^{3+}, Pr^{3+}, and Dy^{3+})) used were only nitrate based. The co-precipitation method was presented in detail previously in my studies (Altunal et al., 2019b; Altunal et al., 2020b; Altunal et al., 2020c; Altunal et al., 2020d), and modified to better control the Ln^{3+}-doped BeO synthesis process in this study. The actual Ln^{3+} contents in the sintered pellets were not verified. The resultant precipitate samples were calcined at 900 °C for 4 h in the air atmosphere for removing the organic formations which come up with the synthesis process and obtaining the BeO nanocrystal structure of the material. Finally, lanthanide-doped BeO powders were prepared in pellet forms to obtain more settled OSL signals. BeO ceramic pellets having dimensions of ~3.1 mm radius and ~0.8 mm thickness were obtained using 25 mg powder samples. To avoid the toxicity of BeO powders, and provide

strength and integrity, the prepared pellets were sintered at 1600 °C for 4 h. After sintering, the weight losses were observed and the average weights appeared as ~23.1 ± 0.2 mg. Inhalation of beryllium powders in the air may cause a serious lung condition, depending on the dose. It should be noted that, unlike BeO powders, the use of solid form BeO ceramics (chips, rods, discs, etc.) does not pose a special health risk. In our work with BeO, I paid attention to safety and environmental protection studies to avoid toxicity and followed safe usage practices. Personal protective equipment such as gloves, dust/gas masks, and/or goggles was used during BeO synthesis.

4.6.2. Crystal Structure

The crystallographic phase formation of BeO was confirmed by comparing it with the ICDD PDF-card no 98-001-5620 revealing the hexagonal crystal structure with the $P6_3mc$ space group. Figure 4.51 shows the well-indexed three highly sensitive peaks with (100), (002), and (101) orientations from undoped and Ln^{3+}-doped BeO ceramics. The XRD patterns showed that BeO ceramics doped with different Ln^{3+} ions synthesized under the same synthesis processes (i.e., calcination and sintering conditions) had the same phase. The XRD patterns do not contain any peaks related to Ln^{3+} ions, this may be attributed to the incorporation of Ln^{3+} ions into Be^{2+} lattice sites rather than interstitial ones (Bilgili, 2019).

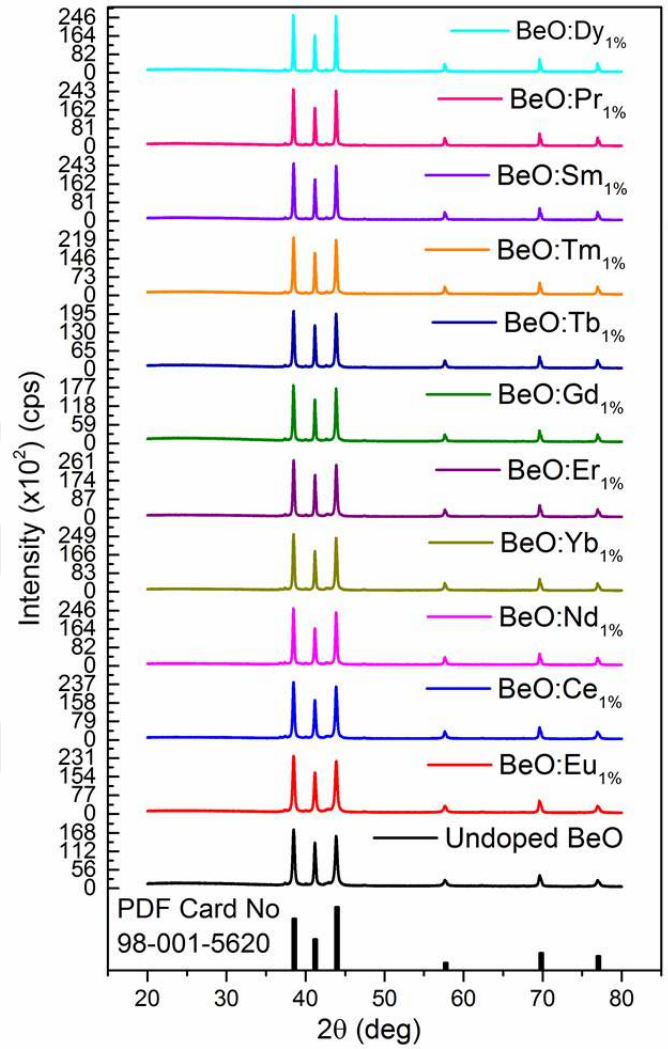

Figure 4.51. XRD patterns of undoped and 1 mol% of Ln^{3+} doped BeO phosphors.

Apart from the general appearance of XRD patterns, lattice parameters were evaluated from the XRD data. The lattice parameters a and c were determined using Equations (4.8) and (4.9) used for hexagonal systems (Köseoğlu, 2015):

$$a = \frac{\lambda}{\sqrt{3}\sin\theta}\sqrt{h^2 + hk + k^2} \tag{4.8}$$

and

$$c = \frac{\lambda}{2\sin\theta} l \tag{4.9}$$

where λ is the wavelength, θ is the Bragg angle of diffraction peaks, and h, k, l are the Miller indices.

The volume of wurtzite unit cell for a hexagonal system of BeO samples was determined using Equation (4.10):

$$V = \frac{\sqrt{3}a^2c}{2} = 0.866a^2c \tag{4.10}$$

V is the lattice volume, a and c are the lattice constants (Pushpa et al., 2017).

Be–O bond length (L) for all samples was determined using the following Equation (4.11):

$$L = \sqrt{\frac{a^2}{3} + \left(\frac{1}{2} - u\right)^2 c^2} \tag{4.11}$$

where a, c are the lattice parameters, and u is the positional parameter of the wurtzite structure. For wurtzite structure, u is given as:

$$u = \frac{a^2}{3c^2} + 0.25 \tag{4.12}$$

As expected from the difference in ionic radii between Ln^{3+} and Be^{2+} host sites (see Table 4.11), a systematic change in lattice parameters was also observed and presented in Table 4.12. Both lattice parameters (a and c) and cell volume (V) were decreased with Ln^{3+}doping due to an increase in the existing defect concentration in the lattice. This may be attributed to the larger ionic radius of Ln^{3+} compared to

that of Be^{2+}, hence leading to a lattice contraction (Bilgili, 2019; Lorbeer et al., 2014). Furthermore, The Be-O bond length values obtained from the XRD data of the BeO:Ln^{3+} samples are slightly lower than that of the undoped BeO sample (see Table 4.12), indicating that the structural defects and especially the oxygen vacancies have been reduced. The oxygen positional parameter (u) and c/a values providing information about the oxygen vacancies in the structure were also evaluated. All the BeO:Ln^{3+} samples showed a significantly higher c/a ratio than undoped BeO, which may indicate reduced oxygen vacancies V_O and extended defects (dislocations and grain-boundaries) (Bilgili, 2019).

Table 4.11. Ionic Radii of Be^{2+} and Ln^{3+} ions

Ion	**Charge**	**Coordination**	**Crystal Radius**	**Ionic Radius**
Be	2	VI	0.59	0.45
Ce	3	VI	1.15	1.01
Dy	3	VI	1.05	0.91
Er	3	VI	1.03	0.89
Eu	3	VI	1.09	0.95
Gd	3	VI	1.08	0.94
Nd	3	VI	1.12	0.98
Pr	3	VI	1.13	0.99
Sm	3	VI	1.10	0.96
Tb	3	VI	1.06	0.92
Tm	3	VI	1.02	0.88
Yb	3	VI	1.01	0.87
Na	1	VI	1.16	1.02
Li	1	VI	0.90	0.76
K	1	VI	1.52	1.38

Table 4.12. Lattice parameters a and c, unit cell volume (V), lattice distortion c/a, positional parameter u and Be-O bond length L of undoped and Ln^{3+}-doped BeO samples synthesized by the co-precipitation method

	Lattice Parameters					**Be – O bond**	
	a (Å)	**c (Å)**	**V ($Å^3$)**	**c/a**	**u**	**Length (Å)**	**L**
BeO	2.459	4.388	22.97	1.7844	0.35468	1.55620	
BeO:Eu	2.397	4.390	21.85	1.8313	0.34939	1.53385	
BeO:Ce	2.397	4.385	21.82	1.8293	0.34962	1.53310	
BeO:Nd	2.397	4.386	21.83	1.8298	0.34956	1.53329	
BeO:Yb	2.397	4.386	21.83	1.8298	0.34956	1.53329	
BeO:Er	2.397	4.386	21.83	1.8298	0.34956	1.53329	
BeO:Gd	2.428	4.388	22.39	1.8074	0.35204	1.54461	
BeO:Tb	2.428	4.388	22.39	1.8074	0.35204	1.54461	
BeO:Tm	2.397	4.386	21.83	1.8298	0.34956	1.53329	
BeO:Sm	2.428	4.386	22.39	1.8069	0.35210	1.54443	
BeO:Pr	2.368	4.385	21.29	1.8521	0.34717	1.52239	
BeO:Dy	2.459	4.388	22.97	1.7844	0.35468	1.55620	

On the other hand, the structural parameters, diffraction peak position (2θ), FWHM (β), the crystallite size (D), micro-strain (ε), and dislocation density (δ) of undoped and Ln^{3+}-doped BeO samples were evaluated from the XRD data and summarized in Table 4.13. A detailed description and model equations related to lattice and structural parameters were presented below.

The average crystallite sizes of undoped and Ln^{3+} doped BeO were calculated by the Debye-Scherrer formula given by Equation (4.4). In addition to the crystallite size, the strain (ε) values were evaluated by the following Equation (4.13) (Norazlina et al., 2013):

$$\varepsilon = \beta cos\theta/4 \quad (4.13)$$

where β is FWHM and θ is half of the diffraction angle.

Another parameter is the dislocation density (δ) that influences many of the properties of materials (Theivasanthi and Alagar, 2011). The dislocation densities in BeO nano-particles were determined using Equation (4.14):

$$\delta = 1/D^2 \quad (4.14)$$

where D is the crystallite size of the BeO nano-particles.

Table 4.13. Structural parameters, diffraction peak position (2θ), FWHM (β), the crystallite size (D), micro-strain (ε) and dislocation density (δ) of undoped and Ln^{3+}-doped BeO samples synthesized by the co-precipitation method

	2θ (°)			**β (°)**			**D (nm)**			**ε x 10^{-2}**			**δ x 10^{-3} (nm^{-2})**		
	(100)	**(002)**	**(101)**	**(100)**	**(002)**	**(101)**	**(100)**	**(002)**	**(101)**	**(100)**	**(002)**	**(101)**	**(100)**	**(002)**	**(101)**
BeO	38.44	41.15	43.83	0.1839	0.1714	0.1922	47.8	51.73	46.55	4.286	4.011	4.457	0.438	0.374	0.461
BeO:Eu	38.46	41.13	43.83	0.3745	0.5379	0.2525	23.48	16.48	35.44	8.693	12.589	5.856	1.814	3.682	0.796
BeO:Ce	38.46	41.17	43.85	0.1955	0.1721	0.2101	44.97	51.52	42.59	4.538	4.028	4.872	0.494	0.377	0.551
BeO:Nd	38.46	41.16	43.84	0.2649	0.2159	0.2953	33.19	41.07	30.3	6.149	5.053	6.849	0.908	0.593	1.089
BeO:Yb	38.46	41.16	43.85	0.209	0.1721	0.2215	51.08	51.52	40.4	4.851	4.028	5.137	0.383	0.377	0.613
BeO:Er	38.46	41.16	43.84	0.2682	0.2543	0.3002	32.78	34.87	29.81	6.226	5.951	6.961	0.931	0.822	1.125
BeO:Gd	38.45	41.15	43.84	0.2035	0.1782	0.2089	43.2	49.76	42.83	4.733	4.171	4.845	0.536	0.404	0.545
BeO:Tb	38.45	41.15	43.84	0.1847	0.1457	0.1928	47.6	60.85	46.41	4.296	3.410	4.471	0.441	0.270	0.464
BeO:Tm	38.46	41.16	43.85	0.1841	0.1847	0.1868	47.75	48.01	47.9	4.273	4.323	4.332	0.439	0.434	0.436
BeO:Sm	38.45	41.16	43.83	0.2776	0.2542	0.2177	31.67	34.88	41.1	6.457	5.949	5.049	0.997	0.822	0.592
BeO:Pr	38.47	41.18	43.86	0.1507	0.1459	0.1493	58.34	60.82	59.94	3.491	3.414	3.463	0.294	0.270	0.278
BeO:Dy	38.44	41.15	43.83	0.1334	0.1234	0.1352	65.9	65.58	67.07	3.109	2.888	3.136	0.230	0.233	0.222

As can be seen from the Table 4.13, the diffraction peak positions (2θ) slightly shifted to the right with Ln^{3+}doping. It can be said that three highly sensitive peaks regarding (100), (002), and (101) orientations shift to the right due to a decrease in lattice parameters a and c when compared to the undoped sample, leading to a resultant increase in the concentration of defects in the structure (Altunal et al., 2020b; Norazlina et al., 2013). In our investigations, as the target material was exposed to severe deformation with Ln^{3+} doping, the resulting deformation and inhomogeneous strain in the crystal lattice led to an increase in full-width at the half maximum (FWHM = β) of the diffraction peak (see Table 4.13). It has been observed that diffraction broadening causes generally an increase in lattice micro-strain (ε) and a decrease in crystallite size (D) of strain-hardened materials. This is an indication of an increase in the overall defect concentration in the structure. Whereas, by adding Yb^{3+}, Pr^{3+}, and Dy^{3+} dopants, while the crystal grew in preferred orientations, it caused a decrease in micro-strain, which means a low lattice imperfection in the structure (see Table 4.13). The calculated dislocation densities increased with Ln^{3+} doping, and consequently, dislocation movements occurred at higher dislocation densities for the doping process. The effect of doping of Ln^{3+} ions having larger ionic radii on the stress and dislocation densities in the synthesized BeO structures is seen in Table 4.13. Larger dislocation density may be associated with greater hardness or a decrease in particle size (Moram et al., 2011; Theivasanthi and Alagar, 2011). As a result of these phase analyzes, it was found that the crystallinity, defect structures, and physical properties of the BeO ceramics depend strongly on the Ln^{3+} dopants.

Figure 4.52 shows the Raman spectra of the undoped and Ln^{3+} doped BeO ceramics excited by a laser with a wavelength of 532 nm. Two major peaks of A_1 (TO) (680.23 cm^{-1}) and E_1 (TO) (722.21 cm^{-1}) optical phonons were detected on all samples. Additionally, a low sensitive peak of A_1 (TO) optical phonon was observed between 1085.85 cm^{-1} and 1096.56 cm^{-1}. Theoretical calculations for the

E_1 and A_1 phonon modes, which are originated from the opposite motion of the Be and O bond in the basal plane, were reported as 697–725 cm^{-1} and 1080–1113 cm^{-1} (Lee et al., 2019; Wdowik, 2010). The E_1 mode oscillates perpendicular to the c-axis, while the A_1 mode oscillates parallel to the c-axis. It can be said that the BeO phase did not change with Ln^{3+} doping, and thus Ln^{3+} ions successfully entered the BeO lattice because no additional peaks associated with the Ln^{3+} ions were observed in Raman spectra (see Figure 4.52). Therefore, Ln^{3+} ions can be suggested that they substitute for Be^{2+} lattice sites rather than locate in interstitial positions.

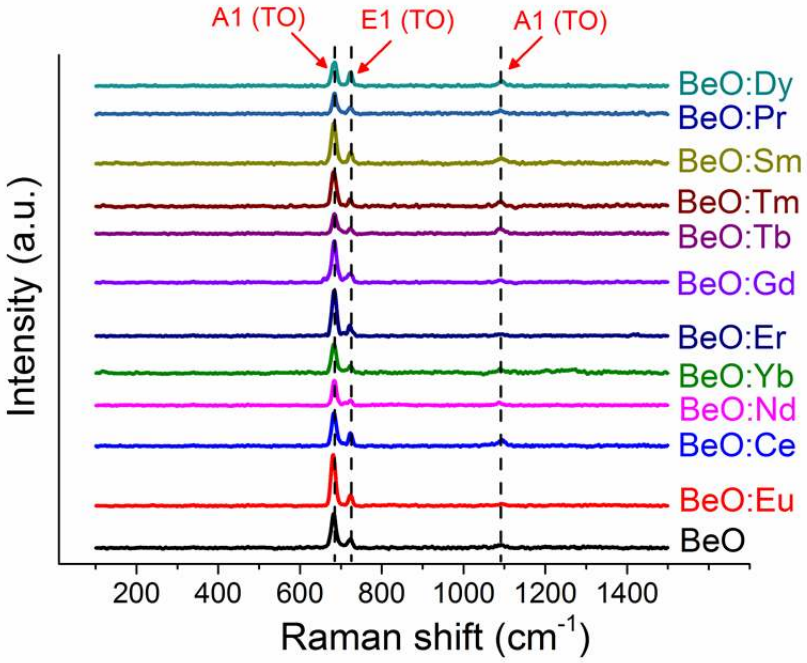

Figure 4.52. Raman spectra of undoped and Ln^{3+} doped BeO ceramics measured using a 532 nm laser.

4.6.3. RL Emissions of Undoped and Single-Doped BeO

It is well known that the optical characteristics and the emission intensity of Ln^{3+} ions are very sensitive to the surrounding crystal structure and crystal field environment. Investigation of RL properties of Ln^{3+} doped nanocrystals is thereby important to provide knowledge about the locations and overview of luminescence bands. In this study, RL emissions of the undoped and singly doped BeO ceramics, with lanthanides at 1 mol% dopant concentration, namely, BeO:$Eu_{1\%}$, BeO:$Ce_{1\%}$, BeO:$Nd_{1\%}$, BeO:$Yb_{1\%}$, BeO:$Er_{1\%}$, BeO:$Gd_{1\%}$, BeO:$Tb_{1\%}$, BeO:$Tm_{1\%}$, BeO:$Sm_{1\%}$, BeO:$Pr_{1\%}$, and BeO:$Dy_{1\%}$ were obtained using a 1 nm resolution at room temperature and presented in Figure 4.53.

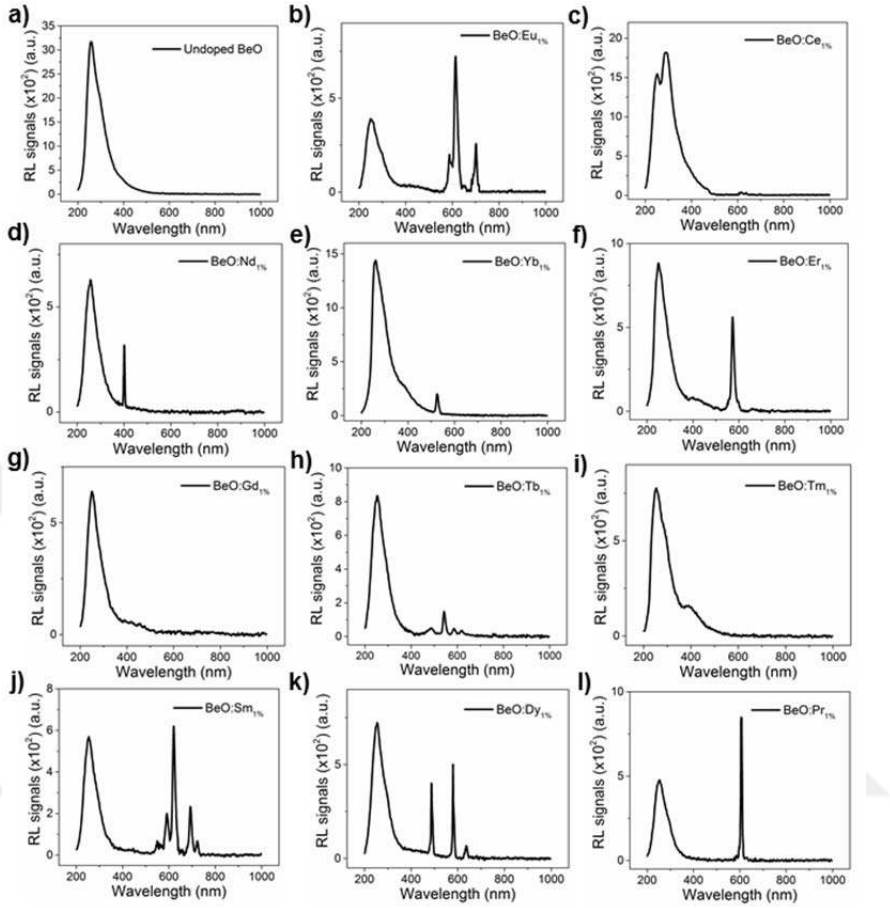

Figure 4.53. The RL emission spectra of undoped BeO and BeO:$Ln_{1\%}$ ceramic samples a) undoped BeO, b) BeO:$Eu_{1\%}$, c) BeO:$Ce_{1\%}$, d) BeO:$Nd_{1\%}$, e) BeO:$Yb_{1\%}$, f) BeO:$Er_{1\%}$, g) BeO:$Gd_{1\%}$, h) BeO:$Tb_{1\%}$, i) BeO:$Tm_{1\%}$, j) BeO:$Sm_{1\%}$, k) BeO:$Pr_{1\%}$, and l) BeO:$Dy_{1\%}$. Samples were sintered at 1600 °C for 4 h after calcination at 900 °C for 4 h.

All the lanthanide-doped BeO ceramic samples were found to exhibit a characteristic wide UV emission band of BeO with a maximum at 250 nm, located between 200-450 nm (see Figure 4.53). The source of the large and sensitive emission at approximately 4.9 eV is the radiative annihilation of self-trapped excitons caused by X-ray excitation (Altunal et al., 2020b; Altunal et al., 2018; Ogorodnikov and Kruzhalov, 1997; Ogorodnikov et al., 1995). The luminescence

in BeO is known to be characterized by the two emission bands at ~3–4 eV (300–400 nm) and 4.9 eV (Ogorodnikov and Kruzhalov, 1997). Because the 4.9 eV emission band is not close to the spectral range of the conventional PMT and transmission range of the Hoya U-340 filter, herein, only 3-4 eV emission bands were observed in OSL readouts. In the literature, the sources of RL and OSL emissions in a Thermalox BeO chip were reported to be different, and the resulting luminescence mechanisms in BeO were suggested to be different (Yukihara, 2011). However, in our studies, the RL and OSL emissions were found to be similar for synthesized Ln^{3+} doped BeO ceramics (will be discussed later).

Eu^{3+}-doped BeO ceramics showed typical RL emission bands of Eu^{3+} ions located between 570 and 750 nm (see Figure 4.53b), which could be ascribed to ${}^5D_0 \rightarrow {}^7F_j$ $(j = 0-4)$ red emission transition of Eu^{3+}. The characteristic emission of Eu^{2+} at 384 nm, which originated from the $5d \rightarrow 4f$ transition, was not observed because it remains under the main emission peak of BeO. In the case of Ce^{3+}-doped BeO ceramics, although RL emission bands located between ~300 nm and 450 nm ($5d \rightarrow 4f$ transition) did not appear as isolated peaks and were probably located under the dominant broadband emission of BeO. As is shown in Figure 4.53c, doping with Ce^{3+} ions caused an increase in the intensity of characteristic peaks in the RL diffractogram. 400 nm RL emission peak was observed from the Nd^{3+}-doped BeO ceramics (see Figure 4.53d), associated with the $4f \rightarrow 4f$ transitions of Nd^{3+}. In Figure 4.53e, Yb^{3+}-doped BeO samples showed a characteristic emission centered at 525 nm, originated from the allowed electric dipole $5d \rightarrow 4f$ transition of Yb^{2+}. The observed emission peak at ~ 570 nm in Figure 4.53f represents the ${}^4S_{3/2} \rightarrow {}^4I_{15/2}$ characteristic transition of Er^{+3}. In Figure 4.53g, the characteristic 315 nm RL emission is likely to be associated with the ${}^6P_{7/2} \rightarrow {}^8S_{7/2}$ transition of Gd^{3+}. This RL emission was observed in the RL spectra of BeO: Gd^{3+} samples as overlapping with the dominant emission of BeO. For the Tb^{3+}-doped BeO samples in Figure 4.53h, at least six overlapped peaks in

the visible region were observed in RL spectra. It can be said that these visible range emission peaks are due to the $^5D_4 \rightarrow {}^7F_j$ ($j = 6-0$) characteristic transitions of Tb^{3+} with the emission bands located at 490, 540, 580, 620, 650, 660 and 675 nm (Bünzli et al., 2010). Only Tm^{3+}-doped BeO ceramics showed a distinct peak with a maximum of about 400 nm occurring as a neck at the right side of the 250 nm broad emission peak of pure BeO (see Figure 4.53i). This 400 nm RL emission is due to the $^1D_2 \rightarrow {}^3F_4$ transition of Tm^{3+}. Sm^{3+}-doped BeO samples showed five characteristic RL emission bands located at 560, 595, 640, 700, 775 nm (see Figure 4.53j), which are denoted by the $^4G_{5/2} \rightarrow {}^6H_j$ ($j = 5/2-13/2$) transitions of Sm^{3+}. The observed characteristic emission from the Pr^{3+}-doped BeO ceramics was at ~600 nm in Figure 4.53k and corresponds to the $^1D_2 \rightarrow {}^3H_4$ transition of Pr^{3+}. Three RL emission bands located at 475, 570, and 660 nm in Dy-doped BeO samples were observed they originate from the $^4F_{9/2} \rightarrow {}^6H_j$ ($j = 15/2-11/2$) transitions of Dy^{3+} (see Figure 4.53l). As a result, peaks corresponding to the characteristic transitions of trivalent lanthanide ions showed that each Ln^{3+} ion plays a role as a luminescence center in the BeO structure.

Another important revealing of RL emissions obtained with lanthanide doping in the BeO structure is a diminution of the luminescence at wavelengths between 200 and 400 nm when compared with the RL emission intensity of undoped BeO (see Figure 4.53). This might be caused by the quenching effect of defect-related Ln^{3+} emissions and the unmatched energy levels relative to the valence (VB) and conduction bands (CB) of BeO. These effects have been mentioned in the literature for various oxide nanocrystal hosts (Zeng et al., 2008).

4.6.4. TL Glow Curves of Undoped and Single-Doped BeO

The TL glow curve of undoped BeO revealed five peaks at ~180, ~250, ~360, ~495, and ~580 °C with a heating rate of 3 °C/s (see Figure 4.54). In Figure 4.54a, a highly sensitive TL peak at ~180 °C possessing its maximum height being

~10^3 times greater than the peak was observed on the high-temperature side of the glow curve. For a better illustration of the low sensitive traps, TL glow curves were deconvoluted and component peaks were given in Figure 4.54b. On the other hand, studies on the TL glow curve of the BeO Thermalox 995 chip showed three main TL peaks at 75, 200, and 340 °C (depending on the heating rates during TL readouts) (Bulur and Goksu, 1998), although some deep traps were also found after 340 °C (Hobzova, 1980). In this thesis, the observed five peaks are suggested to be consistent with the TL glow curve shapes obtained in the undoped and doped BeO ceramic materials specified in our previous studies (Altunal et al., 2020b; Altunal et al., 2020c; Altunal et al., 2020e).

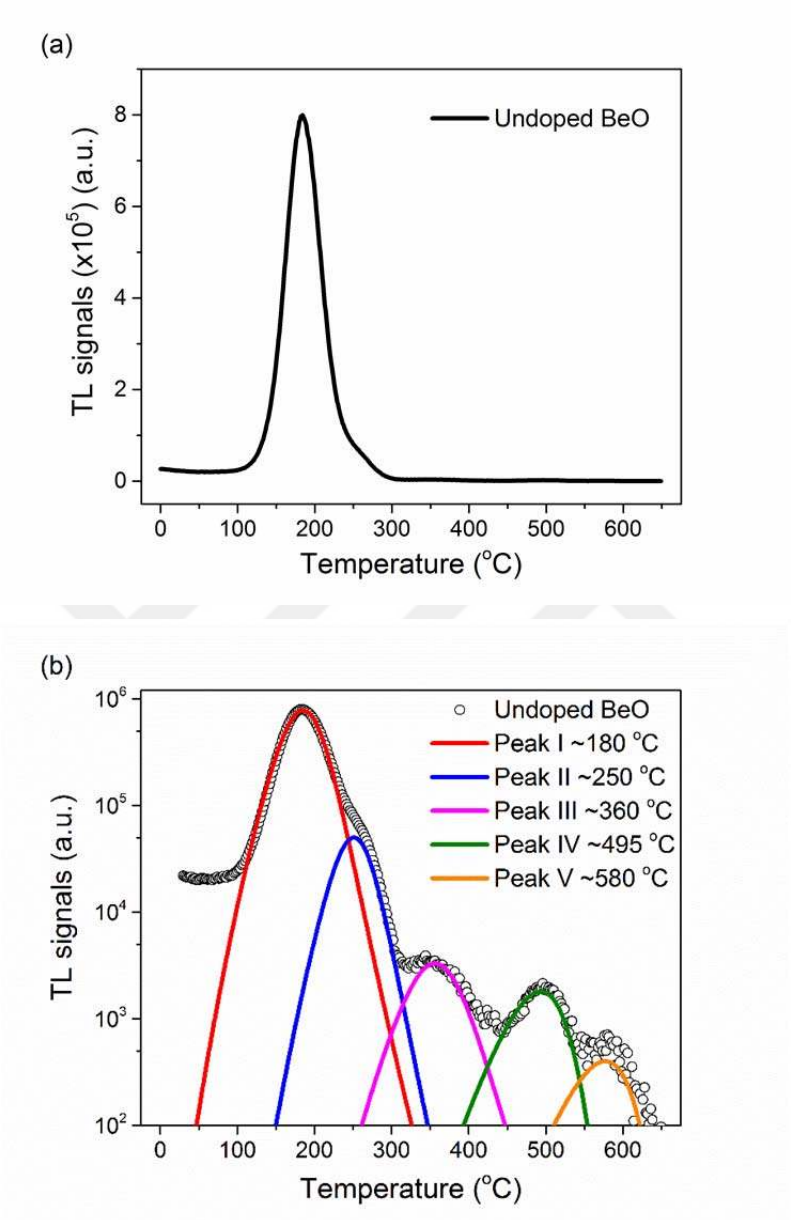

Figure 4.54. TL glow curve of undoped BeO: (a) TL signals in linear scale, (b) Deconvoluted TL signals in semi-log scale.

To investigate the effect of lanthanide doping on TL glow curves of BeO ceramics, TL readouts were carried out by heating the samples exposed to 0.5 Gy beta dose up to 650 °C with a heating rate of 3 °C/s without any preheating procedure. Figure 4.55 shows the TL glow curves of BeO ceramics singly doped with lanthanides at 1 mol% dopant concentration, namely, BeO:$Eu_{1\%}$, BeO:$Ce_{1\%}$, BeO:$Nd_{1\%}$, BeO:$Yb_{1\%}$, BeO:$Er_{1\%}$, BeO:$Gd_{1\%}$, BeO:$Tb_{1\%}$, BeO:$Tm_{1\%}$, BeO:$Sm_{1\%}$, BeO:$Pr_{1\%}$, and BeO:$Dy_{1\%}$. As can be seen in Figure 4.55, all measured TL curves possess four of five characteristic peaks of undoped BeO at ~180, ~360, ~495, and ~580 °C in varying intensities. A low-sensitivity shallow peak at 60 °C was recorded in the Nd^{3+}, $Yb^{3+,}$ and Tm^{3+}doped BeO samples. While all Ln^{3+} dopants activated the traps located between 300 and 400 °C, Yb^{3+}, Tb^{3+}, Tm^{3+}, and Pr^{3+} doped BeO affected the traps in the neighborhood of 180 °C TL peak. The high-temperature portion of the glow curve was exhausted at 495 and 580 °C, and improved only via Ce^{3+} and Gd^{3+} dopant ions. In addition, a shoulder peak appearing around 250 °C in the undoped BeO sample was not observed with the Ln^{3+} ions doping (see Figure 4.55). In certain cases, lanthanide doping has created TL peaks at higher temperatures (see Figure 4.55). These newly observed TL peak formations may be related to the distortion in the BeO lattice produced by the Ln^{3+} ions that substitute for the Be^{2+} ions and originated from other intrinsic defects. Results indicate that Ln^{3+} ions act as luminescence centers during the TL process, as observed by their RL emissions.

The effect of the lanthanide concentrations on the glow curves of these ceramic samples was also investigated using 0.01, and 0.1 % molar ratios to optimize the luminescence efficiency. As the concentration of Ln^{3+} ions was decreased, the main peak intensity, together with the low and higher temperature peaks were increased. In this study, Ce^{3+} with 0.01% mol concentration was chosen as a promising dopant for the BeO host matrix. Herein, it was shown that not only its high-temperature peaks but also the peaks below 250 °C were activated by Ce^{3+} ions.

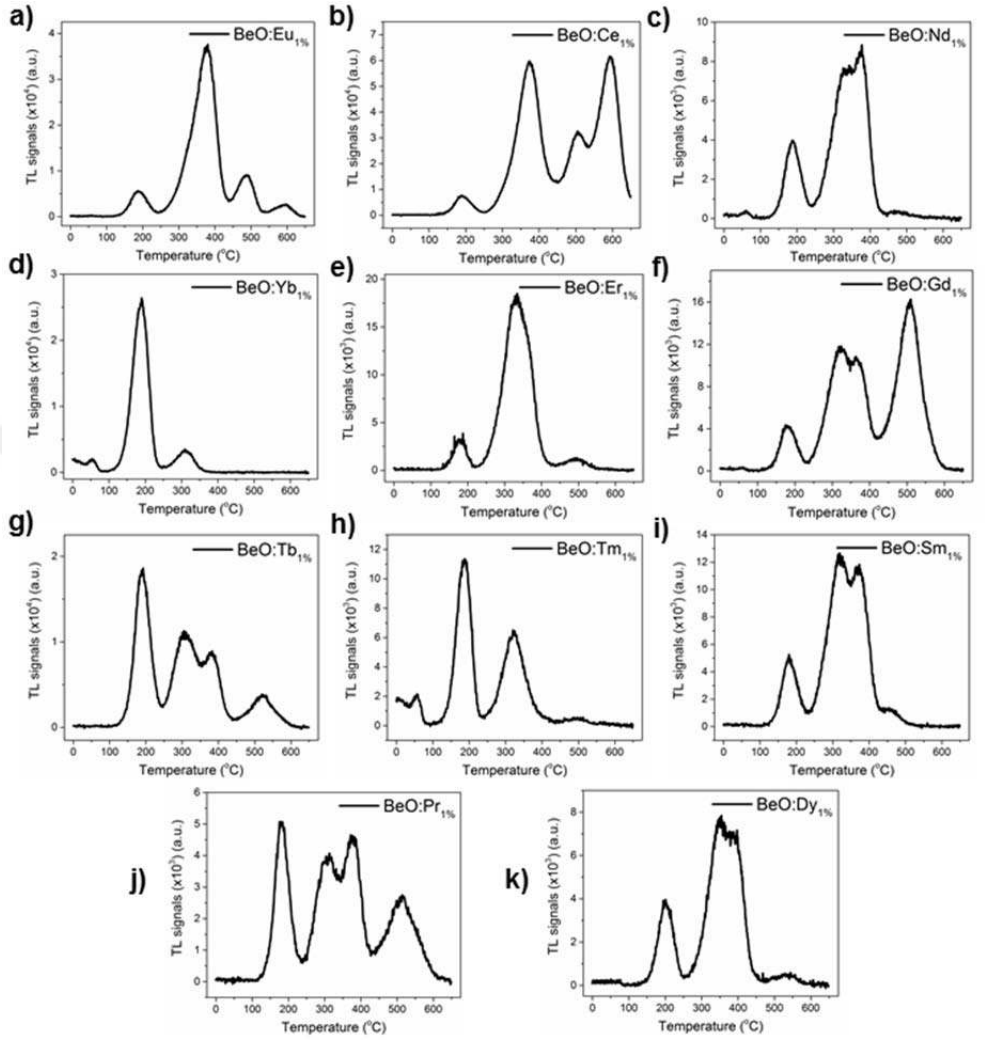

Figure 4.55. The TL glow curves from BeO:$Ln_{1\%}$ ceramic samples, a) BeO:$Eu_{1\%}$, b) BeO:$Ce_{1\%}$, c) BeO:$Nd_{1\%}$, d) BeO:$Yb_{1\%}$, e) BeO:$Er_{1\%}$, f) BeO:$Gd_{1\%}$, g) BeO:$Tb_{1\%}$, h) BeO:$Tm_{1\%}$, i) BeO:$Sm_{1\%}$, j) BeO:$Pr_{1\%}$, and k) BeO:$Dy_{1\%}$.

4.6.5. OSL Decay Curves of Undoped and Single-Doped BeO

The effect of Ln^{3+} doping on the OSL characteristics of undoped BeO ceramics was examined. All the OSL decay curves were recorded after 0.5 Gy irradiation at room temperature at a rate of 10 data points per second using 200 s

blue light stimulation. Figure 4.56 shows the OSL decay curves of undoped and single Ln^{3+}-doped BeO ceramics with their decaying components. As can be seen from Figure 4.56, lanthanide dopings significantly affect the OSL behaviors (shapes and intensities of the OSL curves) when compared to that of the undoped BeO ceramics. The general appearance of OSL signals showed that all undoped and single Ln^{3+}-doped BeO ceramics have two time-decaying components (fast and slow).

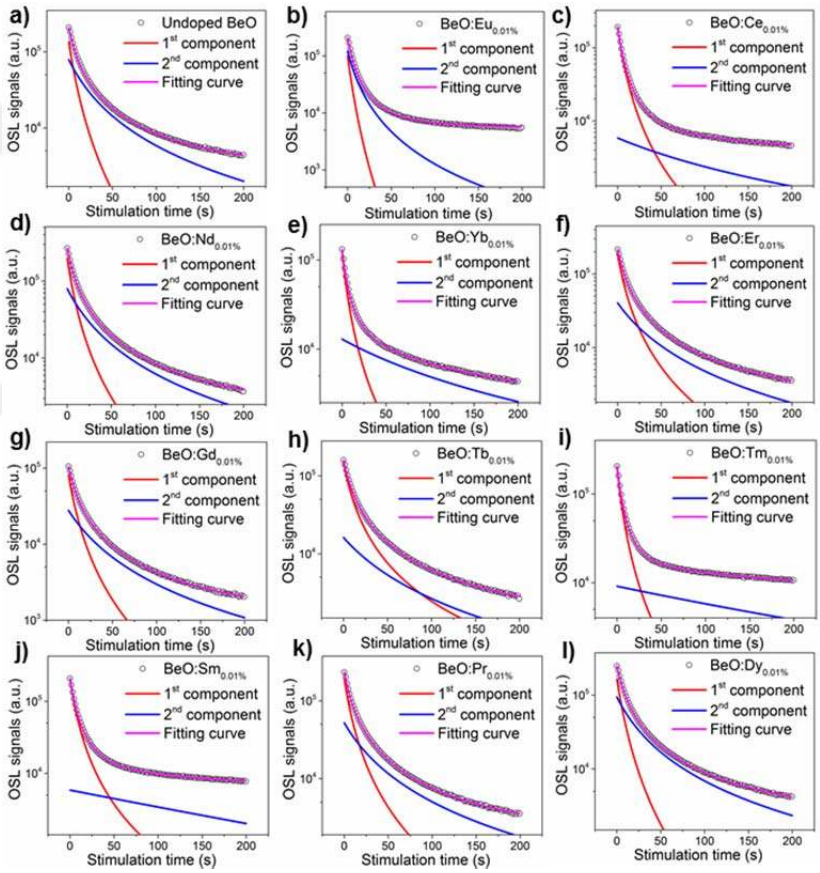

Figure 4.56. The OSL decay curves and resultant components from the curve fitting of undoped BeO and BeO:$Ln_{1\%}$ ceramic samples a) undoped BeO, b) BeO:$Eu_{0.01\%}$, c) BeO:$Ce_{0.01\%}$, d) BeO:$Nd_{0.01\%}$, e) BeO:$Yb_{0.01\%}$, f) BeO:$Er_{0.01\%}$, g) BeO:$Gd_{0.01\%}$, h) BeO:$Tb_{0.01\%}$, i) BeO:$Tm_{0.01\%}$, j) BeO:$Sm_{0.01\%}$, k) BeO:$Pr_{0.01\%}$, and l) BeO:$Dy_{0.01\%}$.

The analyzes of the OSL decay curves were examined via a method by fitting to the combination of the time-decaying functions which is one of the most common methods using the general order kinetic approach (Altunal et al., 2019a; Altunal et al., 2019b; Altunal et al., 2020c; Chen and McKeever, 1997). The used fitting equation was given above as Equation (4.1. $I_{1,2}$, $\tau_{1,2}$ and $b_{1,2}$ values were calculated using Equation (4.1 and given with the FOM values (goodness of the fitting) in Table 4.14.

Table 4.14. $\tau_{1,2}$ decay times, $b_{1,2}$ kinetic orders and FOM values of the OSL decay fittings using two time-decaying functions for undoped and single lanthanide-doped BeO ceramics.

No.	$\mathbf{1^{st}\ (fast)\ component}$			$\mathbf{2^{nd}\ (slow)\ component}$				
	I_1 (count)	τ_1(s)	b_1	I_2 (count)	τ_2(s)	b_2	*bkg* (count)	*FOM* (%)
Undoped BeO	1.38E+05	7.73	1.36	7.94E+04	37.42	2.05	2.38E+03	0.55
BeO:Eu$_{0.01\%}$	1.01E+05	4.48	1.19	1.21E+05	12.46	1.74	5.45E+03	1.21
BeO:Ce$_{0.01\%}$	1.96E+05	7.62	1.54	5.87E+03	178.54	2.05	3.33E+03	0.79
BeO:Nd$_{0.01\%}$	2.01E+05	8.30	1.50	7.99E+04	38.99	2.05	1.65E+03	0.51
BeO:Yb$_{0.01\%}$	1.25E+05	7.02	1.60	1.30E+04	162.67	2.05	1.71E+03	0.73
BeO:Er$_{0.01\%}$	1.86E+05	10.68	1.68	4.06E+04	52.77	2.05	1.50E+03	0.54
BeO:Gd$_{0.01\%}$	8.23E+04	9.70	1.54	2.79E+04	48.88	2.05	9.05E+02	0.74
BeO:Tb$_{0.01\%}$	1.51E+05	14.49	2.05	1.62E+04	68.91	2.05	1.07E+03	0.66
BeO:Tm$_{0.01\%}$	2.04E+05	6.89	1.59	9.10E+03	263.66	1.26	6.76E+03	0.60
BeO:Sm$_{0.01\%}$	2.12E+05	8.33	1.65	5.84E+03	191.09	1.05	5.62E+03	0.65
BeO:Pr$_{0.01\%}$	1.94E+05	9.39	1.61	5.21E+04	45.42	2.05	1.57E+03	0.61
BeO:Dy$_{0.01\%}$	1.67E+05	7.70	1.37	9.44E+04	37.24	2.05	1.86E+03	0.53

First order-kinetic assumes that the rate of retrapping of charge that has been released from a trap is negligible compared to the rate of recombination (Randall et al., 1945). In second-order kinetics, re-trapping is dominant (Garlick et al., 1948). The situation in which both situations are mixed is defined as general-order kinetics (McKeever and Chen, 1997). In this work, we examined the b values, which represent the transition probabilities between the traps, of the 1st (fast) and 2nd (slow) components of the OSL decay curves. As is seen from Table

4.14, the b values of the 1st components resembled the general-order kinetics with the values between 1.19 and 1.68 except for the BeO:$Tb_{0.01\%}$ which exhibited second-order kinetic characteristics with b = 2.05. With the b values of 2.05, 2nd (slow) decaying components exhibited the second-order kinetic characteristics (b = 2) except for BeO:$Eu_{0.01\%}$ and BeO:$Tm_{0.01\%}$ which demonstrated general-order characteristics (1 < b < 2). Only the 2nd components of OSL signals from the BeO:$Sm_{0.01\%}$ ceramics showed first-order kinetic behavior (b = 1.05).

When I worked over the lifetimes of the decay components, no serious differences were found in the τ_1 lifetime values of the 1st (fast)-decaying components of OSL signals. Whereas τ_2 lifetimes of the 2nd (slow) decaying components gave the changing values.

In my previous works, comparable OSL decay curves, and fitting parameters were found for the undoped and doped BeO ceramics (Altunal et al., 2019a; Altunal et al., 2020b; Altunal et al., 2020e). In this work, the OSL decay curves of the studied materials were represented as the resultant of the two decaying curves. The number of time-decaying functions was reported as three for Thermalox BeO chips (Bulur and Goksu, 1998). The results proved the existence of different types of defect centers and a more complex luminescence mechanism in the studied BeO materials. Therefore, these various types of defects in the BeO lattice structure cause a complex charge-carrier interaction between centers and localized bands. The TL and OSL mechanisms of the crystal can only be determined by the physical properties of the defect centers involved (Ln^{3+} ions) and the kinetics associated with transition charge carriers. It should be remembered that this curve fitting is only an oversimplified approximation of the actual situation. To learn more about the traps and transitions involved in OSL development, studies focused on the numerical solutions of the charge trafficking equations are required.

4.6.6 Effect of Lanthanide Co-Doping

According to the data obtained from single-lanthanide doped samples, the effect of another lanthanide co-doping on luminescence from the BeO:Ln^{3+} ceramic pellets was investigated. Although good progress has been observed in Ln^{3+} ion co-doped ceramic BeO, a comprehensive and full understanding of the TL and OSL mechanism originated from Ln^{3+} ions is still a major challenge. In this study, Ln^{3+} (Eu^{3+}, Nd^{3+}, Yb^{3+}, Er^{3+}, Gd^{3+}, Tb^{3+}, Tm^{3+}, Sm^{3+}, Pr^{3+} or Dy^{3+} as the co-dopants) effects on Ce^{3+} ions in host crystal were investigated. Although Eu^{3+} co-doped BeO:Ce^{3+} sample shows a relatively higher TL signal compared to the other samples (will be discussed later), only the results from some promising samples are presented here. Figure 4.57 shows TL intensities from the BeO singly doped with Ce^{3+}, Er^{3+}, Tb^{3+}, Dy^{3+}, and BeO:Ce^{3+},Er^{3+}, BeO:Ce^{3+},Tb^{3+}, BeO:Ce^{3+},Dy^{3+} ceramics in linear and semi-log scale.

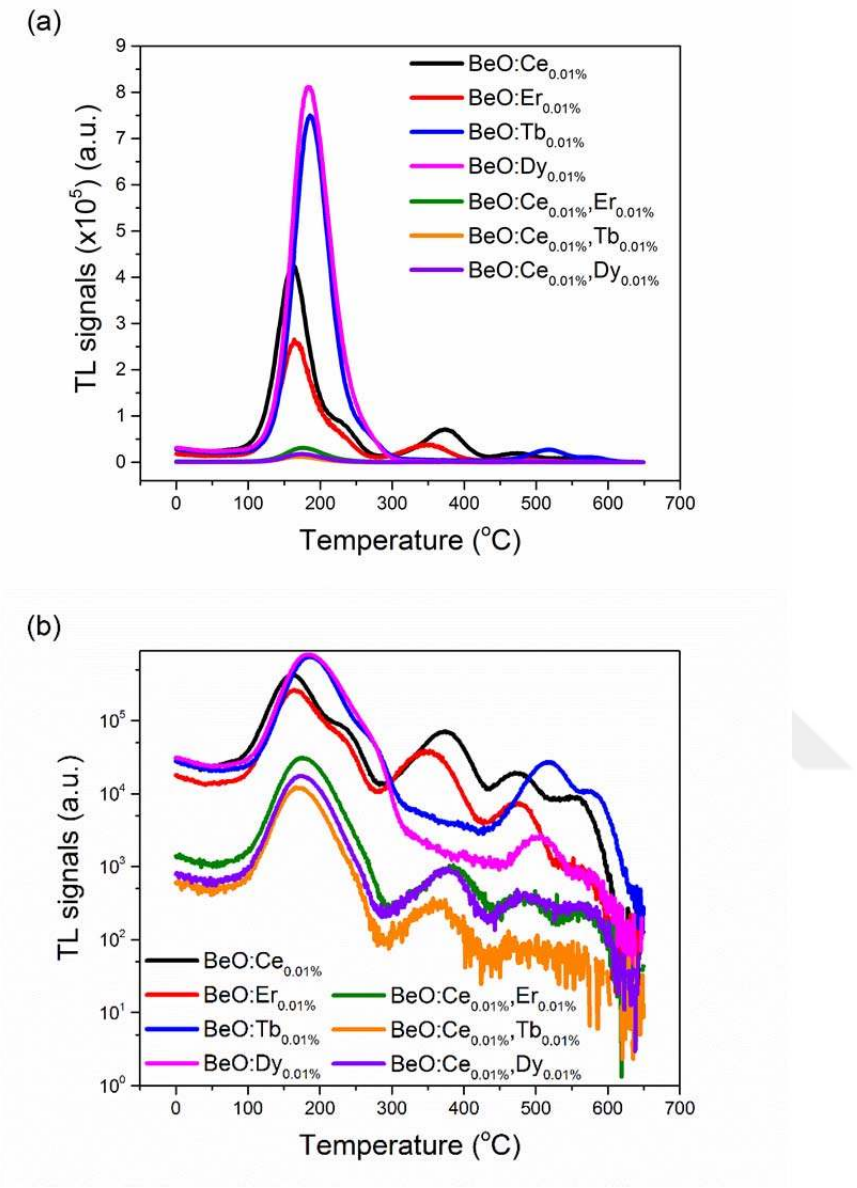

Figure 4.57. TL glow curves of BeO ceramic pellets singly doped with Ce^{3+}, Er^{3+}, Tb^{3+}, Dy^{3+} and co-doped with Ln^{3+} (Ln^{3+} = Er^{3+}, Tb^{3+}, and Dy^{3+}); (a) in linear scale (b) in semi-log scale for better presentation of the high temperature peaks

As is seen from Figure 4.57, although TL glow curves BeO:Tb and BeO:Dy did not show the 350 °C TL peak, the TL glow curves from the BeO:Ce,Tb, and BeO:Ce,Dy samples showed this peak. It may be suggested that Ce^{3+} ions in BeO characterize the emission of the 350 °C TL peak. Furthermore, the TL glow curve shape of the BeO:Ce,Er possessed the same TL peaks of BeO:Er and BeO:Ce samples with changing intensities. One may conclude that the co-doped samples, in general, exhibited lower intensities than single-doped BeO samples (see Figure 4.57). Similar to the decrease in TL intensities of the co-doped samples (Ce^{+}, Ln^{3+}), OSL efficiencies of them also behaved in the same decreasing tendency. This may be originated from the decrease in the Ce^{3+} luminescence efficiency with temperature (i.e., thermal quenching) associated with the increase in possible non-radiative relaxation of the Ce^{3+} from the excited to the ground state (Orante-Barrón et al., 2011). The presence of a charge compensator in the lattice that would promote Ce^{3+} incorporation and cause emission appearing in the UV luminescence band can solve this quenching problem (Oliveira et al., 2016).

4.6.7. Effect of Metal Co-Doping

We also added the alkali metal ions to promote the luminescence sensitivity of the host material by creating more defects. In the literature, it has been shown that the Na^{+} co-doping can significantly improve luminescence efficiency by acting as a probable charge compensator and increasing the incorporation of the lanthanide dopants (Altunal et al., 2020c; Altunal et al., 2020e; Yamashita et al., 1974). In one of our previous studies, the optimal concentration value for Na^{+} co-doping element, which significantly increased the luminescence emission, was found to be 5 mol% (Altunal et al., 2020e). For this reason, a passive admixture (e.g., Na^{+} co-doping) was applied and Na^{+} content was kept constant at 5 mol% in this study.

To investigate the effect of Na^{+} co-doping on TL and OSL behaviors of BeO:$Ce_{0.01\%}$,$Ln_{0.01\%}$ ceramic pellets (Ln^{3+} = Eu^{3+}, Nd^{3+}, Yb^{3+}, Er^{3+}, Gd^{3+}, Tb^{3+},

Tm^{3+}, Sm^{3+}, Pr^{3+} or Dy^{3+}), TL glow curves, and OSL signals were obtained from the produced samples following 0.5 Gy dose exposure. Some of the TL and OSL curves from the promising samples, namely, $BeO:Na_{5\%},Ce_{0.01\%},Er_{0.01\%}$, $BeO:Na_{5\%},Ce_{0.01\%},Tb_{0.01\%}$, $BeO:Na_{5\%},Ce_{0.01\%},Dy_{0.01\%}$ and $BeO:Na_{5\%}$ were presented in Figure 4.58 and Figure 4.59, respectively. As can be seen from these figures, TL and OSL signal intensities were significantly increased by Na^+ co-doping and even single Na^+ doping. While no change occurred in the positions of the TL peaks, especially in the TL glow curves given in Figure 4.58a, the intensities of the peaks located after 300 °C increased by two factors when compared to that of the undoped BeO samples. Although single Na^+ doping increased the characteristic TL signals, no change in the shape of TL glow curves was observed. These results proved that Na^+ ion as a charge compensator in the lattice would promote Ce^{3+} incorporation and cause emission appearing in the UV luminescence band (will be discussed in 0). This causes an increase in luminescence efficiency. On the other hand, it can be said that OSL signals reach the background level (approximately 10^3 counts level) at longer stimulation times as compared with the OSL behavior of the undoped sample, thus, in our measurements, an increase in lifetimes was observed for the $BeO:Na_{5\%},Ce_{0.01\%},Ln_{0.01\%}$ ceramic pellets (see Figure 4.59).

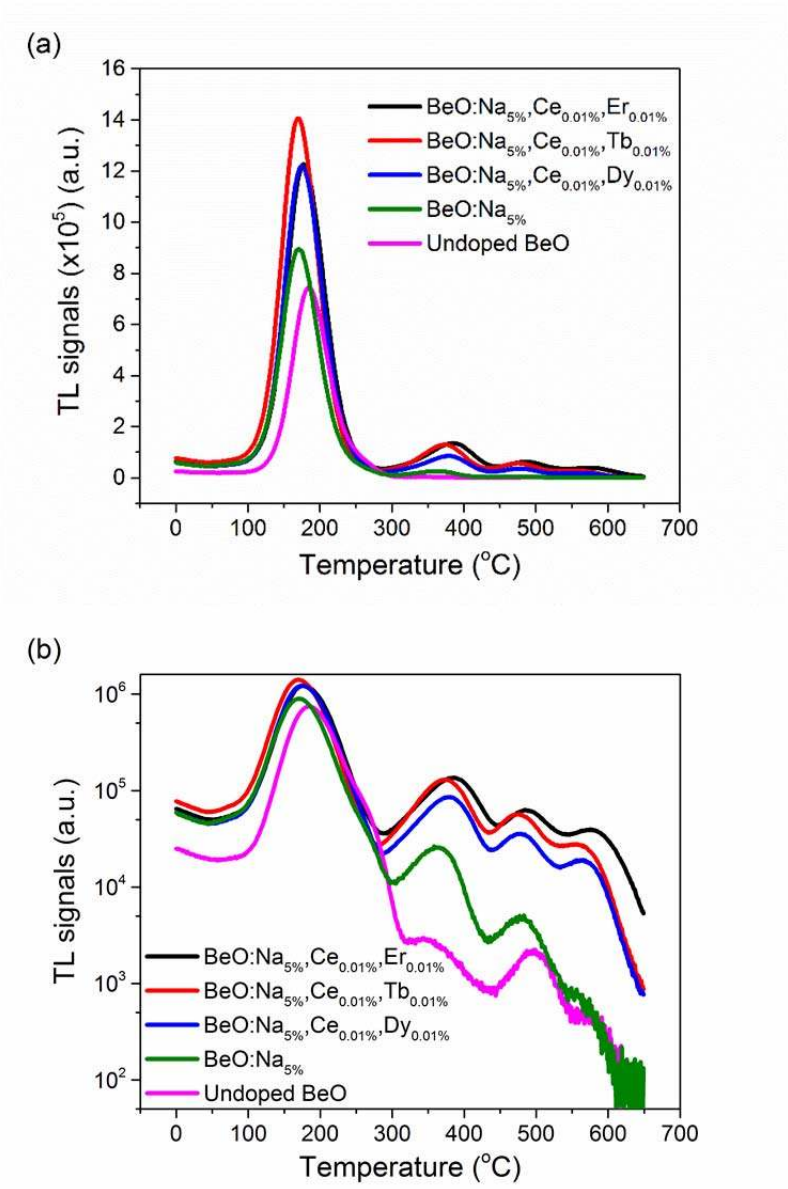

Figure 4.58. TL glow curves of undoped BeO ceramic pellets, BeO doped with Ce^{3+} (0.01 mol%) and Er^{3+}, Tb^{3+}, Dy^{3+} at dopant concentration of 0.01 mol% and co-doped with Na^{+} (5 mol%); (a) in linear scale (b) in semi-log scale for the high temperature peaks to be depicted better.

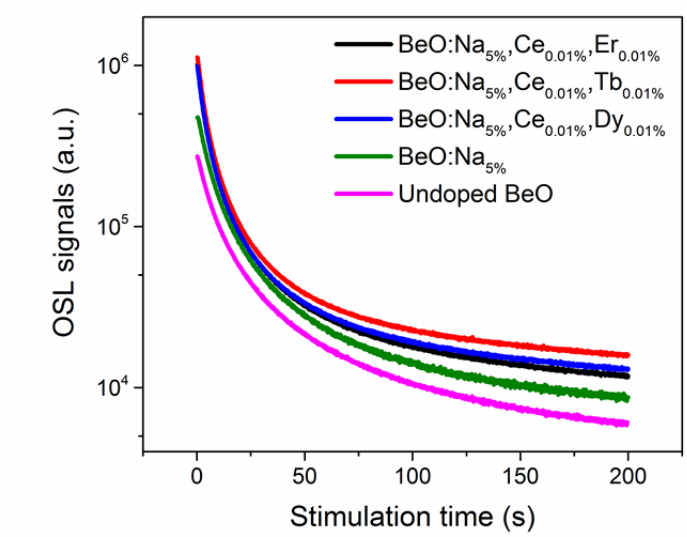

Figure 4.59. OSL decay curves of undoped BeO ceramic pellets, BeO doped with Ce^{3+} (0.01 mol%) and Er^{3+}, Tb^{3+}, Dy^{3+} (0.01 mol%), and co-doped with Na^{+} (5 mol%)

The relative total integrated TL and OSL intensities (the sum of the data from 0 up to 200 s) against the dopant elements were also examined. After Na^{+} co-doping there exists a 2-fold increase in both OSL and TL signal intensities (see Figure 4.60).

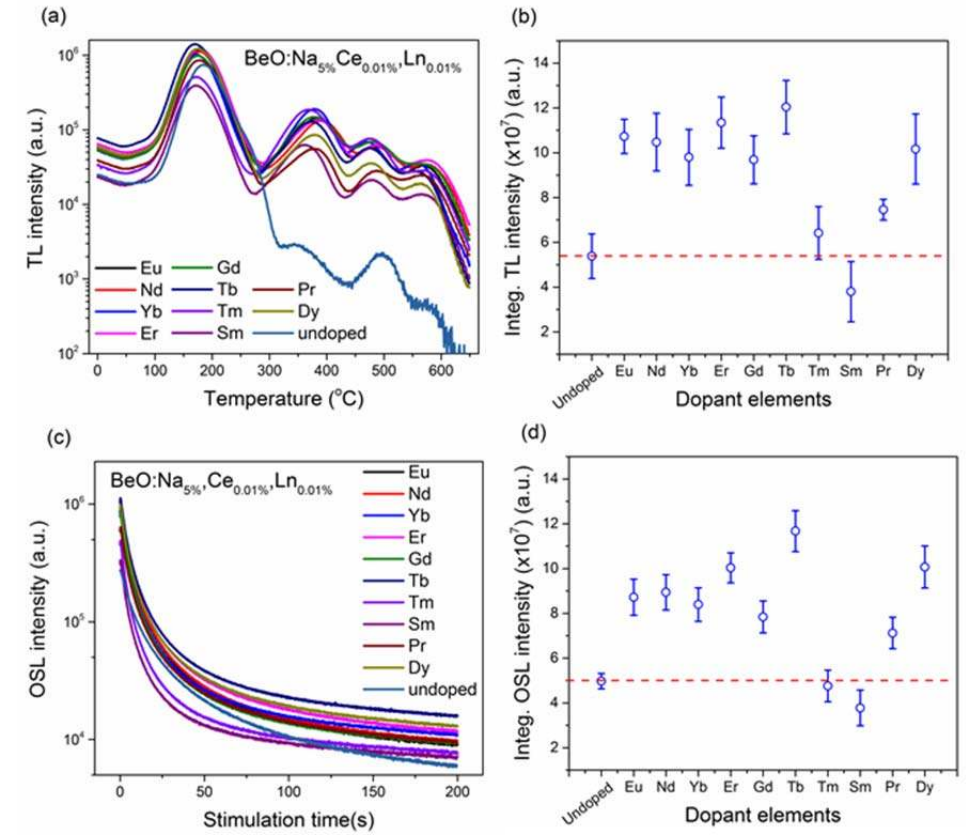

Figure 4.60. After doping with Ce^{3+} (0.01 mol%) and Ln^{3+}, (Ln^{3+} = Eu^{3+}, Nd^{3+}, Yb^{3+}, Er^{3+}, Gd^{3+}, Tb^{3+}, Tm^{3+}, Sm^{3+}, Pr^{3+} or Dy^{3+}) at dopant concentration of 0.01 mol%, and co-doped with Na^{+} (5 mol%); (a) TL glow curves of BeO ceramic pellets (b) The relative integrated TL intensities of BeO ceramic pellets (c) OSL decay curves of BeO ceramic pellets; (d) The relative integrated OSL intensities of BeO ceramic pellets. a and c are given in a semi-log scale. The error bars are the experimental standard deviations of mean values obtained from three pellets in each readout.

Besides Na^{+}, other well-known alkali metals Li^{+} and K^{+} in the literature were also tested along with the lanthanides as co-dopants in this study. TL and OSL signals of Li- and K- co-doped samples ($BeO:Li_{5\%},Ce_{0.01\%},Er_{0.01\%}$, $BeO:Li_{5\%},Ce_{0.005\%},Tb_{0.05\%}$, $BeO:Li_{5\%},Ce_{0.01\%},Dy_{0.01\%}$ $BeO:K_{5\%},Ce_{0.01\%},Er_{0.01\%}$, $BeO:K_{5\%},Ce_{0.005\%},Tb_{0.05\%}$, and $BeO:K_{5\%},Ce_{0.01\%},Dy_{0.01\%}$ ceramic pellets) are

presented in Figure 4.61. The results showed that Na^+ ions provided higher TL and OSL signals than Li^+ and K^+ ions. For this reason, Na^+ ion was chosen as a better charge compensator in BeO structure and the study was continued with Na^+ ion.

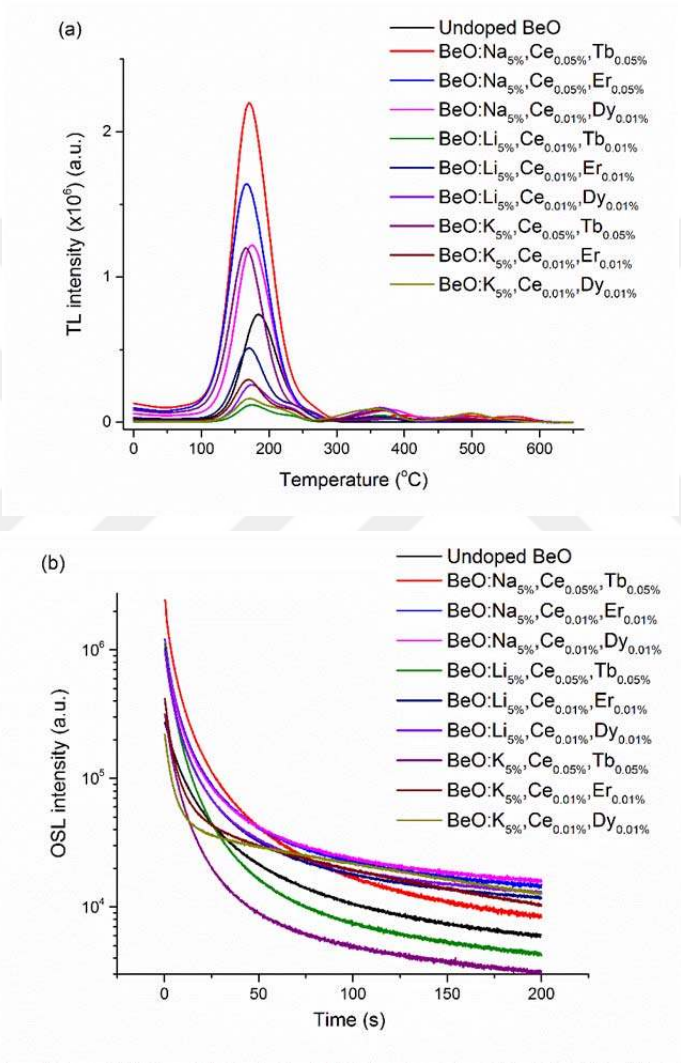

Figure 4.61. (a) TL and (b) OSL signals of Li- and K- co-doped samples ($BeO:Li_{5\%},Ce_{0.01\%},Er_{0.01\%}$, $BeO:Li_{5\%},Ce_{0.005\%},Tb_{0.05\%}$, $BeO:Li_{5\%},Ce_{0.01\%},Dy_{0.01\%}$ $BeO:K_{5\%},Ce_{0.01\%},Er_{0.01\%}$, $BeO:K_{5\%},Ce_{0.005\%},Tb_{0.05\%}$, and $BeO:K_{5\%},Ce_{0.01\%},Dy_{0.01\%}$ ceramic pellets)

4.6.8. Concentration Quenching Study

To investigate the effect of dopant concentration quenching on TL and OSL intensities of Ln^{3+}-doped BeO ceramics and to determine the optimal concentration for achieving highest luminescent sensitivity, TL and OSL readouts of BeO with various $Na_{5\%}$,$Ce_{x\%}$,$Er_{x\%}$; $Na_{5\%}$,$Ce_{x\%}$,$Tb_{x\%}$, and $Na_{5\%}$,$Ce_{x\%}$,$Dy_{x\%}$ concentrations (x = 0.001, 0.005, 0.01, 0.05, 0.1 mol%) were performed after 0.5 Gy beta dose exposure. Figure 4.62 shows the change in TL and OSL intensities of BeO:$Na_{5\%}$,$Ce_{0.01\%}$,$Er_{x\%}$, BeO:$Na_{5\%}$,$Ce_{0.01\%}$,$Tb_{x\%}$, and BeO:$Na_{5\%}$,$Ce_{0.01\%}$,$Dy_{x\%}$ ceramic pellets produced at concentrations given above. First, the Er^{3+}, Tb^{3+} and Dy^{3+} concentrations were changed by keeping the concentrations of Na^{+} and Ce^{3+} ions constant as 5 mol% and 0.01 mol%, respectively. With varying dopant concentrations, TL and OSL intensities showed similar concentration quenching behavior (see Figure 4.62a,b). While the optimal Tb concentration value for BeO:$Na_{5\%}$,$Ce_{0.01\%}$,$Tb_{x\%}$sample was determined to be as 0.05 mol%, and the highest TL and OSL intensities were obtained at 0.01 mol% Er and Dy concentrations for BeO:$Na_{5\%}$,$Ce_{0.01\%}$,$Er_{x\%}$, and BeO:$Na_{5\%}$,$Ce_{0.01\%}$,$Dy_{x\%}$ samples. On the other hand, with varying Ce^{3+} concentration, the maximum TL and OSL intensities were obtained from the combined measurements of the BeO:$Na_{5\%}$,$Ce_{0.01\%}$,$Er_{0.01\%}$; BeO:$Na_{5\%}$,$Ce_{0.005\%}$,$Tb_{0.05\%}$ and BeO:$Na_{5\%}$,$Ce_{0.01\%}$,$Dy_{0.01\%}$ ceramic pellets (see Figure 4.63). The TL and OSL intensities have a great dependence on Ln^{3+} dopant concentration. The luminescence increases with Ln^{3+} concentration to a certain extent, above this point, the luminescence begins to decrease, due to parity or aggregation of Ln^{3+} atoms at a high concentration which leads to efficient resonant energy transfer between Ln^{3+}/Na^{+} ions and a fraction of energy migration to distant quenchers, then quenching behavior appears as a result (Dhananjaya et al., 2011).

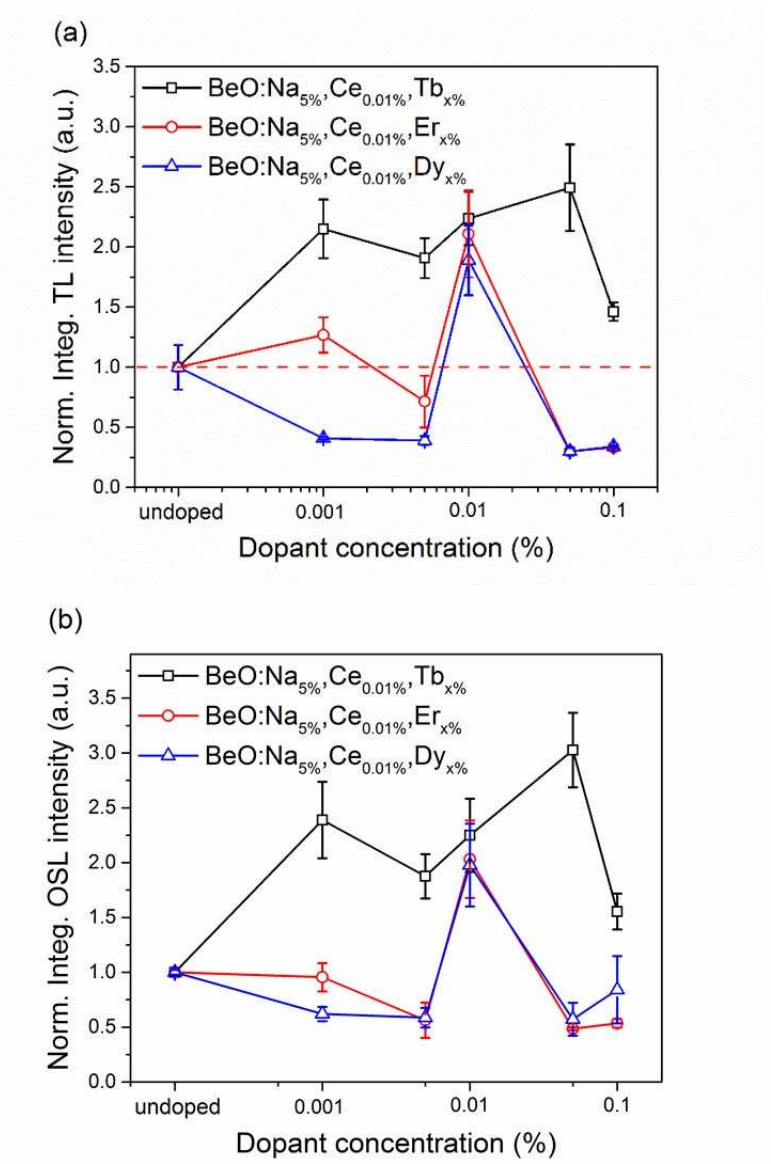

Figure 4.62. The changes in normalized integrated (a) TL intensities; (b) OSL intensities of BeO:$Na_{5\%}$,$Ce_{0.01\%}$,$Er_{x\%}$; BeO:$Na_{5\%}$,$Ce_{0.01\%}$,$Tb_{x\%}$, and BeO:$Na_{5\%}$,$Ce_{0.01\%}$,$Dy_{x\%}$ ceramic pellet samples prepared with various concentrations (x = 0.001, 0.005, 0.01, 0.05, 0.1 mol%) when compared with the TL and OSL intensities of undoped BeO samples in semi-log scale. The error bars show the experimental standard deviations of mean values from three samples in each readout.

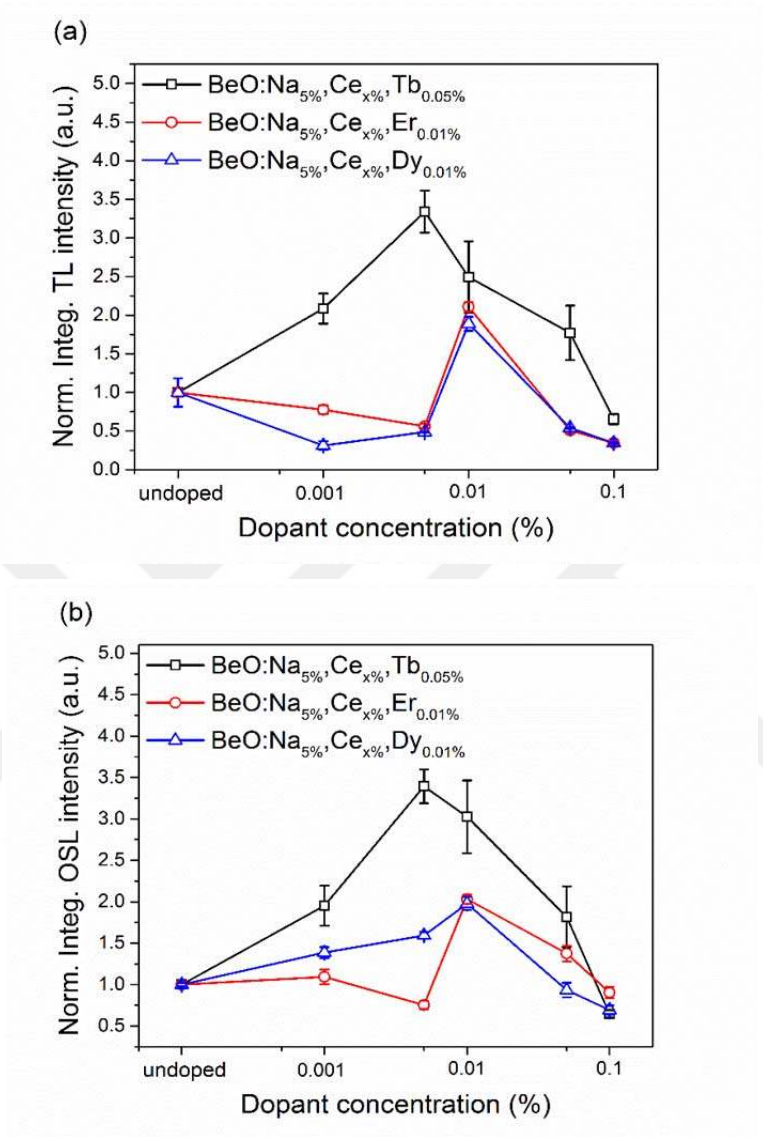

Figure 4.63. The changes in normalized integrated (a) TL intensities; (b) OSL intensities of BeO:$Na_{5\%}$,$Ce_{x\%}$,$Er_{0.01\%}$; BeO:$Na_{5\%}$,$Ce_{x\%}$,$Tb_{0.05\%}$, and BeO:$Na_{5\%}$,$Ce_{x\%}$,$Dy_{0.01\%}$ ceramic pellet samples prepared with different concentrations (x = 0.001, 0.005, 0.01, 0.05, 0.1 mol%) when compared with the TL and OSL intensities of undoped BeO samples in semi-log scale. The error bars show the experimental standard deviations of mean values from three samples in each readout.

In this study, increased luminescence efficiency in desired emission regions and controlled luminescence signals obtained with lanthanide doping on purpose is important for the dosimetric potential of the materials. The minimum detectable dose values were calculated to test the advantage of the three newly developed dosimetric materials over the undoped BeO. MDD values were evaluated by 3σ with 99.73% confidence level as 1.2 ± 0.3 mGy, 721 ± 17 μGy, 271 ± 5 μGy, 554 ± 10 μGy for undoped BeO, BeO:$Na_{5\%}$,$Ce_{0.005\%}$,$Tb_{0.05\%}$, BeO:$Na_{5\%}$,$Ce_{0.01\%}$,$Er_{0.01\%}$, and BeO:$Na_{5\%}$,$Ce_{0.01\%}$,$Dy_{0.01\%}$ ceramic pellets, respectively.

On the other hand, to test whether the charge population in traps is stable or not, after 0.5 Gy beta doses fading characteristics of newly developed BeO ceramics were investigated in three days. It was observed that almost 94% of the OSL signals remained stable after 3 days. We found the fading of around 87% when the undoped BeO was read out at about 3 days after irradiation. This behavior is of course extremely important in the practical use of these materials for dosimetric applications. These results suggest that the OSL and TL intensities of three newly developed BeO pellets (BeO:$Na_{5\%}$,$Ce_{0.01\%}$,$Er_{0.01\%}$; BeO:$Na_{5\%}$,$Ce_{0.005\%}$,$Tb_{0.05\%}$ and BeO:$Na_{5\%}$,$Ce_{0.01\%}$,$Dy_{0.01\%}$) are found to be highly sensitive to radiation with superior dosimetric properties (will be discussed in Section 0).

4.6.9. OSL Emissions

Figure 4.64 shows the OSL emission spectra of Ln^{3+}-doped BeO ceramics following the 300 Gy beta dose through a transmission range of the Hoya U-340 filter which used in the RisØ reader. As is seen from the figure that the main OSL emission bands are located between ~300 and ~360 nm; the first being the dominant band. These results showed that the dominant luminescence bands in RL and OSL processes might be different. However, luminescence bands located between 300 and 400 nm (i.e., 3-4 eV) are dependent on the same luminescence

mechanism in both cases which have been observable using the U-340 filter. When the OSL emissions of single Ln^{3+}-doped BeO samples were compared with the emission obtained from the undoped sample, it was observed that some single Ln^{3+}ions shifted the dominant luminescence band towards higher wavelengths in the BeO structure (see Figure 4.64a). Moreover, only an increase in the emissions of Ce^{3+}, Er^{3+}, Tb^{3+}, Gd^{3+}, Pr^{3+} and Dy^{3+} doped samples was observed. With the Ln^{3+} co-doping, a reduction in OSL emission was observed here as well, while an increase in emissions after 360 nm was observed (see Figure 4.64b). With the addition of Na^{+} ion to the structure, OSL emissions have increased significantly recorded through the Hoya U-340 filter.

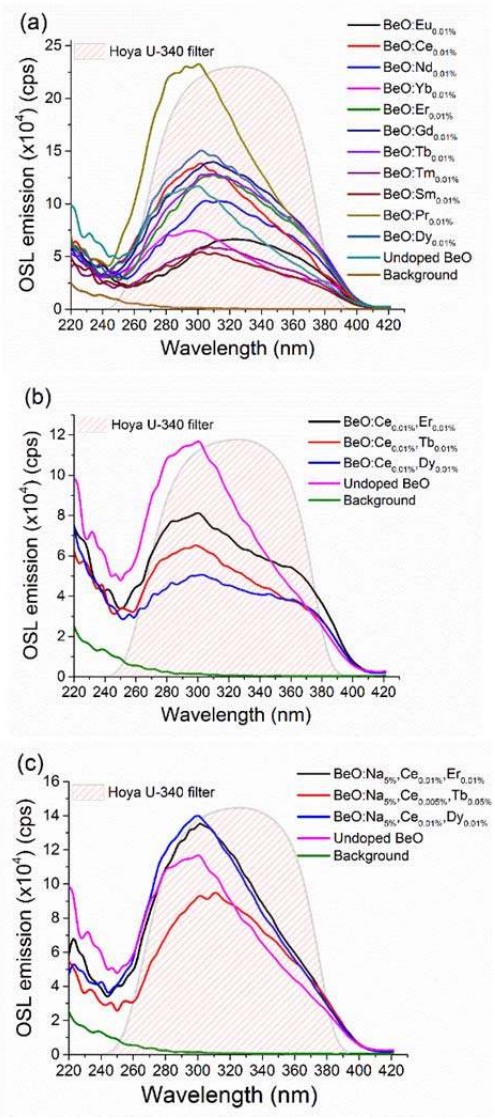

Figure 4.64. OSL emission spectra of previously irradiated BeO ceramics with 300 Gy beta dose and using 475 nm excitation; (a) for the single Ln^{3+}-doped BeO; (b) for the Ln^{3+} doped and co-doped BeO, (c) after adding the alkali metal ions Na^{+} as co-dopants to BeO host oxides. The excitation monochromator was 475 nm, and the emission spectra were scanned from 240 to 420 nm in 3 nm increments using 0.1 s integration time. The excitation time was 60 s. All the OSL emission spectra presented here were previously corrected by the spectral response of the system.

4.6.10. Discussion

The luminescence mechanism of Ln^{3+} ions is known depending on their location in the host lattice. If the Ln^{3+} ions have similar chemical properties with host materials, such as the same oxidation state and similar ionic radius, it is easy to include Ln^{3+} ions in the host lattice in place of host metal ions. Here, due to the remarkable differences between the ionic radius of Ln^{3+} and Be^{2+}, it would create some local distortion that may stabilize holes from the valance band (Dorenbos and Bos, 2008). In such a case, it can be expected that even a small distortion may lead to an increase or decrease in luminescence efficiency. To determine the effect of Ln^{3+} on the BeO lattice and how the luminescence mechanism exists, the results for single-doped, co-doped, and metal-doped BeO ceramics presented here must be discussed from the spectroscopic properties of underlying Ln^{3+} ions.

When we examined the results of TL and OSL obtained from single Ln^{3+} doped BeO samples more closely, a decrease in luminescence efficiency was observed with increasing Ln^{3+} concentration, similar to RL emissions. Concentration quenching, which can be regarded as a non-radiative process, is one of the main things to avoid when optimizing additive concentration. The decrease in luminescence, which was observed as a result of the increasing Ln^{3+} concentration in the structures with rich energy levels (general activators such as Tb^{3+}, Er^{3+}, Tm^{3+}, Pr^{3+}), is the concentration-dependent cross-relaxation (CR) affecting the non-radiative transition population of stimulated Ln^{3+} ions (Chen et al., 2016).

Figure 4.55 shows that the Ce^{3+} ion increases the luminescence sensitivity of the BeO host material by affecting the trap region corresponding to the TL peaks responsible for the OSL signals. Besides, the fact that the Ce^{3+} ion is a good sensitizer that can transfer energy to the activators around in a possible situation has encouraged us to obtain a BeO:Ce^{3+} based "host + sensitizer + activator" type luminescent material. Energy transfer for ions plays an important role in luminescent materials. Energy transfer from the sensitizer to the activator can be

achieved by the spectral overlap of the emission spectrum of the sensitizer ion and the absorption spectrum of the activator ion (Dhoble et al., 2019). The reason why the Eu^{3+} co-doped BeO:Ce^{3+} sample shows a relatively higher TL signal compared to the other samples is the existence of a wide emission band of Ce^{3+} ion, approximately at 330–420 nm related with the transition from 5d level to $^2F_{5/2} \rightarrow {}^2F_{7/2}$ levels and its overlapping with the absorption band of Eu^{3+} ion represented by the transition from $^7F_0 \rightarrow {}^5L_6$ (Dhoble et al., 2019). In this study, the Er^{3+} co-doped BeO:Ce^{3+} sample showed the highest OSL signals. It was concluded that a passive admixture (charge compensator) ion such as Na^+ is needed to facilitate energy transfer between Ln^{3+} ions in the "host (BeO) + sensitizer (Ce^{3+}) + activator (such as Tb^{3+}, Tm^{3+}, Dy^{3+}, Nd^{3+})" type samples, that is, to increase the UC quantum yield and consequently to improve luminescence.

Apparently, Na^+ plays several roles, including charge compensation and possibly lattice stress relief on Ln^{3+} doped BeO. It was observed that TL and OSL efficiencies obtained from the BeO: Ce^{3+},Ln^{3+} samples increased almost 2 times after Na^+ co-doping. Herein, the reason for the remarkable increase in luminescence might be due to Na^+ ions acting as a charge compensator and causing an increase in UC quantum yield and consequently an energy transfer between the emission centers introduced by Na^+ and the Ln^{3+} dopants. The energy transfer mentioned here most probably takes place effectively if the condition of energy resonance and spatial proximity between the involved centers are satisfied. This will be met due to a high Na^+ concentration in the structure (Blasse et al., 1994). As is seen in Figure 4.64c, the broadening UV emission bands mean that they likely match the resonance condition for most of the sensitizers (here specifically Ce^{3+}) or other activators, Ln^{3+} (here specifically Er^{3+}, Tb^{3+}, Dy^{3+}). On the other hand, regarding the role of Na^+ dopant in BeO, it is clear to say that a negative effective charge defect $(Na_{Be})^-$ occurs with the Na^+ substitution for Be^{2+}. This negative charge defect may compensate for the positive effective charge defect $(Ln_{Be})^+$ occurring with the Ln^{3+} substituting for Be^{2+}. As a hypothesis, the assumption that

the ideal substitution of Na^{+} for Be^{2+} needs evidence. One can expect, e.g., an interstitial charge neutralized by OH-. Negative charge $(Na_{Be})^{-}$ defects may compensate for the incorporation of positive effective charge in an intrinsic defect of BeO crystal (Altunal et al., 2020e; Kortov et al., 1993b; Yukihara et al., 2013). As a result of XRD analyzes, a decrease in oxygen vacancies which are capable of improving luminescence in the structure was observed with Ln^{3+} doping. The $(Na_{Be})^{-}$ defects obtained by Na^{+} co-doping, just like oxygen vacancies, cause crystal field distortion and might act as compensators for the energy transfer from host to Ln^{3+} ion due to the strong mixing of charge transfer states and enhances the luminescence intensity (Balakrishnaiah et al., 2011; Dhananjaya et al., 2011). In this work, considering this compensation effect, differences in ionic radius and changes in crystal field energy can be considered to cause a significant increase in luminescence signals. The roles of Na^{+} as a dopant contributing to the enhancement of luminescence and improving dosimetric characteristics of BeO ceramic pellets were presented elsewhere in the literature (Altunal et al., 2020a; Altunal et al., 2020c; Altunal et al., 2020e; Yamashita et al., 1974).

Considering both TL and OSL signals, the most sensitive samples were selected as BeO:Na,Ce,Er; BeO:Na,Ce,Tb, and BeO:Na,Ce,Dy. Optimizing the concentration of optically active ions is potentially the easiest way to improve the UC quantum yield. Therefore, in this study, the concentrations of Ln^{3+} ions contained in "host + sensitizer + activator" type of final products were optimized as the $BeO:Na_{5\%},Ce_{0.01\%},Er_{0.01\%}$, $BeO:Na_{5\%},Ce_{0.005\%},Tb_{0.05\%}$, and $BeO:Na_{5\%},Ce_{0.01\%},Dy_{0.01\%}$. The source of the enhanced luminescence obtained here, besides the concentration optimization, can be the strong energy transfer between Ln^{3+} ions. The energy transfer process simply begins by getting excite the electrons located at ${}^{2}F_{5/2}$ ground state of Ce^{3+} ions to the 5d exciting level. While some electrons return to the ground states of Ce^{3+} ions by exhibiting UV-blue emissions, some electrons transfer to the acceptor levels e.g., ${}^{5}D_{4}$ excited state of Tb^{3+} ions and higher energy levels of Dy^{3+} ions. As a result of the return of electrons to the

ground state energy levels of activator ions, characteristic visible region emissions (blue light and yellow light emissions of Dy^{3+} ions, green emissions of $Er^{3+,}$ and Tb^{3+} ions) of activator ions may be observed. A more detailed energy transfer mechanism in Ln^{3+} ions was discussed in the literature (Dhoble et al., 2019).

Of course, a TL/OSL model is still required to represent the existing complex luminescence process. It is clear to say that trivalent lanthanides in the BeO lattice should establish energy levels in the forbidden band and show themselves actively in recombination processes. The Ln^{3+} can act as electron traps or hole traps, depending on their location concerning the delocalized energy bands and the Fermi level. In this study, the luminescence process simply begins by creating charge carriers as a result of irradiating the crystal as illustrated in Figure 4.65. The electrons and holes move freely inside the crystal and are trapped at defects. Considering the general theory of defects (Stoneham, 2001), and the behavior of the trivalent lanthanide impurities (Ln^{3+}) in various types of phosphors (e.g. YPO_4 and CaF_2 (Dorenbos, 2003; Dorenbos and Bos, 2008)), in our samples, Ce^{3+}, Pr^{3+}, and Tb^{3+} may act as hole traps and become quadrivalent ions (Ce^{4+}, Pr^{4+}, Tb^{4+}) during irradiation. With heat or light stimulation, trapped electrons are escaped from the electron traps (Sm^{3+}, Eu^{3+}, Yb^{3+}, Dy^{3+}, Er^{3+}). As a result of the recombination of these released electrons with Ln^{4+} ions, Ln^{3+} ions occur in excited states. After the relaxation of Ln^{3+} ions, they decay to the ground states, and simultaneous emission of the photons i.e. luminescence is observed (see Figure 4.65). More detailed studies on the role of lanthanides in BeO ceramic pellets such as temperature dependence of RL signals and TL emissions are necessary to confirm the proposed luminescence mechanism.

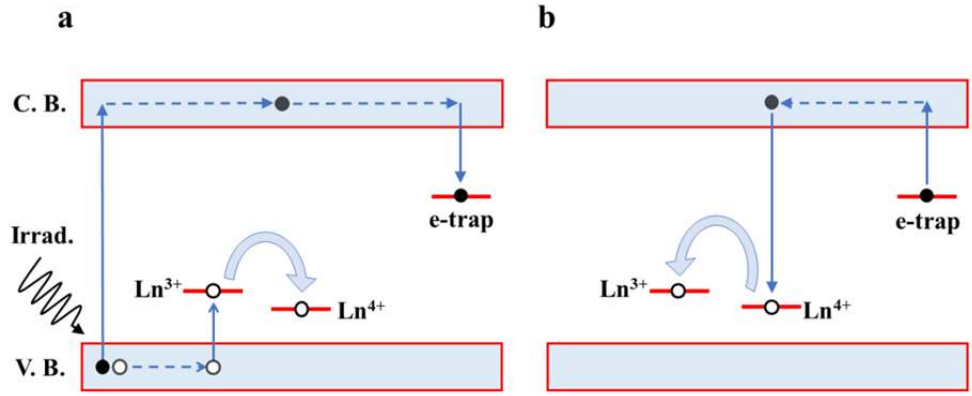

Figure 4.65. Proposed TL/OSL mechanism: (a) During irradiation, charge carriers (electron and holes) are created, and trapped by electron-traps and hole-traps (Ce^{3+}, Pr^{3+}, Tb^{3+}), ($Ln^{3+} + h^{+} \rightarrow Ln^{4+}$). (b) During TL/OSL readout (thermal or optical stimulation), electrons are released from trapping centers (Sm^{3+}, Eu^{3+}, Yb^{3+}, Dy^{3+}, Er^{3+}) and recombine with Ln^{4+} ions (Ce^{4+}, Pr^{4+}, Tb^{4+}), converting them to Ln^{3+} in an excited state. Luminescence occurs with the relaxation of these compounds. Electrons and holes are represented by solid and open circles, respectively.

4.7. BeO:Na,Tb,Gd Ceramics

This study presents the structure and luminescent characterization of the new BeO:Na,Tb,Gd ceramic pellets as a promising material for dosimetric applications. To understand structural formations and surface morphologies of the products, X-ray diffraction (XRD), Scanning electron microscopy (SEM) and Energy Dispersive Spectrometry (EDS) analyzes were performed. Luminescence from the BeO:Na,Tb,Gd ceramic pellets was characterized by using OSL, TL, and Radioluminescence (RL) techniques. We performed the investigations on correlations between OSL and TL signals, dose linearity, energy dependency, reusability and fading properties of OSL signals to develop new OSL materials and use in personal or medical dosimetry applications.

4.7.1. Material Synthesis

BeO samples were synthesized with a known synthesis method, Co-precipitation technique, using Beryllium sulfate tetrahydrate ($BeSO_4 \cdot 4H_2O$, ≥99.0%), Poly (ethyleneimine) solution (50% (w/v) in H_2O) and Ammonium hydroxide solution (H_5NO, ACS reagent, 28.0-30.0% NH_3 basis) (Altunal et al., 2019b). Doping of the BeO samples was performed using Sodium nitrate ($NaNO_3$ ≥99.0%), Terbium (III) nitrate pentahydrate ($Tb(NO_3)_3 \cdot 5H_2O$ ≥99.99%) and Gadolinium (III) nitrate hexahydrate ($Gd(NO_3)_3 \cdot 6H_2O$ ≥99.99%). Here, while Na concentration values were selected high, the concentration percentages of Lanthanide ion additives were chosen too small to avoid increasing Z_{eff} value.

The co-precipitation synthesis was performed in several steps. First, beryllium sulfate salts were completely dissolved in distilled water using a magnetic stirrer. Next, nitrate base doping material was added to this solution at different concentrations. After dilution of a predetermined amount of polyethyleneimine (PEI) solution with water in a separate vessel, PEI solution was added slowly to the main solution containing beryllium sulfate and dopants. And so, the precipitation process started. To increase the efficiency of the precipitation process, the pH of the mixture was kept constant at 7 by adding a predetermined amount of ammonia solution. With the pH balance of the mixture was achieved, the white BeO precipitate was observed. After drying the precipitate with a heater, to remove formed organics and to achieve BeO particles, the dried sample was calcined at 800 °C for 4 h in an oxygen atmosphere. Finally, $BeO:Na_{10\%},Tb_{0.005\%},Gd_{0.01\%}$ white powders were achieved and used in pellet form which provided more settled OSL signals. $BeO:Na_{10\%},Tb_{0.005\%},Gd_{0.01\%}$ ceramic pellets were prepared using a hydraulic press with evacuable pellets dies under 500 kg force/cm^2 pressure for 20 seconds. To provide strength, integrity and avoid the toxicity of BeO in powder form, prepared pellets, as discs with 25 mg mass, 3.07 mm in radius and 0.82 mm in thickness, were sintered at 1600 °C, for 4h (Altunal et al., 2019b). After 1600 °C sintering process, the volumetric shrinkage cause some reductions in sizes of the $BeO:Na_{10\%},Tb_{0.005\%},Gd_{0.01\%}$ ceramic pellets. As a result of shrinkage regarding sintering, while the pellets were measured at 2.51 mm

in radius and 0.54 mm in thickness, the mass of the prepared pellets was at 23 mg. To be a comparison example, a photograph of BeO:Na,Tb,Gd ceramic pellet used in this study, a commercial Thermalox995 OSL chip detector of diameter 4 mm and thickness of 1 mm (Thermalox 995, Brush Wellman Inc., USA), and a widely used nanoDot OSL detector with a disk-shaped Al_2O_3:C of 5 mm diameter and 0.2 mm thickness which encased in a light-tight plastic with dimensions of 10x10x2 mm^3 (nanoDot OSLd, Landauer Inc., USA) were shown together with a Turkish coin (10 kr.) 1.925 cm in diameter and 1.7 mm in thickness in Figure 4.66. As can be seen in Figure 4.66, BeO:Na,Tb,Gd ceramic is very close to the dimensions of other commercially available dosimeters and provides ease of measurement and use.

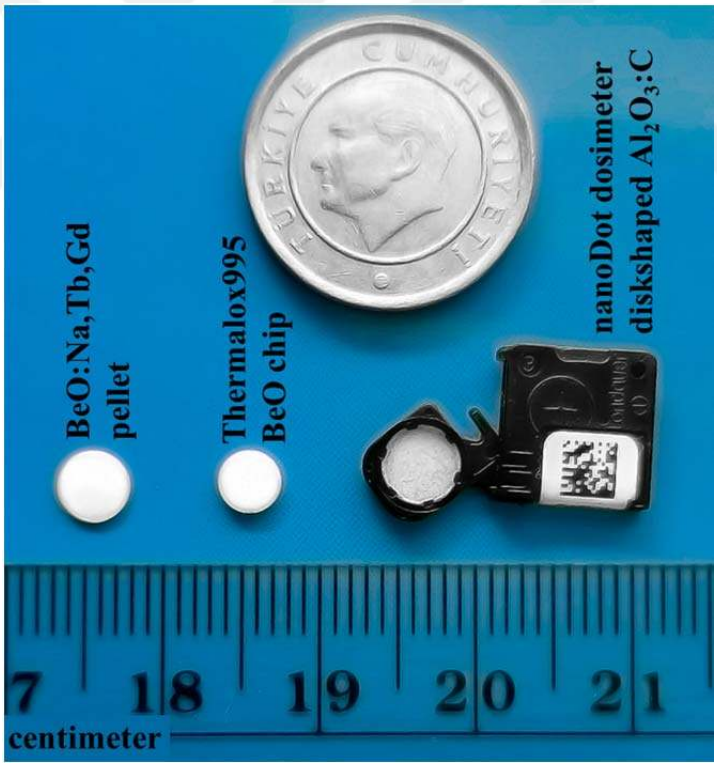

Figure 4.66. A photograph of BeO:Na,Tb,Gd ceramic pellet sample under room light with a Thermalox 995 BeO chip and a nanoDot Al_2O_3:C dosimeter.

4.7.2. Structural Characterization

The structural analysis of the synthesized BeO:$Na_{10\%}$,$Tb_{0.005\%}$,$Gd_{0.01\%}$ ceramics was carried out using XRD, EDS, and SEM methods. XRD pattern was obtained using Cu-Kα (40 kV, 30 mA) to have information about crystallographic phases. Investigation of the surface morphology and particle size of the material were analyzed from the SEM picture which was taken at room temperature (RT). On the other hand, to investigate elemental impurities formed in the structure, EDS analysis was carried out by FE-SEM, Zeiss equipped with the compact GEMINI® objective lens with a take-off angle of 35°.

4.7.2.1. X-Ray Diffractions

To investigate the crystalline structure and phase composition of a sintered BeO:Na,Tb,Gd ceramic pellet, XRD pattern was recorded using a step size of 0.02° (2θ) from 10° to 90° (2θ). In Figure 4.67, the XRD peaks from the sample were presented with the well-matched data of BeO phase reported in the ICDD-PDF-card no 98-016-3468.

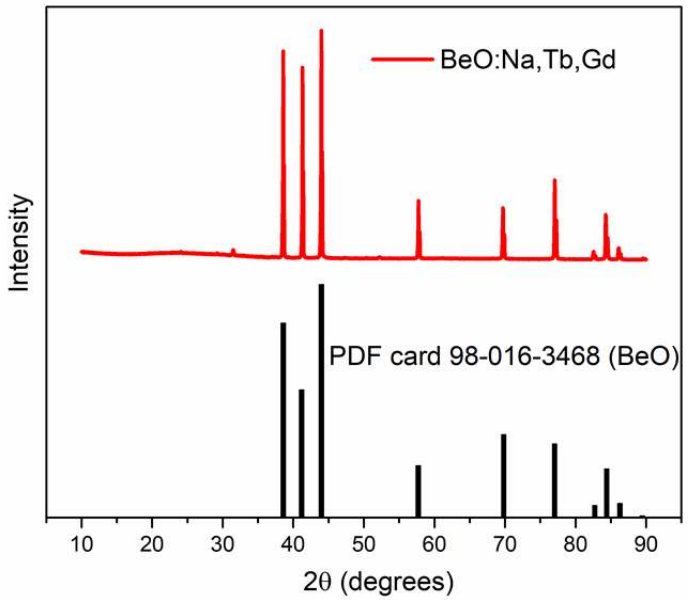

Figure 4.67. XRD patterns of BeO:Na,Tb,Gd pellet and reference BeO with PDF card no 98-016-3468.

4.7.2.2. SEM Pictures

Figure 4.68 shows the SEM image of BeO:Na,Tb,Gd sintered ceramic pellet which is characterized by regularly formed and well-bonded particles with a very low porous structure providing more settled luminescent signals.

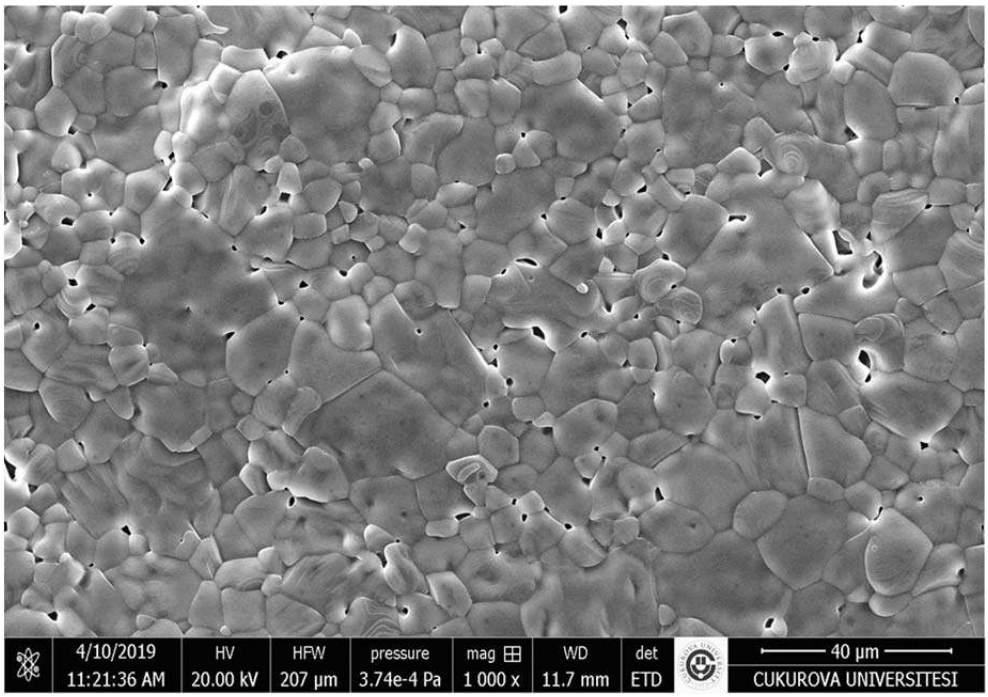

Figure 4.68. SEM micrograph of of BeO:Na,Tb,Gd sintered ceramic pellet

4.7.2.3. EDS Analyzes

In this study, the percentages of dopants are nominal values and it is not accurately known which ratio occurs in the crystal lattice during the synthesis process. To estimate the accuracy of the specified dopants and their rates, EDS analysis was carried out following the SEM analysis. EDS spectrum of a sintered BeO:Na,Tb,Gd ceramic pellet was illustrated in Figure 4.69. The results confirm that O, Na, Gd, Tb elements exist in the BeO:Na,Tb,Gd structure and the sample is highly pure. Except for coating elements such as Au, Pt, and C, there are almost no

other elements. Due to the absorption of low-energy X-rays by the Beryllium window placed in front of the detector in the measurement system, the presence of Be was not observed in the EDS spectrum. The atomic percentage of O, Na, Tb, and Gd elements were found as 90.28, 9.52, 0.08 and 0.12 at%, respectively. These values were the average of the data obtained from three different regions that appear to be more homogeneous on the BeO:Na,Tb,Gd ceramic surface. The three different regions error of the O, Na, Tb and Gd elements were calculated as ± 0.33, 0.26, 0.02 and 0.01.

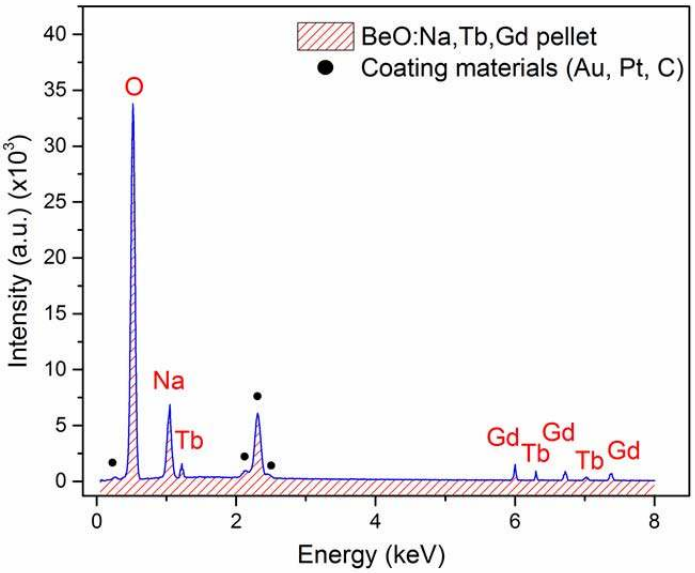

Figure 4.69. EDS spectrum of the BeO:Na,Tb,Gd ceramic pellet.

4.7.3. Luminescence Characterization

TL and OSL readings were done using DA-20 model Risø TL/OSL system endowed with a $^{90}Sr/^{90}Y$ β-radiation source (2.27 MeV maximum energy, 6.689 Gy/min dose rate) for irradiation, a bialkali PM tube (Electron Tubes, 9235QA) for detection of luminescence emitted from a dosimeter and Blue LEDs (λ_{photon}~ 470 nm, FWHM ~30 nm) for stimulation. OSL readouts were recorded while 200 s

blue light continues wave (CW) stimulations with ~80 $mWcm^{-2}$ power density at RT. To avoid scattered stimulation light during the stimulation process, a UV bandpass Hoya U-340 detection filter with 340 nm max transmittance wavelength was used in front of the PMT. On the other hand, TL measurements of the pellets were performed up to 650 °C at a heating rate (HT) of 3 °C/s in a nitrogen atmosphere. The TL and OSL measurements of the pellets were started after half an hour of waiting at the RT after the sintering of the samples for stabilization of traps. Previously irradiated materials were subjected to 110 °C pre-heating for 10 s to completely remove unstable charge carriers from the shallow traps (capable of discharging at a relatively low temperature, such as RT) and to avoid unstable signals that would affect the measurement results.

The radioluminescence (RL) spectra of $BeO:Na_{10\%},Tb_{0.005\%},Gd_{0.01\%}$ ceramics were obtained from a homemade x-ray luminescence system endowed with an Ocean Optics branded highly sensitive QE Pro-model spectrometer. RL emissions were collected by using a back-thinned CCD detector, while pellets were exposed to X-rays with ~20 kV voltage.

4.7.3.1. Basic TL and OSL Signals

In this study, after the synthesis of BeO:Na,Tb,Gd material and producing pellets, TL and OSL signals of the ceramics were obtained to see whether the luminescence signals have convenient common curves or not. The typical OSL and TL curves of BeO:Na,Tb,Gd ceramic pellets recorded after 0.2 Gy beta dose are shown as an example in Figure 4.70.

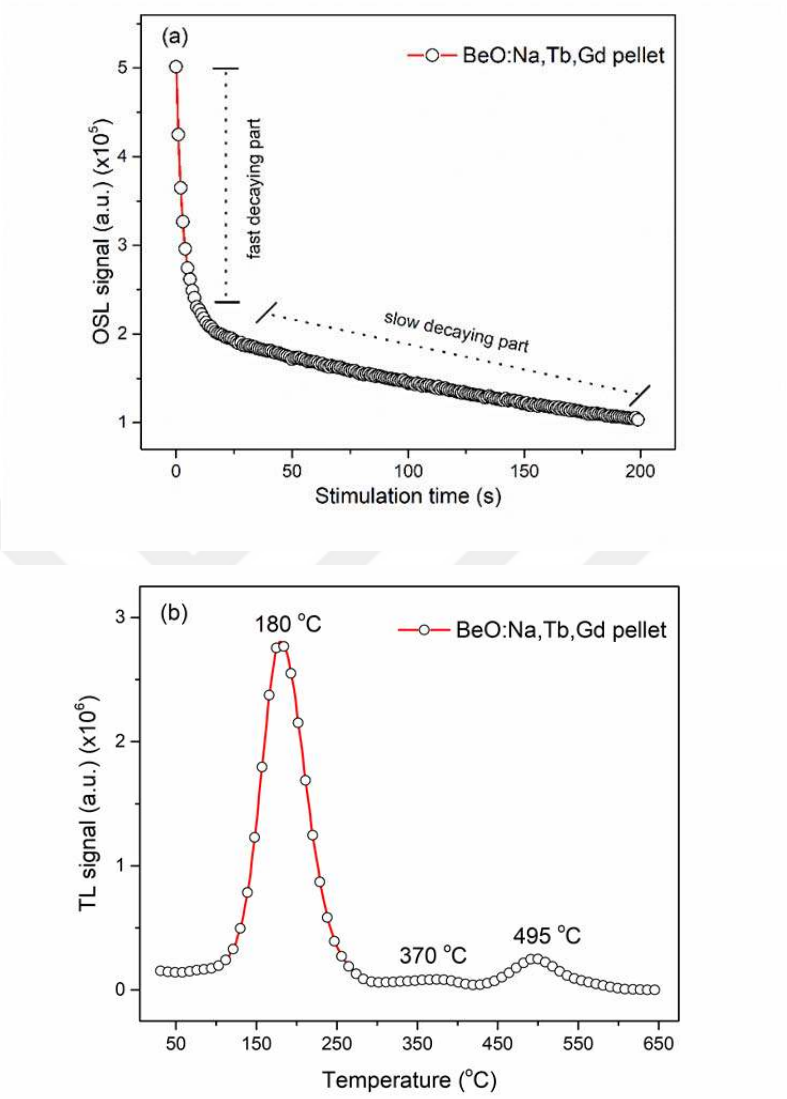

Figure 4.70. (a) OSL and (b) TL signals from BeO:Na,Tb,Gd ceramic pellet. In all measurements, the Hoya U-340 filter was used. Each curve is the average of three pellets. HT was 3 °C/s.

As is seen from Figure 4.70a, the OSL decay curve is the combination of the fast and slow decaying parts. OSL signals are reached zero levels (background signal level) after at least 200 s. The presented data in Figure 4.70b shows that the TL glow curve of the BeO:Na,Tb,Gd ceramic pellet occurs from a 180 °C peak high sensitive to ionizing radiation, a low sensitive 370 °C peak and a high-temperature peak located 495 °C. The OSL and TL intensities of BeO:Na,Tb,Gd are found to be high and sufficient for dosimetry applications. Of course, the signals of the produced ceramics vary from synthesis batch to batch. Therefore, to increase the reliability of the experiments under laboratory conditions, newly produced samples were used in each experiment.

4.7.3.2. Effect of Dopant Elements on TL and OSL Signals

In order to investigate the effect of dopant on luminescence signals of BeO, OSL and TL signals were obtained from the different dopants, namely, undoped BeO, BeO:$Na_{10\%}$, BeO:$Tb_{0.005\%}$, BeO:$Gd_{0.01\%}$, BeO:$Na_{10\%}$,$Tb_{0.005\%}$, BeO:$Na_{10\%}$,$Gd_{0.01\%}$, BeO:$Tb_{0.005\%}$,$Gd_{0.01\%}$, and BeO:$Na_{10\%}$,$Tb_{0.005\%}$,$Gd_{0.01\%}$, and presented in Figure 4.71. While the combination Tb and Gd give the high OSL signals in Figure 4.71a, TL signals were found to be lower than the signals of other doped BeO ceramic pellets. As is seen from Figure 4.71a, Na co-doping increases both OSL and TL signals obtained from BeO:Tb,Gd at least 2 times. On the other hand, it can be concluded that all the dopants did not cause any significant changes in the characteristic TL glow curve of undoped BeO (see Figure 4.71b).

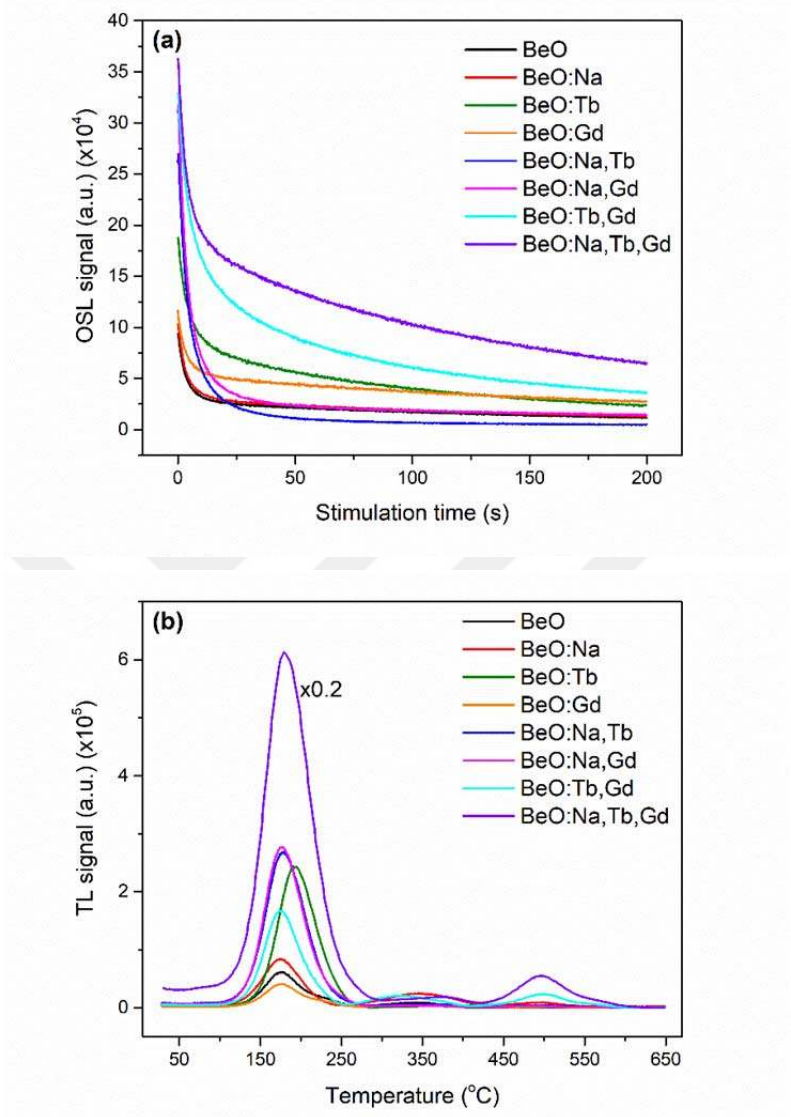

Figure 4.71. (a) OSL curves, (b) TL glow curves of BeO:$Na_{10\%}$, BeO:$Tb_{0.005\%}$, BeO:$Gd_{0.01\%}$, BeO: BeO:$Na_{10\%}$,$Tb_{0.005\%}$, BeO:$Na_{10\%}$,$Gd_{0.01\%}$, BeO:$Tb_{0.005\%}$,$Gd_{0.01\%}$, and BeO:$Na_{10\%}$,$Tb_{0.005\%}$,$Gd_{0.01\%}$ ceramics.

4.7.3.3. Concentration Quenching Study

To examine the effect of dopant concentration on OSL signals of BeO, OSL measurements of BeO with various Na, Tb, and Gd concentrations were performed using 200s blue light stimulation after 0.2 Gy beta irradiation. Figure 4.72 shows the changes in OSL signal intensities of BeO:Na,Tb,Gd samples prepared with different concentrations. The error bars represent the experimental standard deviations related to three pellets from the same batch. First, we fixed Na and Gd concentrations as 0.1 % and 0.001 %, respectively and changed the Tb concentration. As is seen from the black curve in Figure 4.72, the highest OSL intensity of BeO:Na,Tb,Gd was obtained with the Tb concentration of 0.005 %. Then, OSL signals of BeO:$Na_{x\%}$,$Tb_{0.005\%}$,$Gd_{0.01\%}$, were illustrated according to Na 0.05, 0.1, 0.3, 0.5, 1, 3, 5, 6, 8, 10 and 12 % concentrations (the red curve in Figure 4.72). A doping percentage of Na 10 % which gave the maximum OSL intensity was chosen for the Na concentration of the material. Finally, OSL signals of BeO:$Na_{10\%}$,$Gd_{x\%}$,$Tb_{0.005\%}$, were examined according to various Gd concentrations (the blue curve in Figure 4.72). The OSL signals with the maximum intensities were obtained from the combination of BeO:$Na_{10\%}$,$Tb_{0.005\%}$,$Gd_{0.01\%}$. For this reason, the doping percentage of Gd was chosen as 0.01 %.

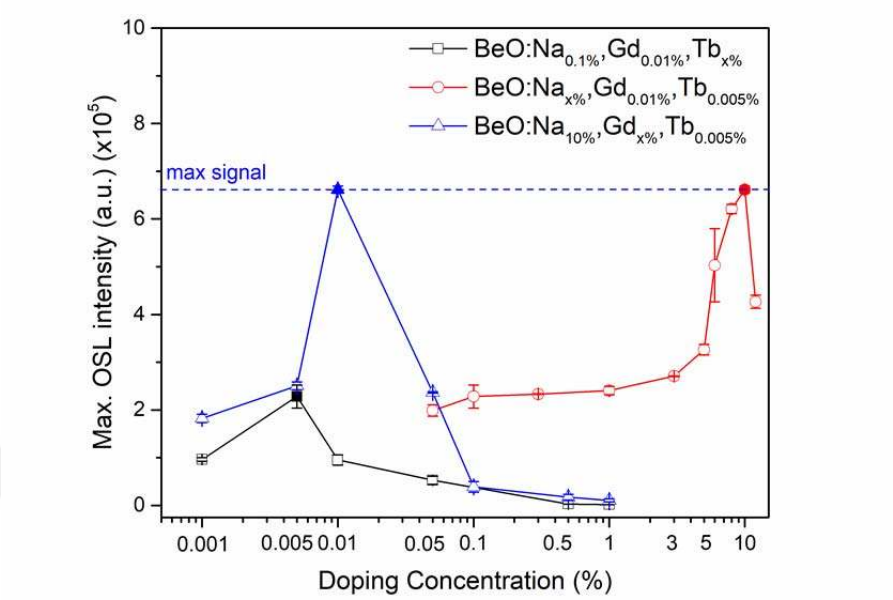

Figure 4.72. The changing in OSL signals of BeO:Na,Tb,Gd ceramic pellets prepared with different doping concentrations

4.7.3.4. RL Emissions

Investigation of RL characteristics is a good starting point for knowledge of the positions and general appearance of the luminescence bands. In this work, RL spectra were obtained from the different dopants, namely, undoped BeO, BeO:$Na_{10\%}$, BeO:$Tb_{0.005\%}$, BeO:$Gd_{0.01\%}$, BeO: BeO:$Na_{10\%}$,$Tb_{0.005\%}$, BeO:$Na_{10\%}$,$Gd_{0.01\%}$, BeO:$Tb_{0.005\%}$,$Gd_{0.01\%}$, and BeO:$Na_{10\%}$,$Tb_{0.005\%}$,$Gd_{0.01\%}$, using a 1 nm resolution at RT and presented in Figure 4.73. The RL spectra of all BeO ceramic pellets demonstrated the same wide emission peak located between 200 and ~450 nm with the maximum at 250 nm (photon energies of ~4.9 eV). This dominant luminescence band located at 4.9 eV is observed with the radiative annihilation of self-trapped emerging with X-ray irradiation (Altunal et al., 2019a; Altunal et al., 2019b; Ogorodnikov and Kruzhalov, 1997; Ogorodnikov et al., 1995). It is known that the luminescence band in BeO is characterized by 3–4 eV

and 4.9 eV two emission bands (Ogorodnikov and Kruzhalov, 1997). The 4.9 eV emission band is not close to the conventional PMT spectral range and Hoya U-340 filter transmittance range. However, even though the transmittance range used was very suitable for the OSL measurements, only a 3-4 eV emission band was observed.

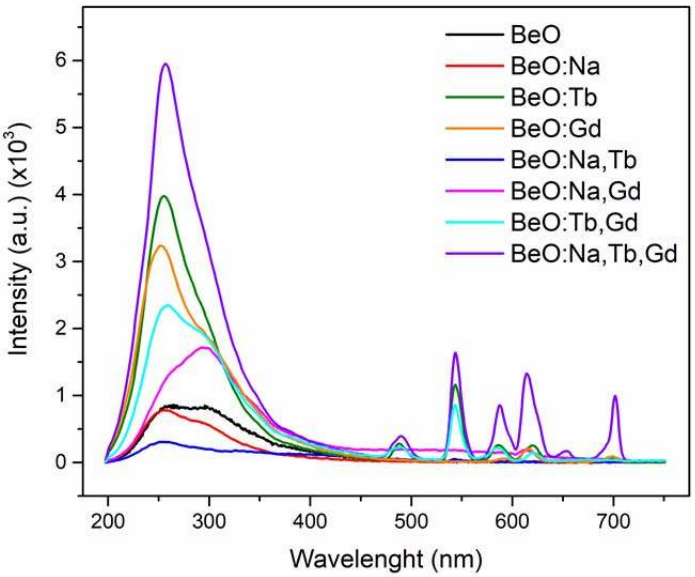

Figure 4.73. The changing in RL spectra of systematically doped BeO ceramic pellets

While the RL spectrum of BeO singly doped with Na was not significantly different than the RL spectrum of the undoped BeO, for the sample singly doped with Tb, at least six peaks in the visible region and remarkable increases in intensity were observed in RL spectra. It can be said that these visible range emission peaks are due to the $^5D_4 - {}^7F_j$ $(j = 6-0)$ characteristic transitions of Tb^{3+} with the emission bands, 490, 540, 580, 620 nm, 650, 660 and 675 nm (Bünzli and Eliseeva, 2010). From the RL spectra of BeO samples doped with Gd, it is seen that another peak with a maximum of about 300 nm occurred as a neck to the right of the 250 nm broad emission peak of pure BeO. This 300 nm RL emission is

likely to be attributed to the ${}^{6}P_{7/2} - {}^{8}S_{7/2}$ transition of Gd^{3+} (Bünzli and Eliseeva, 2010), thus luminescent intensity enhanced in the UV region. In addition, a sample with high UV region sensitivity and visible region emissions was obtained at the end of the double and triple dopants.

4.7.3.5. Analysis of OSL Decay Curve

The analysis of the aforementioned OSL decay curve is a very important starting point to recognize the product in OSL dosimetry and figure out how the luminescence mechanism takes place. OSL decay curve of a 0.2 Gy previously irradiated BeO:Na,Tb,Gd pellet was studied by fitting to the linear integration of two time decaying functions and presented in Figure 4.74. The fitting technique is realized with a general kinetic approach of a luminescence decay curve, and it was also used for a phosphorescence decay (Chen and McKeever, 1997), prompt isothermal decay curves of MgB4O7:Dy,Na (Kitis et al., 2016), CW-OSL decay curves from the undoped BeO samples produced at different sintering temperatures (Altunal et al., 2019b), CW-OSL decay curves for undoped and doped BeO samples (Altunal et al., 2019a). The model equation for this fitting was presented above as Equation (4.1).

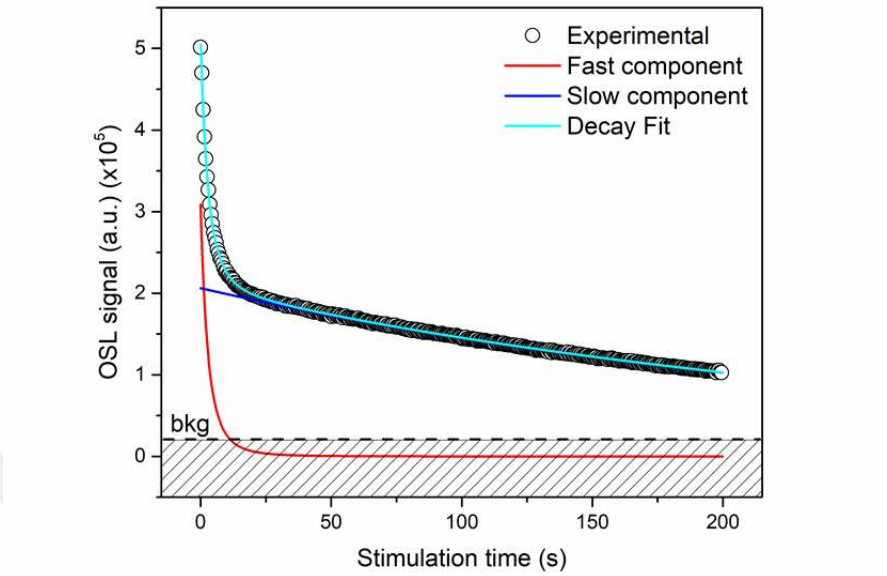

Figure 4.74. Experimental OSL signals and the resultant components from the curve fitting for BeO:Na,Tb,Gd ceramic pellets.

Considering Equation (4.1), the curve fitting process was continued using different parameters ($I_{1,2}$ amplitudes, $\tau_{1,2}$ decay times, $b_{1,2}$ kinetic orders) until the smallest figure of merit (FOM) value was obtained. All parameters obtained as a result of the curve fitting and the final FOM value were presented in Table 4.15. It should be noted that this OSL decay curve fitting to such a function is only an oversimplified approximation of the real luminescence mechanism. To discover the charge of trafficking, more studies are necessary on this.

Table 4.15. $\tau_{1,2,3}$ decay times and $b_{1,2,3}$ kinetic orders from the curve fitting for a BeO:Na,Tb,Gd ceramic pellet.

	S_1 (fast component)			***S_2 (slow component)***				
	I_1 (count)	τ_1(s)	b_1	I_2 (count)	τ_2(s)	b_2	*bkg* (count)	*FOM* (%)
BeO:Na,Tb,Gd	3.1E+05	3.9	1.40	2.7E+05	296.7	1.05	2.86E+02	0.37

4.7.3.6. TL and OSL Signals Correlation

To determine which part of the TL glow curve from BeO:Na,Tb,Gd ceramic pellets is optically active or not, the TL glow curves (direct TL and residual TL) were measured by heating the 0.5 Gy irradiated sample from RT up to 650 °C at 3 °C/s (HT). While the direct TL curve was obtained following the irradiation without any OSL measurement, the residual TL curve was obtained following the irradiation after an OSL measurement. Figure 4.75 represents direct and residual TL curves with the bleached TL curve which is a resultant curve obtained by subtracting the residual TL from the direct TL. The bleached TL curve for the BeO:Na,Tb,Gd ceramic corresponds to the optically active parts in the TL glow curve. It is seen from Figure 4.75, the 1st peak of the TL curve of BeO:Na,Tb,Gd ceramic was extremely affected by optical stimulation whereas the 2nd and 3rd peaks were not. This remarkable light effect can provide us to have evidence that the OSL signal might be originated from the 180 °C TL peak.

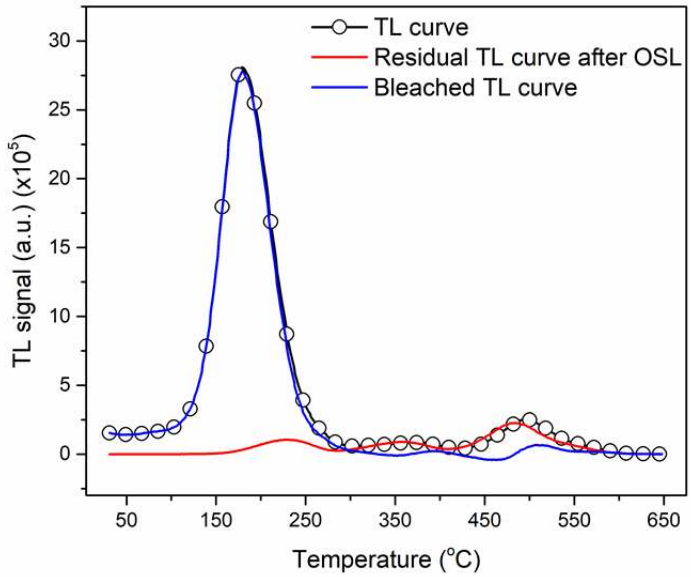

Figure 4.75. TL, residual TL, and bleached TL curves of the 0.5 Gy irradiated BeO:Na,Tb,Gd ceramic pellet.

To investigate whether there is any correlation between the light-affected TL peak and the source of the OSL signal for the BeO:Na,Tb,Gd ceramic pellet, the step-annealing experiment (named as thermal stability) were carried out in the preheating temperature range from 50 to 500 °C in 10 °C steps, 5 °C/s (HT). For this purpose, the 0.5 Gy irradiated BeO:Na,Tb,Gd pellet was continuously annealed, and the residual OSL signal was recorded each time. The stimulation time of the readouts and duration time of the step annealing treatments were 200 s and 10 s, respectively. At the end of each cycle, the sample was deleted using TL readout up to 650 °C following the OSL readout. The variations of the integrated OSL signals versus the annealing temperatures were plotted together with the bleached TL curve for BeO:Na,Tb,Gd ceramic in Figure 4.76. As in Figure 4.76, the first decrease in OSL signals starting after 130 °C annealing temperature, is responsible for discharging of the 180 °C TL peak after the OSL stimulation. After stable OSL signals up to 330 °C in the step-annealing curve, OSL signals faced a

second decrease. With the discharging of 370 °C TL peak, the OSL signals reach the background value. It demonstrates that the OSL signals may be originated from both the 180 and 370 °C TL peaks. OSL may be using the same recombination centers as the 180 and 370 °C TL peaks. Similar results were presented for undoped and doped BeO ceramic pellets (Altunal et al., 2019a; Altunal et al., 2019b; Altunal et al., 2018).

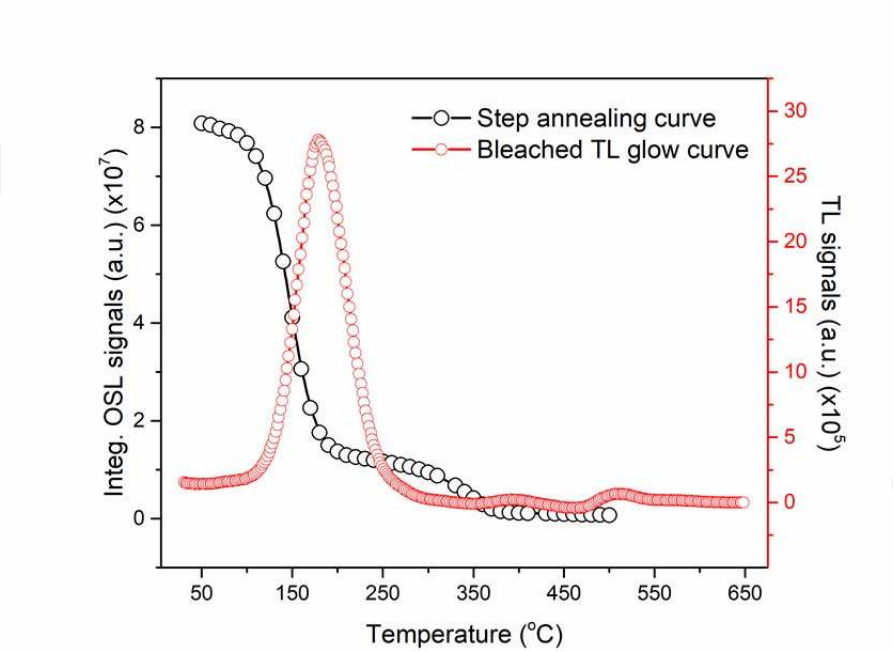

Figure 4.76. Step annealing and bleached TL glow curves of OSL signals from 0.5 Gy irradiated BeO:Na,Tb,Gd ceramic pellet

4.7.3.7. Temperature Dependency of OSL Signals

Temperature dependence of the OSL signals (known as thermal quenching) is a reduction in luminescence outputs observed in many materials at temperatures higher than RT. According to the Mott-Seitz model, it can be physically explained as the increase in the probability of non-radiative transitions from the excited to the ground state of the luminescence centers (Bøtter-Jensen et al., 2003). The equation of temperature dependence for the OSL signal was given above as Equation (4.2).

The study of the temperature dependence of OSL signals from the BeO:Na,Tb,Gd ceramic pellet was investigated to obtain have an idea about the probability of non-radiative transitions. After the 0.5 Gy beta radiation and 110 °C preheating for 10 s, OSL signals were obtained at reading temperatures ranging from 50 to 115 °C in 5 °C steps and presented in Figure 4.77 (static case). At the end of each OSL measurement, residual signals were depleted by heating the samples to 650 °C via TL readout. The samples were exposed to the same dose for the next measurement. In Figure 4.77, the integrated OSL signals obtained at 110 °C decreased by 25 % when compared with that of OSL signals obtained at the first reading temperature, 50 °C. The presence of strong thermal quenching due to this reduction in OSL signals with increasing readout temperature can be mentioned.

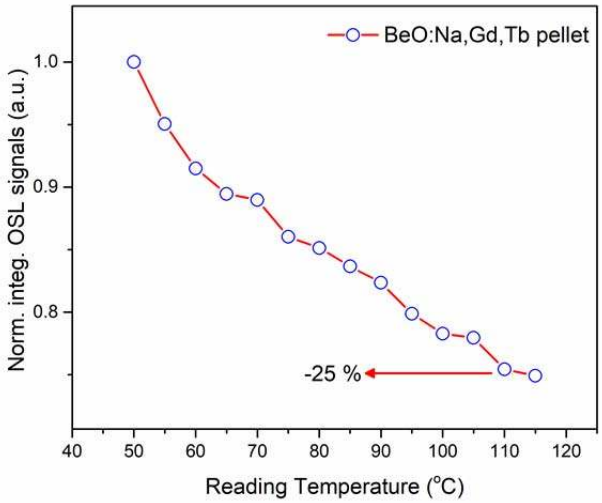

Figure 4.77. Integrated OSL signals of the BeO:Na,Tb,Gd ceramic pellet at various reading temperatures after 0.5 Gy beta doses and 110 °C preheating for 10 s

On the other hand, to have a deeper understanding of the thermal quenching mechanism for BeO: Na, Tb, Gd ceramics, a TOSL curve which indicates the temperature dependence of the OSL signal, can be examined as

another method. TOSL is a resultant curve obtained by subtracting the TL curves with and without OSL stimulation. This technique was reported in the literature for BeO chips (Thermalox995) (Bulur and Goksu, 1998) and undoped and doped BeO ceramic pellets (Altunal et al., 2019a; Altunal et al., 2019b). We applied this technique using 0.1 s pulsed light stimulation with 0.9 s time interval between the pulses while TL readout (dynamic case). Luminescence signals recorded during the 0.1 s pulsed light stimulation period are the combinations of the OSL and TL (i.e. TL+OSL). On the other hand, luminescent signals during the 0.9 s time interval between the pulses provide us the TL signals (TL). The difference between these TL+OSL and TL signals gives the TOSL signals representing the temperature dependence of the OSL signals. Figure 4.78 shows TL+OSL, TL and TOSL curves for the BeO:Na,Tb,Gd.

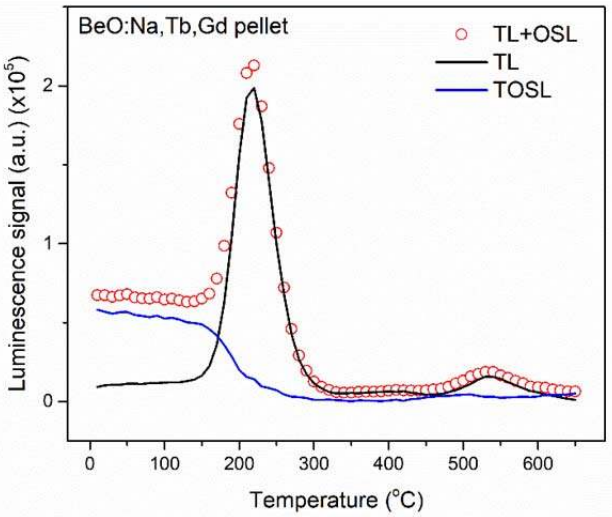

Figure 4.78. The TL, TL+OSL and TOSL curves from 0.5 Gy irradiated BeO:Na,Tb,Gd ceramic pellet.

In Figure 4.78, as is seen from the TOSL curve, the OSL outputs have two decreased curves. The first decrease is up to 150 °C and the second one begins at 150 °C and reaches zero levels at 250 °C. It can be made inferences that the first

slow decrease may be related to the strong thermal quenching, and the second decrease may be associated with the emptying of traps responsible for the 180 °C dosimetric peaks. The thermal quenching energy for the BeO:Na,Tb,Gd pellet was evaluated by using the OSL data recorded at various readout temperatures in a static case (Figure 4.77) and by fitting them into Equation (4.2. On the other hand, we also evaluated thermal quenching energy value by using the reduction data from the initial parts of the TOSL curve in the dynamic case (Figure 4.78) and by fitting them into Equation (4.3). The fitting curves and the evaluated E_Q values (0.52 and 0.55 eV) using both methods were presented in Figure 4.79, which plot the normalized OSL signal intensity as a function of temperature. These evaluated E_Q values for two methods are almost the same as previously presented thermal quenching values for a different form of the BeO ceramics (Altunal et al., 2019a; Altunal et al., 2019b; Bulur and Goksu, 1998; Yukihara, 2011).

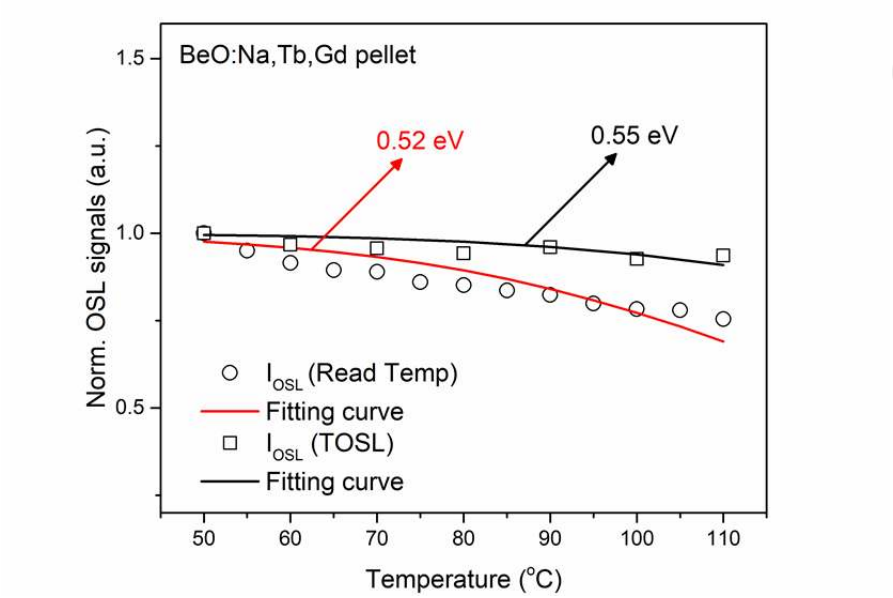

Figure 4.79. Calculation of the thermal quenching energy using the reduction data from the initial parts of the TOSL curve in the dynamic case and the OSL data obtained at various readout temperatures in the static case (from 50 °C to 150 °C)

4.7.4. Dosimetric Characteristics

4.7.4.1. Reusable OSL Signals

In dosimetric applications, the OSL dosimeters should be reusable, i.e., the dosimeters should give the same OSL signals after the same irradiations under carefully checked conditions. The reusability property was investigated for three BeO:Na,Tb,Gd ceramic pellets. Experimental treatments started with irradiation of the samples at a dose of 0.5 Gy, following the preheating process at 110 °C for 10 s. OSL signals were obtained by using 200 s blue light stimulations. At the end of each OSL readout, the residual OSL signals were depleted by heating the samples to 650 °C via TL readout. Measurement cycles were repeated 20 times under the same conditions and inter-cycle deviations were calculated. In Figure 4.80, the integrated OSL signals normalized to the first cycle were plotted against the experimental cycle. The error bars represent the experimental standard deviations of mean values obtained from three pellets in each cycle. As is seen from Figure 4.80, all samples gave the same OSL responses under the same and repeated laboratory conditions. Very good reusability over thirty cycles was observed and the deviation from the first readout value was evaluated as a maximum of ~3%.

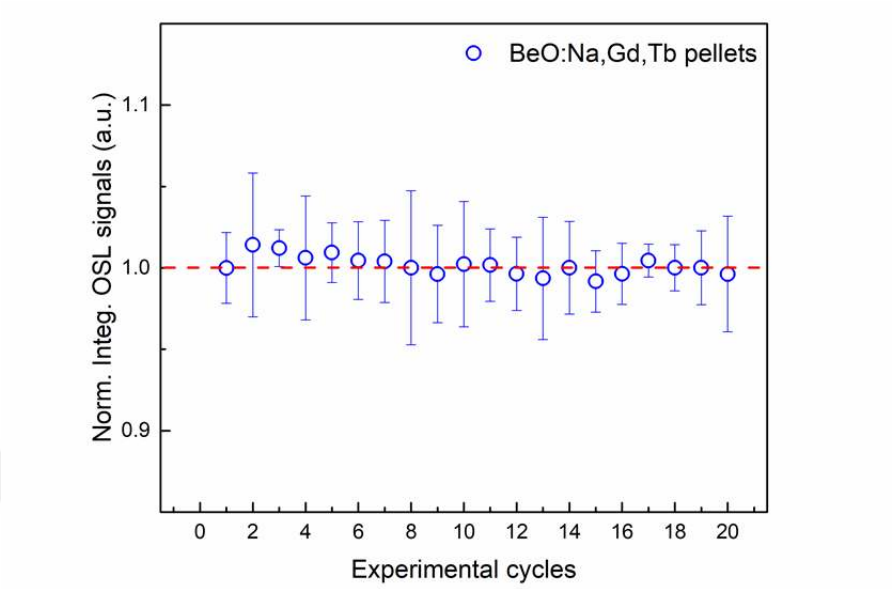

Figure 4.80. The reusability characteristics of OSL signals of BeO:Na,Tb,Gd ceramic pellets. After irradiation of 0.5 Gy beta dose and preheating of 110 °C for 10 s, OSL signals were recorded with 200 s optical stimulations.

4.7.4.2. Linear Dose-Response

It is extremely important to determine the range in which the dose-response is linear. Because knowing the range where the dose-response is linear is one of the most important parameters determining the application area of the dosimeter. For this purpose, the dose linearity of the OSL signals from BeO:Na,Tb,Gd pellets were studied in the dose range between 0.1 Gy (the minimum applicable dose value of TL/OSL readout system) and 100 Gy. Three BeO:Na,Tb,Gd ceramic pellets were irradiated 0.1, 0.2, 0.5, 1, 2, 5, 10, 20, 50 and 100 Gy beta test doses in repeated experimental conditions. After the irradiated samples were preheated at 110 °C for 10 s, OSL measurements were performed using 200 s blue light stimulations. At the end of the OSL measurements, residual signals were deleted by heating the samples to 650 °C via TL readout. The plots of integrated OSL signals versus the absorbed dose were shown in Figure 4.81. The error bars represent the

experimental standard deviations of mean values obtained from three pellets in each applied dose. From the linear fitting and considering the slope value, the BeO:Na,Tb,Gd ceramic pellets had a linear dose-response with the 1.02 slope value between 0.1 and 100 Gy (see Figure 4.81). With the linear fitting, evaluated fit parameters such as slope, intercept, etc. were presented in the inset table of Figure 4.81.

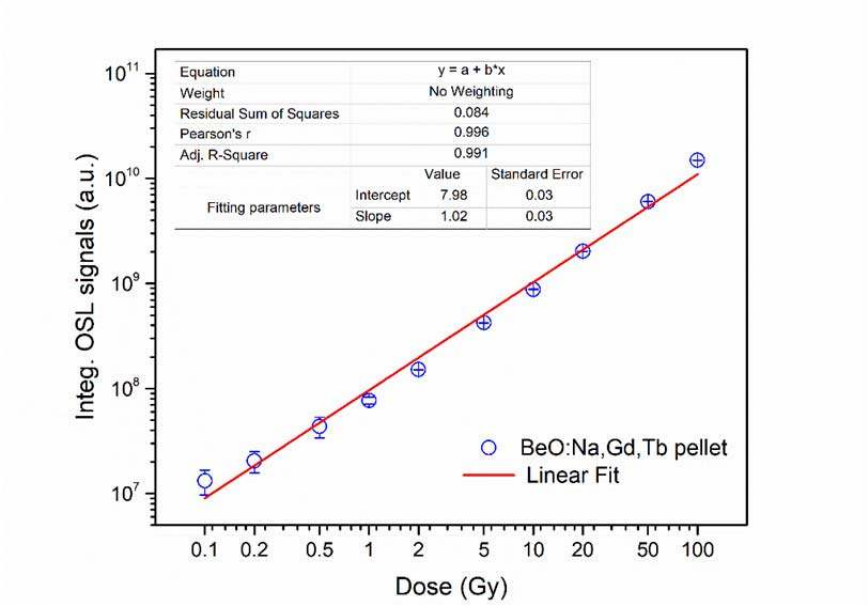

Figure 4.81. The integrated OSL signals from BeO:Na,Tb,Gd ceramic pellets with the beta dose range from 0.1 to 100 Gy.

4.7.4.3. Almost No Fading

As a desirable property for all dosimetry applications, the number of trapped charges must be stable (not fade) at RT. To investigate whether the charge population in traps is stable or not, after irradiation with 0.5 Gy beta dose, fading characteristics of BeO:Na,Tb,Gd ceramic pellets were tested by keeping three calibrated pellets in dark at RT. The fading feature of the pellets was investigated for different time intervals for one month. The first readout started after half an hour from the irradiation (see Figure 4.82).

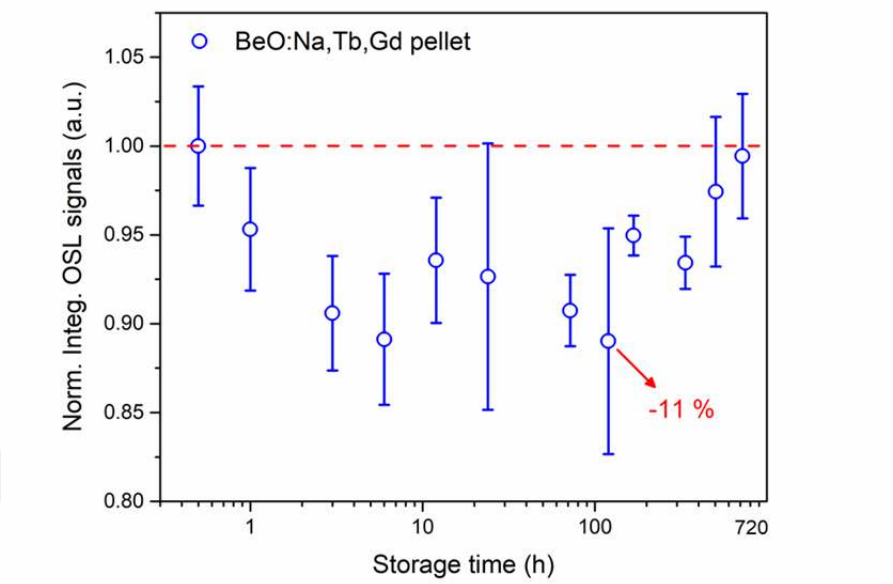

Figure 4.82. Fading characteristic of the OSL signals versus the storage time up to 1 month for the BeO:Na,Tb,Gd ceramic pellets after 0.5 Gy beta radiation.

The first decrease in the integrated OSL signal was observed as ~11% at the end of 1 h. While the following fall in the signals at the end of the 6 h could be associated with escaping of the unstable electrons from the shallow traps at RT (Guckan et al., 2017; Ozdemir et al., 2018; Yukihara et al., 2017), the unexpected increase in luminescent signals with storage time during 12 h period might be responsible for the transition of the charges from the shallow traps to deep traps (Nambi, 1977; Ozdemir et al., 2016). Additionally, the OSL signals from the BeO:Na,Tb,Gd pellets were very stable up to 1 week and slightly decreased (~10%) up to two weeks when compared with the OSL signals obtained at the first readout. At the end of the one month, the fading of the OSL signals was found to be negligible i.e. almost the same value as the first readout. With these values, BeO:Na,Tb,Gd ceramic pellets can be used in environmental and personal dosimetry, which does not pay attention to short-time fading. These results are

consistent with the results of previously studied different BeO ceramics forms (Altunal et al., 2019a; Altunal et al., 2019b; Sommer et al., 2007).

4.7.5. Discussion

To determine the effect of lanthanide (Ln) on the BeO lattice and how the luminescence mechanism exists, a simplified luminescence process is required rather than a complex luminescence process that exists. It is possible to say that lanthanides in BeO lattice should establish local levels in the forbidden band and show themselves actively in recombination processes. The difference of ionic radius between Na^{2+} (1.16 Å), Tb^{3+} (1.06 Å), Gd^{3+} (1.07 Å) and Be^{2+} (0.59 Å) would cause lattice constant decrease and thus produces a lattice distortion in the BeO structure. Due to the remarkable differences between the ionic radius of Ln^{3+} and Be^{2+}, the Ln^{3+} ion may be inclined to settle into crystalline vacancies instead of replacing the Be^{2+} ion. Even if Ln^{3+} acts as an interstitial defect, it would create a similar distortion to the structural distortion observed in the substitutional defects. On the other hand, when the lattice changes by doping, the crystalline field energy must have a distortion. In such a case, it can be expected that even a small distortion leads to any increase or decrease in luminescence efficiency.

It is possible to say that the luminescence mechanism of Ln-doped BeO can be interpreted more than the simplest luminescence type (one trap-one recombination center, OTOR model). Tb and Gd in divalent states are usually located inside or below the conduction band, which means that Tb^{3+} and Gd^{3+} cannot act as electron traps due to the electron would be immediately released into the conduction band (Dorenbos, 2003; Dorenbos and Bos, 2008; Milliken et al., 2012; Yukihara et al., 2014). On the other hand, considering the required energy to add and remove an electron to or from a lanthanide, while Gd^{3+} cannot trap a hole, Tb^{3+} acts as a deep trap (Dorenbos and Bos, 2008; Milliken et al., 2012; Yukihara et al., 2014). But Gd^{3+} on the somewhat smaller Be^{2+} site causes a lattice distortion. Such distortion that may occur in this way, may stabilize a hole from the valence

band (Dorenbos and Bos, 2008). In this work, the luminescence process simply begins by exposing the crystal to ionizing radiation and then creating charge carriers, i.e., electrons and holes moving freely inside the crystal. The trivalent substitution impurity (Tb^{3+}) may act as a hole trap and become a quadrivalent ion (Tb^{4+}) during delivering irradiation. On stimulation with heat or light, trapped electrons are released from the electron traps, and Tb^{3+} ion in excited states occurs with recombination of the released electrons with Tb^{4+} ion. With the relaxation processes of Tb^{3+} ion, observable luminescence emission is achieved. This proposed process is summarized in Figure 4.83. Similar luminescence mechanisms and lanthanide behaviors were demonstrated in several materials (Altunal et al., 2019a; Oliveira et al., 2019; Oliveira et al., 2016; Yukihara et al., 2013).

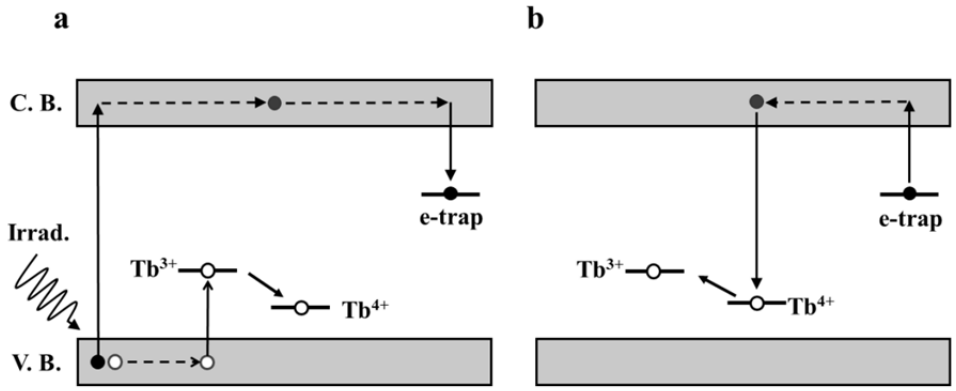

Figure 4.83. Proposed luminescence mechanism: (a) During irradiation, creating electron and holes, and electron- and hole (Ln^{3+})- trapping, (Ln^{3+} + $h^{+}\rightarrow$ Ln^{4+}). (b) During thermal or optical stimulation, releasing electrons from the traps. Ln^{3+} in an excited state occurs with the recombination with Ln^{4+} ions. Luminescence occurs with the relaxation of Ln^{3+}. Solid and open circles represent electrons and holes, respectively.

Regarding the role of Na dopant in BeO, it is clear to say that a negative effective charge defect $(Na_{Be})^{-}$ occurs with the Na^{+} substituting for Be^{2+}. This negative charge defect may compensate for the positive effective charge defect

$(Ln_{Be})^{+}$ occurring with the Ln^{3+} substituting for Be^{2+}. Similar co-dopant behavior was represented for Li^{+} ion (Oliveira et al., 2016; Yukihara et al., 2013). Considering this compensation effect, differences in ionic radius and changing crystal field energy may cause a significant increase in luminescence signals. More detailed studies on BeO:Na,Tb,Gd ceramic pellets are necessary to confirm the proposed luminescence mechanism.

4.8. BeO:Na,Dy,Er Ceramics

This study includes advancing the material synthesis method that made it possible to produce the OSL material with desired dosimetric and luminescence properties. In this study, we successfully synthesized BeO by doping with La, Ce, Pr, Nd, Sm, Eu, Gd, Tb, Dy, Er lanthanides and Mg, Al, Ca, Li, Na transition metal ions in different concentrations and combinations using the precipitation synthesis method. Further development of BeO samples and their characterization by doping Na^{+}, $Dy^{3+,}$ and Er^{3+} provided the highest luminescence efficiency. As a result of this data mentioned, the research was expanded into studies of the main dosimetric and luminescence properties of BeO:$Na_{5\%}$,$Dy_{0.1\%}$,$Er_{0.05\%}$. Morphological and structural characterizations were analyzed by Scanning Electron Microscope (SEM), Energy Dispersive X-Ray (EDS), and X-ray Diffraction (XRD) methods. Luminescence of the material was characterized using TL, OSL, and X-ray luminescence (XL) techniques. We performed the investigations on correlations between TL curves and OSL signals, dose-response, reusability and fading properties of OSL signals of the samples for personal and medical dosimetry applications.

4.8.1. Synthesis of Material

BeO samples were synthesized by co-precipitation technique using Beryllium sulfate tetrahydrate ($BeSO_4 \cdot 4H_2O$, ≥99.0%, Sigma Aldrich) salts, Poly(ethyleneimine) solution (50% (w/v) in H_2O, Sigma Aldrich) and Ammonium

hydroxide solution (H_5NO, ACS reagent, 28.0-30.0% NH_3 basis, Sigma Aldrich). BeO samples were doped using Sodium nitrate ($NaNO_3$ ≥99.0%, Sigma Aldrich), Dysprosium (III) nitrate hydrate ($Dy(NO_3)_3 \cdot xH_2O$ ≥99.9%, Sigma Aldrich) and Erbium (III) nitrate pentahydrate ($Er(NO_3)_3 \cdot 5H_2O$ ≥99.9%, Sigma Aldrich). Doping with 5% of Na and a small percentage of Lanthanides were intentionally chosen to enhance the OSL sensitivity and avoid increasing Z_{eff} of the material (Z_{eff}=7.31). The general co-precipitation synthesis procedure has been performed earlier and was reported by Altunal et al. (Altunal et al., 2019b). We used the nominal composition of the BeO samples as BeO:$Na_{5\%}$,$Dy_{0.1\%}$,$Er_{0.05\%}$ enhancing the material's OSL sensitivity. Calcination, a thermal process used to synthesize or prepare ceramic powders before dispersion or shaping was carried out in an ash furnace (Nabartherm, model P330) within the atmosphere, at 800 °C for 4 h. The phase composition, particle size and aggregation of ceramic powders are determined primarily during the calcination process. A highly calcined powder will have a low specific surface area, a large crystallite size, will require a very high sintering temperature, and will have low drying and firing shrinkage. In this study, 25 mg pellets were prepared using a manual hydraulic press (Carver, model 3853-9) without adding any binding material. The applied pressure was 250 kg-force/cm^2 for 1 min. After the palletization process, the prepared pellets in disk form were sintered in a high-temperature furnace (Thermoscientific, model Lindberg/Blue M™) within the atmosphere (Altunal et al., 2019b).

The variation of shrinkage in diameter and thickness was observed against high sintering temperature (1600 °C) for sintered pellets. The shrinkage was found to decrease from 6.15 to 5.05 mm in diameter and from 0.82 to 0.54 mm in thickness. After the 1600 °C sintering of the pellets, the weight losses were also observed in the studied BeO pellets. The measured weights were ~ 23 ± 0.2 mg.

Handling beryllium oxide ceramics in solid form (chips, rods, discs, etc.) poses no special health risk. Inhalation of airborne beryllium may cause a serious lung disorder in susceptible individuals. We performed safety and environmental

efforts and followed the safe handling practices in our work with BeO. We used personal protective equipment such as gloves, dust and gas masks, goggles, etc. in the laboratory during the synthesis of this material.

4.8.2. Structural Characterization

BeO:Na,Dy,Er pellets were characterized using XRD, SEM and EDS analyses. XRD analysis was performed with Cu-Kα (40 kV, 30 mA) for the determination of crystallographic phases. The pattern was achieved from 10° to 90° (2θ) with 0.02° (2θ) increments. Phase identification was performed using the International Center for Diffraction Data (ICDD) PDF card 98-016-3468. To examine the surface morphology and grain sizes of the material, the SEM analyses were taken by FE-SEM, Zeiss, Supra 55 with the spectral slit width of 1.5 nm at room temperature. The images presented here were taken at 1000x direct magnification, 10 and 20 kV, and a spot size of 2.5. Using SEM micrographs, the sizes and the shapes of grains, as well as the number of grains can be obtained. EDS analysis was carried out by the same FE-SEM (Zeiss) to investigate elemental impurities formed in the structure during synthesis.

4.8.2.1. X-Ray Diffractions

To confirm the product and investigate crystalline phase composition, the diffraction data was collected in the step scanning mode throughout 10-90^{o} (2θ), using a step increment of 0.02° (2θ) and a count time of 1 sec/step. Analysis for phase composition was carried out by comparing the data for experimental specimens to that of reference spectra compiled by the International Centre for Diffraction Data (ICDD). In Figure 4.84, the X-ray diffraction spectrum was found to be well-matched with the main data of the BeO phase reported in the ICDD-PDF-card no 98-016-3468. The average crystallite sizes were calculated by the Debye-Scherer formula given above as Equation (4.4. The average crystallite size of the BeO:Na,Dy,Er sintered at 1600 °C was found as (325 ± 7) nm.

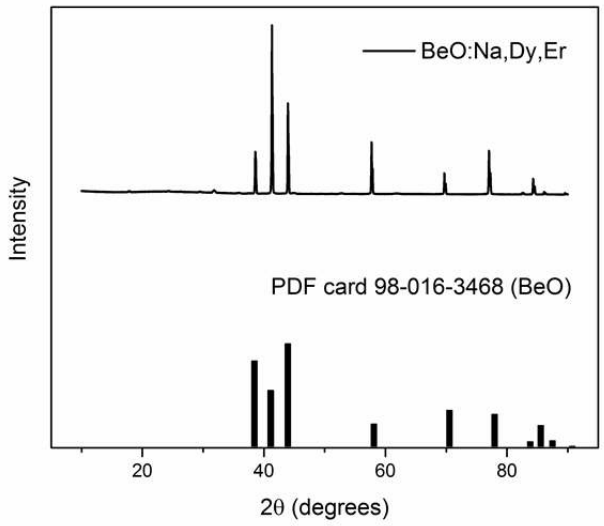

Figure 4.84. XRD patterns of BeO:Na,Dy,Er pellet with reference BeO (PDF card no 98-016-3468).

4.8.2.2. SEM Pictures

A micrograph of a BeO-ceramic sample with additives 5% Na, 0.1%Dy and 0.05%Er is shown in Figure 4.85a. The high-resolution SEM indicates the presence of no porosity (see Figure 4.85a). The SEM photomicrograph of pure BeO is shown in Figure 4.85b. The microstructure shows an average grain size of ~ 3 μm, besides, some of the grains grew up to ~ 10 μm. On the other hand, sintered BeO:Na,Dy,Er ceramics were found to have average grain sizes above ~ 25 μm. It was found that the rate of grain growth for the BeO sample containing Na, Dy and Er was qualitatively larger with less porosity than that of the pure BeO sample. The luminescence intensity of BeO:Na,Dy,Er ceramics sintered at 1600 °C were found to be higher than those obtained for pure BeO sintered at the same temperature. The growth of the grain sizes due to both the dopants and the sintering process lead to a reduction in the porous structures and more luminescence signals from a non-porous surface (see Fig. 3a).

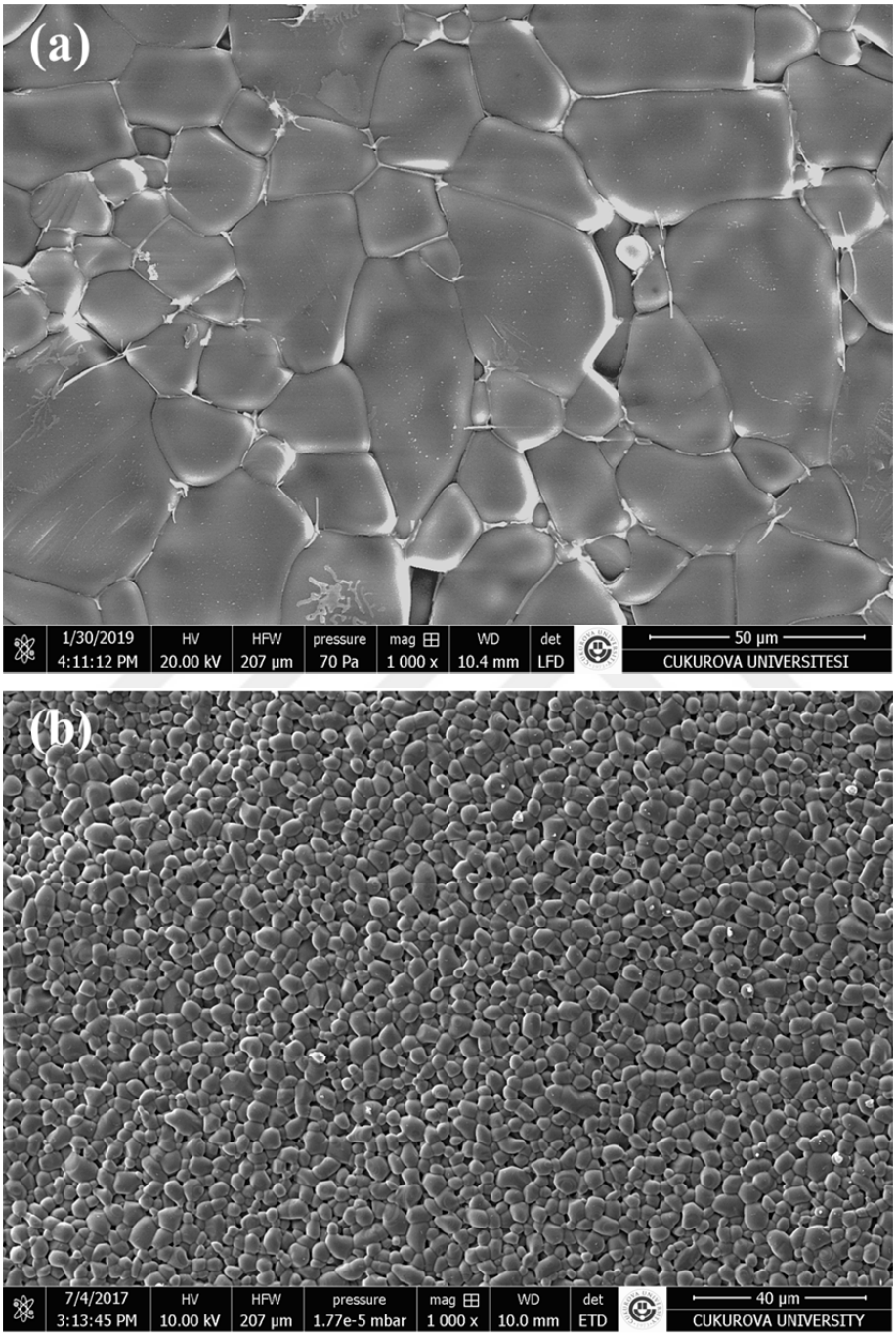

Figure 4.85. (a) SEM micrograph of BeO:Na,Dy,Er pellet, (b) SEM micrograph of pure BeO pellet.

4.8.2.3. EDS Analysis

In addition to the SEM micrograph, the EDS analysis was performed to investigate the existence of elemental impurities and indirectly confirm the accuracy of the specified dopants. As a result of this analysis, the presence of Oxygen (O), Sodium (Na), Dysprosium (Dy) and Erbium (Er) in the host structure was confirmed by EDS (see Figure 4.86). As can be seen from Figure 4.86, except for the peaks of Carbon (C), Platinum (Pt) and Gold (Au) coating elements, no impurity peaks were found in the EDS spectrum. Beryllium (Be) contents with an atomic number less than 5 are not observed in the EDS analysis due to the absorption of low-energy X-rays by the beryllium window in front of the detector.

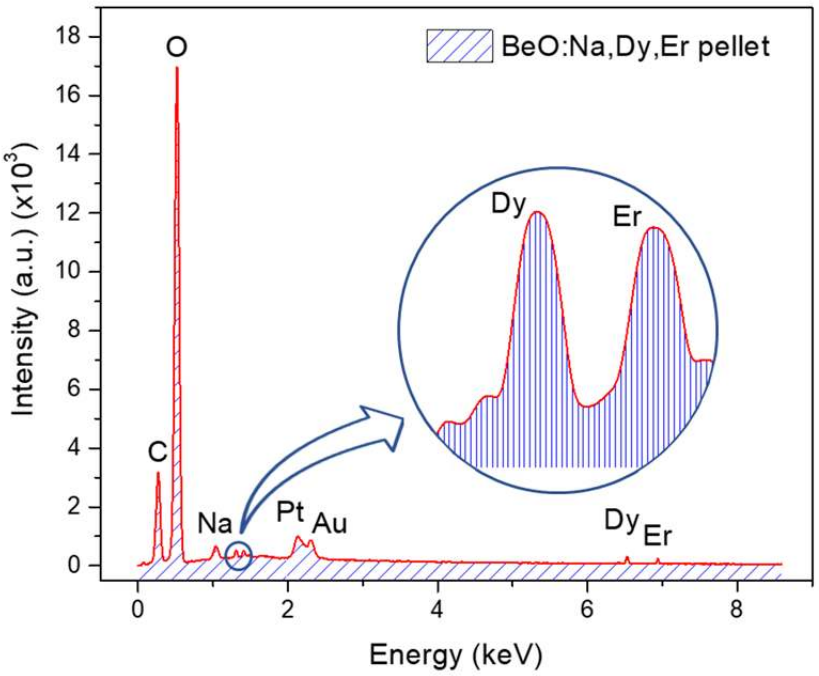

Figure 4.86. EDS spectrum of the BeO:Na,Dy,Er pellet.

4.8.3. Luminescence Characterization

OSL and TL measurements were performed using a Risø, DA-20 model TL/OSL reader system which has a $^{90}Sr/^{90}Y$ beta radiation source (2.27 MeV max. energy) and the dose rate of the radiation source is approximately 6.689 Gy/min. Continuous Wave (CW)-OSL stimulation mode was used with a light power of ~80 $mWcm^{-2}$. To detect emitted light from the samples and avoid scattered light, a UV bandpass detection filter, Hoya U-340 (7.5 mm thickness) was used in all measurements. The TL readouts were carried out by heating the samples from room temperature to a target temperature and using the heating rates of 2 °C/s and 5 °C/s within a nitrogen atmosphere.

The X-ray luminescence (XL) analyses of BeO:Na,Dy,Er pellets were performed using a homemade XL system equipped with a high-sensitivity spectrometer QE Pro, Ocean Optics. The Hamamatsu FFT-CCD detector coupled with the fiber-optic cable in the QE Pro provides 90 % quantum efficiency and offers significant improvement in the signal-to-noise ratio (>1000:1). This enables low-light-level detection and long integration times from 8 milliseconds to 15 minutes, with virtually no spectral distortion. In XL measurements, a mini X-ray tube with 20 kV energy was used for stimulating the pellets.

4.8.3.1. TL and OSL Signals

TL and OSL signals of the newly developed BeO:Na,Dy,Er pellets were examined to ensure the goodness of the material for this study. The typical TL and OSL curves which were obtained from a BeO:Na,Dy,Er pellet after exposure to 0.5 Gy beta dose are shown together with the TL and OSL curves obtained from a commercial OSL dosimeter, Thermalox 995 BeO chip, and a previously studied undoped BeO pellet (Altunal et al., 2019b) for the comparison (see Figure 4.87).

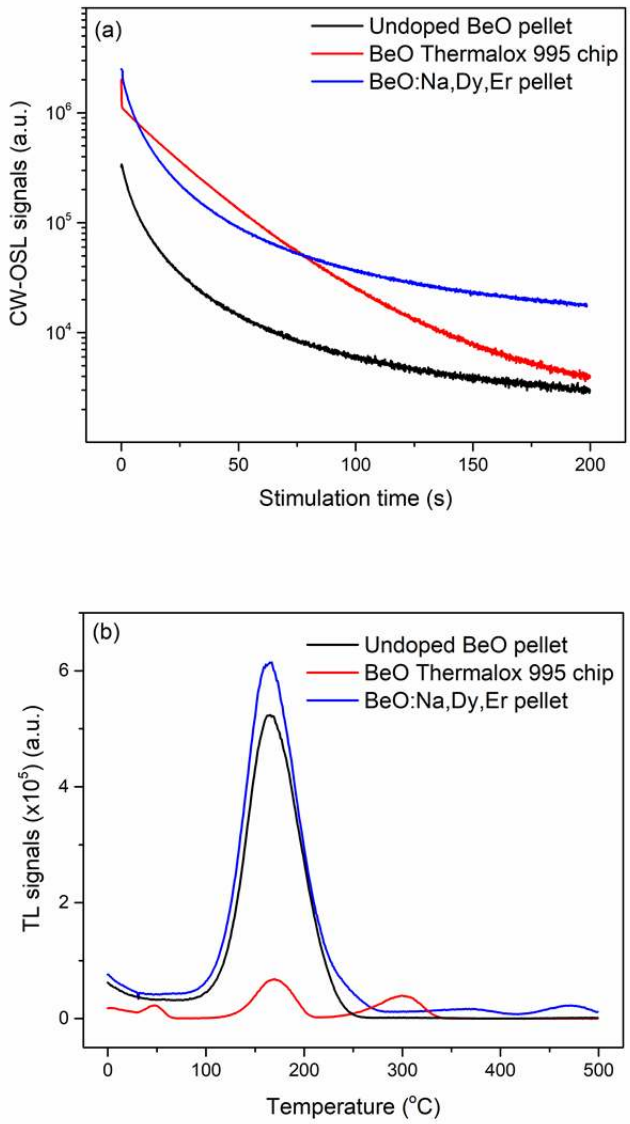

Figure 4.87. (a) OSL and (b) TL signals from BeO:$Na_{5\%}$,$Dy_{0.1\%}$,$Er_{0.05\%}$ pellet, compared to the OSL/TL from commercial used BeO (Thermalox 995) chip and previously studied undoped BeO pellet. All measurements were done with Hoya U-340 filters. Each curve is the average of three pellets or chips. The heating rate was 1 °C/s.

As is seen from Figure 4.87a, the OSL intensity from BeO:Na,Dy,Er is almost the same as that of the BeO chip and higher than that of the previously studied undoped BeO pellet. The data presented in Figure 4.87b shows that the TL intensity of the BeO:Na,Dy,Er pellet is more sensitive to radiation exposure than that of the other two samples, the Thermalox 995 BeO chip and undoped pellet. The OSL and TL sensitivities of BeO:Na,Dy,Er material after exposure to ionizing radiation are found to be high and sufficient for dosimetry applications.

The effects of dopants on TL signals were investigated to ensure whether dopants introduced new TL peaks when compared with the TL glow curve of undoped BeO. TL signals were obtained from the different dopants with optimum concentrations, namely, undoped BeO, BeO:$Dy_{0.1\%}$, BeO:$Er_{0.05\%}$, BeO: $Dy_{0.1\%}$,$Er_{0.05\%}$, and BeO: $Na_{5\%}$,$Dy_{0.1\%}$,$Er_{0.05\%}$, and presented in Figure 4.88.

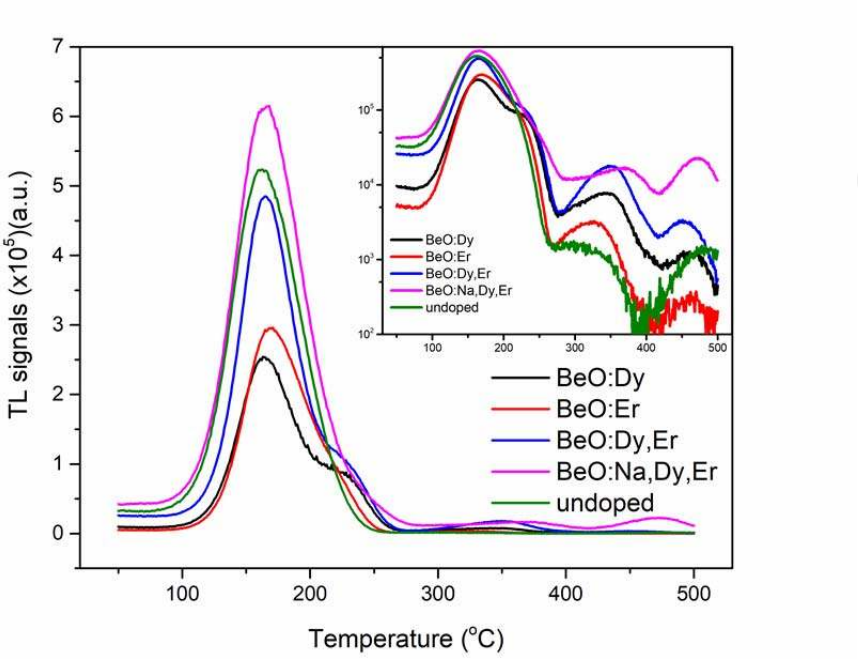

Figure 4.88. TL glow curves of 0.5 Gy irradiated BeO pellets, namely, undoped BeO, BeO:$Dy_{0.1\%}$, BeO:$Er_{0.05\%}$, BeO: $Dy_{0.1\%}$,$Er_{0.05\%}$, and BeO:$Na_{5\%}$,$Dy_{0.1\%}$,$Er_{0.05\%}$. Inset: TL glow curves in logarithmic scale for better viewing of low sensitive peaks.

As is seen from Figure 4.88, a shoulder peak formation around 230 °C was observed in the obtained TL glow curves of BeO doped with a single Ln (BeO:Dy or BeO:Er). When Dy and Er pairs were added together, it was observed that TL sensitivity increased two times when compared to single doped materials for the same peak. The similarity of the location of the shoulders around 230 °C in the TL glow curves suggested that the trapping centers for singly doped BeO samples may locate in the region of the same activation energy levels.

To confirm the new energy levels in Na, Dy and Er-doped BeO material, the activation energies were calculated for the undoped and doped BeO pellets, separately using an extended variance of the extended initial rise method (IRM) similar to Gobrecht and Hofmann Gobrecht et al. (1966). The data was obtained and is presented in Section 0, but the results are ambiguous because of the large overlap of the TL peaks.

On the other hand, step annealing studies (see Section 4.8.3.6) have shown that another important region of the TL glow curve for the OSL signal might be considered after 300 °C. This region of the TL glow curve is assumed as one of the major contributors to the OSL signal. In Figure 4.87, while the 170 °C TL peak of the BeO:Na,Dy,Er pellet is slightly higher than that of the undoped BeO pellet, the 350 °C TL peak intensity increased almost ten times. This shows the main source of the increase in the OSL signal intensities given in Figure 4.87a. It can be concluded that the presence of dopants in BeO caused some changes in the characteristic TL glow curve of undoped BeO and the traps associated with 350 °C TL peak in BeO:$Na_{5\%}$,$Dy_{0.1\%}$,$Er_{0.05\%}$ was activated during the optical stimulation to cause improvement in OSL sensitivity in the ultimate material. Further discussion related to the effect of dopants and dopant concentrations on OSL signals is presented in Section 4.8.3.3.

4.8.3.2. Extended Initial Rise Method

The technique multiple initial rise can be described as follows (Furetta, 2010): When a single, unique TL measurement is applied up to the level of 20% of the maximum intensity I_m, the plot of ln(I) versus 1/kT should yield a line, the slope of which is the activation energy of the corresponding trap; this is the well-known initial rise method (IRM) (Furetta, 2010). Gobrecht and Hofmann (Gobrecht and Hofmann, 1966) have introduced a repetitive application of the IRM (Pagonis et al., 2006), for sequentially increasing maximum measurement temperatures T_{fin}, with a short step interval; the technique is suggested as an extended variance of the IRM (Chruścińska, 2001; Pietkun et al., 1992; Strickertsson, 1985).

TL activation energies of undoped BeO and BeO: $Na_{5\%}$,$Dy_{0.1\%}$,$Er_{0.05\%}$ samples were determined using the mentioned method in a region including the shoulder peak where the difference in TL signals was observed. The FGT is performed using a series of successive heating (TL readouts) and cooling cycles. In the framework of the present study, a sample was irradiated with a 10 Gy beta dose at the beginning of the TL measurements. TL measurements with a heating rate of 1 °C/s were performed from room temperature, first to 75 °C (T_{fin}) and then successively, up to 500 °C with 5 °C increments. The plot of ln(I) against 1/kT was drawn for each TL readout. Linear fitting was used to obtain the slope, namely –E; the intercept (ln(s) value) was also calculated from the measured data for each T_{fin}. The corresponding TL measurements according to Gobrecht and Hofmann (Gobrecht and Hofmann, 1966) are given in Figure 4.89 and Figure 4.90 for undoped BeO and BeO:Na,Dy,Er pellets throughout the entire T_{fin} region (from 75 °C to 500 °C in steps of 5 °C).

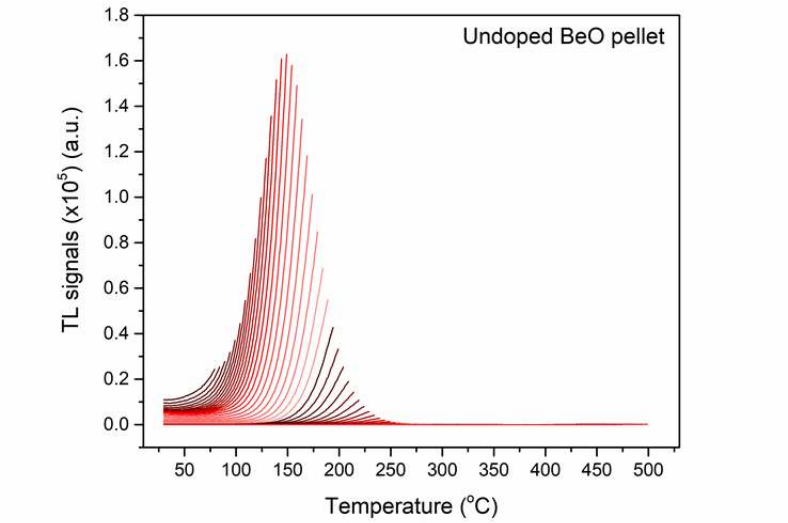

Figure 4.89. TL signals of undoped BeO pellet, measured for various T_{fin} ıtemperatures ranging from 75 °C to 500 °C in steps of 5 °C in the framework of the extended IRM.

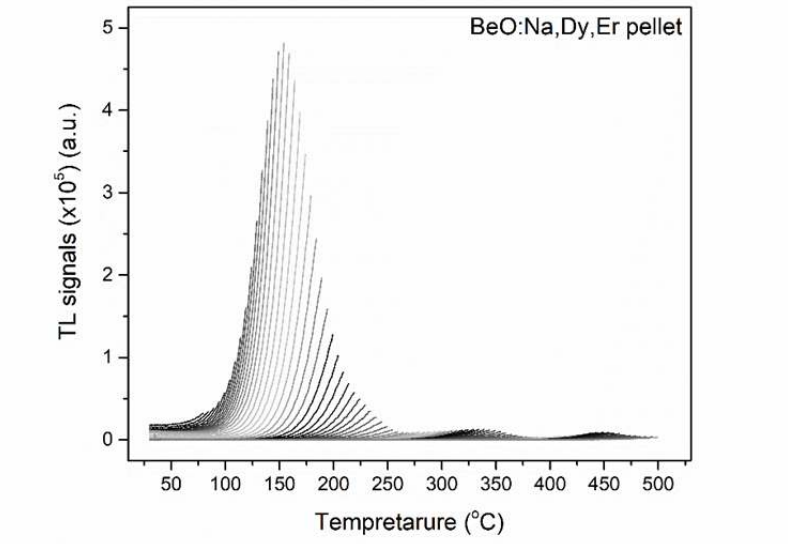

Figure 4.90. TL signals of BeO:Na,Dy,Er pellet, measured for various T_{fin} temperatures ranging from 75 °C to 500 °C in steps of 5 °C in the framework of the extended IRM.

In this study, reconstruction was applied by using the following Equation;

$$\Delta E = \frac{WC\ exp(^{-W}/_{kT})}{1 + C\ exp(^{-W}/_{kT})} \tag{4.15}$$

where W and C are the thermal quenching activation energy and pre-exponential factor, respectively. The average values of thermal quenching parameters W, C were obtained by Altunal et. al. (Altunal et al., 2019b) for undoped BeO ceramic and evaluated for BeO:Na,Dy,Er ceramic in this study; the specific values used were W = 0.52 eV and C = 1.35×10^6 for undoped BeO and W = 0.43 eV and C = 1.33×10^5 for BeO:Na,Dy,Er. Subsequently reconstruction, the extended IRM was re-applied to calculate the activation energies. Figure 4.91 and Figure 4.92 present the plot of activation energies versus T_{fin} before and after reconstruction. In general, the E-T_{fin} curves are expected to yield specific stability areas, which are also known as plateaus. As Figure 4.91 and Figure 4.92 are going to further reveal, the corresponding plots for the cases of undoped BeO and BeO:Na,Dy,Er seem to yield similar continuum plateau regions. Each straight line might be accepted as being corresponding to a plateau value in the E-T_{fin} curve, representing an individual trap with individual activation energy. While the activation energies for undoped BeO were found using experimental data as (0.99 ± 0.01), (1.06 ± 0.01), (1.14 ± 0.02) and (1.82 ± 0.02) eV, reconstructed activation energies were evaluated as (1.28 ± 0.02), (1.49 ± 0.01), (1.65 ± 0.01) and (2.34 ± 0.02) eV. On the other hand, activation energies for BeO:Na,Dy,Er were evaluated using experimental data as (1.12 ± 0.01), (1.15 ± 0.01), (1.08 ± 0.02), (1.44 ± 0.01) and (1.94 ± 0.01) eV, after reconstruction, thermal activation energies were determined as (1.36 ± 0.01), (1.49 ± 0.01), (1.46 ± 0.02), (1.86 ± 0.01) and (2.36 ± 0.02) eV. Each value corresponds to the average of the values over the plateau and the error values to the respective standard deviation.

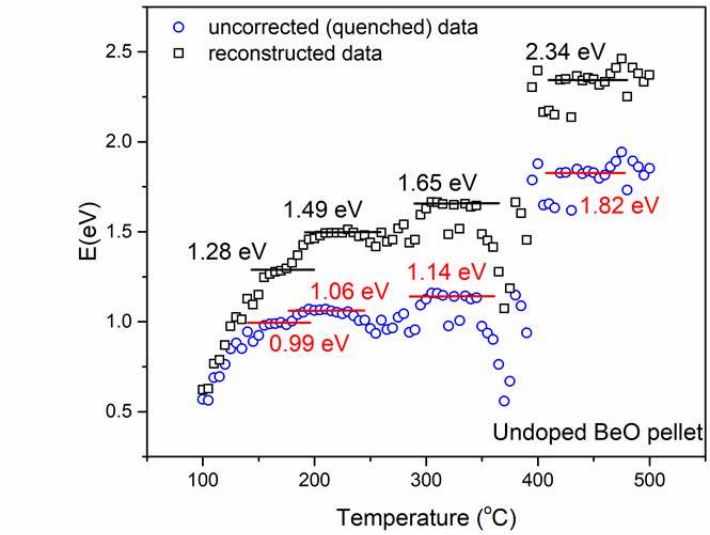

Figure 4.91. Activation energy plateaus based on both quenched and reconstructed data throughout the temperature region between 100 and 500 °C for undoped BeO pellet.

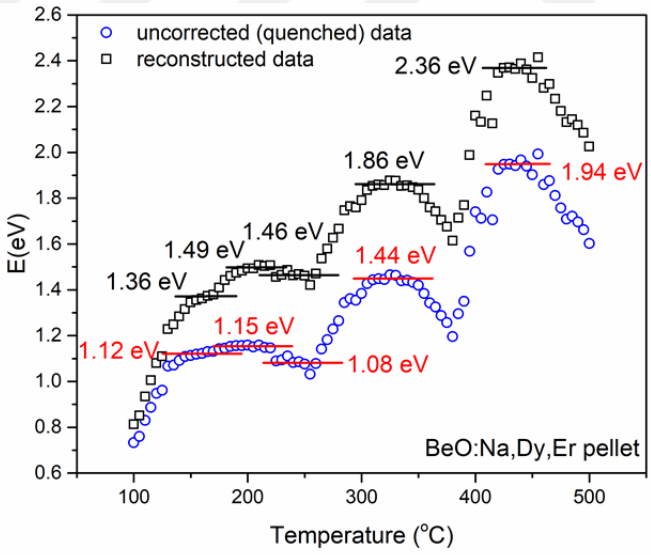

Figure 4.92. Activation energy plateaus based on both quenched and reconstructed data throughout the temperature region between 100 and 500 °C for BeO:Na,Dy,Er pellet.

As a result, one may say that these (Dy and Er) dopants introduced a new shoulder TL peak located at ~ 230 °C with a new experimental activation energy level of (1.08 ± 0.02), and a reconstructed activation energy value of (1.46 ± 0.02) eV.

4.8.3.3. Effect of Dopants and Dopant Concentrations

To investigate the effect of dopant concentration on OSL signals of BeO, OSL signals were recorded from BeO doped with Na, Dy, and Er at various concentrations using 200s blue light stimulation after the irradiation with 0.5 Gy beta doses. Figure 4.93 shows the changing of the OSL intensities obtained from BeO:Na,Dy,Er pellets prepared with different concentration values. Firstly, Na and Dy concentrations in the structure were kept at constant values of 0.1 % and 0.005 %, respectively, and Er concentrations were changed as 0.001, 0.01, 0.05, and 0.5%. As is seen from the solid line in the plot, the highest OSL intensity of BeO:Na,Dy,Er was obtained with the Er concentration of 0.05 %. After the determination of the appropriate Er concentration, Dy and Er concentrations in the structure were kept at constant values of 0.005 % and 0.05 %, respectively, and Na concentrations were changed as 0.05, 0.1, 0.3, 0.5, 1, 3, 5 and 10%. Since the maximum OSL intensity was obtained from the BeO:$Na_{5\%}$,$Dy_{0.05\%}$,$Er_{0.05\%}$ pellets, the appropriate Na concentration was determined as 5 %. After the determination of appropriate Na concentration with 5%, Dy concentrations were changed in the structure and OSL signals were obtained from the samples prepared at 0.003, 0.01, 0.05, 0.1, 0.5, 1 and 2% concentrations. The maximum OSL intensities were observed from the combination of BeO:$Na_{5\%}$,$Dy_{0.1\%}$,$Er_{0.05\%}$. For this reason, the doping percentage of Dy was chosen as 0.1 %.

On the other hand, to better understand the contributions of Na, Dy and Er dopants to the OSL signals of BeO, the samples were compared as single, double and triple-doped. Although no significant increase was observed in the peak signals around 170 °C in the TL curves, the increase in the region after 300 °C with triple

dopant caused an increase in the OSL signals in this combination of BeO: $Na_{5\%}$,$Dy_{0.1\%}$,$Er_{0.05\%}$. Step annealing experiment results supported this result.

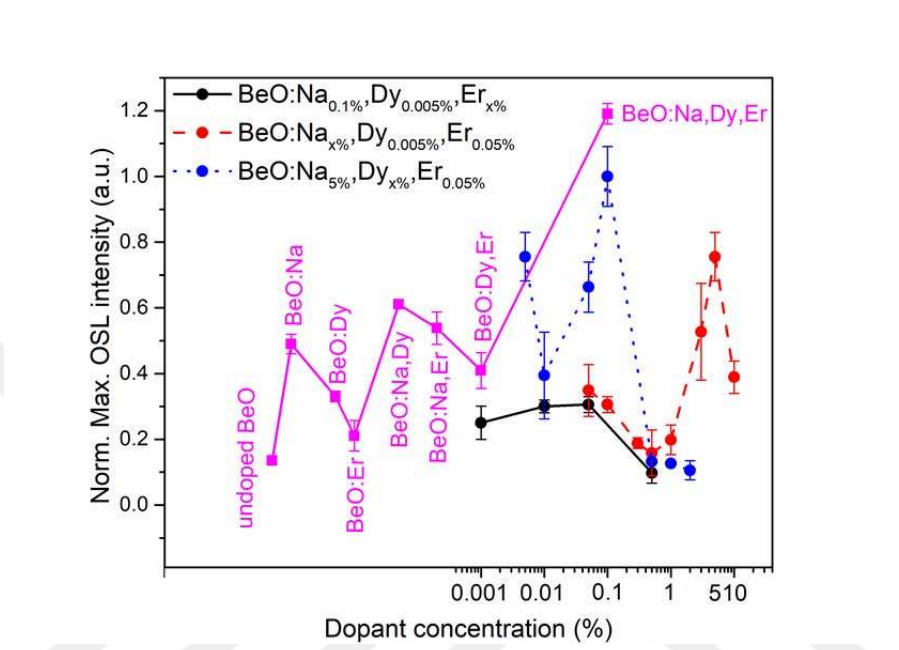

Figure 4.93. The changes in OSL signals of BeO:Na,Dy,Er samples were prepared with different concentrations compared with the max. OSL signals which were obtained from the undoped BeO, BeO:$Na_{5\%}$, BeO: $Dy_{0.1\%}$, BeO: $Er_{0.05\%}$, BeO:$Na_{5\%}$,$Dy_{0.1\%}$, BeO: $Na_{5\%}$,$Er_{0.05\%}$, BeO:$Dy_{0.1\%}$,$Er_{0.05\%}$, and BeO: $Na_{5\%}$,$Dy_{0.1\%}$,$Er_{0.05\%}$ pellets. Each data point demonstrates the average of the OSL signal intensities. The error bars represent the experimental standard deviations of mean values obtained from three pellets in each readout. The data points for BeO:$Na_{5\%}$,$Dy_{0.1\%}$,$Er_{0.05\%}$ for the two series do not match exactly, because the samples for the two series were synthesized in separate experiments (different batches), and some variation or error in the conditions may occur.

4.8.3.4. XL Emissions

The characterization of radioluminescence (X-ray luminescence, XL) signals is very important to obtain information about luminescence band locations of the newly developed dosimetric materials. In Figure 4.94, the obtained XL

spectra at room temperature from the BeO with changing Na, Dy, and Er concentrations were presented together with that of undoped BeO.

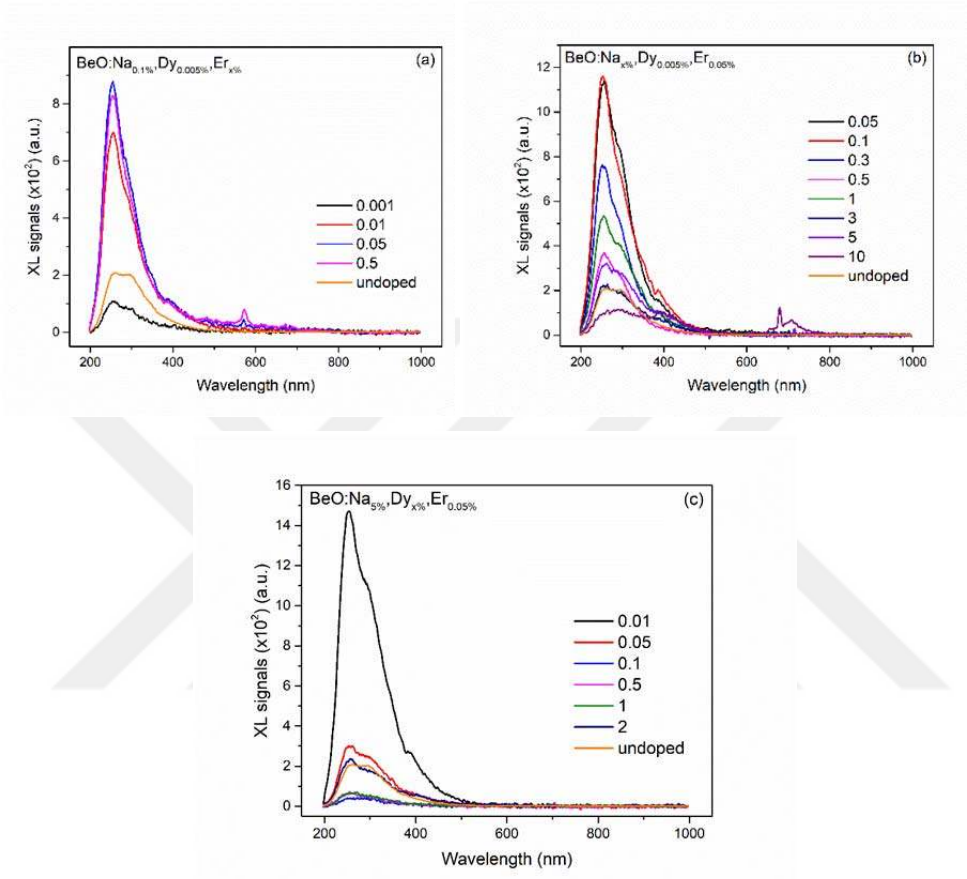

Figure 4.94. The changing in RL spectra of BeO:Na,Dy,Er ceramic pellet with various (a) Er, (b) Na, (c) Dy concentrations.

As seen from the XL spectra of the BeO:Na,Dy,Er pellets having various dopant concentrations, a similar wide emission band with a maximum at 250 nm ranging from 200 nm up to 500 nm was observed. During X-ray irradiation, the observed dominant luminescence at 250 nm in XL spectra is represented by the 4.9 eV emission band which is originated from the radiative annihilation of self-trapped excitons produced (Altunal et al., 2019b; Ogorodnikov and Kruzhalov, 1997; Ogorodnikov et al., 1995). Previous work has shown that BeO had 3–4 eV

and 4.9 eV emission bands (Ogorodnikov and Kruzhalov, 1997). In this study, the luminescence associated with the 4.9 eV emission band which is located far from the spectral efficiency of the PMT and transmittance range of the Hoya U-340 filter was not observed. Similar comments were noted for BeO Thermalox 995 chips by Yukihara *et. al.* (Yukihara, 2011). On the other hand, OSL emission spectra of undoped BeO and BeO:Na,Dy,Er pellets were also measured and presented in Section 0. OSL emission spectra of undoped and BeO:Na,Dy,Er pellets were found to be almost the same as the XL emission spectra. When compared to the OSL spectrum of the BeO Thermalox chip (Yukihara, 2011), results indicate that a different luminescence mechanism is taking place in BeO:Na,Dy,Er.

The effects of dopant concentrations on X-ray luminescence signals were also investigated. With an increase in Er concentration in the material, a compound emission peak appeared with increasing intensity at ~ 570 nm (see Figure 4.94a). The observed emission peak represents the $^4F_{9/2} - {}^6H_{13/2}$ characteristic transition of Dy^{+3} and the $^4S_{3/2} - {}^4I_{15/2}$ characteristic transition of Er^{+3}. With the increase in the Na concentration, the $^4F_{9/2} - {}^6H_j$ ($j = 11/2, 9/2$) characteristic transitions of Dy^{+3} were observed from 650 to 750 nm for only 10% Na doped sample among the others (see Figure 4.94b). As a surprising result, the increase in Dy concentration resulted in a significant reduction in the main BeO emission (see Figure 4.94c), the characteristic emission of Er at 407 nm and the characteristic emission of Dy at 475 nm was not be observed because they remained under the main emission peak of BeO.

4.8.3.5. OSL Emissions

OSL emission spectra of undoped BeO and BeO:Na,Dy,Er pellets were measured with Fluorolog-3 spectrofluorometer (with scanning monochromator and PMT). The excitation monochromator was set to 470 nm and the emission monochromator was scanned from 290 nm to 410 nm in 1 nm steps using 0.1 s

integration time. The excitation and emission slits were set to 5 nm bandpass. OSL emission spectra of undoped and BeO:Na,Dy,Er pellets were given in Figure 4.95.

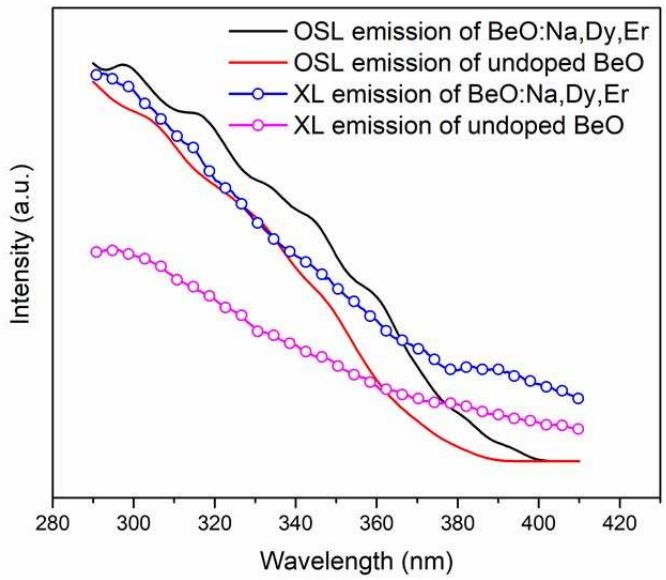

Figure 4.95. OSL and XL emission spectra of undoped BeO and BeO:Na,Dy,Er pellets.

OSL emission in Thermalox chips is different from RL emission and the resulting luminescence mechanism can be said to be different (Yukihara, 2011). However, as is seen from the figure, since the XL and OSL emissions of the undoped BeO and BeO:Na,Dy,Er pellets produced by the precipitation method show similar behavior, it is not wrong to say that a similar luminescence process has occurred between XL and OSL emissions. More detailed investigations (for example on the temperature dependence of this XL emission) are required to clarify this issue.

4.8.3.6. Relationship between TL and OSL Signals

To examine the nature of OSL signals more deeply, it is necessary to determine which traps in the material are optically active or not. Determining and investigating the correlation between residual and direct TL glow curves is a widely used method for reaching the source of OSL signals. Here, the direct TL glow curve was obtained by performing the TL reading to the dosimeter after irradiation, while the residual TL glow curve was obtained by the first optical stimulation (200 s) of the dosimeter after irradiation and the subsequent TL reading process. TL readouts were performed up to 650 °C (2 °C/s) after 0.5 Gy beta dose exposure. Figure 4.96a shows direct TL, residual TL, and bleached TL glow curves. The bleached TL curve which represents the optically active parts of the TL glow curve was evaluated by subtracting the residual TL from the direct TL.

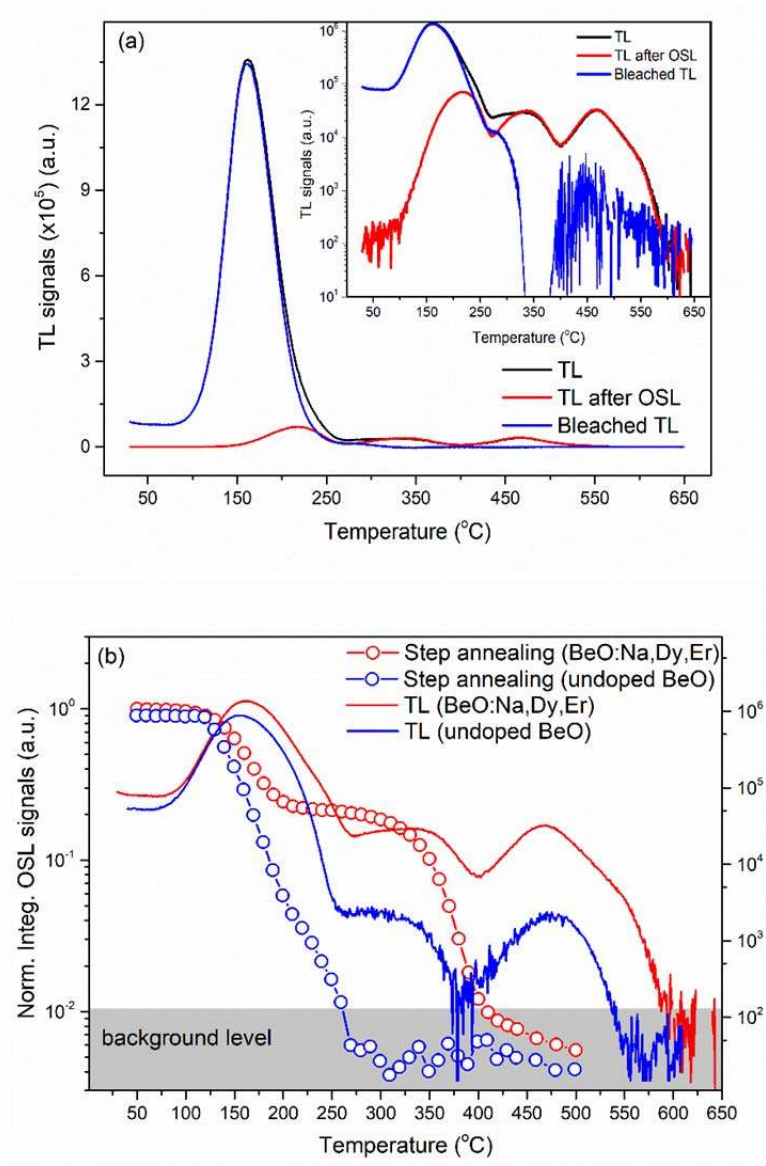

Figure 4.96. (a) TL glow curve (direct TL), TL glow curve (residual TL) obtained after OSL measurement and Bleached TL curve from the 0.5 Gy irradiated pellets, (b) Step annealing curves of OSL signals from BeO:Na,Dy,Er pellets.

As is seen from the figure, the 1st peak located at ~170 °C in the TL glow curve of BeO:Na,Dy,Er pellet was affected by optical stimulation whereas the 2nd and 3rd TL peaks located at ~350 and ~470 °C, respectively were not. This effect of light exposure on TL signals provides evidence that the origin of the OSL signal might be mostly related to the 170 °C TL peak. The inset of Figure 4.96a is for better viewing of the 2nd and 3rd peaks due to low TL signal intensities.

Another method for determination and investigation of the source of the OSL signals, the step annealing (thermal-stability) experiments were carried out by heating the sample to a target pre-heating temperature and recording the remaining OSL signals. The experimental steps are given as follow:

Step 1: Irradiation of the sample with 0.5 Gy beta dose

Step 2: Heating the sample to a target pre-heating temperature

Step 3: Recording OSL signal using 200 s blue light stimulation

Step 4: Resetting the sample by performing TL measurements up to 650 °C (5 °C/s)

Step 5: Go back to Step 1 increasing the preheating temperature by 10 °C steps, up to 500 °C

Figure 4.96b. shows the integrated OSL signals of undoped and BeO:Na,Dy,Er pellets versus the temperatures of pre-heating together with the TL glow curves for comparison. As is seen from the figure that OSL signals of both undoped and BeO:Na,Dy,Er pellets started to decrease after 130 °C and this decrease is corresponding to the emptying of the 170 °C TL peak. On the other hand, with increasing preheating temperature, the OSL signals of the undoped sample reaches the background level whereas the OSL signals of BeO:Na,Dy,Er sample were constant up to 350 °C. After the second reduction in OSL signals of BeO:Na,Dy,Er pellet, with the discharge of the TL traps associated with the 350 °C TL peak, the OSL signals come to an end by reaching the background level. These results confirm that the OSL signals of BeO:Na,Dy,Er pellets might be originated both from the 170 and 350 °C TL peaks, whereas only the 170 °C TL peak of the

undoped sample contributes to the OSL signals. Furthermore, it is not clear, for the time being, whether the OSL and TL signals originate from the same traps or not. It is also probable that the TL peaks (170 and 350 °C) are not due to a single trap but a combination of overlapping peaks. A similar correlation between TL and OSL signals was presented for undoped BeO ceramic pellets synthesized using the sol-gel and the precipitation methods in our earlier studies (Altunal et al., 2019b; Altunal et al., 2018).

4.8.3.7. Thermal Quenching of OSL Signals

Thermal quenching is known as the decrease in luminescence efficiency observed in most luminescence materials at temperatures higher than room temperature. Basically, thermal quenching is the increase in the probability of electrons transited to the ground state of the luminescence centers by non-radiative transitions (the Mott-Seitz model) (Bøtter-Jensen et al., 2003). To examine whether there is thermal quenching, the temperature dependence experiments were performed using BeO:Na,Dy,Er ceramic pellets irradiated with 0.5 Gy beta dose. Following the irradiation, preheating at 110 °C for 60 s was applied to eliminate the contribution of unstable signals which are originated from the shallow traps. The temperature dependence of the OSL signal is given above by Equation (4.2.

In the temperature dependence experiments, OSL signals were obtained from a hot sample heated at temperatures in steps of 10 °C between 50 to 150 °C (see Figure 4.97a). At the end of each measurement, the sample was reset by performing a TL readout up to 650 °C to remove the residual luminescent signals and make the sample ready for the next measurements. In Figure 4.97a, strong thermal quenching was observed with the reduction in luminescence intensity with increasing readout temperature. Comparing the integrated OSL signals obtained at 50 and 110 °C readout temperatures, almost a 25 % reduction in OSL signals was observed. This decrease proves the presence of a considerable thermal quenching. After this temperature, the reduction in OSL signals has approached 40% at 150 °C. But the source of the ongoing decline here can be explained by both thermal quenching and depletion of the dosimetric traps settled around 170 °C.

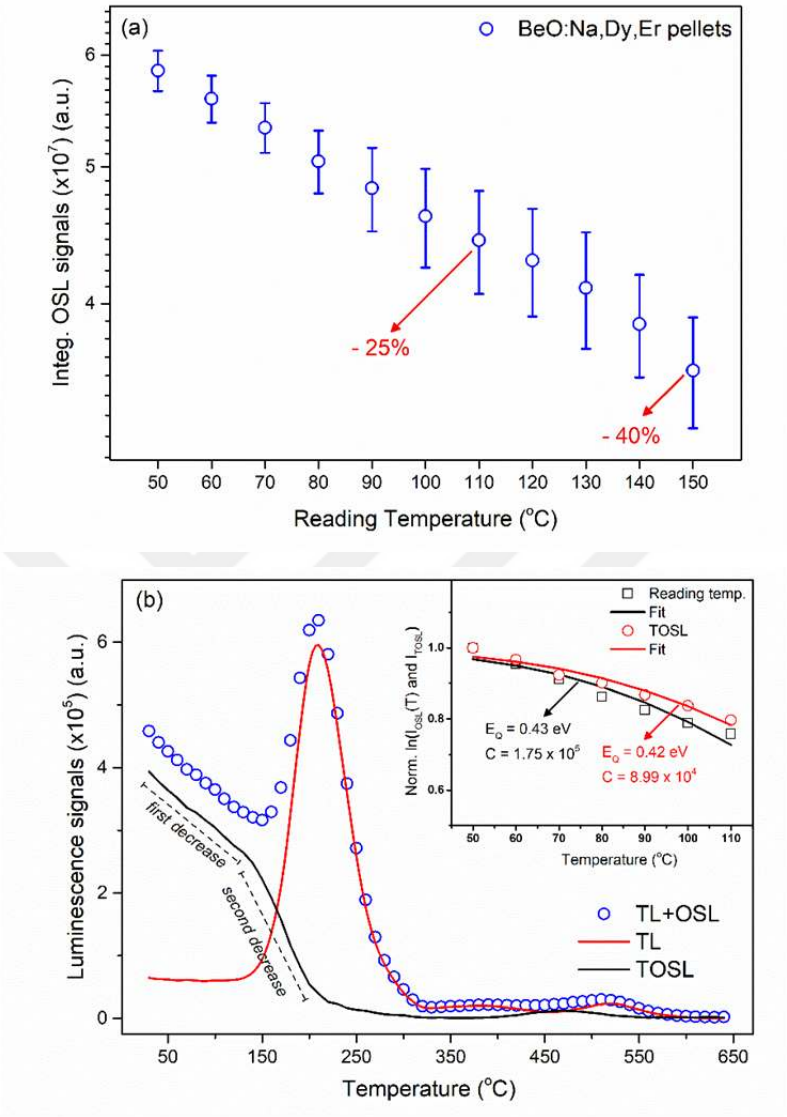

Figure 4.97. (a) Integrated OSL signals at various reading temperatures after preheating the BeO:Na,Dy,Er ceramic pellet at 110 °C for 60 s. (b) The TOSL curves from the 0.5 Gy irradiated BeO:Na,Dy,Er ceramic pellet. Insets: calculation of the thermal quenching energy using the signal intensities obtained at various readout temperatures and the TOSL method. Each data point indicates the average of the integrated OSL signals (the total OSL signal counts from 0 to 200 s). The error bars are the experimental standard deviations of mean values obtained from three pellets in each readout.

On the other hand, to obtain more information on the thermal quenching mechanism, it has been shown in the previous studies that TOSL (temperature-dependent OSL signals) is a suitable method for BeO chips (Thermalox995) (Bulur and Goksu, 1998), undoped and doped BeO ceramic pellets (Altunal et al., 2019a; Altunal et al., 2019b). Briefly, a TOSL curve is obtained by subtracting the TL glow curve obtained while performing the OSL measurement (usually pulsed OSL is used) from the TL glow curve. In this study, 0.1 s pulsed stimulation with 0.9 s time interval between the pulses was used during TL readout. As expected, the luminescent signals obtained during the pulsed OSL are the combinations of the OSL and TL (i.e. TL+OSL). Additionally, the luminescent signals obtained during the time interval are the TL signals (TL). The subtraction of these luminescent signals gives us the TOSL curve. Figure 4.97b shows TL+OSL, TL and TOSL curves for the BeO:Na,Dy,Er pellet. Measurements were carried out by heating the sample to 650 °C at a rate of 5 °C/s having blue-light stimulation by short-pulses of 0.1 s every 0.9 s while heating the sample. As seen from the TOSL curve, the OSL outputs have two decreased curves. The first decrease is from 50 °C up to 150 °C and the second decrease begins with 150 °C and reaches zero level at 250 °C. It can be concluded that the first decrease may prove the presence of strong thermal quenching, while the second may be due to the discharge of dosimetric traps settled around 170 °C. On the other hand, using the data collected in OSL readouts (see Figure 4.97a) and the reduction data in the initial parts of TOSL curves, the thermal quenching energies of the materials were evaluated by fitting them into Equation (4.2. The goodness of the fitting curves in the two methods was tested with the use of the figure of merit (FOM) (Balian and Eddy, 1977), which is a sign of agreement between experimental and theoretical data; the FOM values were evaluated as 0.34 and 0.15 %. The fitting curves, the estimated E_Q (0.43 and 0.42 eV) and C values (1.75E+05 and 8.99E+04) using both methods were presented in the graphs of the insets of Figure 4.97b. These evaluated E_Q values for the two

methods are slightly lower than previously presented values for BeO ceramic pellets synthesized with the precipitation method in one of our studies (Altunal et al., 2019b). The differences in the indicated E_Q values may be due to using BeO ceramics with dopants that may increase slightly the possibility of non-radiative transitions. The existing data are not sufficient to state the type of the quenching mechanism(s) involved in the luminescence processes. The investigation of radioluminescence (XL) spectra as a function of temperature can be helpful and ESR observations carried out at various temperatures may also give some information for the fabrication of the target dosimeters.

4.8.4. Dosimetric Characteristics

4.8.4.1. Reusability Properties

In radiation dosimetry, a desirable feature is that the OSL dosimeters should be reusable. To extend this definition, OSL signals from dosimeters under the same measuring conditions and following the same exposures are expected to give the same response. The reusability properties of three BeO:Na,Dy,Er ceramic pellets irradiated with 0.5 Gy beta dose were investigated by measuring OSL signals. Before OSL measurements, samples were preheated at 110 °C for 60 s to eliminate the unstable signals which are originated from the shallow traps. Following each OSL readout, the residual OSL signals were reset by performing TL readout up to 650 °C (5 °C/s). The same measurements were performed without changing the experimental process 30 times. The integrated OSL signals, which are normalized to the first cycle, versus the experimental cycles, were illustrated in Figure 4.98.

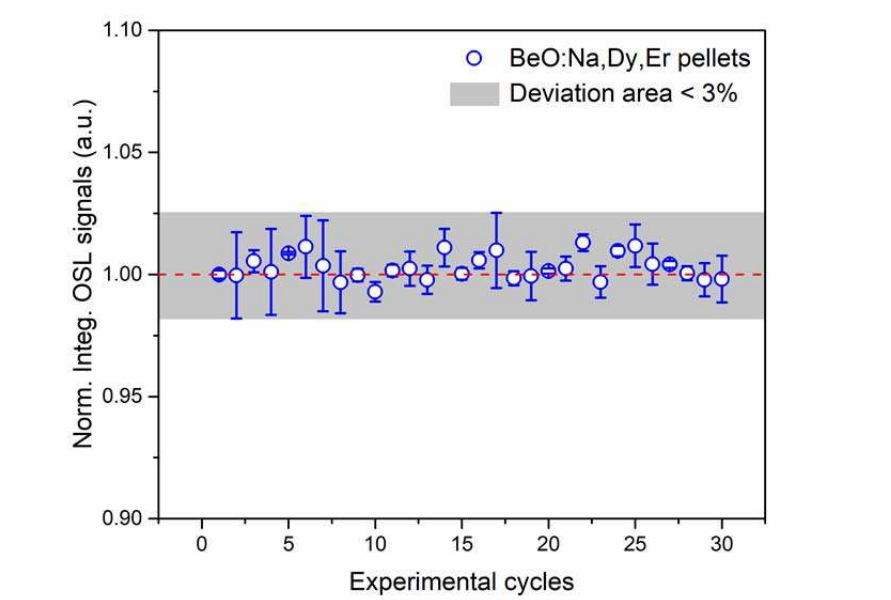

Figure 4.98. The reusability characteristics of OSL signals of BeO:Na,Dy,Er ceramic pellets. After 0.5 Gy beta test dose and 110 °C for 60 s preheating, OSL signals were recorded during 200 s optical stimulations. Each data point represents the mean of integrated (the total OSL signal counts from 0 to 200 s) and normalized (according to the first readout) OSL signals. The error bars represent the experimental standard deviations of mean values obtained from three pellets in each cycle.

It is seen from Figure 4.98, OSL signals have very good reusability over thirty cycles. The deviation from the first readout value was evaluated as a maximum of ~3 %.

4.8.4.2. Dose-Response Features

The dose-response behavior of the OSL signals from BeO:Na,Dy,Er ceramic pellets were investigated in the beta dose range between 0.1 Gy and 50 Gy. The three 0.5 Gy irradiated BeO:Na,Dy,Er ceramic pellets were irradiated with 0.1, 0.2, 0.5, 1, 2, 5, 10, 20 and 50 Gy beta dose. After preheating the samples at 110 °C for 60 s, the OSL measurements were performed using 200 s blue light

stimulations. Residual luminescent signals were reset by heating the samples to 650 °C (5 °C/s). The plots of integrated OSL signals, which were obtained at each dose value, versus the absorbed beta dose values were presented in Figure 4.99. The data points on the plot represent the average of the integrated OSL signals of three pellets used and the error bars are the standard deviations (1σ). Dose-response behaviors of the BeO:Na,Dy,Er ceramic pellets were found to be slightly linear with the 1.03 slope value in the dose range between 0.1 and 50 Gy. The parameters such as slope, intercept, etc. evaluated were presented through the linear fitting in the inset figure of Figure 4.99.

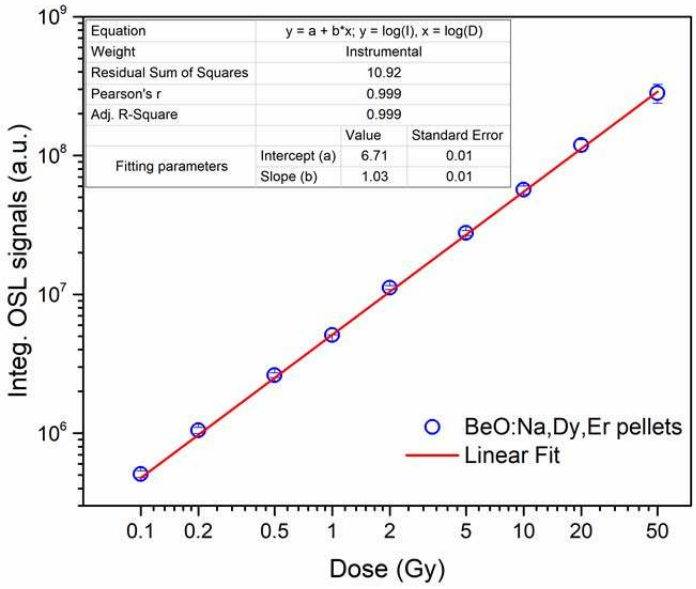

Figure 4.99. Dose-response curve of the integrated whole OSL signals from three BeO:Na,Dy,Er ceramic pellets in the dose range between 0.1 and 50 Gy. Inset: Linear fitting parameters was obtained by equation of y = a + bx, where refers to y = log(I), x = log(D), a is intercept, b is slope, (I) represents Integrated OSL signals, and D is dose value. The data points on the plot represent the average of the integrated OSL signals (the total OSL signal counts from 0 to 200 s) of three pellets used and the error bars are the standard deviations (1σ).

4.8.4.3. Dark Storage Fading Characteristics

In all dosimetric applications, the stability of the trapped charge population at room temperature is one of the most important desirable properties. To determine whether the charge populations in the material traps were stable, a group of BeO:Na,Dy,Er ceramic pellets were initially calibrated for a radiation dose of 0.5 Gy. As a result of the calibration process, the mean and experimental standard deviation values of the integrated OSL signals which were obtained from three repeated measurements were recorded. Before each OSL measurement, samples were preheated at 110 °C for 60 s to erase the unstable signals arising from the shallow traps. Forty-five pellets with an experimental standard deviation of less than 3% were selected and calibration factors were determined for each pellet. After calibration factors were determined, all BeO:Na,Dy,Er ceramic pellets were exposed to a dose of 0.5 Gy and stored at room temperature in the dark at predetermined time intervals (0.5, 1, 3, 6, 12, 24, 72, 120, 168, 336, 504, 720, 1080, 2160, 2520 h). Here, three pellets were used for each time interval. Figure 4.100 shows the fading characteristics of the OSL signals starting after half an hour from the exposure. During fading experiments, OSL signals were obtained under the same laboratory (room temperature at 24 °C, a constant humidity of 46% RH, in the dark, etc.) and equipment (quartz window cleaning before each measurement, same high-voltage supply for PM tube, etc.) conditions. We used three well-known BeO Thermalox995 chips as reference material for the readout sensitivity. OSL signals at different readout times were obtained from BeO Thermalox995 chips irradiated with 0.5 Gy beta dose, after preheating the sample at 125 °C for 125 s to remove the possible contributions that might come from unstable centers (see the inset of Figure 4.100). As is seen from the inset of Figure 4.100 that integrated OSL signals obtained at the third month were decreased by 2 %.

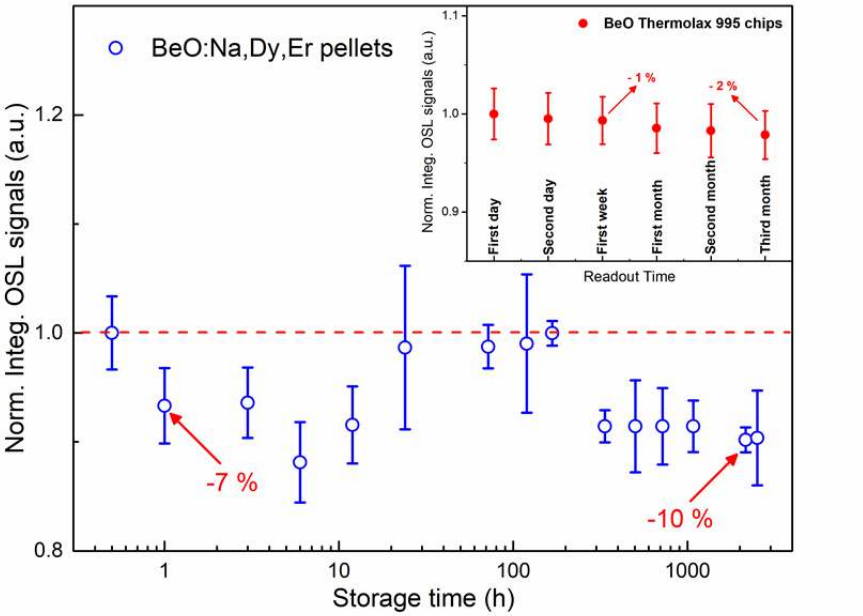

Figure 4.100. Fading characteristics of the OSL signals from the BeO:Na,Dy,Er ceramic pellets as a function of storage time up to three months and 15 days after 0.5 Gy beta dose initial exposure. The data points on the plot represent the average of integrated (the total OSL signal counts from 0 to 200 s) and normalized (according to the first readout) OSL signals. The error bars represent the experimental standard deviations of mean values obtained from three pellets in each measurement.

As can be seen from Figure 4.100, the decrease in the integrated OSL signals after 1 h of storage is around 7 %. After a short-term decline, an unexpected increase in OSL signals was observed until the 24-hour storage period. After fluctuations in the short-term storage of OSL signals, it was observed that the OSL signals remained almost the same until the 1-week storage time. Following this stabilization, it was noted that a 10 % reduction occurred in OSL signals and this level of reduction continued almost unchanged by the last storage time (15 weeks). This mechanism may involve tunneling between the different states, but the exact mechanism cannot be determined.

4.8.5. Discussion

Regarding the existence of the mentioned complex luminescence process, it is very difficult to understand the roles of the dopants in the structure of BeO and the type of the mechanism that occurred. However, the mechanism could be discussed with the assumptions through simplified processes. As known, lanthanides in the material structure produce different and stable energy levels in the forbidden energy gap and may directly contribute to the recombination processes. The used dopants in this study produce some local distortions in the BeO lattice and the differences between the dopant ionic radii (Na^{2+} (1.16 Å), Dy^{3+} (1.05 Å), Er^{3+} (1.03 Å)) and the host matrix (Be^{2+} (0.59 Å)) cause interstitial type defects in the crystal lattice rather than substitution of Ln^{3+} with Be^{2+} ions. The data obtained from the TL glow curves and XL spectra for Dy and Er dopants seems to indicate that they are not acting as luminescence centers, but it is not clear whether they are introducing new trapping centers directly or indirectly. In our OSL and XL experiments, the nature of the dopant quenching and the roles of Ln dopants for the luminescence mechanisms have been remaining still unsolved. To better understand the correlation between the quenching mechanisms and the Ln emission intensities in BeO, a further study could be done on the emission dynamics of the singly-doped BeO materials by changing concentrations. The main difficulties in the interpretation of the data could serve as a starting point for future studies.

It was shown that Na doping did not change the shape of the TL glow curve of BeO:Na,Dy,Er, but it enhanced the TL intensity. Increasing the Na concentration in the BeO structure led to an increase in the TL and OSL intensities. For the role of Na ions in the BeO structure, it could be explained that the substitution between Na^{+} and Be^{2+} ions will produce a defect $(Na_{Be})^{-}$ with a negative charge capability, while the substitution between Ln^{+} and Be^{2+} ions will produce a defect $(Na_{Be})^{-}$ with a positive charge capability. These opposing defects may compensate for each other. A similar compensation mechanism for Li^{+} ions has been reported in the literature (Oliveira et al., 2019; Oliveira et al., 2016;

Yukihara et al., 2013). One may say that such a compensation effect and differences in ionic radii might affect significantly the luminescence efficiency. More detailed studies on luminescence signals of BeO:Na,Dy,Er ceramic pellets are required to confirm the suggested luminescence mechanism.

4.9. A Comparison Study on BeO-based Dosimeters

The aim of this study is to investigate the structural, morphological, luminescent and dosimetric characteristics of newly produced BeO based ceramic pellets, namely, BeO:$Na_{5\%}$,$Ce_{0.01\%}$,$Er_{0.01\%}$, BeO:$Na_{5\%}$,$Ce_{0.005\%}$,$Tb_{0.05\%}$, and BeO:$Na_{5\%}$,$Ce_{0.01\%}$,$Dy_{0.01\%}$, by a simultaneous comparison with commercialized BeO Thermalox 995 chip. The phase formation and morphology of the newly produced BeO-based ceramic pellets were studied using x-ray diffraction (XRD), scanning electron microscopy (SEM), and Energy Dispersive x-ray (EDS) analyses methods. Radioluminescence (RL), TL, and OSL techniques were used to characterize the luminescent signals originating from the samples. The correlation between TL and OSL signals was investigated by step annealing and TL after OSL experiments. Thermal quenching energy values were estimated using static and active techniques. Dosimetric characteristics such as the dose-response, energy response, minimum detectable dose (MDD) value, re-usability, fading curves were studied in detail. The results are discussed and some general conclusions were drawn.

4.9.1. Synthesis of Material

BeO ceramics were synthesized and doped using the co-precipitation method previously presented in detail in our studies (Altunal et al., 2019b; Altunal et al., 2020b; Altunal et al., 2020c; Altunal et al., 2020d). Beryllium sulfate tetrahydrate (99.90%, $BeSO_4 \cdot 4H_2O$), polyethyleneimine solution ($(NHCH_2CH_2)_n$, 50% (w/v) in H_2O), and ammonium hydroxide (28.0-30.0% NH_3 basis, NH_4OH) precursor reactants were used for initial salt, polymerization, and initiator of the

precipitate, respectively. All raw dopant materials (Na^{+} and Ln^{3+} (Ce^{3+}, Er^{3+}, Tb^{3+}, and Dy^{3+})) used were only nitrate based. Doping with 5% mol Na and a small percentage of lanthanide (Ln) was deliberately chosen to avoid increasing the Z_{eff} of the material (Z_{eff} ~7.31). The nominal compositions of $BeO:Na_{5\%},Ce_{0.005\%},Tb_{0.05\%}$, $BeO:Na_{5\%},Ce_{0.01\%},Er_{0.01\%}$, and $BeO:Na_{5\%},Ce_{0.01\%},Dy_{0.01\%}$ ceramic pellets were accomplished and used to enhance luminescence efficiencies of the materials (Altunal et al., 2021). To remove the organic formations occurring during synthesis and obtain the BeO nano- phosphors, the calcination process was applied at 900 °C for 4 h in an air atmosphere. Finally, calcinated BeO powder was prepared in pellet form possessing ~3.1 mm radius and ~0.8 mm thickness. To provide strength and integrity, the prepared ceramic pellets, each 25 mg, were sintered at 1600 °C for 4 h. After sintering, the weight losses were observed and the average weights appeared as ~23.1 ± 0.2 mg. The Thermalox 995 BeO chip dosimeters used in this study are in the form of discs with a diameter of 4 mm and thickness of ~1 mm (American company, Brush Wellman Inc.) and having a mass of 32 mg. Since the Thermalox chips and the BeO pellets differ in size and mass, all emission data obtained in the luminescence characterization and dosimetric studies are presented after evaluating as the counts/mg for comparison.

Inhalation of beryllium powders in the air may cause a serious lung condition, depending on the dose. It should be noted that, unlike BeO powders, the use of solid form BeO ceramics (sintered chips, rods, discs, etc.) does not pose a special health risk. In our work with BeO, we paid attention to safety and environmental protection studies to avoid toxicity and followed safe usage practices. Personal protective equipment such as gloves, dust/gas masks, and/or goggles was used during BeO synthesis.

4.9.2. Characterization techniques

Powder x-ray diffractograms (XRD) were obtained using a PANalytical EMPYREAN XRD diffractometer with Cu-Kα (the generator voltage of 60 kV, the current of 40 mA) by scanning from 10° to 90° (2θ) with 0.02° (2θ) steps. The XRD patterns were compared with the reference data by the International Centre for Diffraction Data (ICDD). To investigate the surface morphologies of the newly produced ceramics, the SEM analyzes were carried out by Zeiss, Supra 55 at room temperature. The SEM micrographs were taken at 20000x direct magnification and a high voltage of 20 kV. EDS analyzes were performed by the same system to investigate elemental impurities formed during synthesis and existing dopant ions in the structure.

4.9.2.1. X-Ray Diffractions

To confirm the product and investigate the crystalline phase composition, XRD analyzes were carried out using 0.02° (2θ) steps from 10° to 90° (2θ). In Figure 4.101, the XRD patterns from the newly developed samples were presented by comparison of an undoped BeO ceramic sample and Ln^{3+}-doped BeO ceramics with the reference data of the BeO phase reported in the ICDD-PDF-card no 98-006-2737. The results confirmed that all the obtained XRD peaks well matched to the reference BeO phase, and no additional peaks possibly originated from the impurity phases appeared. Comparing with the XRD patterns of the undoped BeO sample, the halo peaks from 20° to 30° resulting from amorphous phases formed due to the presence of additive elements in the structure were observed in BeO:$Na_{5\%}$,$Ce_{0.005\%}$,$Tb_{0.05\%}$, BeO:$Na_{5\%}$,$Ce_{0.01\%}$,$Er_{0.01\%}$, and BeO:$Na_{5\%}$,$Ce_{0.01\%}$,$Dy_{0.01\%}$ ceramic samples.

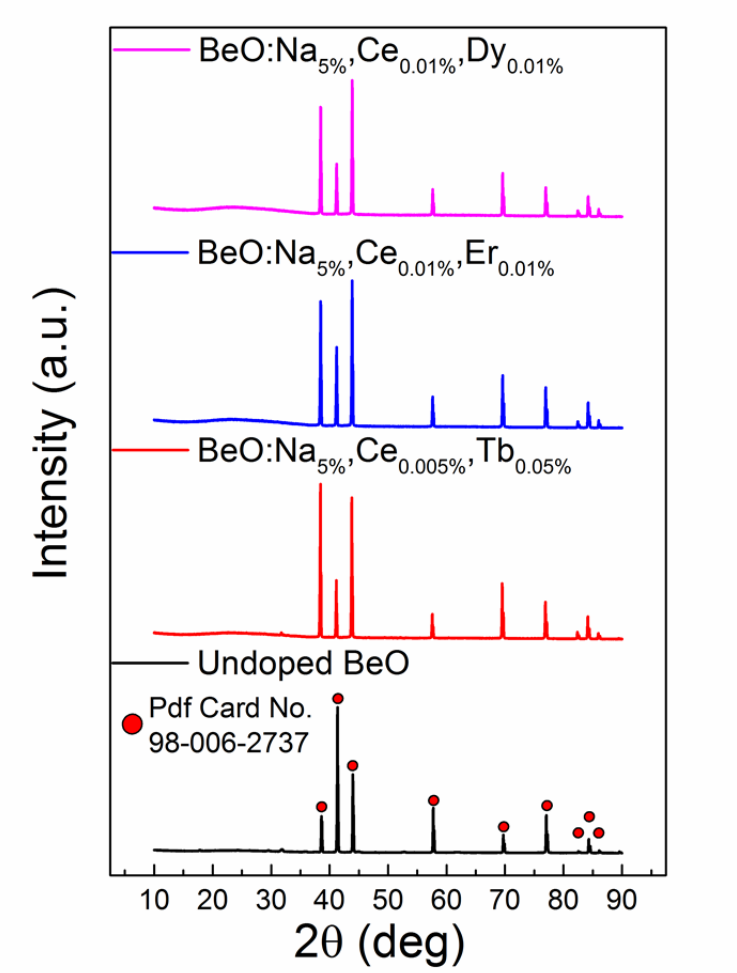

Figure 4.101. XRD patterns of undoped BeO and three newly developed BeO ceramics, namely, BeO:$Na_{5\%}$,$Ce_{0.005\%}$,$Tb_{0.05\%}$, BeO:$Na_{5\%}$,$Ce_{0.01\%}$,$Er_{0.01\%}$, and BeO:$Na_{5\%}$,$Ce_{0.01\%}$,$Dy_{0.01\%}$ compared with the reference BeO data of ICDD Pdf Card No 98-006-2737

4.9.2.2. SEM Pictures

The SEM images of the BeO:$Na_{5\%}$,$Ce_{0.005\%}$,$Tb_{0.05\%}$, BeO:$Na_{5\%}$,$Ce_{0.01\%}$,$Er_{0.01\%}$, and BeO:$Na_{5\%}$,$Ce_{0.01\%}$,$Dy_{0.01\%}$ sintered ceramic pellets were presented in Figure 4.102, Figure 4.103, and Figure 4.104, respectively, and characterized by regularly formed and well-bonded particles with a very low porosity providing more effective luminescent signals. In this study, the percentages of the dopants mentioned are nominal values and it is not known exactly in what percentage they are formed in the crystal lattice during the synthesis process.

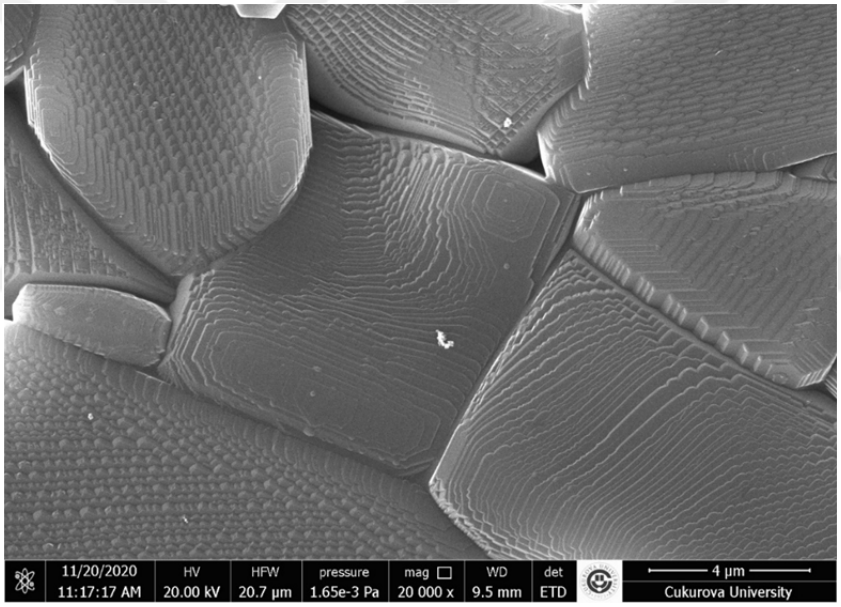

Figure 4.102. Sem image of BeO:$Na_{5\%}$,$Ce_{0.005\%}$,$Tb_{0.05\%}$ ceramic pellet.

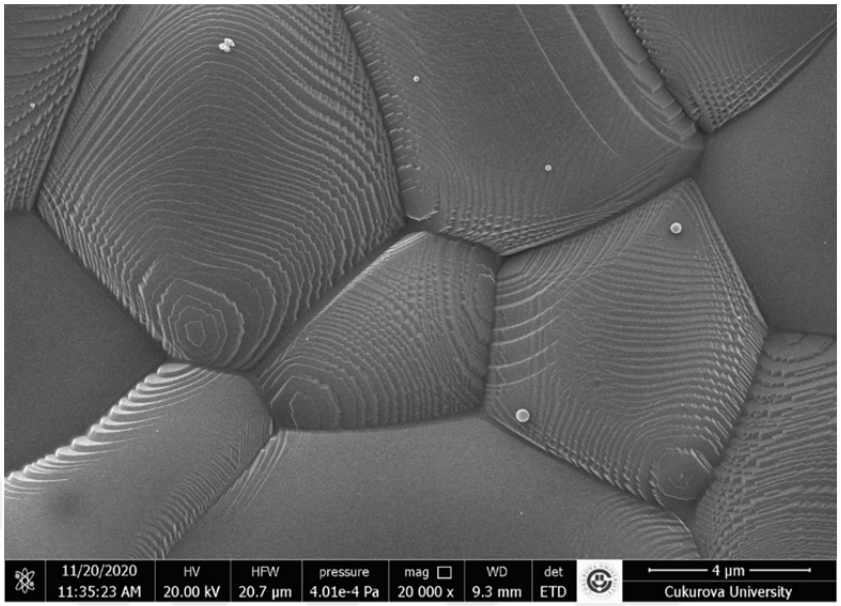

Figure 4.103. Sem image of BeO:$Na_{5\%}$,$Ce_{0.01\%}$,$Er_{0.01\%}$ ceramic pellet.

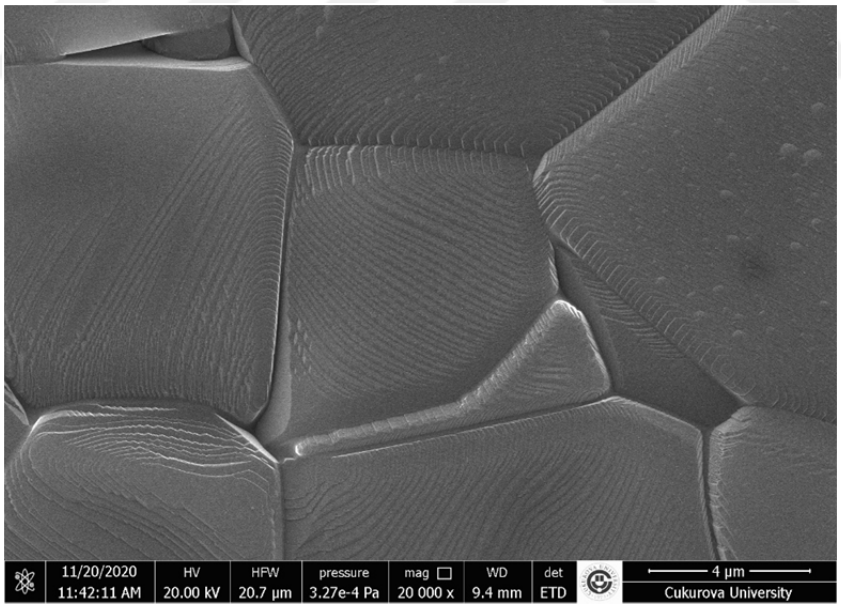

Figure 4.104. Sem image BeO:$Na_{5\%}$,$Ce_{0.01\%}$,$Dy_{0.01\%}$ ceramic pellet.

4.9.2.3. EDS Analyzes

EDS analyzes were performed, followed by SEM analysis to estimate the accuracy and rates of the specified dopants. EDS spectra of the BeO:$Na_{5\%}$,$Ce_{0.005\%}$,$Tb_{0.05\%}$, BeO:$Na_{5\%}$,$Ce_{0.01\%}$,$Er_{0.01\%}$, and BeO:$Na_{5\%}$,$Ce_{0.01\%}$,$Dy_{0.01\%}$ sintered ceramic pellets were illustrated in Figure 4.105. The results confirm that all the intended elements are found in the BeO:$Na_{5\%}$,$Ce_{0.005\%}$,$Tb_{0.05\%}$, BeO:$Na_{5\%}$,$Ce_{0.01\%}$,$Er_{0.01\%}$, and BeO:$Na_{5\%}$,$Ce_{0.01\%}$,$Dy_{0.01\%}$ structures and the samples are found as highly pure. It was seen that there were no peaks of any other element in the structure other than the peaks of the coating elements (Au, Pt, and C). The presence of Be was not observed in the EDS spectrum, because the low-energy X-rays are absorbed by the Beryllium window in the measurement system.

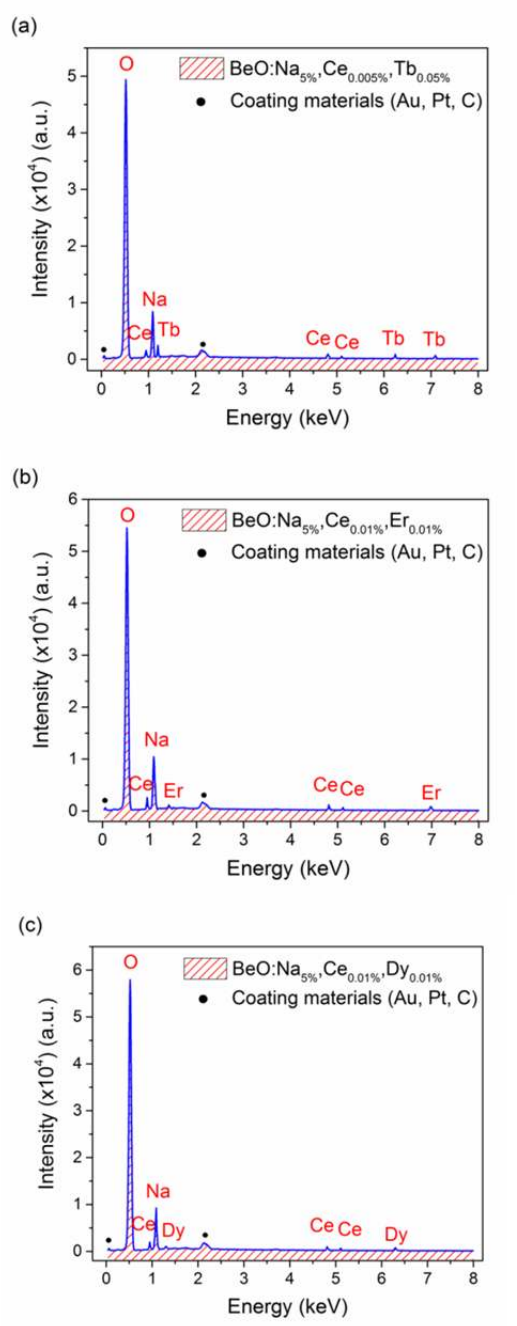

Figure 4.105. EDS spectra of (a) $BeO:Na_{5\%},Ce_{0.005\%},Tb_{0.05\%}$ (b) $BeO:Na_{5\%},Ce_{0.01\%},Er_{0.01\%}$ (c) $BeO:Na_{5\%},Ce_{0.01\%},Dy_{0.01\%}$ ceramic pellets

4.9.3. Luminescence Characterizations

TL and OSL emission spectra were measured using a Horiba Jobin-Yvon Fluorolog-3 spectrofluorometer with a 450 W continuous xenon lamp for excitation and optical detection with a Hamamatsu R928P photomultiplier operating in the photon counting mode. TL spectra of previously irradiated samples with 600 Gy beta dose were obtained at stabilized temperatures of 140 °C and 320 °C temperatures. All the TL emission spectra were corrected by the spectral response of the detection system and the dark signal subtraction. The excitation monochromator was set to 475 nm and the OSL emission spectra of the previously irradiated samples with 300 Gy beta dose were recorded by scanning from 240 to 420 nm in 3 nm increments using 0.1 s integration time. The slits of excitation and emission were selected as 5 nm and 9.5 nm, respectively. A 450 nm long-pass filter for excitation and a UFS-1 short-pass filter was used. The excitation time was 60 s. All the OSL emission spectra presented here were previously corrected by the spectral response of the system. To reduce the effect of change over time, all spectra were recorded as quickly as possible, and each was averaged after 3 consecutive scans.

TL emissions were studied also in the Technical University of DENMARK, RisØ Campus using a DA-20 model TL/OSL reader system with Detection and Stimulation Head (DASHed) unit and ANDOR spectrometer which can perform TL emission measurement simultaneously with increasing sample temperature. The system was also used for RL emissions at different temperatures. The obtained TL emission graph was presented as a 2D Mapping Plot.

A DA-20 model RisØ TL/OSL reader system was used for the TL and OSL measurements. The samples were irradiated using a ^{90}Sr-^{90}Y beta particle source (2.27 MeV maximum energy, 6.689 Gy/min dose rate). TL and OSL emissions in the UV region were detected using a Hoya U-340 filter placed in front of the bialkali photomultiplier tube (PMT) unit. In OSL readouts, samples were firstly irradiated with a 0.5 Gy beta dose and preheated to 100 °C for 10 s for

eliminating the signals that come from the shallow traps. 470 nm Blue LEDs were used for the light stimulation for 200 s in continuous wave OSL mode (CW-OSL mode). TL readouts were conducted by heating the previously irradiated samples with 0.5 Gy dose to 650 °C without any preheating. In all the TL measurements, the heating rate was 3 °C/s. Before TL/OSL comparison measurements of Ln^{3+}-doped BeO ceramics, each sample was individually calibrated according to a reference dose of 0.5 Gy for better identification of variations in responses in the same batch. All the experimental data reported in this study is presented after the corrections made using calibration factors. To increase the reliability of the luminescent experiments, both the fresh pellets and used pellets were measured after annealing at 650 °C for 10 min.

RL emissions were examined by a homemade RL system equipped with a highly sensitive spectrometer QE Pro, Ocean Optics, and Hamamatsu FFT-CCD detector. The excitation system was developed by a Moxtek mini x-rays device and a high sensitive Ocean Optics spectrometer. Mini x-ray device has 4-40 kV voltage for accelerating electrons from tungsten cathode to silver anode. The flamed current varied between 0 - 0.1 mA. The x-ray excitation energies are ~ 22 keV (Ag-Kα) and 25 keV (Ag- Kβ) possessing 0.056 and 0.049 nm wavelengths, respectively from the silver anode. The spectroscopic wavelength range was between 185-1100 nm with a 5 ms integration time. The optical resolution was around 1 nm. The quantum efficiency of this spectrometer is about 90 %.

Hologic Selenia Dimensions SecurView (25–32 kVp), General Electric Pristina (Mo/Mo 26 kV and Rh/Rh 34 kV duo anodes), and Kilovoltage range SARRP 225 kVp X-ray irradiator were used for low energy range in Sidney Kimmel Medical College at Thomas Jefferson University. All the high-energy irradiations performed at the Sheba Medical Center were to the specified dose delivered at the specific D_{max} (depth of maximum dose) of each energy/beam. D_{max} for electrons: 6 MeV 1.2 cm, 9 MeV 2.0 cm, 12 MeV 2.7 cm, 15 MeV 2.9 cm, 22 MeV 1.7 cm. D_{max} for photons: 6 MV 1.5 cm, 10 MV 2.4 cm, 15 MV 3 cm.

Samples were placed upon a bottom slab consisting of 5 cm solid water + 1 cm bolus. The upper slab (D_{max} thickness) consisted of solid water. The electron applicator size was 15 cm X 15 cm, with a source-to-surface distance of 100 cm. The photon field size was 10 cm X 10 cm, with a source-axis distance of 100 cm.

4.9.3.1. RL emissions

It is well known that the optical characteristics and the emission intensity of Ln^{3+} ions are very sensitive to the surrounding crystal structure and crystal field environment. Investigation of RL properties of Ln^{3+} doped nanocrystals is thereby important to provide knowledge about the locations and overview of luminescence bands. In this study, RL emissions of the undoped BeO and BeO:$Na_{5\%}$,$Ce_{0.005\%}$,$Tb_{0.05\%}$, BeO:$Na_{5\%}$,$Ce_{0.01\%}$,$Er_{0.01\%}$, and BeO:$Na_{5\%}$,$Ce_{0.01\%}$,$Dy_{0.01\%}$ ceramic pellets were obtained using a 1 nm resolution at room temperature and presented by comparing with that of Thermalox 995 BeO chips in Figure 4.106. It is noted that the samples are in the disc form and intensities were evaluated as the counts/mg for the comparison. As is seen from Figure 4.106, all the BeO ceramic pellets were found to exhibit a characteristic wide UV emission band of BeO located between 200-450 nm. Our products revealed higher RL sensitivity than that of commercial Thermalox 995 chips. The source of the RL emission at the maximum of 250 nm (approximately 4.9 eV) is known as the radiative annihilation of self-trapped excitons caused by X-ray excitation (Altunal et al., 2020b; Altunal et al., 2018; Ogorodnikov and Kruzhalov, 1997; Ogorodnikov et al., 1995). The luminescence in BeO is known to be characterized by the two emission bands at ~3–4 eV (300–400 nm) and 4.9 eV (Ogorodnikov and Kruzhalov, 1997). When compared with the undoped BeO sample, it has been observed that the RL signals of newly developed ceramic samples increase between 200-450 nm. The reason for this increase may be the overlap of the emission bands of Ce^{3+} ions between ~300 nm and 450 nm ($5d \rightarrow 4f$ transition) and the 3-4 eV emission bands of BeO. A similar Ce^{3+} emission was reported by Prasad et. al. (Prasad et al., 2017). In their

study, the characteristic 5d-4f emission of Ce^{3+} in YPO_4:Ce,Sm, due to the increase of Sm^{2+} and Ce^{4+} ions with increasing X-ray exposure, was observed at 3.47 and 3.73 eV. For the BeO:$Na_{5\%}$,$Ce_{0.005\%}$,$Tb_{0.05\%}$ sample, at least six overlapped peaks in the visible region appeared in RL spectra. It can be said that these visible range emission peaks are due to the $^5D_4 \rightarrow {}^7F_j$ $(j = 6-0)$ characteristic transitions of Tb^{3+} with the emission bands located at 490, 540, 580, 620, 650, 660 and 675 nm (Bünzli and Eliseeva, 2010). The observed emission peak at ~ 570 nm in RL spectrum of BeO:$Na_{5\%}$,$Ce_{0.01\%}$,$Er_{0.01\%}$ sample represents the $^4S_{3/2} \rightarrow {}^4I_{15/2}$ characteristic transition of Er^{+3}. Three RL emission bands located at 475, 580, and 640 nm which are originated from the $^4F_{9/2} \rightarrow {}^6H_j$ $(j = 15/2-11/2)$ transitions of Dy^{3+} were observed in BeO:$Na_{5\%}$,$Ce_{0.01\%}$,$Dy_{0.01\%}$ sample (see Figure 4.106). As a result, the peaks corresponding to the characteristic transitions of Ln^{3+} ions and increasing RL signal intensities demonstrated that each Ln^{3+} ion plays a role as a luminescence center in the BeO structure.

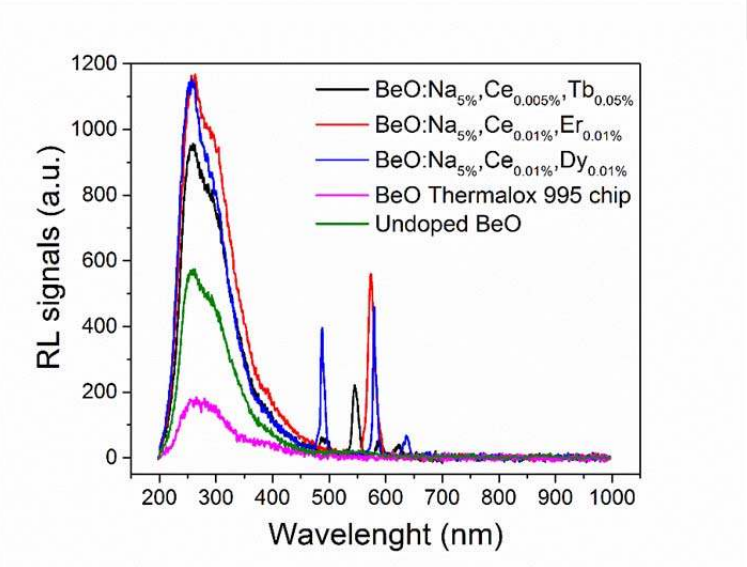

Figure 4.106. RL emissions of the undoped BeO, BeO:$Na_{5\%}$,$Ce_{0.005\%}$,$Tb_{0.05\%}$, BeO:$Na_{5\%}$,$Ce_{0.01\%}$,$Er_{0.01\%}$, BeO:$Na_{5\%}$,$Ce_{0.01\%}$,$Dy_{0.01\%}$ ceramic pellets and BeO Thermalox 995 chip. RL signals were evaluated as the counts/mg for the comparison.

On the other hand, the temperature dependence of RL emissions was also studied in the RisØ system in DENMARK, by irradiating the samples at a certain reading temperature and simultaneously reading emission. RL emissions of the undoped BeO and BeO:$Na_{5\%}$,$Ce_{0.005\%}$,$Tb_{0.05\%}$, BeO:$Na_{5\%}$,$Ce_{0.01\%}$,$Er_{0.01\%}$, and BeO:$Na_{5\%}$,$Ce_{0.01\%}$,$Dy_{0.01\%}$ ceramic pellets were obtained from 180 nm up to 620 nm at different reading temperature (up to 300 °C) and presented by comparing with that of Thermalox 995 BeO chips in Figure 4.107, Figure 4.108, Figure 4.109, Figure 4.110, and Figure 4.111, respectively.

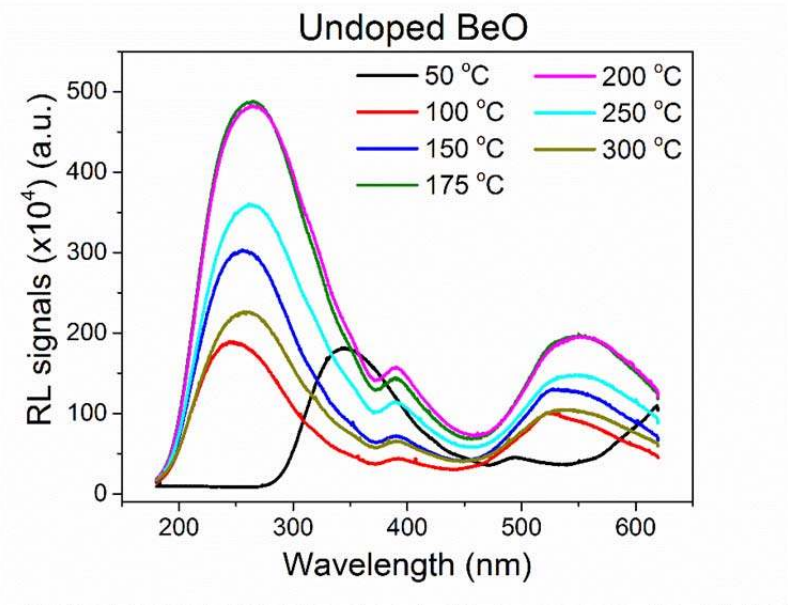

Figure 4.107. Temperature dependence of RL emissions obtained from undoped BeO ceramic pellets

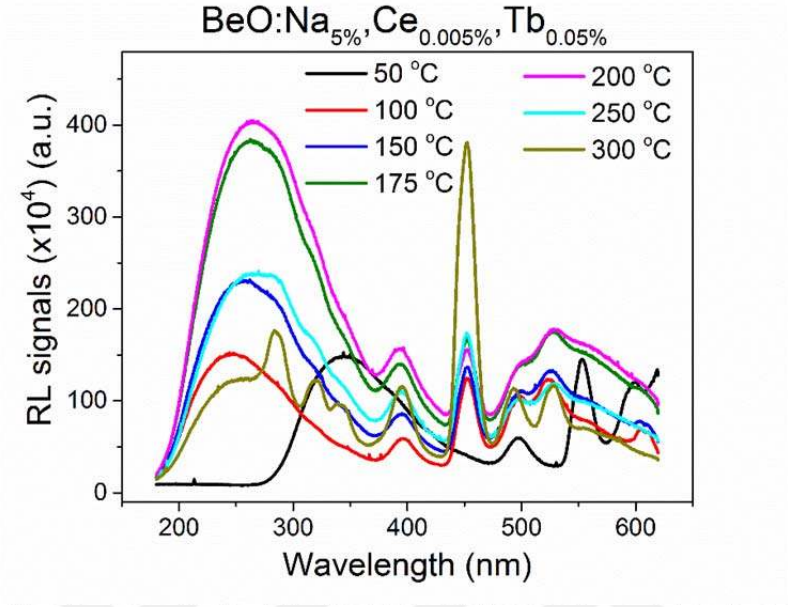

Figure 4.108. Temperature dependence of RL emissions obtained from $BeO:Na_{5\%},Ce_{0.005\%},Tb_{0.05\%}$ ceramic pellets

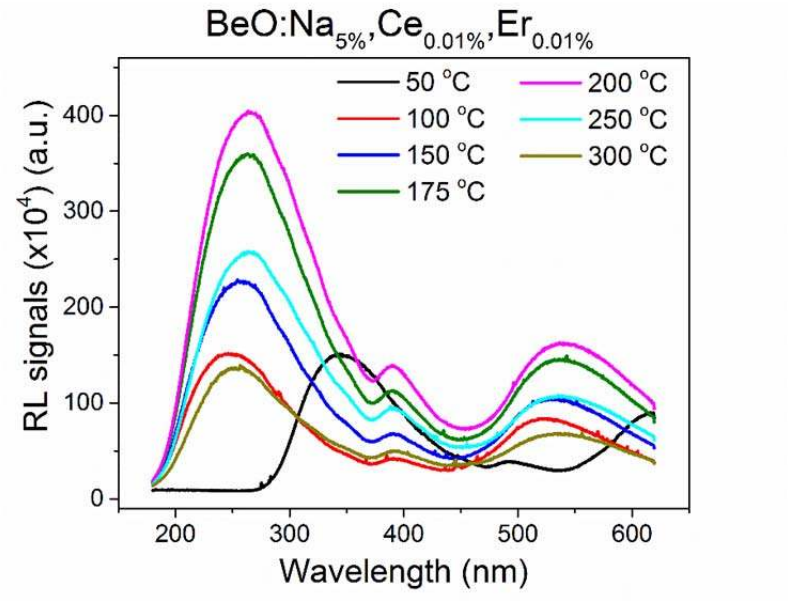

Figure 4.109. Temperature dependence of RL emissions obtained from $BeO:Na_{5\%},Ce_{0.01\%},Er_{0.01\%}$ ceramic pellets

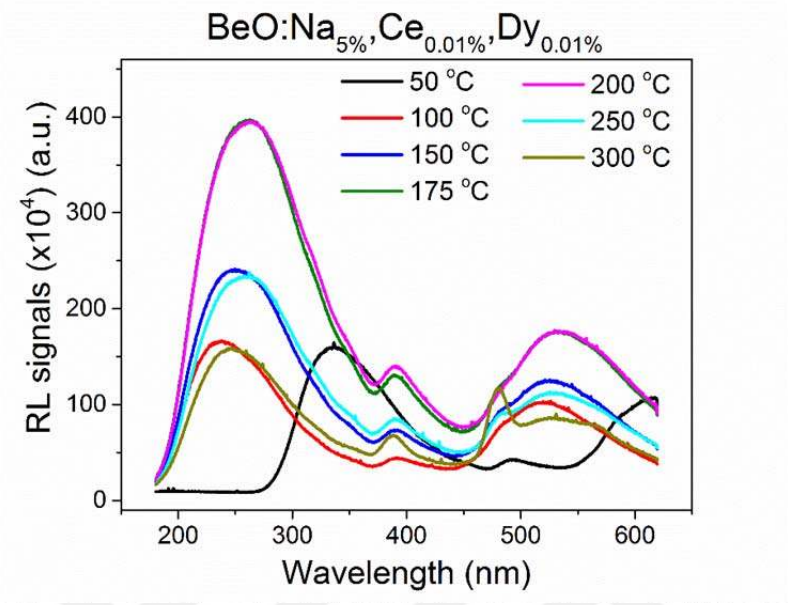

Figure 4.110. Temperature dependence of RL emissions obtained from $BeO:Na_{5\%},Ce_{0.01\%},Dy_{0.01\%}$ ceramic pellets

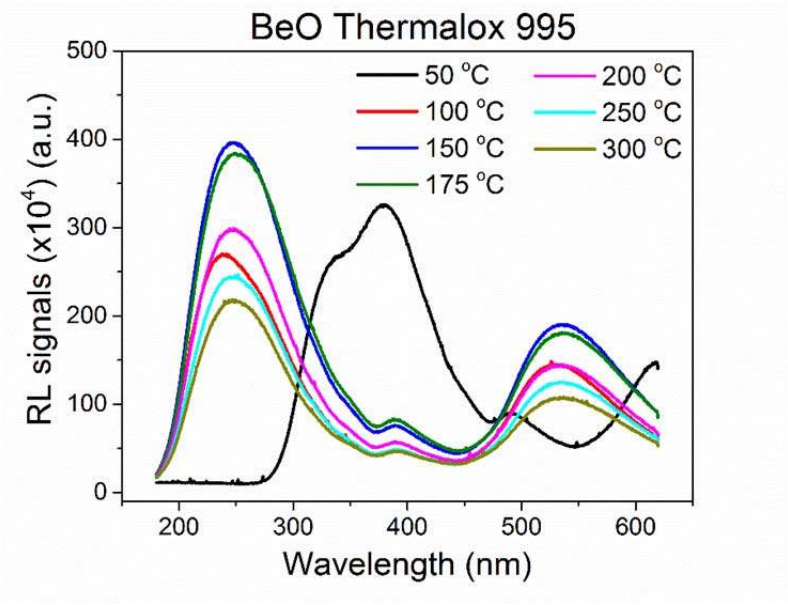

Figure 4.111. Temperature dependence of RL emissions obtained from Thermalox 995 BeO chips ceramic pellets

As is seen from Figure 4.107, Figure 4.108, Figure 4.109, Figure 4.110, and Figure 4.111, the RL emissions were significantly affected in each sample by changing the reading temperature. Especially in Figure 4.108, if we examine the $BeO:Na_{5\%},Ce_{0.005\%},Tb_{0.05\%}$ ceramic pellets, it is seen that Tb^{3+} emission is more dominant in the structure with increasing temperature. This shows us that Tb^{3+} emission activates the traps located after 300 °C in the TL glow curve. In addition, it was observed that the emission of Ce dopant ion became more dominant with increasing temperature.

On the other hand, since the emissions of Er and Dy dopant ions could not be observed separately in Figure 4.109 and Figure 4.110, their thermal dependence of RL emissions could not be fully understood. As an unexpected result, if we look at the emissions obtained in the RL experiments carried out at 50 °C, it was observed that it was very different from the measurement results carried out at room temperature at Mersin University (see Figure 4.106). Similarly, the signals with increasing temperature showed similar results in two different systems. It should be noted that further research is needed since the physical basis of measurements taken at 50 °C is not fully understood.

4.9.3.2. TL of BeO ceramics

Although the TL emission spectrum of BeO is characterized by a wide emission band with the maximum peak point at 335 nm (McKeever et al., 1995), more in-depth data on recombination pathways in BeO are needed. However, the representation of wavelength vs TL intensity curve at stabilized temperatures (see Figure 4.112) is a good starting point to learn more about the recombination pathways for three newly developed lanthanide-doped BeO samples. It was observed that 140 °C and 320 °C TL traps of undoped BeO gave emission in two emission bands separated by 500 nm. The first and second emission bands appeared at 300 and 700 nm maxima, respectively. These results showed that the dominant luminescence bands in RL and TL processes for undoped BeO might be

different (see Figure 4.107 and Figure 4.112) from each other. However, in both cases, the luminescence bands located between 300 and 400 nm (i.e., 3-4 eV) and were observed using the U-340 filter, are dependent on the same luminescence mechanism. Similar behavior has been observed in three newly developed BeO ceramic pellets indicating recombination pathways for different TL traps. It was observed that the sensitivity of TL emissions obtained at 140 °C increased compared to the TL emission of undoped BeO. However, TL emissions of newly developed BeO-based dosimeters could not be recorded at a stabilized temperature of 320 °C. Significant change in TL emission was observed only for $BeO:Na_{5\%},Ce_{0.01\%},Er_{0.01\%}$ sample when compared with the TL emissions of the other ceramic products, $BeO:Na_{5\%},Ce_{0.005\%},Tb_{0.05\%}$ and $BeO:Na_{5\%},Ce_{0.01\%},Dy_{0.01\%}$. Since the characteristic emission of Ce^{3+} ion is at 300-450 nm and the dominant emission of Er^{3+} ion is at 570 nm, it may have caused a shift to the right in the first part of the TL emission spectrum and towards the visible region in the second part. As a result of these shifts in TL emission, an increase in measurable emission of $BeO:Na_{5\%},Ce_{0.01\%},Er_{0.01\%}$ can be expected to be between 300 and 400 nm in the transmittance range of the Hoya-340 filter.

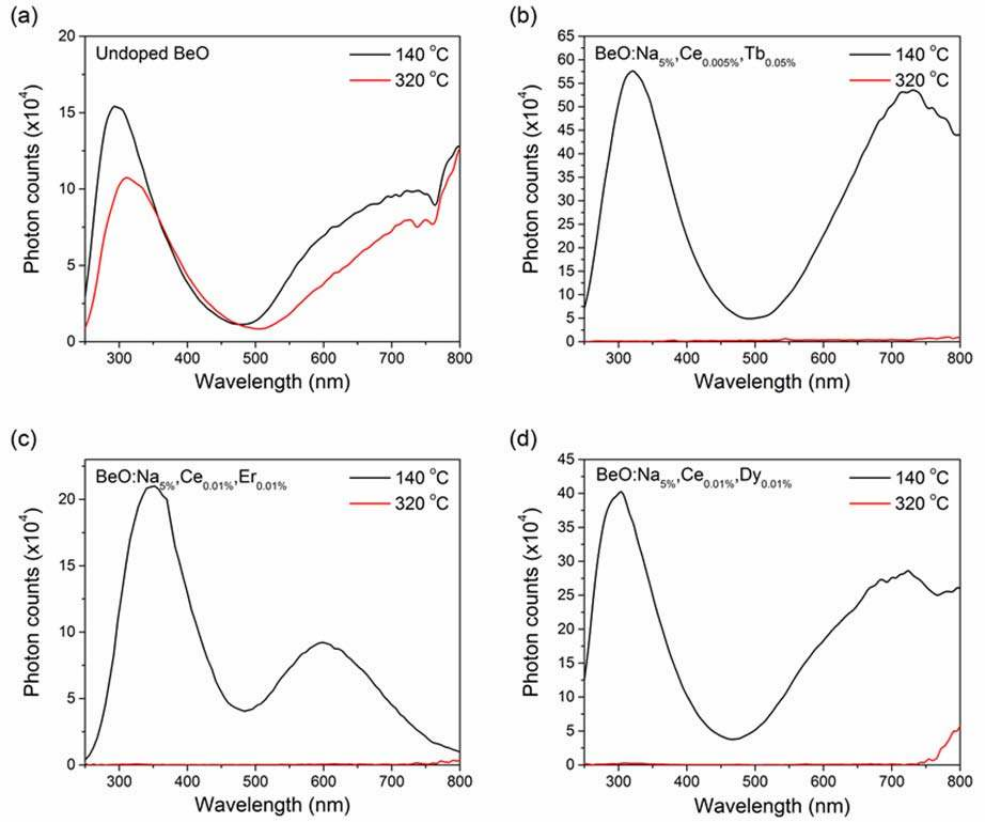

Figure 4.112. TL emissions of (a) the undoped BeO (b) BeO:$Na_{5\%}$,$Ce_{0.005\%}$,$Tb_{0.05\%}$ (c) BeO:$Na_{5\%}$,$Ce_{0.01\%}$,$Er_{0.01\%}$ (d) BeO:$Na_{5\%}$,$Ce_{0.01\%}$,$Dy_{0.01\%}$ ceramic pellets

On the other hand, TL emissions were also studied in the Risø system in DENMARK, by heating up to a target temperature and reading the sample emission simultaneously. TL emissions of the undoped BeO and BeO:$Na_{5\%}$,$Ce_{0.005\%}$,$Tb_{0.05\%}$, BeO:$Na_{5\%}$,$Ce_{0.01\%}$,$Er_{0.01\%}$, and BeO:$Na_{5\%}$,$Ce_{0.01\%}$,$Dy_{0.01\%}$ ceramic pellets were illustrated as a contour plots and presented in Figure 4.113, Figure 4.114, Figure 4.115, Figure 4.116, and Figure 4.117, respectively.

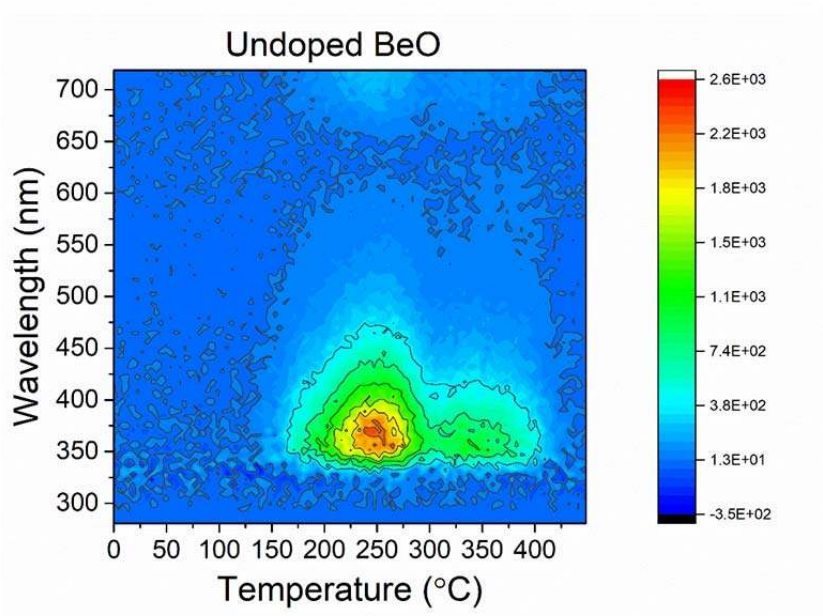

Figure 4.113. TL emission spectrum of undoped BeO ceramic sample shown as a contour plot.

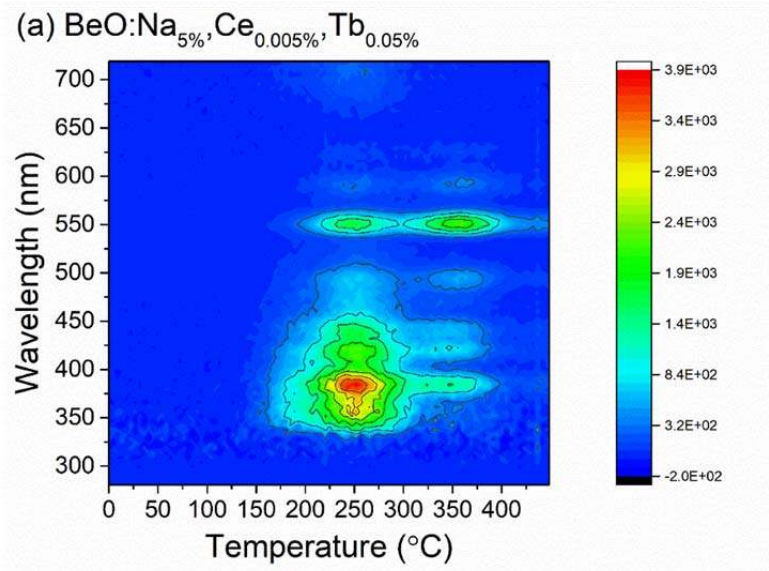

Figure 4.114. TL emission spectrum of BeO:$Na_{5\%}$,$Ce_{0.005\%}$,$Tb_{0.05\%}$ ceramic sample shown as a contour plot.

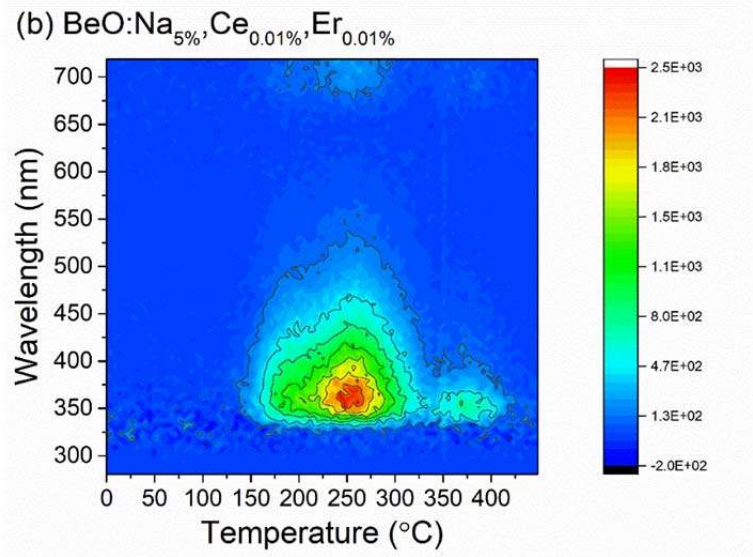

Figure 4.115. TL emission spectrum of BeO:$Na_{5\%}$,$Ce_{0.01\%}$,$Er_{0.01\%}$ ceramic sample shown as a contour plot.

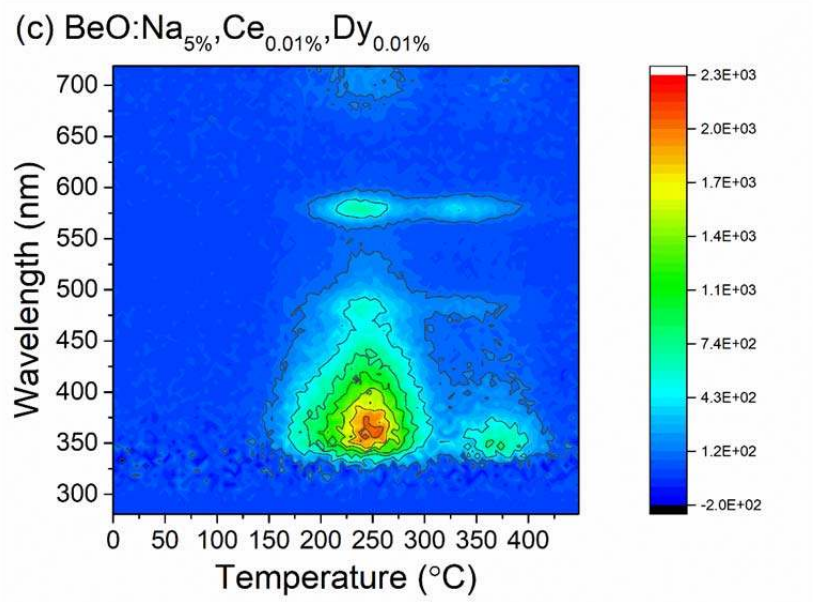

Figure 4.116. TL emission spectrum of BeO:$Na_{5\%}$,$Ce_{0.01\%}$,$Dy_{0.01\%}$ ceramic sample shown as a contour plot.

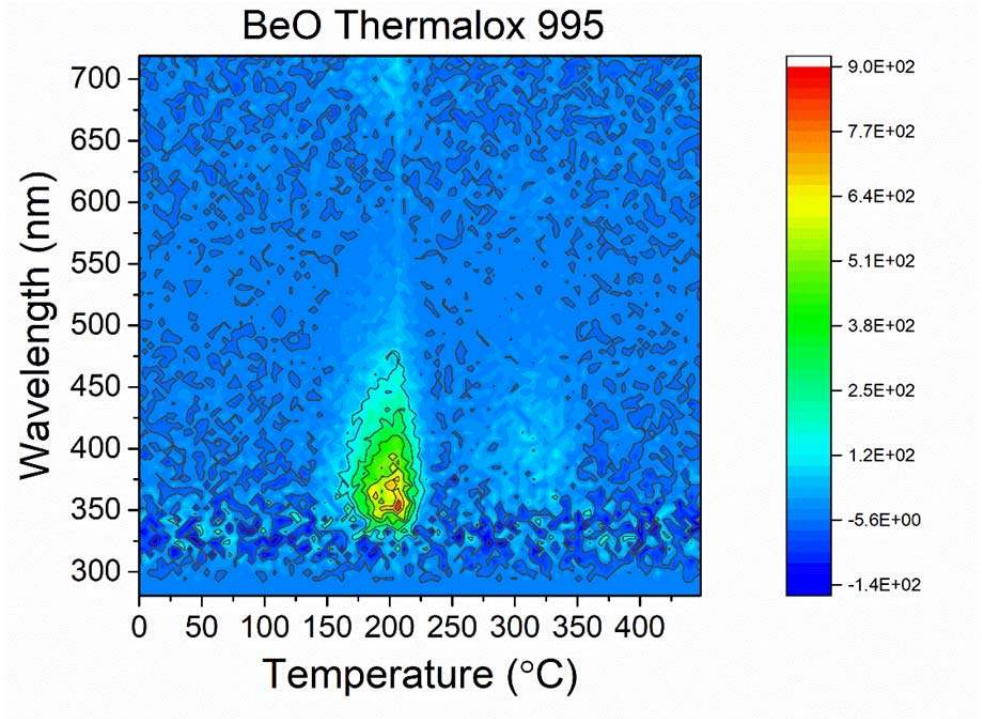

Figure 4.117. TL emission spectrum of Thermalox 995 BeO chip sample shown as a contour plot.

As can be seen from Figure 4.113, the characteristic TL emission of undoped BeO is located between 300 nm and 450 nm. Considering the TL glow curve, at 200 °C the center of the dominant emission is 325 nm and widely seen, while the emission of TL traps after 300 °C is relatively weak and located at 300 nm. In the TL emission spectrum of BeO:$Na_{5\%}$,$Ce_{0.005\%}$,$Tb_{0.05\%}$ sample, it was observed that Tb^{3+} dopant ion was activated in deeper traps and exhibited characteristic emissions. According to the TL spectrum of the undoped BeO sample, it was observed that Ce^{3+} dopant ion activates the traps located around 200 °C and 340 °C, exhibiting its characteristic emissions. While the characteristic emission of the Er^{3+} dopant ion in Figure 4.115 cannot be observed separately, in Figure 4.116 it is seen that the characteristic emission of the Dy dopant ion contributes to the TL peaks after 300 °C. In the light of these results, it can be said

that undoped BeO significantly improves TL emission with the characteristic ions of additive ions aimed to enhance luminescence. The TL emission obtained from the Thermalox 995 BeO sample is compatible with the literature, and it was observed to be very weak from the BeO-based ceramic dosimeters synthesized in this study.

Figure 4.118 shows the TL glow curves of the BeO samples in linear and semi-log scales. The undoped BeO pellet exhibited five peaks at ~180, ~250, ~360, ~495, and ~580 °C with a heating rate of 3 °C/s after 0.5 Gy beta dose exposure. The first peak located at 180 °C dominated the TL glow curve compared to the peaks located in the high-temperature region. On the other hand, the TL glow curve of the BeO Thermalox 995 chip revealed three main TL peaks at 75, 180, and 320 °C, although some deep traps having very low sensitivities were also found after 320 °C. The shoulder peak located at 250 °C in the TL signals of our synthesized samples was not observed in Thermalox 995 BeO chips. Conversely, a double TL peak (180 °C and 250 °C) in the main dosimetric peak region of Thermalox 995 has been reported in the literature (Aşlar et al., 2021). Similar to the undoped BeO sample, three newly developed BeO samples have 5 peaks, each. The shallow TL peak at 75 °C in the Thermalox 995 chip did not appear in our samples. When compared to each other, a decrease in the sensitivity of TL peaks located before 300 °C and a significant increase in high-temperature peaks were observed for BeO:$Na_{5\%}$,$Ce_{0.005\%}$,$Tb_{0.05\%}$. However, a leftward shift occurred at its maximum peak temperatures. TL signals of BeO:$Na_{5\%}$,$Ce_{0.01\%}$,$Er_{0.01\%}$ sample were found to be ten times more sensitive than that of the BeO Thermalox 995 chip. BeO:$Na_{5\%}$,$Ce_{0.005\%}$,$Tb_{0.05\%}$ and BeO:$Na_{5\%}$,$Ce_{0.01\%}$,$Dy_{0.01\%}$ samples showed higher TL emissions as compared to that of BeO:$Na_{5\%}$,$Ce_{0.01\%}$,$Er_{0.01\%}$ (see Figure 4.118), whereas the latter phosphor showed the highest TL signal intensity in the results presented in Figure 4.118. This observed difference probably coincides with the shift seen in TL emissions with doping (mentioned above) and the consequent maximum transmittance of the Hoya U-340 filter.

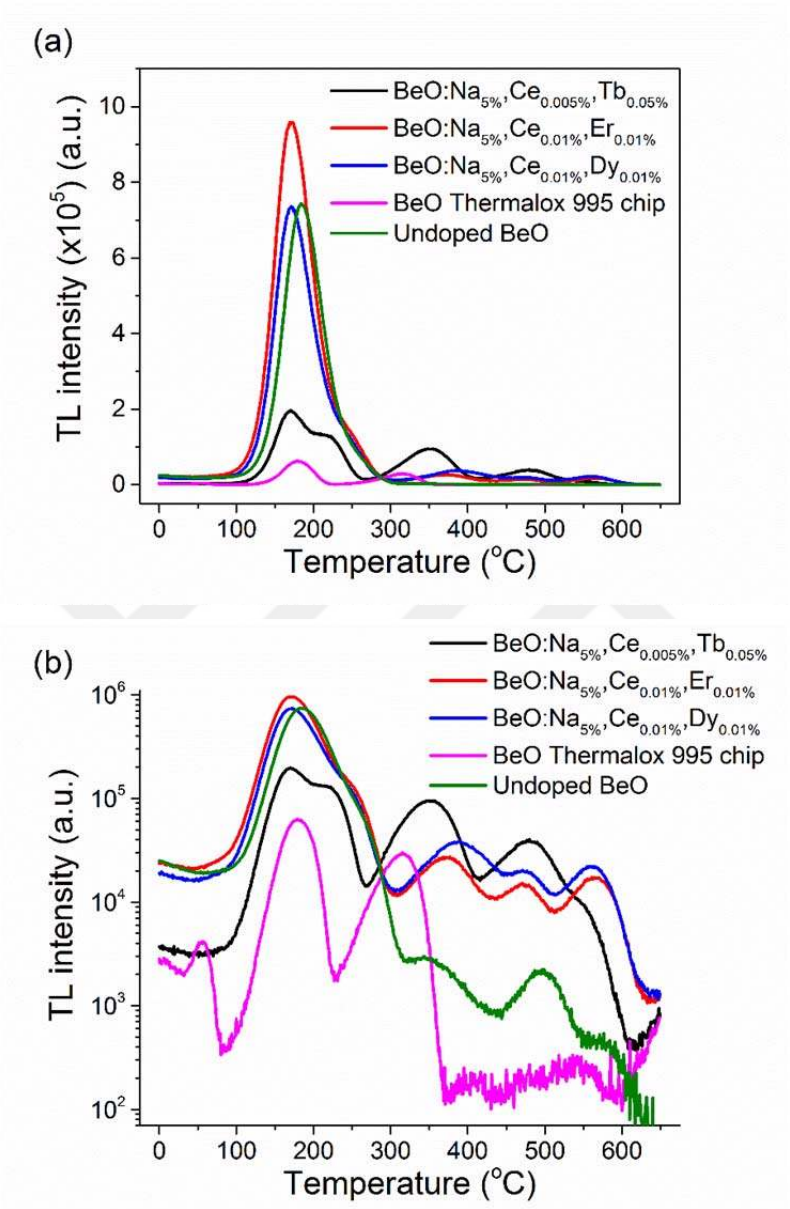

Figure 4.118. TL glow curves of undoped BeO, BeO:$Na_{5\%}$,$Ce_{0.005\%}$,$Tb_{0.05\%}$, BeO:$Na_{5\%}$,$Ce_{0.01\%}$,$Er_{0.01\%}$, BeO:$Na_{5\%}$,$Ce_{0.01\%}$,$Dy_{0.01\%}$ ceramic pellets and BeO Thermalox 995 chips in (a) linear scale (b) semi-log scale for a better presentation of low sensitive peaks at high temperature region

4.9.3.3. OSL of BeO ceramics

Figure 4.119 shows the OSL emission spectra of previously irradiated BeO ceramics with 300 Gy beta dose together with a transmission range of the Hoya U-340 filter which is used in the TL/OSL Risø reader.

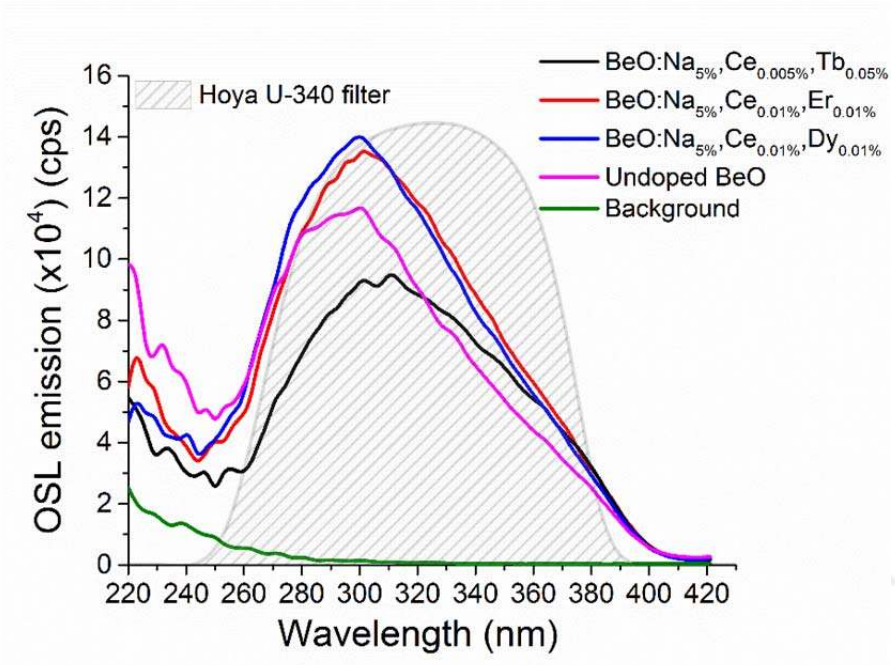

Figure 4.119. OSL emissions of the undoped BeO, BeO:$Na_{5\%}$,$Ce_{0.005\%}$,$Tb_{0.05\%}$, BeO:$Na_{5\%}$,$Ce_{0.01\%}$,$Er_{0.01\%}$, and BeO:$Na_{5\%}$,$Ce_{0.01\%}$,$Dy_{0.01\%}$ ceramic pellets

As is seen from Figure 4.119 that the main OSL emission bands are located between ~250 and ~400 nm with a maximum peak point around 300 nm. BeO:$Na_{5\%}$,$Ce_{0.01\%}$,$Dy_{0.01\%}$ appeared as the dominant band with maximum OSL emission intensity. These results showed that the dominant luminescence bands in TL and OSL processes are appearing as most the same, but the emission bands are different in RL processes. It can be suggested that the commonly appeared emission bands in each case, located between 300 and 400 nm (i.e., 3-4 eV) are dependent on the same luminescence mechanism in all luminescence processes

(RL, TL, and OSL). When the OSL emissions of three newly developed BeO samples were compared with the emission band obtained from the undoped sample, it was observed that the main luminescence bands of the doped-BeO samples shifted towards higher wavelengths (see Figure 4.119). It is clear that with different dopants it is possible to produce differences (wavelength and sensitivity) in the OSL emissions of BeO.

Simple OSL decay curves of the undoped BeO, BeO:$Na_{5\%}$,$Ce_{0.005\%}$,$Tb_{0.05\%}$, BeO:$Na_{5\%}$,$Ce_{0.01\%}$,$Er_{0.01\%}$, BeO:$Na_{5\%}$,$Ce_{0.01\%}$,$Dy_{0.01\%}$ ceramic pellets, and BeO Thermalox 995 chips were presented in Figure 4.120. Each decay curve represents the average of OSL signals obtained from three samples irradiated with a 0.5 Gy dose. As is seen in the Figure 4.120, BeO:$Na_{5\%}$,$Ce_{0.01\%}$,$Er_{0.01\%}$ ceramic pellets have the highest OSL sensitivity. OSL signals of the undoped BeO were developed with appropriate dopants, and the OSL signal intensities of the newly produced BeO samples are found to be very close to or higher than that of BeO Thermalox 995 chips.

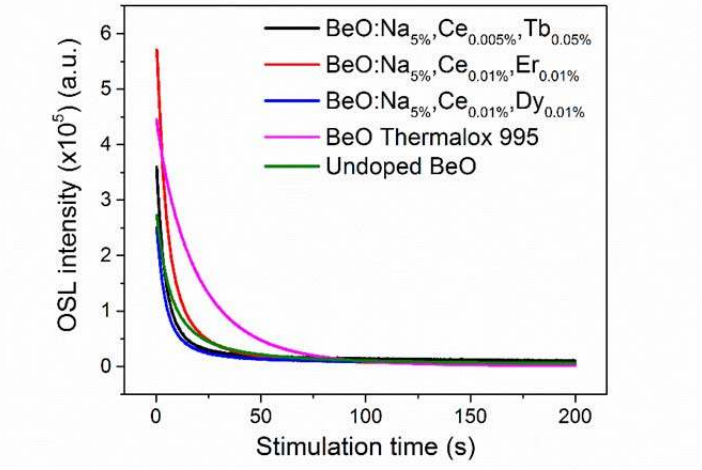

Figure 4.120. OSL decay curves of the undoped BeO, BeO:$Na_{5\%}$,$Ce_{0.005\%}$,$Tb_{0.05\%}$, BeO:$Na_{5\%}$,$Ce_{0.01\%}$,$Er_{0.01\%}$, BeO:$Na_{5\%}$,$Ce_{0.01\%}$,$Dy_{0.01\%}$ ceramic pellets, and BeO Thermalox 995 chips in linear scale after 0.5 Gy beta dose exposure. The samples were stimulated with blue light for 200 s

Besides the determination of OSL sensitivities, the analyzes of the OSL decay curves of newly developed samples were also examined via a fitting method to the combination of the time-decaying functions. Figure 4.121 shows the OSL decay curves and their decaying components obtained using a linear sum of the first-order curves. The fitting equation used for the analyzes can be written as:

$$y = background\ (bkg) + 1^{st}\ (fast)component + 2^{nd}\ (medium)component + 3^{rd}\ (slow)component + \cdots \quad (4.16)$$

$$I(t) = bkg + I_1\exp(\frac{t}{\tau_1}) + I_2\exp(\frac{t}{\tau_2}) + I_3\exp(\frac{t}{\tau_3}) + \cdots$$

where 1^{st}, 2^{nd}, and 3^{rd}components are the first-order ($b = 1$) time decaying components representing the fast, medium and slow decaying parts of the OSL signals, respectively. t is the stimulation time; $I(t)$ is the intensity of the OSL signals as a function of time; bkg is the background signal of the OSL reader. $I_{1,2}$ and $\tau_{1,2}$ are the amplitudes, and lifetimes of the separate components, respectively. The goodness of the curve fitting was estimated via the figure of merit (FOM) values (Balian and Eddy, 1977). The curve fitting using two components did not well fit the data points in the last 25 s readout of OSL curves which were obtained from the BeO:$Na_{5\%}$,$Ce_{0.005\%}$,$Tb_{0.05\%}$, BeO:$Na_{5\%}$,$Ce_{0.01\%}$,$Er_{0.01\%}$, BeO:$Na_{5\%}$,$Ce_{0.01\%}$,$Dy_{0.01\%}$ ceramic pellets. For BeO Thermalox 995, the FOM value was evaluated as 0.71 and two components' first-order curves were well fitted with the data. The fitting curve obtained using the three components with the acceptable FOM values (less than 3.00) was statistically found better than that obtained using the two components. FOM values and the other fitting parameters are given in Table 4.16.

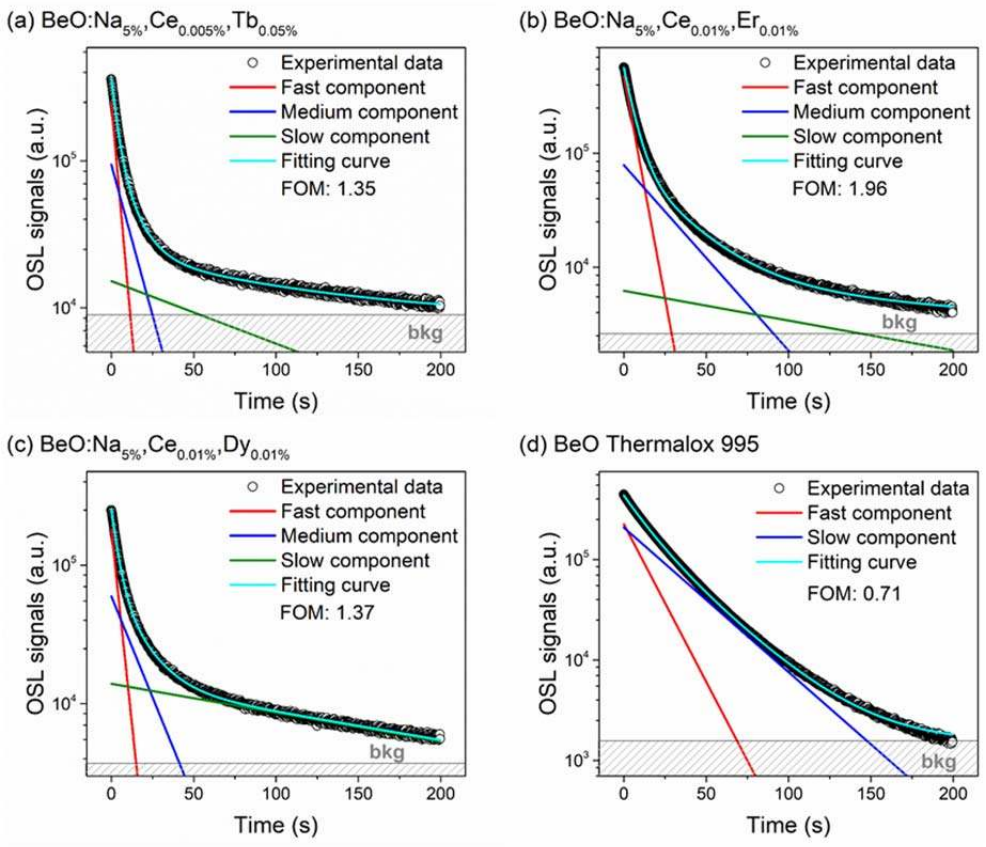

Figure 4.121. OSL decay curves and their decaying components of the $BeO:Na_{5\%},Ce_{0.005\%},Tb_{0.05\%}$, $BeO:Na_{5\%},Ce_{0.01\%},Er_{0.01\%}$, $BeO:Na_{5\%},Ce_{0.01\%},Dy_{0.01\%}$ ceramic pellets, and BeO Thermalox 995 chips in semi-log scale with goodness of fitting FOM values.

Table 4. 16. $\tau_{1,2}$ decay times, $b_{1,2}$ kinetic orders and FOM values of the components of OSL decay curves for newly developed BeO samples and Thermalox 995. Decay fittings were done using two time-decaying functions.

No.	*Fast component*		*Medium component*		*Slow component*			
	I_1 (count)	τ_1 (s)	I_2 (count)	τ_2 (s)	I_3 (count)	τ_3 (s)	bkg (count)	FOM (%)
BeO:Na,Ce,Tb	2.47E+05	3.46	9.42E+04	10.60	1.52E+04	101.99	8.42E+03	1.35
BeO:Na,Ce,Er	4.75E+05	5.58	7.90E+04	26.66	6.21E+03	166.12	2.60E+03	1.96
BeO:Na,Ce,Dy	1.81E+05	3.87	5.97E+04	14.88	1.39E+04	208.44	1.36E+02	1.37
Thermalox 995	2.25E+05	13.85	2.08E+05	30.20	-	-	1.54E+03	0.71

It should be remembered that this curve fitting is only an oversimplified approximation of the actual situation. To learn more about the traps and transitions involved in OSL development, studies focused on the numerical solutions of the charge trafficking equations are required.

4.9.3.4. Correlation between TL and OSL signals

To determine which part of the TL glow curves obtained from the BeO samples is optically active or not, three TL glow curves (TL, TL after OSL, residual TL) for each sample were measured and presented in Figure 4.122. The residual TL curve was obtained by subtracting the TL after OSL measurement data from the TL data. The residual TL curves for the BeO samples correspond to the optically active parts in the TL glow curves. As is seen in Figure 4.122a, all peaks of the BeO:$Na_{5\%}$,$Ce_{0.005\%}$,$Tb_{0.05\%}$ were affected by light stimulation. This result is not desirable because in this case, it will be difficult to identify the source of OSL signals. In Figure 4.122b, only the first 180 °C TL peak was emptied by OSL measurements whereas the others were not. It is evident that the source of the OSL signals of BeO:$Na_{5\%}$,$Ce_{0.01\%}$,$Er_{0.01\%}$ sample was associated with the 180 °C TL peak. Similarly, we observed the same light effect for the BeO:$Na_{5\%}$,$Ce_{0.01\%}$,$Dy_{0.01\%}$ sample, and the source of the OSL signals appeared to be a 180 °C TL peak (see Figure 4.122c). In Thermalox 995 BeO chip, the first and second TL peaks were severely affected by light, while the third peak was partially affected. According to this result, the origin of the OSL signals in the Thermalox 995 BeO chip could be these three peaks (see Figure 4.122d). It should be noted that the change in TL intensity due to light exposure can also occur because of the depletion of the recombination centers. This would occur if both OSL and TL traps use the same centers. Therefore, the examination of the step annealing curve is a better method for finding the position of the OSL traps.

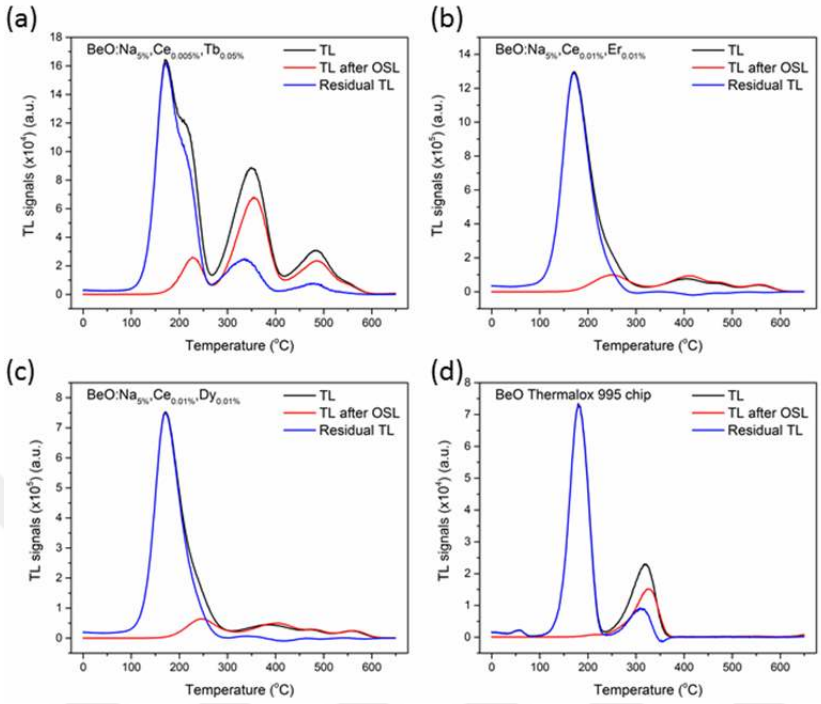

Figure 4.122. TL, TL after OSL, and residual TL glow curves of (a) $BeO:Na_{5\%},Ce_{0.005\%},Tb_{0.05\%}$ (b) $BeO:Na_{5\%},Ce_{0.01\%},Er_{0.01\%}$ (c) $BeO:Na_{5\%},Ce_{0.01\%},Dy_{0.01\%}$ ceramic pellets (d) BeO Thermalox 995 chips

If there are light-affected TL traps in a region, there are also thermally unstable OSL traps in this area. The fact that both are in the same region will provide us an important unknown in finding exactly where the OSL traps correspond in a TL glow curve and the source of luminescence in BeO. For this purpose, thermal stability measurements were performed by preheating the sample from 50 to 500 °C in 10 °C steps. First, the 0.5 Gy irradiated samples were continuously annealed, and the residual OSL data were obtained each time. Following the OSL measurement, TL readout was carried out up to 650 °C for preparing the sample for the following cycle. The changes in the integrated OSL signals versus the annealing temperatures were illustrated together with the residual TL curve for BeO samples in Figure 4.123.

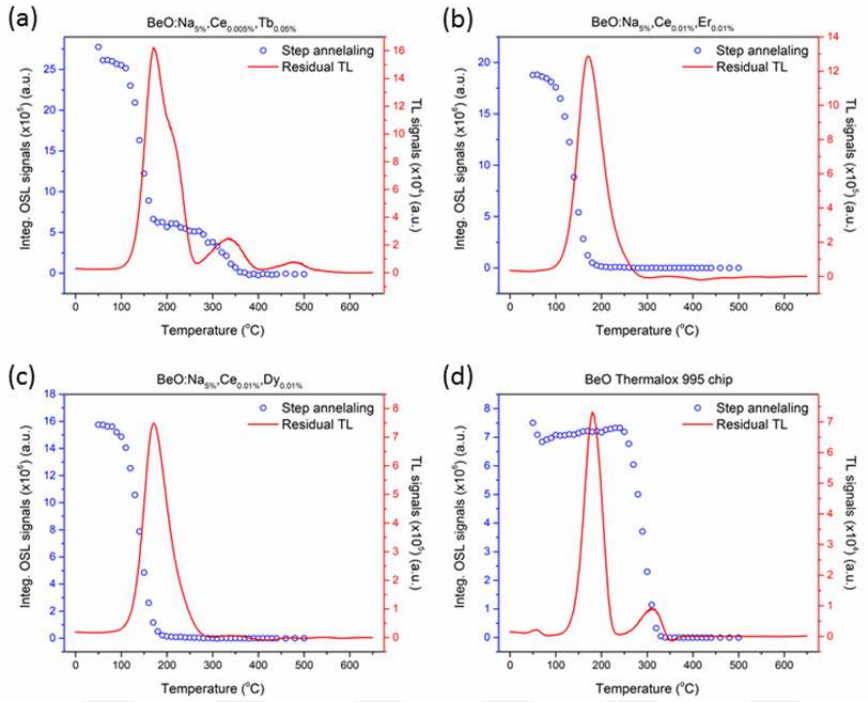

Figure 4.123. Step annealing curves and residual TL signals of (a) $BeO:Na_{5\%},Ce_{0.005\%},Tb_{0.05\%}$ (b) $BeO:Na_{5\%},Ce_{0.01\%},Er_{0.01\%}$ (c) $BeO:Na_{5\%},Ce_{0.01\%},Dy_{0.01\%}$ ceramic pellets (d) BeO Thermalox 995 chip

As is seen in Figure 4.123a, the first decrease in OSL signals starts after discharging of the 180 °C TL peak in $BeO:Na_{5\%},Ce_{0.005\%},Tb_{0.05\%}$. After stable OSL signals up to 280 °C in the step-annealing curve, OSL signals decreased for the second time. With the discharging of 360 °C TL peak, the OSL signals reached zero value. Results demonstrate that the OSL signals might originate from both the 180 and 370 °C TL peaks i.e., traps responsible for the TL peak at 250 °C, affected by light, have no contribution to the OSL signals. Optical stimulation might use the same recombination centers associated with the 180 and 370 °C TL peaks. Figure 4.123b and Figure 4.123c show that there exists only one thermal decrease in OSL signals indicating that the origin of OSL signals responsible only for 180 °C TL peaks in TL glow curves of $BeO:Na_{5\%},Ce_{0.01\%},Er_{0.01\%}$ and

,BeO:$Na_{5\%}$,$Ce_{0.01\%}$,$Dy_{0.01\%}$. Similar thermal stability behaviors were reported in our previous studies for BeO samples with various dopants (Altunal et al., 2019a; Altunal et al., 2019b; Altunal et al., 2020c; Altunal et al., 2020e). As an interesting observation, OSL depletion in the step annealing curves was observed much earlier than the appearance of the corresponding 180 °C TL peak. For a given trap, since the thermal + optical excitation energy will be greater than the thermal excitation energy, i.e., higher optical energy is needed to reach the excited state potential in terms of configuration coordinate diagrams, it can be said that electrons are freed from the traps coinciding with lower temperatures. Thus, it can be presumed that OSL depletion in the step annealing curve occurred much earlier than the 180 °C TL peak. As an expected result, the TL peak at 180 °C does not contribute to OSL signals as there is no reduction in total OSL signals up to almost 260 °C (see Figure 4.123d). Although the 180 °C TL peak is very sensitive to light, too, the OSL signals are only caused by the TL traps responsible for the TL peak located around 340 °C and by the shallow traps with a small contribution.

To take a closer look at the relationship between TL and OSL traps and to gain insight into the possible transmission mechanism of charges, the method known as Thermally transferred OSL (TT-OSL) was also investigated. The process can be briefly explained as a thermally transferred charge transfer from the "hard-to-bleach" trapping centers by heating the samples, to the optically active trapping centers responsible for the deeper OSL signal (Jain et al., 2003). TT-OSL signals of the previously 0.5 Gy irradiated three newly developed ceramics were examined by firstly optical bleaching (200 s blue light stimulation), secondly preheating to T_{stop} at 5 °C/s, followed by cooling to room temperature, and thirdly performing 200 s OSL readout. The subsequent readings were done in 25 °C steps, and reading up to 650 °C at 5 °C/s was followed after each step. Figure 4.124 compares the TT-OSL signal measured in the previously mentioned third step via the step-annealing data of the OSL signal and two TL areas (the integrated TL signals obtained from 150 to 290 °C, and from 290 to440 °C) vs the pre-heating temperature T_{stop}.

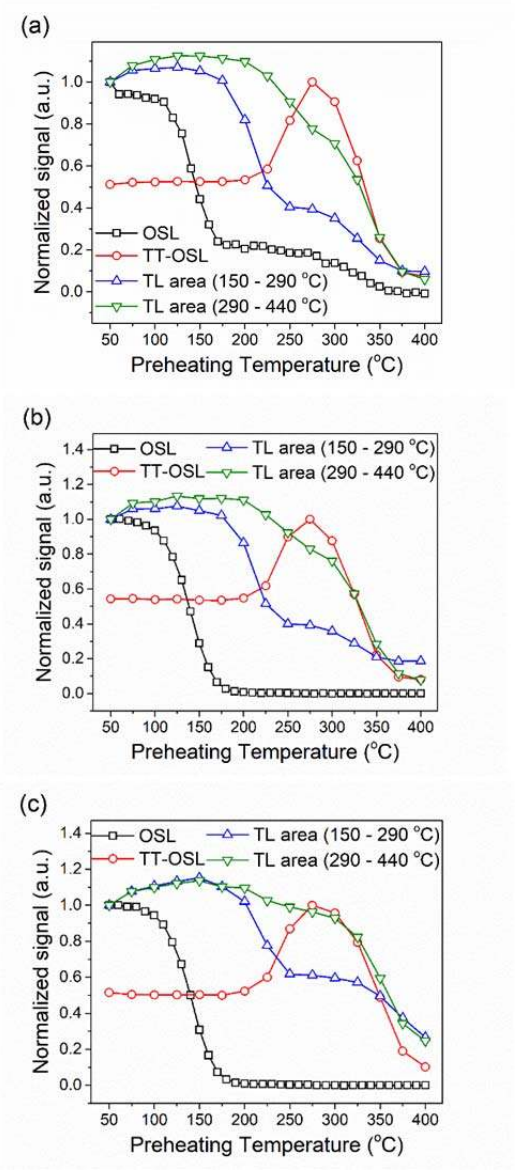

Figure 4.124. TT-OSL signals of three newly developed ceramic samples previously irradiated with 0.5 Gy beta dose (a) BeO:$Na_{5\%}$,$Ce_{0.005\%}$,$Tb_{0.05\%}$ (b) BeO:$Na_{5\%}$,$Ce_{0.01\%}$,$Er_{0.01\%}$ (c) BeO:$Na_{5\%}$,$Ce_{0.01\%}$,$Dy_{0.01\%}$ and comparison with the OSL signal over two TL areas (150 - 290 °C, and 290 - 440 °C), as a function of the pre-heating temperature T_{stop}.

As is seen from Figure 4.124 that TT-OSL signals tended to increase while TL signals are decreasing in two temperature ranges. While TT-OSL signals were stable in a value of almost 50 % of the original OSL signals by decreasing TL area (150 - 290 °C), TT-OSL signals increased with decreasing the TL signals of deeper traps. This proved that the 180 and 370 °C TL peaks as the main sources of charges responsible for the recuperation of OSL signals in BeO ceramics. It should be noted that dose-dependency and reproducibility of TT-OSL signals have to be performed to obtain further information about TL and OSL traps in our products. Recently, TT-OSL in BeO Thermalox 995 was observed in pre-irradiated and bleached samples after heating to temperatures of ~180–320 ºC with maximum intensity depending on heating rate, maximum temperature and heating time (Yukihara, 2019; Yukihara, 2020). They indicated that the traps associated with 340 ºC may be the source of the charges transferred to the traps responsible for both the OSL and TT-OSL signals.

4.9.3.5. Thermal Quenching

Thermal quenching of the OSL signals (known as temperature dependence) is a reduction in luminescence outputs observed in many materials at temperatures higher than room temperature. According to the Mott-Seitz model, it can be physically explained as the increase in the probability of non-radiative transitions from the excited to the ground state of the luminescence centers (Bøtter-Jensen et al., 2003). The equation of temperature dependence for an OSL signal was given above as Equation (4.2. The thermal quenching of OSL signals from the BeO samples was investigated to have an idea about the probability of non-radiative transitions. The samples were preheated up to 150 °C for 10 s following exposure of 0.5 Gy. After waiting for approximately two minutes in the reader system, the samples were heated from room temperature to the target temperature and isothermal signals (ITL) were recorded at this temperature without light stimulation to make sure that there is no ITL signal during OSL measurements (see Figure 4.125).

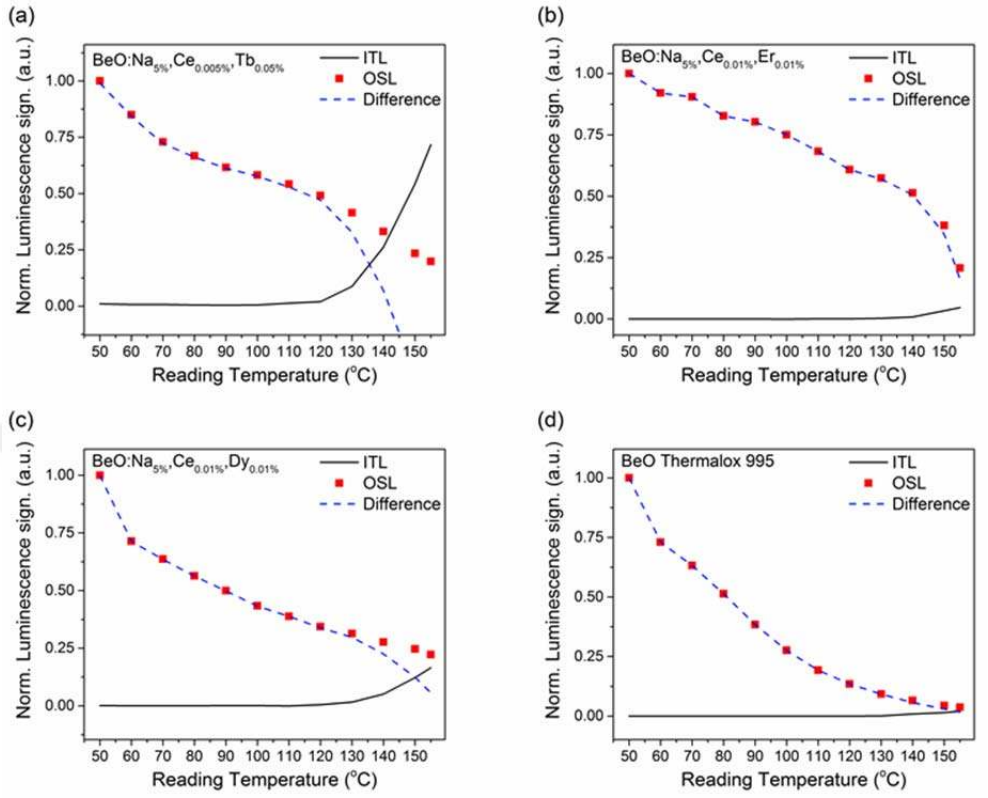

Figure 4.125. ITL, OSL and the Difference signals of (a) BeO:$Na_{5\%}$,$Ce_{0.005\%}$,$Tb_{0.05\%}$ (b) BeO:$Na_{5\%}$,$Ce_{0.01\%}$,$Er_{0.01\%}$ (c) BeO:$Na_{5\%}$,$Ce_{0.01\%}$,$Dy_{0.01\%}$ ceramic pellets (d) BeO Thermalox 995 chip

As is seen from the Figure 4.125, the data obtained at high stimulation temperatures was affected by the isothermal signals. For this reason, the data obtained up to 120, 140, 130 and 140 °C was used for BeO:$Na_{5\%}$,$Ce_{0.005\%}$,$Tb_{0.05\%}$, BeO:$Na_{5\%}$,$Ce_{0.01\%}$,$Er_{0.01\%}$, BeO:$Na_{5\%}$,$Ce_{0.01\%}$,$Dy_{0.01\%}$ and Thermalox 995 samples, respectively.

After this process, OSL signals were obtained at reading temperatures ranging from 50 to 155 °C in 10 °C steps and presented in Figure 4.126 (stabilized case). At the end of each OSL measurement, residual signals were depleted by heating the samples to 650 °C via TL readout. The samples were exposed to the

same dose for the next measurement. In Figure 4.126, the integrated OSL signals obtained by stimulating the samples at 120 °C decreased by 49 %, 40 %, 62 %, 87 % for BeO:$Na_{5\%}$,$Ce_{0.005\%}$,$Tb_{0.05\%}$, BeO:$Na_{5\%}$,$Ce_{0.01\%}$,$Er_{0.01\%}$, BeO:$Na_{5\%}$,$Ce_{0.01\%}$,$Dy_{0.01\%}$, and BeO Thermalox 995 chips, respectively, when compared with that of the OSL signals obtained at the first reading temperature of 50 °C. It was found that a strong thermal quenching due to the apparent reduction in OSL signals exists in all samples.

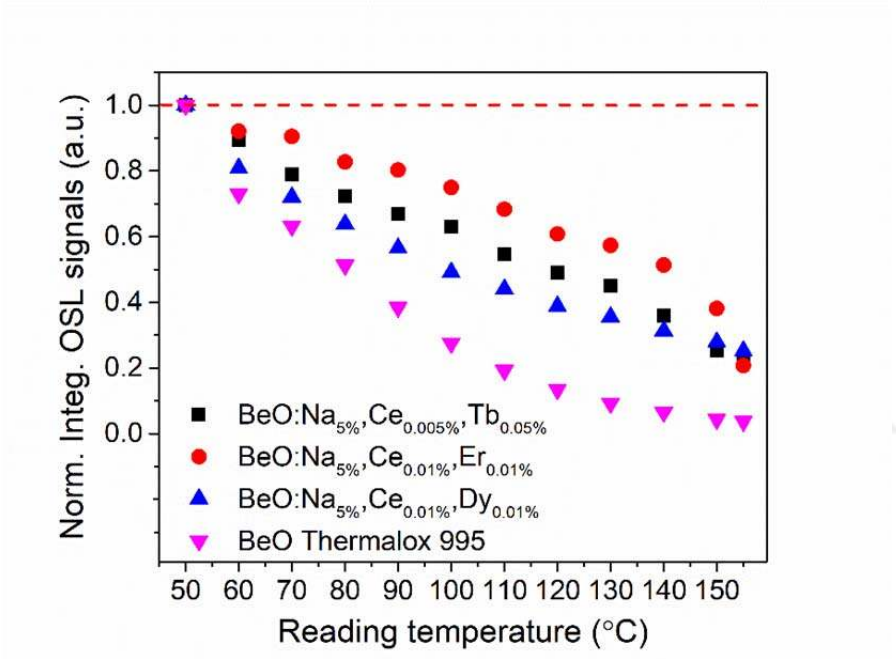

Figure 4.126. Normalized OSL intensities of 0.5 Gy irradiated and preheated (110 °C, 60 s) BeO samples recorded at various readout temperatures

As another method for understanding the thermal quenching mechanism, a TOSL curve indicating the temperature dependence of the OSL signal can be examined. TOSL is a resultant curve obtained by subtracting the TL curves with and without OSL stimulation. This technique was reported in the literature for BeO chips (Thermalox 995) (Bulur and Goksu, 1998) and undoped and doped BeO ceramic pellets (Altunal et al., 2019a; Altunal et al., 2019b; Altunal et al., 2020c;

Altunal et al., 2020e). We applied this technique using 0.1 s pulsed light stimulations with 0.9 s time intervals between the pulses during TL readout (active case). Luminescence signals recorded during the 0.1 s pulsed light stimulation period are the combinations of the OSL and TL (i.e., TL+OSL). On the other hand, luminescent signals recorded during the 0.9 s time interval between the pulses provide us the TL signals (TL). The difference between these TL+OSL and TL signals gives the TOSL signals representing the temperature dependence of the OSL signals. Figure 4.127 shows TL+OSL, TL, and TOSL curves for the BeO samples.

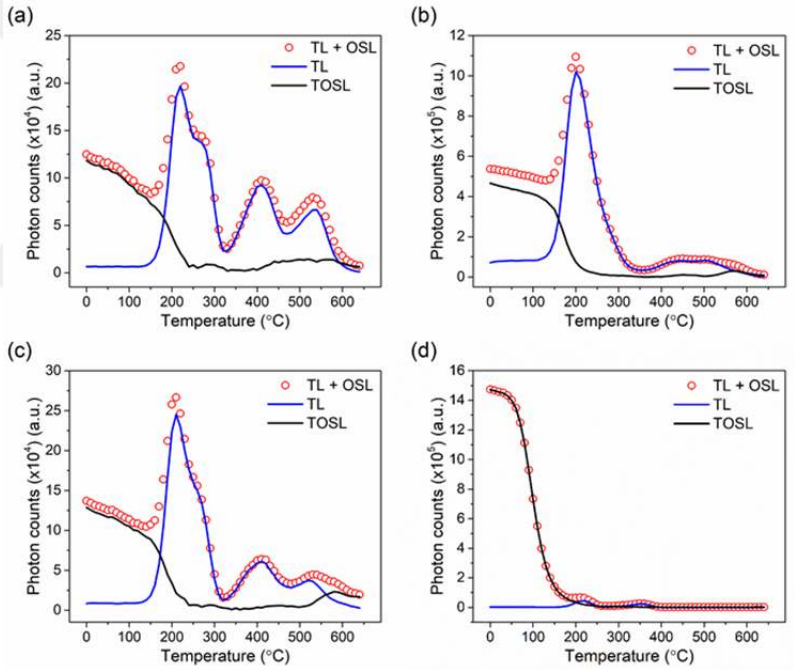

Figure 4. 127. TL + OSL, TL and TOSL curves of (a) BeO:$Na_{5\%}$,$Ce_{0.005\%}$,$Tb_{0.05\%}$ (b) BeO:$Na_{5\%}$,$Ce_{0.01\%}$,$Er_{0.01\%}$ (c) BeO:$Na_{5\%}$,$Ce_{0.01\%}$,$Dy_{0.01\%}$ ceramic pellets (d) BeO Thermalox 995 chips.

In Figure 4.127a-c, as is seen from the TOSL curve, the OSL outputs have two decreased curves. The first decrease is up to 150 °C and the second one begins at 150 °C and reaches zero levels at 250 °C. On the other hand, for BeO Thermalox 995 chips, the first decrease appeared up to 60 °C and the second decrease reached the background value at 180 °C. There might be inferences that the first slow decrease in TOSL signals of BeO samples may be related to the strong thermal quenching, and the second decrease may be associated with the emptying of traps responsible for the 180 °C dosimetric peaks.

The thermal quenching energies for the BeO samples were evaluated by using the OSL data recorded at various readout temperatures in static case (Figure 4.126) and by fitting them into Equation (4.2). The data obtained at higher stimulation temperatures was not included in the fitting process since the effect of thermal depletion of the OSL signal becomes very important. The data obtained up to 120 °C for the BeO:$Na_{5\%}$,$Ce_{0.005\%}$,$Tb_{0.05\%}$, 140 °C for the BeO:$Na_{5\%}$,$Ce_{0.01\%}$,$Er_{0.01\%}$, 130 °C for the BeO:$Na_{5\%}$,$Ce_{0.01\%}$,$Dy_{0.01\%}$ and 140 °C for the Thermalox 995 samples were used. On the other hand, we also evaluated thermal quenching energy value by using the reduction data from the initial parts of the TOSL curve in the dynamic case (Figure 4.127) and by fitting them into Equation (4.2). The fitting model was presented in Figure 4.128.

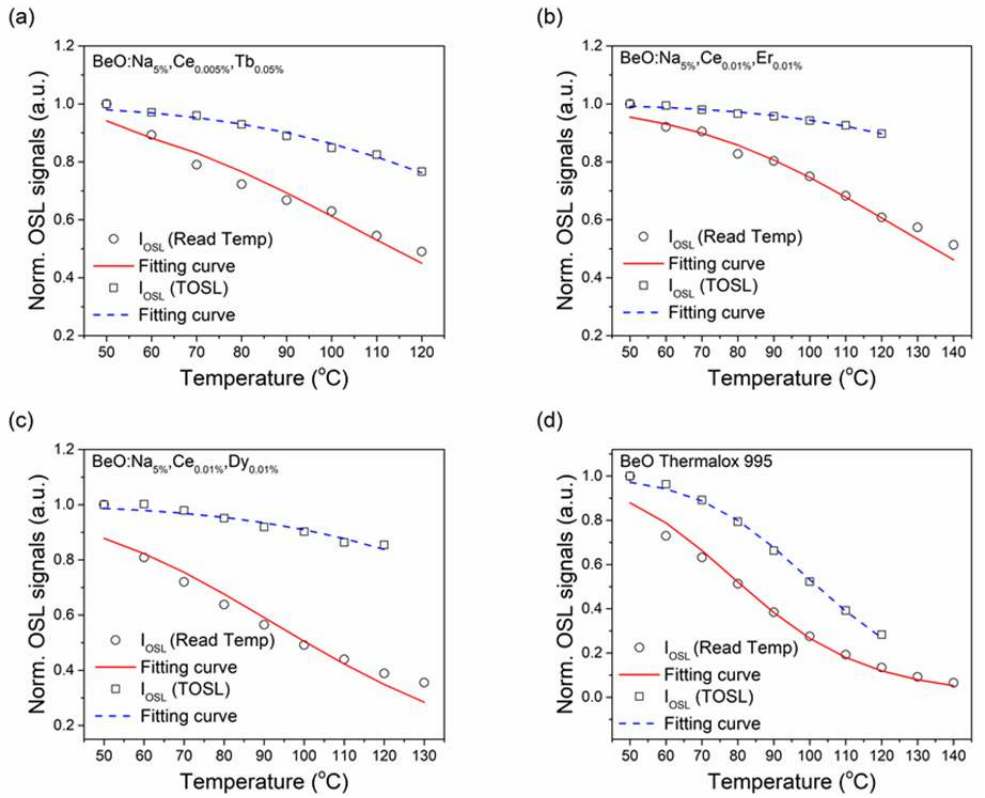

Figure 4.128. Calculation of the thermal quenching energy using the reduction data from the initial parts of TOSL curve in the dynamic cases and the OSL data obtained at various readout temperatures in static cases for (a) BeO:$Na_{5\%}$,$Ce_{0.005\%}$,$Tb_{0.05\%}$ (b) BeO:$Na_{5\%}$,$Ce_{0.01\%}$,$Er_{0.01\%}$ (c) BeO:$Na_{5\%}$,$Ce_{0.01\%}$,$Dy_{0.01\%}$ ceramic pellets (d) BeO Thermalox 995 chip.

The evaluated W values using both methods are presented in Table 4.17 and are almost the same as previously presented thermal quenching values for a different form of the BeO ceramics (Altunal et al., 2019a; Altunal et al., 2019b; Bulur and Goksu, 1998; Yukihara, 2011). The available data are not sufficient to indicate the type of quenching mechanism(s) involved in luminescence processes. Investigating radioluminescence spectra at different temperatures may be helpful, and ESR observations at various temperatures may also provide some insight.

Table 4.17. The evaluated thermal quenching energy values and fitting parameters of BeO samples.

	Reading Temperature			TOSL		
	W (eV)	C	FOM	W (eV)	C	FOM
BeO:Na,Ce,Tb	0.41	2.64E+05	2.24%	0.43	8.99E+04	0.09%
BeO:Na,Ce,Er	0.41	1.10E+05	0.32%	0.42	2.47E+04	0.02%
BeO:Na,Ce,Dy	0.41	3.04E+05	2.04%	0.42	4.34E+04	0.16%
BeO Thermalox 995	0.62	7.00E+08	1.95%	0.71	3.73E+09	0.17%

4.9.3.6. Photo transferred Luminescence

Photo transferred TL (PTTL) signal, i.e. the TL signal-induced due to transfer of charges from deeper traps to shallower ones after heating to temperatures higher than 400 °C, has been reported for BeO Thermalox 995 chips (Bulur, 2007; Yukihara et al., 2016). It was also noted that an annealing procedure temperature > 600 °C is needed to remove the sources of these photo transferred charges (Bulur, 2007; Yukihara et al., 2016). To investigate the PTTL mechanism of three newly produced BeO ceramics, all the TL peaks of the previously irradiated samples were removed one after another. Firstly, to remove peaks at maximum temperatures of ~180, ~250, ~360, ~495, and ~580 °C (for 3 °C/s heating rates), the preheat temperatures were selected as 300, 425 ($BeO:Na_{5\%},Ce_{0.005\%},Tb_{0.05\%}$), 450 ($BeO:Na_{5\%},Ce_{0.01\%},Er_{0.01\%}$ and $BeO:Na_{5\%},Ce_{0.01\%},Dy_{0.01\%}$), 550 and 625 °C (see Figure 4.129). Secondly, the samples were exposed to blue light for 200 s to induce a PTTL signal for each step. Thirdly, TL readouts were performed by reheating the samples up to 650 °C to record any PTTL peak. After each step, residual signals were deleted by TL readouts for being the samples ready next cycle. Figure 4.129a-c shows the PTTL glow curves of the $BeO:Na_{5\%},Ce_{0.005\%},Tb_{0.05\%}$, $BeO:Na_{5\%},Ce_{0.01\%},Er_{0.01\%}$ and $BeO:Na_{5\%},Ce_{0.01\%},Dy_{0.01\%}$ ceramic pellets for different preheating temperatures. As is seen from the PTTL glow curves of all samples, two PTTL peaks were observed at the maximum of ~ 235 and ~ 360 °C. The observable depletion in TL signals

indicates the decrease of trapped charges in deep traps. The inset figure in Figure 4.129 shows the PT-OSL signals measured during illuminations. Excluding the 300 °C and 625 °C PT-OSL curves in all samples, the PT-OSL curves have a peak-shaped form rather than a monotonous decay which indicates at least two competing processes (i.e. the trapping of the evicted charges and radiative recombination) are in action simultaneously. The presented result confirmed that three newly developed BeO ceramics have similar PTTL mechanisms with that of the BeO Thermalox 995 chips (Bulur, 2007).

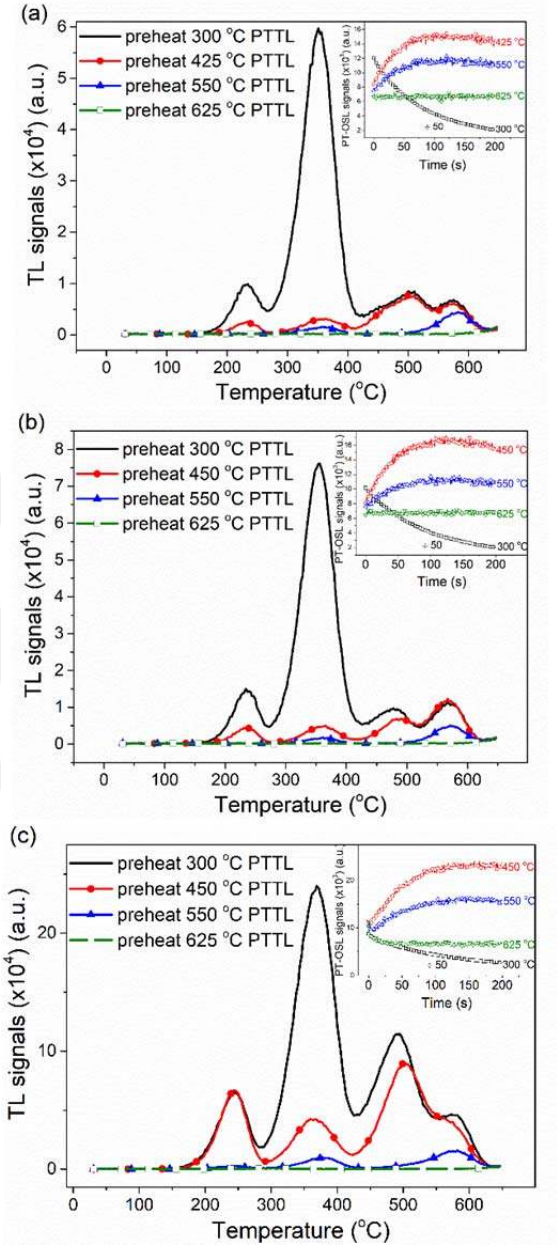

Figure 4.129. PTTL glow curves of (a) BeO:$Na_{5\%}$,$Ce_{0.005\%}$,$Tb_{0.05\%}$ (b) BeO:$Na_{5\%}$,$Ce_{0.01\%}$,$Er_{0.01\%}$ (c) BeO:$Na_{5\%}$,$Ce_{0.01\%}$,$Dy_{0.01\%}$ ceramic pellets. Inset Figure: the PT-OSL curves for different pre-heating temperatures.

4.9.4. Dosimetric Properties

4.9.4.1. Reusability of OSL signals

In dosimetric applications, the dosimeters should be reusable, that is, the luminescence signals obtained from the dosimeters give the same response to the same dose values for repeated readouts. We investigated the reusability properties of OSL signals for the BeO:$Na_{5\%}$,$Ce_{0.005\%}$,$Tb_{0.05\%}$, BeO:$Na_{5\%}$,$Ce_{0.01\%}$,$Er_{0.01\%}$, BeO:$Na_{5\%}$,$Ce_{0.01\%}$,$Dy_{0.01\%}$, and BeO Thermalox 995 samples. OSL readings were performed for three samples from each group previously exposed to a beta dose of 0.5 Gy using 200 s blue light stimulation following 10 s preheat at 120 °C. Residual doses remained in the dosimeters after each OSL reading were erased with a TL reading up to 650 °C. This experimental cycle was repeated 10 times, and deviations between samples and cycles were calculated. The total OSL signals normalized to that of the OSL signals obtained in the first cycle versus the experimental cycles were plotted (see Figure 4.130). As can be seen from the figure, the three newly developed dosimeters showed a maximum deviation of 3 % within 10 experimental cycles. Besides, an increase of 6 % was observed in the OSL signals of the widely used commercial BeO Thermalox 995 chips at the end of 10 cycles compared to its first reading.

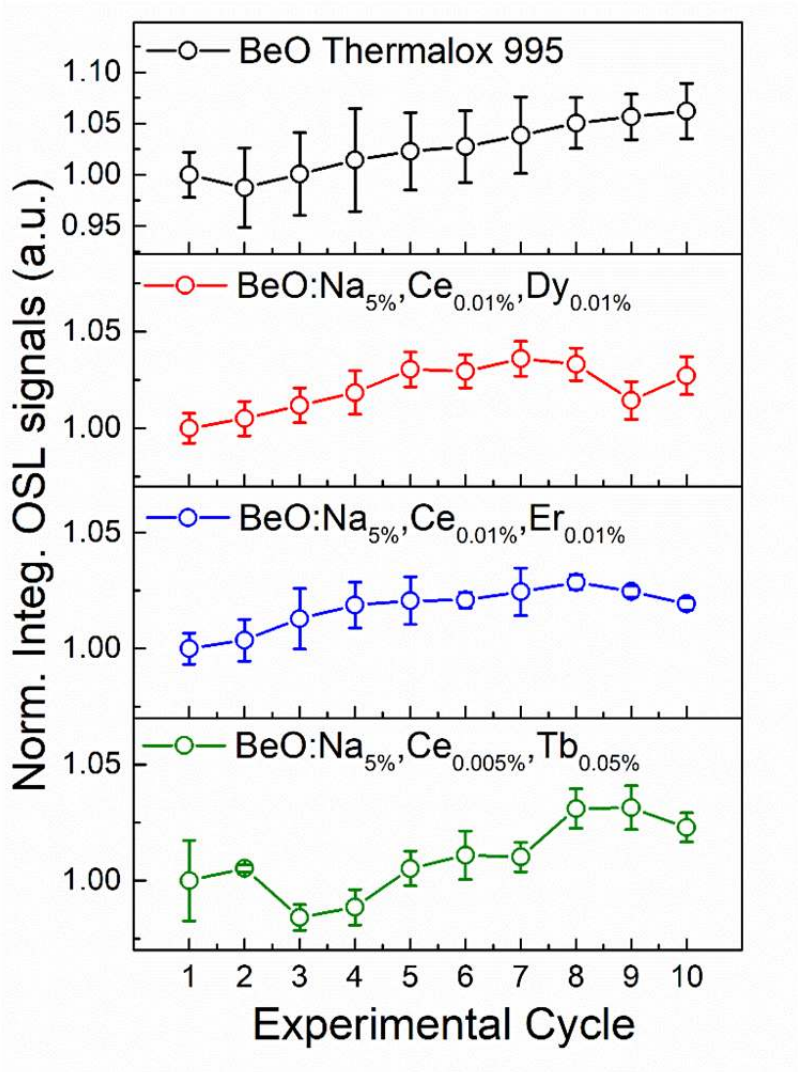

Figure 4.130. Reusability behaviors of the OSL signals from the $BeO:Na_{5\%},Ce_{0.005\%},Tb_{0.05\%}$, $BeO:Na_{5\%},Ce_{0.01\%},Er_{0.01\%}$, $BeO:Na_{5\%},Ce_{0.01\%},Dy_{0.01\%}$, and BeO Thermalox 995 samples

4.9.4.2. Dose-Response of OSL signals

Investigating the linear dose-response range is one of the most important parameters to determine the application area of a dosimeter. Figure 4.131 shows the OSL dose-response curves of the three newly developed dosimeters as a function of beta-ray exposure in comparison with the Thermalox 995 BeO chips. After the irradiation of the samples, OSL readings were performed with blue light stimulation for 200 s following a 10 s preheating at 120 °C. At the end of each experimental cycle, residual doses were erased by heating the sample to 650 °C via TL reading. The dose-response data were fitted with a linear function ($y = ax + b$) on a logarithmic scale. According to the parameters obtained by linear fitting, the response is essentially linear for exposures between 0.5 and 100 Gy for BeO:$Na_{5\%}$,$Ce_{0.01\%}$,$Er_{0.01\%}$ and BeO:$Na_{5\%}$,$Ce_{0.01\%}$,$Dy_{0.01\%}$. The slopes of the response curves of these samples are 1.00 and 1.01, respectively. While, the BeO:$Na_{5\%}$,$Ce_{0.005\%}$,$Tb_{0.05\%}$ sample showed slightly linear characteristics with the slope of 1.03 (see inset Table in Figure 4.131). Moreover, Thermalox 995 chips were found to exhibit sublinear properties within a given dose range with a slope value of 0.96. In the literature, it has been reported that the Thermalox 995 chips show linear dose-response up to 30 Gy, and after this value, OSL signals tend to saturate (Sommer and Henniger, 2006).

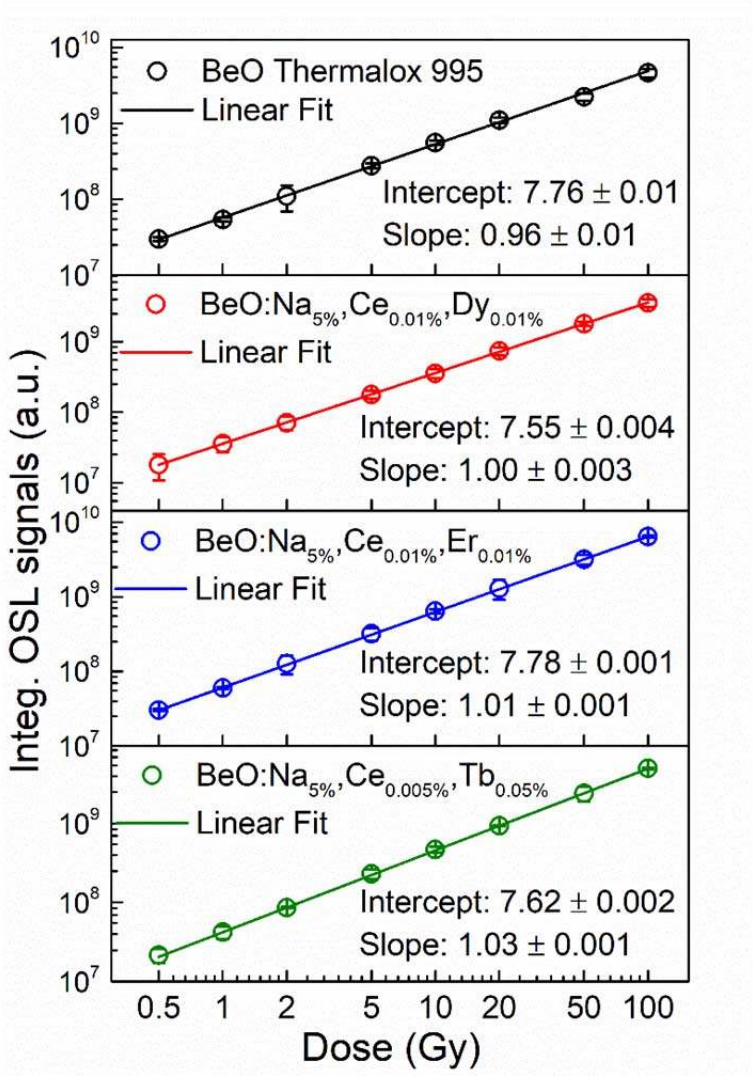

Figure 4.131. Dose linearities of the OSL signals from the $BeO:Na_{5\%},Ce_{0.005\%},Tb_{0.05\%}$, $BeO:Na_{5\%},Ce_{0.01\%},Er_{0.01\%}$, $BeO:Na_{5\%},Ce_{0.01\%},Dy_{0.01\%}$, and BeO Thermalox 995 samples

The estimation of the minimum detectable dose (MDD) values was performed for the dosimeters studied under the current experimental conditions. First, three non-irradiated samples from each group were read multiple (10) times (variation of background, σ). The samples were then exposed to a dose of 0.1 Gy,

the minimum dose that can be applied in the measuring system, and the OSL readings of each sample were recorded. Due to the deviation in the background signals and the total OSL signals of the samples to the smallest dose, the minimum detectable dose (MDD) was estimated as three times the standard deviation of the signal of the non-irradiated samples (Altunal et al., 2020e). MDD values were evaluated by 3σ with 99.73% confidence level as 1.2 ± 0.3 mGy, 721 ± 17 μGy, 271 ± 5 μGy, 554 ± 10 μGy, and 190 ± 8 μGy for undoped BeO, BeO:$Na_{5\%}$,$Ce_{0.005\%}$,$Tb_{0.05\%}$, BeO:$Na_{5\%}$,$Ce_{0.01\%}$,$Er_{0.01\%}$, BeO:$Na_{5\%}$,$Ce_{0.01\%}$,$Dy_{0.01\%}$ ceramic pellets and BeO Thermalox 995 chips, respectively. In the literature, the MDD value of BeO Thermalox chips was reported as approximately ~10-20 μGy (Sommer and Henniger, 2006; Yukihara et al., 2016). It should be noted that this difference may be due to the batch-to-batch difference of the commercially produced Thermalox 995 chips, the different measurement system, and reading conditions, or the differences in the types of equipment (PMT, optical power, etc.).

4.9.4.3. Energy-Response of OSL signals

The luminescence behavior of a dosimeter in connection with the radiation energies is important for the processing and correction of these signals. For this reason, initially calibrated BeO:$Na_{5\%}$,$Ce_{0.005\%}$,$Tb_{0.05\%}$, BeO:$Na_{5\%}$,$Ce_{0.01\%}$,$Er_{0.01\%}$, and BeO:$Na_{5\%}$,$Ce_{0.01\%}$,$Dy_{0.01\%}$ ceramic pellets were irradiated with photons and electrons at different energies to see their energy responses. The absorbed dose in each irradiation was determined as a constant value of 0.5 Gy, photon energies were chosen as 225 kV, 6 MV, 10 MV, and 15 MV, while applied electron energies were 18 keV, 20 keV, 6 MeV, 9 MeV, 12 MeV, 15 MeV, and 22 MeV. Figure 4.132 shows the energy dependence of the studied samples and depicts the response to 0.5 Gy dose by photon (see Figure 4.132a) and electron (see Figure 4.132b) delivering. It can be considered that newly produced dosimeters responded to high-energy mega-voltage photons and electrons with higher OSL sensitivities than the sensitivities obtained at low kilo-voltage energies. Thus, the photon energy

dependence of the samples is the same as that of electrons for high energies. It was assumed that the response was constant per Gy of absorbed dose in the samples for both photons and electrons in the mega-voltage energy range. In the literature, it was reported that BeO Thermalox 995 chips weakly underestimate radiation below 100 keV (Sommer and Henniger, 2006). More investigations are needed at low energies to gain in-depth insight into the energy dependence of newly developed BeO-based dosimeters.

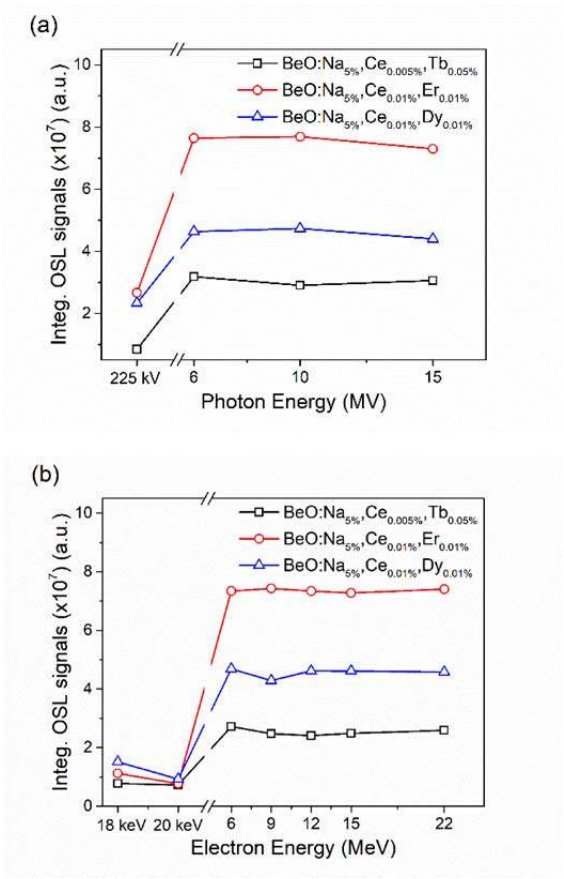

Figure 4.132. Energy responses of the OSL signals from BeO:Na$_{5\%}$,Ce$_{0.005\%}$,Tb$_{0.05\%}$, BeO:Na$_{5\%}$,Ce$_{0.01\%}$,Er$_{0.01\%}$, and BeO:Na$_{5\%}$,Ce$_{0.01\%}$,Dy$_{0.01\%}$ ceramic pellets at varying (a) photon; (b) electron energies

4.9.4.4. Dark Storage Fading of OSL signals

Another desirable feature in dosimetric applications is that the luminescence signals are being stable (no fading) at room temperature. To investigate whether OSL signals obtained from three newly developed dosimeters are stable during certain dark storage periods, a group of BeO:$Na_{5\%}$,$Ce_{0.005\%}$,$Tb_{0.05\%}$, BeO:$Na_{5\%}$,$Ce_{0.01\%}$,$Er_{0.01\%}$, BeO:$Na_{5\%}$,$Ce_{0.01\%}$,$Dy_{0.01\%}$, and BeO Thermalox 995 samples were initially calibrated for a radiation dose of 0.5 Gy. As a result of the calibration process, the mean and experimental standard deviation values of the integrated OSL signals obtained from three repeated measurements were recorded. During this process, before each OSL measurement, the samples were preheated at 120 °C for 60 s to eliminate the signals that may come from the shallow traps. At the end of this calibration study, forty-two pellets with an experimental standard deviation of less than 3 % were selected and calibration factors were determined for each sample. Following this procedure, all the samples were exposed to a 0.5 Gy beta dose and preheated to 120 °C for 60 s. Fading properties of these samples were tested for up to 3 months by keeping them in the dark at room temperature (see Figure 4.133). In this fading study, three samples were used for each intended time interval. The OSL signals were recorded following a preheating at 120 °C for 10 s. The first readings of the samples were recorded after half an hour following the irradiation.

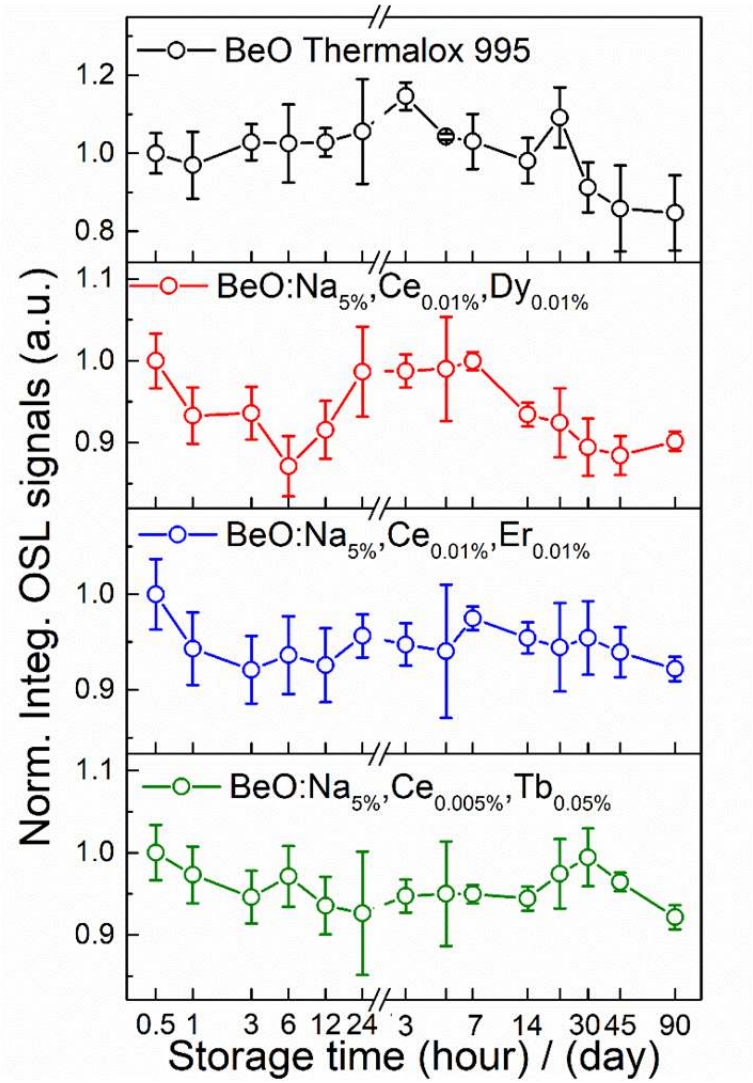

Figure 4.133. Fading rates of the OSL signals from the BeO:$Na_{5\%}$,$Ce_{0.005\%}$,$Tb_{0.05\%}$, BeO:$Na_{5\%}$,$Ce_{0.01\%}$,$Er_{0.01\%}$, BeO:$Na_{5\%}$,$Ce_{0.01\%}$,$Dy_{0.01\%}$, and BeO Thermalox 995 samples

As can be seen from Figure 4.133, the first decrease was obtained as ~ 5 % using the total OSL signals in 1 hour of storage time. At the end of the 6-hour storage time, it was observed that ~ 87 % of the OSL signals of the BeO:$Na_{5\%}$,$Ce_{0.01\%}$,$Dy_{0.01\%}$ sample remained, and after this significant decrease, the

OSL signals increased until the end of 24 hours. At the end of 24 hours, there was a 5 % decrease in the total OSL signals of BeO:$Na_{5\%}$,$Ce_{0.005\%}$,$Tb_{0.05\%}$ and BeO:$Na_{5\%}$,$Ce_{0.01\%}$,$Er_{0.01\%}$ samples when compared to the values obtained at the first reading.

During fading experiments, three BeO Thermalox995 chips were used as the reference materials for the readout sensitivity. OSL signals at different readout times were obtained from 0.5 Gy irradiated BeO Thermalox 995 chips after preheating the samples at 125 °C for 125 s and presented in Figure 4.134. As is seen from the figure that integrated OSL signals obtained at different times were found to be almost the same level.

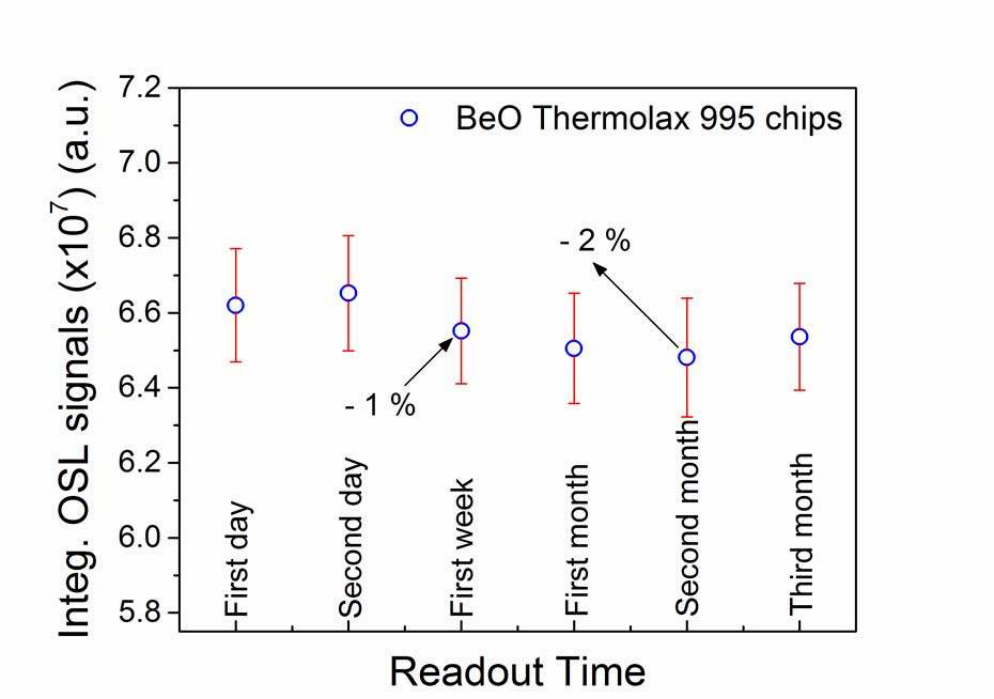

Figure 4.134. Integrated OSL signals from BeO Thermalox 995 chips at different readout times.

In general, since a stable response is observed from the equipment over long periods (see Figure 4.134), the reason for the fluctuation observed in OSL signals in the first 24 hours might be the electron migration from deep traps to

relatively shallow traps. If the fluctuations observed in the signals in the first 24 h are ignored, it has been observed that the OSL signals of the newly developed dosimeters are stable up to about 1 week. After 1 week of storage time, the second party decrease of 7 % was observed in the OSL signals of the BeO:$Na_{5\%}$,$Ce_{0.01\%}$,$Dy_{0.01\%}$ sample, and this decrease reached 10 % at the end of 3 months. For both the BeO:$Na_{5\%}$,$Ce_{0.005\%}$,$Tb_{0.05\%}$ and BeO:$Na_{5\%}$,$Ce_{0.01\%}$,$Er_{0.01\%}$ samples, the maximum loss in OSL signals reached approximately 7 % at the end of 3 months. On the other hand, it was observed that OSL signals of the BeO Thermalox 995 chips increased significantly after an initial decrease of 3 % at the end of 1 hour, up to 3 days storage time. At the end of this increase, OSL signals increased by 15 % compared to the first reading. Up to 14 days, OSL signals had a second decrease of 2 % from the first reading. Only 84 % of OSL signals remained after 90 days in Thermalox 995 samples. In the literature, short-term fading of Thermalox 995 BeO chips after 10 hours of storage time has been reported as approximately 6 % less compared to 30 minutes of measurement (Sommer et al., 2007). The fading of this commercial dosimeter was determined to be 5 % loss and 8 % loss after 24 hours and 1-week of storage in the dark, respectively (Sommer and Henniger, 2006). Its long-term fading has been reported to be negligible (less than 1 % in 6 months) (Sommer et al., 2007; Sommer and Henniger, 2006). We cannot exclude the possibility of fading caused by the room light used during sample handling in spite of the dim red light (~650 nm) used for this purpose.

4.9.5. Discussion

Considering the possible luminescence mechanism of the main results obtained in this study, an in-depth discussion is needed. Considering the possible charge transfer between traps with different properties, the TL and OSL processes of the studied BeO ceramics might be very complex. In the oversimplified case, the TL and OSL processes begin with the irradiation of the samples. Electrons in the excited valance band are trapped in electron traps, and holes in hole traps.

Electrons trapped by thermal or optical stimulation escape from the traps and recombine with the holes at the recombination centers. At the end of this process, TL and OSL emissions are observed depending on the simulation method. The luminescence mechanism of three newly developed BeO-based dosimeters has been presented in detail in our previous study (Altunal et al., 2021). It has been reported that Na^{+} ion acted as a charge compensator among these Ln^{3+} elements and helped transfer energy between them, thereby significantly increasing luminescence efficiency. Moreover, Ce^{3+} and Tb^{3+} ions act as hole traps, while Dy^{3+} and Er^{3+} ions play a role in the structure like electron traps.

If we consider the proposed luminescence mechanism together with the TL and OSL trap properties of the newly developed dosimeters in Sections 0 and 0, a schematic diagram can be obtained for the possible trap energy levels between the valance and conduction bands. TL glow curves of three newly produced samples show five TL peaks (see Figure 4.135). In all our samples, the first peaks located at approximately 180 °C are due to optically active traps (OAT1), while TL peaks responsible for shoulder TL traps (STT) located at 250 °C contribute to OSL with a low probability. In only BeO:$Na_{5\%}$,$Ce_{0.005\%}$,$Tb_{0.05\%}$ samples, it is clear that the source of the OSL signals is (OAT1) and optically active traps (OAT2) at 370 °C (see Figure 4.135), although all of the TL peaks are light sensitive (see Figure 4.135). In BeO:$Na_{5\%}$,$Ce_{0.01\%}$,$Er_{0.01\%}$ and BeO:$Na_{5\%}$,$Ce_{0.01\%}$,$Dy_{0.01\%}$ samples, the TL peaks located at 370 °C are not sensitive to light and also do not contribute to OSL signals (see Figure 4.122 and Figure 4.123). Therefore, it can be said that the traps placed in this region only behave like a deep TL trap (DTT1). Similarly, TL peaks settled around 495 °C and 580 °C are caused by deep traps (DTT2 and DTT3). These trap levels are only sensitive to light in BeO:$Na_{5\%}$,$Ce_{0.005\%}$,$Tb_{0.05\%}$ samples and promote the OSL signals with low probability (see Figure 4.122 and Figure 4.123). The depletion in TL signals indicated the decrease of trapped charges in the determined deep traps and two PTTL peaks were observed at the maximum of ~ 235 and ~ 360 °C (see Figure 4.129). Considering the presented data of PTTL

behavior of the deep TL traps, one can say that electrons migrate from deep traps (DTT1, DTT2, DTT3) to shallower traps (OAT1, STT, OAT2). In general, if we assume that there are two recombination centers (RC1 and RC2) in BeO to indicate that there may be more than one recombination pathway, which was proven with time-resolved (TR-OSL) studies for the BeO Thermalox chips (Bulur, 2014; Bulur et al., 2013), the observable TL and OSL emissions being due to one of them (RC1) is the most obvious explanation. It should be noted that further measurements on TR-OSL signals and photoluminescence lifetime must be needed to prove this recombination mechanism.

Figure 4.135 shows the schematic diagram indicating TL and OSL processes for newly developed BeO-based ceramic dosimeters. As is seen in Figure 4.129, a rotated typical TL glow curve demonstrates the possible locations of the characteristic TL traps in the band range and the qualitative depths of these traps. Electrons and holes were plotted by solid and open circles, respectively. While solid lines show possible electron transitions, the dashed lines represent the transitions of the electrons that contribute to the OSL signals with a low probability of escaping from light-sensitive TL traps. The re-trapping and recombination transitions were illustrated by the black line. The red line represents the possible transition of escaping electrons by TL stimulation, and the blue represents the possible electron transitions as a result of optical stimulation. A similar model has recently reported for BeO Thermalox 995 chips (Yukihara, 2020), containing 75 °C TL peak due to shallow traps (STs), and a different OSL mechanism which is originated from only 340 °C TL peaks (OATs).

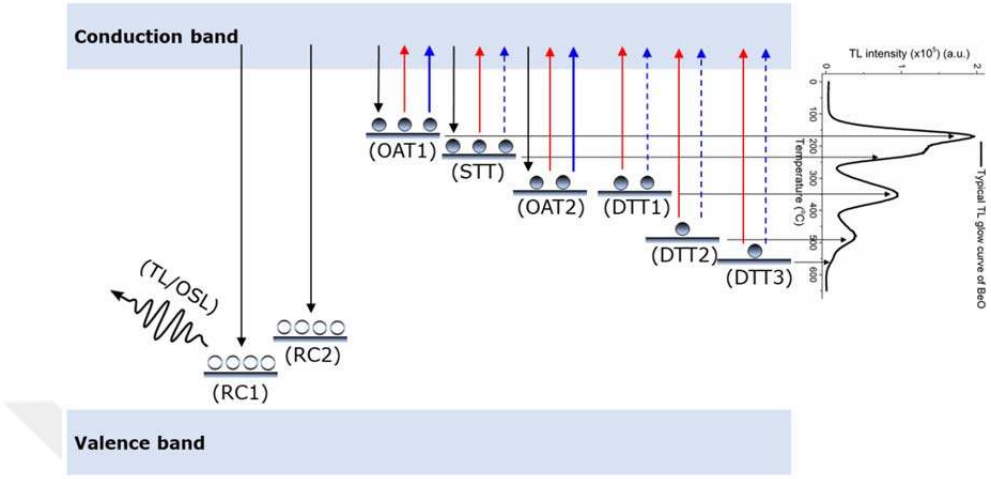

Figure 4.135. A proposed model for the luminescence in three newly produced BeO ceramic dosimeters, including optically active traps (OAT1 and OAT2), shoulder TL traps (STT), deep TL traps (DTT1, DTT2, and DTT3), and recombination centers (RC1 and RC2). Solid and open circles show the electrons and holes, respectively. Solid lines show possible electron transitions. The black line represents re-trapping and recombination transitions, the red line represents the possible transition of escaping electrons by TL stimulation, and the blue represents the possible electron transitions as a result of optical stimulation. On the other hand, the dashed line shows the transitions of the electrons that contribute to the OSL signals with a low probability of escaping from light-sensitive TL traps.

As a result of the proposed mechanism and Ln^{3+} ion behaviors in BeO, it can be said that the Ce^{3+} and Tb^{3+} ions in the structure combine with the holes that escape from the irradiation valance band to form Ce^{4+} and Tb^{4+} ions. After stimulation, Ce^{4+} and Tb^{4+} ions recombine with electrons escaping electron traps to form Ce^{3+} and Tb^{3+} ions in the excited state. At the end of the relaxation process of these lanthanides, TL and OSL emissions are observed. It is clear here that Ce^{3+} and Tb^{3+} ions activate characteristic recombination centers (RC1 and RC2) in the structure of BeO. Similarly, Er^{3+} and Dy^{3+} ions can be said to play a role in the luminescence process by affecting BeO's characteristics.

Since the proposed model in the view of the data obtained in this study depends on factors such as dose, preheating, emission, dopants, etc., more detailed investigations on TL emissions with increasing temperature, OSL emissions at various reading temperatures, and TR-OSL studies to obtain more knowledge on possible recombination centers are needed.

5. CONCLUSION

In this thesis, the structural, morphological and luminescence characteristics of BeO ceramic dosimeters produced by different methods were investigated dosimetrically. With this thesis, the most suitable synthesis stages (sintering and calcination processes) of BeO material were determined, and the luminescence nature, which has not been clarified until now, is fully discussed in this thesis so that the material can be developed as an OSL dosimeter. The luminescence nature of the most suitable metal and lanthanide dopants in the structure was investigated in depth.

In the first study of this thesis, BeO pellets were prepared using the precipitation method and sintered at 1200, 1400 and 1600 °C. The variation of the structural, morphological and relevant dosimetric and luminescent properties of the BeO pellets was investigated as a function of the sintering temperatures. With increasing sintering temperature, the crystallinity improved, the FWHM decreased and the grain size of the BeO pellets increased. The average grain size was observed between the range (1 - 5) μm for the BeO pellets sintered at 1600 °C. The step-annealing curves of BeO samples sintered at 1200 °C showed that the source of the OSL signals is associated with both the 170 °C and 275 °C bleached TL peaks and the OSL employs the same recombination centers as the 170 °C and 275 °C bleached TL peaks. For the BeO pellets sintered at 1400 °C, we suggested that the origin of the OSL signals might be associated with only the 275 °C TL peak. The source of the OSL signal of BeO pellets sintered at 1600 °C might be associated with the 170 °C TL peak, and the OSL signals probably occur from the same recombination centers with the 170 °C TL peak. The general characteristics of BeO pellets sintered at 1600 °C for use in dosimetry can be summarized as follows: *i)* Very high sensitivity to beta irradiation with a minimum detectable dose value of 8 μGy by calculating the whole OSL signal *ii)* Wide range of linear response for beta dose exposures from 0.1 to 50 Gy *iii)* Very good reusability with

the deviation of 1 % from the first cycle of ten repeated exposure and readout measurements *iv)* Almost no fading after delivering 1 Gy beta dose after 24 h at room temperature in dark.

In the second study of this thesis, BeO nano-particles were synthesized by using co-precipitation and sol-gel methods. In the thermogravimetric analysis of the precursor materials, it was concluded that suitable calcination conditions should occur at a temperature higher than 800 °C. In the phase analysis of BeO nano-particles produced under different calcination conditions, it has been observed that the particle size has increased and the structure has improved in both synthesis methods at increasing calcination temperature and duration. As a result of morphological analysis, BeO nano-particles produced by the co-precipitation method were found to have a homogeneity after 900 °C, while the temperature at which the homogeneity was first encountered at 1000 °C in the sol-gel method. RL emissions proved the presence of characteristic emission bands of BeO besides an unexpected broad peak with low sensitivity observed in the red region, in both methods. It was concluded that the presence of this unexpected peak is due to the oxygen vacancies of the ceramic material that act as anion defects formed in the structure during the synthesis. In both methods, TL glow curves showed six different peaks and the total TL signals gave a maximum intensity at 900 °C calcination temperature in the co-precipitation method and 1000 °C in the sol-gel method. It was concluded that the 4-hour calcination condition was the most suitable calcination time to produce a highly sensitive luminescence dosimeter in both methods. It was observed that the OSL decay curves obtained in the OSL measurements were well fit to the linear integration of two-time decaying functions, and it was observed that the sensitivity of the OSL could be increased using the appropriate calcination conditions. It was found that the dosimetric characteristics of BeO samples increased significantly under appropriate calcination conditions: the dose-response approached linearity and the fading characteristic improved for a short storage time. We consider that this study will

guide future studies in the field of radiation dosimeters related to BeO dosimeters, and will contribute to the usage of the material as a personal OSL dosimeter with appropriate synthesis processes.

In the third study of this thesis, we prepared the BeO materials as pellets after the calcination process and sintered separately at 1600 °C at different durations (1, 2, 3, 4, 5, 8, 12, 18, 24 h) to determine the time parameter of the sintering condition of the BeO material. It was stated that the optimum sintering time was chosen as 2 hours since the material exhibited a higher OSL sensitivity despite the relatively low TL signals. At the end of this complementary study, the most suitable sintering conditions were determined for the production methods used in this thesis, sol-gel and co-precipitation synthesis methods.

In the fourth study of this thesis, we indicated that the Al and Ca ions added to BeO ceramic host material (BeO:$Al_{1\%}$, BeO:$Ca_{1\%}$, and BeO:$Al_{1\%}$,$Ca_{0.1\%}$) profoundly affect all the important luminescence characteristics (luminescence intensity, XL, glow peak temperatures, thermal stability, fading, etc.) of BeO. The materials studied were prepared by the sol-gel method and measured in pellet form after sintering at 1600 °C. The structural analysis showed no secondary phase formations in the XRD patterns. Hexagonal particles had a narrow size distribution (data not shown) in SEM images. In the XL spectra, a broad emission peak with a maximum at 230 nm was observed from the host material and Al-doped host material between 200 and 400 nm. With Ca doping, the emission intensity increased and one more peak was created at 300 nm in the XL spectra of BeO:$Ca_{1\%}$ and BeO:$Al_{1\%}$,$Ca_{0.1\%}$ pellets. In both cases, the XL obtained was in the transmittance range of the filter used in all OSL/TL measurements in this study. Four peaks, located at 80, 200, 370, and 520 °C, for BeO and BeO:$Ca_{1\%}$ pellets and three peaks, located at 200, 350, and 500 °C, for BeO:$Al_{1\%}$ and BeO:$Al_{1\%}$,$Ca_{0.1\%}$ pellets were observed from the TL glow curves. On excitation with blue light, the doped materials exhibited intense OSL signals in the UV region due to efficient energy transfer from Al to Ca, and more intense OSL signals were realized by

appropriate adjustment of the Ca concentration. From the experiments of TL and OSL signal correlation, it was found that BeO and BeO:$Ca_{1\%}$ pellets have light-sensitive TL traps located in the regions corresponding to the 80, 200 and 370 °C TL peaks. The TL glow curve of the BeO:$Al_{1\%}$ pellet has two light-sensitive TL peaks, located at 200 and 350 °C, whereas all peaks in the TL glow curve obtained from the BeO:$Al_{1\%}$,$Ca_{0.1\%}$ pellet were affected by light. From the step-annealing experiment, it was concluded that 370 °C TL traps might be responsible for OSL signals obtained from the BeO and BeO:$Ca_{1\%}$ pellets. The origin of the OSL signal from the BeO:$Al_{1\%}$ pellet was perhaps associated with both the 200 °C and the 350 °C TL peaks. The source of the OSL signal from the BeO:$Al_{1\%}$,$Ca_{0.1\%}$ pellet might be associated with only the 350 °C TL peak. Furthermore, BeO:$Al_{1\%}$ had good thermal stability up to 150 °C, while the thermal stability region expands from room temperature to 300 °C after Ca ions are incorporated into the singly doped sample. This work may help to better understand the interactions between Al and Ca transition metal ions, and it might also be helpful in the future design of dosimetric materials. The OSL intensities obtained at 130 °C decreased by approximately 35% for BeO:$Al_{1\%}$, by approximately 65% for BeO, and by approximately 80% for BeO:$Ca_{1\%}$ and BeO:$Al_{1\%}$,$Ca_{1\%}$ pellets when compared with the OSL intensities obtained at 50 °C for each type of pellet studied. Using two methods, we evaluated the activation energies for the nonradiative decay of the luminescence centers for BeO pellets as 0.54 and 0.51 eV, respectively. On the other hand, the thermal quenching energies were 0.50 and 0.57 eV for the BeO:$Al_{1\%}$ pellet, 0.70 and 0.72 eV for the BeO:$Ca_{1\%}$ pellet, and 0.67 and 0.67 eV for the BeO:$Al_{1\%}$,$Ca_{0.1\%}$ pellet with the two methods, static and dynamic, respectively.

The dose responses of all pellets studied were linear in the dose range from 0.1 to 100 Gy. The MDD was estimated as approximately 0.9 mGy for BeO, approximately 4 mGy for BeO:$Al_{1\%}$, and approximately 0.5 mGy for both of BeO:$Ca_{1\%}$ and BeO:$Al_{1\%}$,$Ca_{0.1\%}$. The reusability of the pellets studied was very

stable up to ten repeated experimental cycles. In the fading experiments, BeO:$Al_{1\%}$,$Ca_{1\%}$ pellets with residual signal (about 97%) from the first readout exhibited almost no fading at the end of 1 month. We conclude that studied BeO:$Al_{1\%}$,$Ca_{0.1\%}$ material with bright OSL signal and low fading characteristic is very promising luminescent dosimetric ceramic for detection of radiation dose ranging from 0.1 to 100 Gy.

In the fifth study of this thesis, structural, morphological, and luminescent characterizations of single metal-doped BeO ceramic pellets synthesized using the co-precipitation method were reported and discussed for personal/clinical dosimetry. In the XRD analyzes of the ceramic pellets, the single metal-doped BeO samples had the same wurtzite hexagonal phase and it was observed that intensities of the characteristic peaks increased with metal doping, which means that the BeO grains have grown and the crystallites have been improved RL emission bands (located between 200-400 nm) of BeO ceramics were observed. Besides this, an unexpected low-intensity luminescence emission at a high wavelength between 650 and ~820 nm with the maximum at 730 nm appeared in the spectra of BeO:Mg samples. Considering TL measurements, BeO:$Al_{1\%}$, BeO:$Mg_{0.1\%}$, BeO:$Na_{5\%}$, BeO:$K_{5\%}$, BeO:$B_{0.1\%}$, and BeO:$Zn_{0.1\%}$ with high sensitivity to ionizing radiation were selected as the promising TL samples for dosimetric studies. In the OSL measurements, it was observed that only Na^{2+}, Li^{+}, K^{+}, Cu^{4+} dopants at a concentration of 5% enhanced the OSL signals of undoped BeO pellets. It was found that BeO:$Na_{5\%}$ and BeO:$Cu_{5\%}$ pellets exhibited linear OSL dose-response characteristics, and BeO:$Na_{5\%}$, and BeO:$K_{5\%}$ had linear TL dose-response characteristics in the dose range between 0.1 and 10 Gy. Except for the BeO:$K_{5\%}$ samples, the TL and OSL reusability experiment outputs for all of the samples were found within acceptable limits. In short-time fading experiments, instability was found due to the discharge of electrons in shallow trap groups in the single metal-doped BeO materials. The deviation of measurements due to the first TL and OSL readouts at half an hour after irradiation did not exceed -15.3% and -19.2% at

the end of one-week storage, in dark. We consider that this work will guide the studies on BeO dosimeters in the field of radiation dosimeters and contribute to the use of the material as a personal/clinical OSL dosimeter with a controllable luminescence by adding appropriate dopants.

In the sixth study of this thesis, the successful incorporation of Ln^{3+} and Na^{+} alkali ions into the lattice of BeO ceramic was achieved using the conventional co-precipitation method. It was investigated that co-doping of BeO with impurities such as Ln^{3+} ions abovementioned is an effective way to enhance luminescence efficiency. In our experiments, the incorporated impurity Ce^{3+} served as a sensitizer. Besides Ce^{3+} ions, other impurities like Er^{3+}, $Tb^{3+,}$ and Dy^{3+}ions participated in energy transfer within the matrix. We revealed a luminescence mechanism based on beryllium sublattice-mediated energy migration, which facilitates efficient upconversion emissions from a series of Ln^{3+} ions (Er^{3+}, Tb^{3+} and Dy^{3+}) without intermediary energy levels. Contrary to Ln^{3+} ions, alkali ions, intentionally incorporated into Ln^{3+} doped BeO did not directly participate in the optical process (e.g., energy transfer) within the hosts, but were capable of enhancing upconversion efficiency as well. OSL emission intensities of the BeO:Ce^{3+},Ln^{3+} (Ln= Er^{3+}, Tb^{3+} and Dy^{3+}) co-doped with 5% mol Na^{1+} ions were enhanced by about 2 times. Such improvement could be attributed to charge compensation with Na^{+} ions because the $(Na_{Be})^{-}$ defects located around the Ln^{3+} ions cause the strong mixing of charge-transfer states. We investigated the luminescence characteristics of the Ln^{3+} and Na^{+} doped BeO ceramic pellets using RL, TL, and OSL techniques. The XRD patterns and Raman spectra showed that Ln^{3+} ions were incorporated into the BeO lattice and might be suggested as substituting for Be^{2+} lattice sites rather than locating in interstitial positions. All the Ln^{3+} doped BeO ceramic samples exhibited their typical RL emissions along with the characteristic RL emission of BeO ranging between 200-450 nm. With increasing Ln^{3+} concentration, there was a significant decrease in TL and OSL signals due to parity or aggregation of Ln^{3+} atoms at high concentrations. The

luminescence mechanism model in BeO is complex. It can be suggested that the recombination process in BeO might be improved by adding suitable Ln^{3+} dopants. In this work, a model was also proposed to explain the basic luminescence properties of Ln^{3+} doped BeO ceramics. These results strongly suggest that the newly developed three ceramic pellets BeO:$Na_{5\%}$,$Ce_{0.01\%}$,$Er_{0.01\%}$; BeO:$Na_{5\%}$,$Ce_{0.005\%}$,$Tb_{0.05\%}$ and BeO:$Na_{5\%}$,$Ce_{0.01\%}$,$Dy_{0.01\%}$ performed the high OSL and TL intensities. In the future, the aforementioned ceramics with these outstanding Ln^{3+} and Na^{+} dopants will be tested and involved in several comparison studies with the commercial dosimeters.

In the seventh study of this thesis, characterization, well-rounded dosimetric and luminescent characteristics of the newly produced triply doped BeO:Na,Tb,Gd ceramic pellets were reported and discussed for the first time. With the XRD, SEM and EDS analyses, It was demonstrated that synthesis of triply doped BeO:Na,Tb,Gd samples were successfully performed using the precipitation method. It can be concluded that Na, Tb and Gd ions in the crystal lattice were observed following the specified doping ratios. BeO:Na,Tb,Gd pellets showed three TL peaks located at 180, 370 and 495 °C in the TL curve. In step annealing experiments, it was concluded the origin of the OSL signals may be related to both the 180 and 370 °C TL peaks, and the OSL traps use the same recombination centers as the TL traps responsible for the 180 and 370 °C TL peaks. Thermal quenching energies were estimated as 0.52 and 0.55 eV using static (reading temp.) and dynamic (TOSL) methods. The reason why these values are lower than the values presented in previous studies may be the difference in measurement systems, the production and structural differences of the samples. With the triple doping of BeO, it was observed that most of the properties desired in the new OSL and TL dosimeters for different applications are met by the produced material. In summary, the OSL signal of the BeO:Na,Tb,Gd ceramic pellet was thermally stable up to 120 °C, reusable under carefully controlled laboratory conditions, and sensitive to radiation dose with the linear dose range from 0.1 to 100 Gy indicating

the possibility of usage in radiation dosimetry. OSL signals were also found to be almost the same level at different radiation energies, and almost no fading up to one month.

In the eighth study of this thesis, characterization, and the relevant dosimetric and luminescent properties of the newly produced OSL/TL material (Z_{eff}=7.31) based on triply doped BeO:Na,Dy,Er ceramic pellets were reported and discussed. In XRD, SEM and EDS analyses, it was shown that triply doped BeO:Na,Dy,Er samples were successfully synthesized using the precipitation method. BeO:Na,Dy,Er pellets have three TL peaks located at 170, 350 and 470 °C (2 °C/s) in the TL glow curves. With the step annealing experiments, it was found that OSL signals may originate from both the 170 and 350 °C TL peaks and the OSL, most likely, employs in the same recombination centers with the 170 and 350 °C TL peaks. We compared the XL spectra of the triply doped BeO samples at different concentrations, and all XL spectra showed that BeO has a broad emission band located between 200 and 500 nm. It was observed that the effective luminescence emission band of 3-4 eV (310-410 nm) can be detected in the transmittance range of the luminescent measurement system. Thermal quenching energies of the material were determined as 0.43 and 0.42 eV using static (reading temp.) and dynamic (TOSL) methods. With the triple doping of BeO, it was observed that most of the properties desired in a new OSL dosimeter for radiation dosimetry applications are met by the developed material. In summary, the OSL signal was found to be thermally stable up to 150 °C, reusable under carefully controlled laboratory conditions, and sensitive to radiation dose with a slightly linear dose range from 0.1 to 50 Gy. Except for instability in short storage times, 10% long-term fading was observed for up to three months under ambient laboratory conditions. Reusable, and thermally stable OSL signals were found to be very encouraging and convenient for personal and medical dosimetry applications.

In the ninth study of this thesis, demonstrated the structural, morphological, luminescent, and dosimetric characteristics of three newly produced BeO ceramics by comparing them with undoped BeO ceramics and commercially used BeO Thermalox 995 chips. The dominant luminescence bands in TL and OSL processes were determined to be range in the same region, but the emission band was different when we performed RL. It can be said that the radiation bands between 300 and 400 nm (i.e., 3-4 eV) are due to the same emission mechanism in all cases (RL, TL, and OSL) that can be observed using the U-340 filter. Although a single trapping center associated with the OSL signal was found for BeO:$Na_{5\%}$,$Ce_{0.01\%}$,$Er_{0.01\%}$ and BeO:$Na_{5\%}$,$Ce_{0.01\%}$,$Dy_{0.01\%}$ ceramics in step annealing experiments, TT-OSL signals showed that two trapping centers were responsible for the source of the OSL signals in all samples. It is clear that there is strong thermal quenching in the signals of the samples, but It is not clear what kind of quenching phenomenon the sample exhibits, further work needs to be done to prove this. It was observed that PTTL signals ~235 and ~360 °C were induced by blue light stimulation on annealed samples (at 450 °C after irradiation). Annealing to temperatures higher than 600 °C is required to remove the sources of these photo transferred charges. In reusability measurements performed over 10 experimental cycles, three newly developed BeO-based ceramics were found to be superior to Thermalox995 chips. While all samples exhibited an almost linear dose-response, it was observed that both for the photons and electrons, the samples showed higher OSL sensitivity to mega-voltage energies than that of the kilo-voltage energies in our experiments. Contrary to the literature, it has been noted that the long-term fading of Thermalox 995 chips is high and the OSL signals of three newly developed BeO-based ceramics fade relatively less than this commercial product. One can conclude that the OSL signals of the three newly developed BeO dosimeters can compete with the BeO Thermalox 995 dosimeters for their use in many dosimetric applications due to their reusable, linear dose-response, energy dependence for high energies and, almost no fading properties.

With the studies carried out in this thesis, it has been demonstrated that in general, BeO ceramics can be successfully synthesized and doped in the laboratory environment and that with appropriate additives, BeO ceramics can exhibit properties far superior to those of common commercial dosimeters, and that purposeful defect can be created in the structures of BeO ceramics. Most importantly, with the doping studies carried out in this thesis, the light was shed on the luminescence nature of BeO ceramics, which has not been understood until now. It can be concluded that the material is a promising tissue-equivalent material that can completely replace Al_2O_3:C dosimeter rather than being an alternative. In further studies, radiation dosimetry of the material and more detailed energy dependence studies for clinical applications should be carried out and its possible use in these areas should be investigated.

BIBLIOGRAPHY

Aitken, M. J., 1985. Thermoluminescence dating: Academic press.

Akselrod, M., Kortov, V., Kravetsky, D., and Gotlib, V., 1990. Highly sensitive thermoluminescent anion-defective alpha-Al203: C single crystal detectors. Radiation Protection Dosimetry, 32(1), 15-20,

Akselrod, M. S., Bøtter-Jensen, L., and McKeever, S. W. S., 2006. Optically stimulated luminescence and its use in medical dosimetry. Radiation Measurements, 41, S78-S99, 10.1016/j.radmeas.2007.01.004.

Akselrod, M. S., Lucas, A. C., Polf, J. C., and McKeever, S. W. S., 1998. Optically stimulated luminescence of Al2O3. Radiation Measurements, 29(3-4), 391-399, Doi 10.1016/S1350-4487(98)00061-4.

Allen, P., and McKeever, S., 1990. Studies of PTTL and OSL in TLD-400. Radiation Protection Dosimetry, 33(1-4), 19-22,

Altunal, V., Guckan, V., Ozdemir, A., Can, N., and Yegingil, Z., 2019a. Luminescence characteristics of Al-and Ca-doped BeO obtained via a sol-gel method. Journal of Physics and Chemistry of Solids, https://doi.org/10.1016/j.jpcs.2019.04.003.

Altunal, V., Guckan, V., Ozdemir, A., Ekicibil, A., Karadag, F., Yegingil, I., Zydhachevskyy, Y., and Yegingil, Z., 2021. A systematic study on luminescence characterization of lanthanide-doped BeO ceramic dosimeters. Journal of Alloys and Compounds, 876, 160105, https://doi.org/10.1016/j.jallcom.2021.160105.

Altunal, V., Guckan, V., Ozdemir, A., Kurt, K., Ekicibil, A., and Yegingil, Z., 2020a. Investigation of luminescence properties of BeO ceramics doped with metals for medical dosimetry. Optical Materials, 108, 110436,

Altunal, V., Guckan, V., Ozdemir, A., Sotelo, A., and Yegingil, Z., 2019b. Effect of sintering temperature on dosimetric properties of BeO ceramic pellets synthesized using precipitation method. Nuclear Instruments and Methods in Physics Research Section B: Beam Interactions with Materials and Atoms, 441, 46-55,

Altunal, V., Guckan, V., Ozdemir, A., and Yegingil, Z., 2020b. A Calcination Study on BeO Ceramics for Radiation Dosimetry. Materials Research Bulletin, 110921,

Altunal, V., Guckan, V., Ozdemir, A., and Yegingil, Z., 2020c. Radiation dosimeter utilizing optically stimulated luminescence of BeO:Na,Tb,Gd ceramics. Journal of Alloys and Compounds, 817, 152809, https://doi.org/10.1016/j.jallcom.2019.152809.

Altunal, V., Guckan, V., Yu, Y., Dicker, A., and Yegingil, Z., 2020d. A newly developed OSL dosimeter based on beryllium oxide: BeO: Na, Dy, Er. Journal of Luminescence, 222, 117140,

Altunal, V., Guckan, V., Yu, Y., Dicker, A., and Yegingil, Z., 2020e. A newly developed OSL dosimeter based on beryllium oxide: BeO:Na,Dy,Er. Journal of Luminescence, 222, 117140, https://doi.org/10.1016/j.jlumin.2020.117140.

Altunal, V., Yegingil, Z., Tuken, T., Depci, T., Ozdemir, A., Guckan, V., Nur, N., Kurt, K., and Bulur, E., 2018. Optically stimulated luminescence characteristics of BeO nanoparticles synthesized by sol-gel method. Radiation Measurements, 118, 54-66, https://doi.org/10.1016/j.radmeas.2018.08.009.

Anderson, P., and Horlock, R., 1967. Calcination of microporous BeO powders. Transactions of the Faraday Society, 63, 2316-2323,

Arabi, S., Akbari Javar, H., and Khoobi, M., 2016. Preparation and characterization of modified polyethyleneimine magnetic nanoparticles for cancer drug delivery. Journal of Nanomaterials, 2016,

Aşlar, E., Meriç, N., Şahiner, E., Kitis, G., and Polymeris, G. S., 2017. Calculation of thermal quenching parameters in BeO ceramics using solely TL measurements. Radiation Measurements, 103(Supplement C), 13-25, https://doi.org/10.1016/j.radmeas.2017.06.011.

Aşlar, E., Şahiner, E., Polymeris, G. S., and Meriç, N., 2021. Thermally and optically stimulated luminescence properties of BeO dosimeter with double TL peak in the main dosimetric region. Applied Radiation and Isotopes, 170, 109635, https://doi.org/10.1016/j.apradiso.2021.109635.

Azorín-Vega, J. C., Azorín-Nieto, J., García-Hipólito, M., and Rivera-Montalvo, T., 2007. Thermoluminescence properties of nanopowder. Radiation Measurements, 42(4-5), 613-616, 10.1016/j.radmeas.2007.01.084.

Balakrishnaiah, R., Yi, S. S., Jang, K., Lee, H. S., Moon, B. K., and Jeong, J. H., 2011. Enhanced luminescence properties of YBO3: Eu3+ phosphors by Li-doping. Materials Research Bulletin, 46(4), 621-626,

Balian, H. G., and Eddy, N. W., 1977. Figure-of-merit (FOM), an improved criterion over the normalized chi-squared test for assessing goodness-of-fit of gamma-ray spectral peaks. Nuclear Instruments and Methods, 145(2), 389-395, https://doi.org/10.1016/0029-554X(77)90437-2.

Bilgili, O., 2019. The Effects of Mn Doping on the Structural and Optical Properties of ZnO. Acta Physica Polonica, A., 136(3),

Blasse, G., and Grabmaier, B. (1994). A general introduction to luminescent materials. In *Luminescent materials* (pp. 1-9): Springer.

Boch, P., and Niepce, J.-C., 2010. Ceramic Materials: Processes, Properties, and Applications (Vol. 98): John Wiley & Sons.

Bohlender, C., Kahnes, M., Müller, R., and Töpfer, J., 2019. Phase formation, magnetic properties, and phase stability in reducing atmosphere of M-type strontium hexaferrite nanoparticles synthesized via a modified citrate process. Journal of Materials Science, 54(2), 1136-1146,

Bomlai, P., Wichianrat, P., Muensit, S., and Milne, S. J., 2007. Effect of calcination conditions and excess alkali carbonate on the phase formation and particle morphology of Na0. 5K0. 5NbO3 powders. Journal of the American Ceramic Society, 90(5), 1650-1655,

Bøtter-Jensen, L., 1997. Luminescence techniques: instrumentation and methods. Radiation Measurements, 27(5-6), 749-768,

Bøtter-Jensen, L., McKeever, S. W., and Wintle, A. G., 2003. Optically stimulated luminescence dosimetry: Elsevier.

Brinker, C. J., and Scherer, G. W., 2013. Sol-gel science: the physics and chemistry of sol-gel processing: Academic press.

Bulur, E., 2007. Photo-transferred luminescence from BeO ceramics. Radiation Measurements, 42(3), 334-340, 10.1016/j.radmeas.2007.02.065.

Bulur, E., 2014. More on the TR-OSL signal from BeO ceramics. Radiation Measurements, 66, 12-20, 10.1016/j.radmeas.2014.04.018.

Bulur, E., and Goksu, H. Y., 1998. OSL from BEO ceramics: New observations from an old material. Radiation Measurements, 29(6), 639-650, Doi 10.1016/S1350-4487(98)00084-5.

Bulur, E., and Saraç, B. E., 2013. Time-resolved OSL studies on BeO ceramics. Radiation Measurements, 59, 129-138, 10.1016/j.radmeas.2013.04.009.

Bulur, E., and Yeltik, A., 2010. Optically stimulated luminescence from BeO ceramics: An LM-OSL study. Radiation Measurements, 45(1), 29-34, 10.1016/j.radmeas.2009.08.007.

Bünzli, J.-C. G., and Eliseeva, S. V. (2010). Basics of lanthanide photophysics. In *Lanthanide Luminescence* (pp. 1-45): Springer.

Carter, C. B., and Norton, M. G., 2007. Ceramic materials: science and engineering (Vol. 716): Springer.

Chang, C., Yuan, Z., and Mao, D., 2006. Eu2+ activated long persistent strontium aluminate nano scaled phosphor prepared by precipitation method. Journal of Alloys and Compounds, 415(1-2), 220-224,

Chen, R., and McKeever, S. W., 1997. Theory of thermoluminescence and related phenomena: World Scientific.

Chen, X., Liu, Y., and Tu, D., 2016. Lanthanide-doped luminescent nanomaterials: Springer.

Chernov, V., Ao, R. M., Piters, T., and Barboza-Flores, M., 2001. Thermally and optically stimulated luminescence correlated processes in X-ray irradiated KCl: Eu2+. Radiation Measurements, 33(5), 797-800,

Chruścińska, A., 2001. THE FRACTIONAL GLOW TECHNIQUE AS A TOOL OF INVESTIGATION OF TL BLEACHING EFFICIENCY IN K-FELDSPAR. Geochronometria: Journal on Methods & Applications of Absolute Chronology, 20,

Daniel, P. M., Dawes, J., and Prichard, M. M., 1953. Studies of the carotid rete and its associated arteries. Phil. Trans. R. Soc. Lond. B, 237(645), 173-208,

Dhananjaya, N., Nagabhushana, H., Nagabhushana, B., Rudraswamy, B., Shivakumara, C., and Chakradhar, R., 2011. Effect of Li+-ion on enhancement of photoluminescence in Gd2O3: Eu3+ nanophosphors prepared by combustion technique. Journal of Alloys and Compounds, 509(5), 2368-2374,

Dhoble, S. J., Pawade, V. B., Swart, H. C., and Chopra, V., 2019. Spectroscopy of lanthanide doped oxide materials: Woodhead Publishing.

Dopita, M., Rudolph, M., Salomon, A., Emmel, M., Aneziris, C. G., and Rafaja, D., 2013. Simulations of X-Ray Scattering on Two-Dimensional, Graphitic and Turbostratic Carbon Structures. Advanced Engineering Materials, 15(12), 1280-1291,

Dorenbos, P., 2003. Systematic behaviour in trivalent lanthanide charge transfer energies. Journal of Physics: Condensed Matter, 15(49), 8417,

Dorenbos, P., and Bos, A. J. J., 2008. Lanthanide level location and related thermoluminescence phenomena. Radiation Measurements, 43(2-6), 139-145, 10.1016/j.radmeas.2007.10.007.

Duller, G., and Bøtter-Jensen, L., 1993. Luminescence from potassium feldspars stimulated by infrared and green light. Radiation Protection Dosimetry, 47(1-4), 683-688,

Furetta, C., 2010. Handbook of thermoluminescence: World Scientific.

Garcia-Guinea, J., Correcher, V., Can, N., Garrido, F., and Townsend, P. D., 2018. Cathodoluminescence spectra recorded from surfaces of solids with hydrous molecules. Journal of Electron Spectroscopy and Related Phenomena,

Garlick, G., and Gibson, A., 1948. The electron trap mechanism of luminescence in sulphide and silicate phosphors. Proceedings of the Physical Society (1926-1948), 60(6), 574,

Gobrecht, H., and Hofmann, D., 1966. Spectroscopy of traps by fractional glow technique. Journal of Physics and Chemistry of Solids, 27(3), 509-522,

Guckan, V., Altunal, V., Nur, N., Depci, T., Ozdemir, A., Kurt, K., Yu, Y., Yegingil, I., and Yegingil, Z., 2017. Studying CaSO4: Eu as an OSL phosphor. Nuclear Instruments and Methods in Physics Research Section B: Beam Interactions with Materials and Atoms, 407, 145-154,

Guckan, V., Altunal, V., Ozdemir, A., Tsiumra, V., Zhydachevskyy, Y., and Yegingil, Z., 2020. Calcination effects on europium doped zinc oxide as a luminescent material synthesized via sol-gel and precipitation methods. Journal of Alloys and Compounds, 153878, https://doi.org/10.1016/j.jallcom.2020.153878.

Hazen, R., and Finger, L., 1986. High-pressure and high-temperature crystal chemistry of beryllium oxide. Journal of Applied Physics, 59(11), 3728-3733,

Hobzova, L., 1980. Improved band model of BeO ceramics. Physica Status Solidi. A, Applied Research, 60(2), K207-K209,

Horowitz, Y. S., 1984. Thermoluminescence and Thermoluminescent Dosimetry, v. 2.

Huntley, D. J., Godfrey-Smith, D. I., and Thewalt, M. L., 1985. Optical dating of sediments. Nature, 313(5998), 105,

Huston, A., Justus, B., Falkenstein, P., Miller, R., Ning, H., and Altemus, R., 2001. Remote optical fiber dosimetry. Nuclear Instruments and Methods in Physics Research Section B: Beam Interactions with Materials and Atoms, 184(1-2), 55-67,

Ivanov, V. Y., Pustovarov, V., Gorbunov, S., and Kruzhalov, A., 1994. Relaxation of electronic excitations in beryllium oxide. I. Self-trapped excitons. Physics of the Solid State, 36, 1436-1442,

J. Thomsen, K., Bøtter-Jensen, L., and S. Murray, A., 2002. Household and workplace chemicals as retrospective luminescence dosemeters. Radiation Protection Dosimetry, 101(1-4), 515-518,

Jahn, A., Sommer, M., and Henniger, J., 2014. OSL efficiency for BeO OSL dosimeters. Radiation Measurements, 71, 104-107, 10.1016/j.radmeas.2014.03.024.

Jahn, A., Sommer, M., Ullrich, W., Wickert, M., and Henniger, J., 2013. The BeOmax system – Dosimetry using OSL of BeO for several applications. Radiation Measurements, 56, 324-327, 10.1016/j.radmeas.2013.01.069.

Jain, M., Murray, A. S., and Bøtter-Jensen, L., 2003. Characterisation of blue-light stimulated luminescence components in different quartz samples: implications for dose measurement. Radiation Measurements, 37(4), 441-449, https://doi.org/10.1016/S1350-4487(03)00052-0.

Jones, R. W., 1990. Fundamental Principles of Sol--Gel Technology. The Institute of Metals, 1990, 128,

Kiiko, V., 2004. Transparent beryllia ceramics for laser technology and ionizing radiation dosimetry. Refractories and Industrial Ceramics, 45(4), 266-272,

Kim, H. J., Kim, T. G., Kim, J. J., Park, S. S., Hong, S. S., and Lee, G. D., 2008. Influences of precursor and additive on the morphology of nanocrystalline α-alumina. Journal of Physics and Chemistry of Solids, 69(5-6), 1521-1524,

Kitis, G., Polymeris, G. S., Sfampa, I. K., Prokic, M., Meriç, N., and Pagonis, V., 2016. Prompt isothermal decay of thermoluminescence in MgB4O7: Dy, Na and LiB4O7: Cu, In dosimeters. Radiation Measurements, 84, 15-25,

Klug, H. P., and Alexander, L. E., 1974. X-ray diffraction procedures: for polycrystalline and amorphous materials. X-Ray Diffraction Procedures: For Polycrystalline and Amorphous Materials, 2nd Edition, by Harold P. Klug, Leroy E. Alexander, pp. 992. ISBN 0-471-49369-4. Wiley-VCH, May 1974., 992,

Kortov, V., Milman, J., Slesarev, A., Surdo, A., Lesz, J., and Sujak-Lesz, K., 1993a. BeO Ceramics with a High Conductivity - A New Material for TSEE Dosimetry? Radiation Protection Dosimetry, 47(1-4), 599-602, 10.1093/oxfordjournals.rpd.a081816.

Kortov, V. S., and Milman, I. I., 1996. Luminescence properties of transparent BeO:Li ceramics. Radiation Protection Dosimetry, 65(1-4), 355-358,

Kortov, V. S., Milman, I. I., Slesarev, A. I., and Kijko, V. S., 1993b. New Beo Ceramics for Tl Esr Dosimetry. Radiation Protection Dosimetry, 47(1-4), 267-270,

Köseoğlu, Y., 2015. Rapid synthesis of room temperature ferromagnetic Fe and Co co-doped ZnO DMS nanoparticles. Ceramics International, 41(9), 11655-11661,

Kruzhalov, A., Ogorodnikov, I., and Kudyakov, S., 1996. Radiative relaxation of low-energy electron excitations and point defects in beryllium oxide. Russian Physics Journal, 39(11), 1067-1081,

Lakowicz, J. R., 2013. Principles of fluorescence spectroscopy: Springer science & business media.

Lakshmanan, A., 2012. Sintering of ceramics: new emerging techniques: BoD–Books on Demand.

Lee, S. M., Jang, Y., Jung, J., Yum, J. H., Larsen, E. S., Bielawski, C. W., Wang, W., Ryou, J.-H., Kim, H.-S., and Cha, H.-Y., 2019. Atomic-layer deposition of crystalline BeO on SiC. Applied Surface Science, 469, 634-640,

Lele, S., and Anantharaman, T. (1966). *Influence of crystallite shape on particle size broadening of Debye-Scherrer reflections.* Paper presented at the Proceedings of the Indian Academy of Sciences-Section A.

Li, J.-G., Ikegami, T., Lee, J.-H., Mori, T., and Yajima, Y., 2000. Co-precipitation synthesis and sintering of yttrium aluminum garnet (YAG) powders: the effect of precipitant. Journal of the European Ceramic Society, 20(14-15), 2395-2405,

Liao, L.-S., Bao, X.-M., Li, N.-S., Zheng, X.-Q., and Min, N.-B., 1996. Blue-, green-, and red-light emission from Si+-implanted thermal SiO2 films on crystalline silicon. Journal of Luminescence, 68(2-4), 199-204,

Lngford, J., and Wilson, A., 1978. Scherer after sixty years. J. Appl. Cryst, 11, 102,

Lorbeer, C., Behrends, F., Cybinska, J., Eckert, H., and Mudring, A.-V., 2014. Charge compensation in RE 3+(RE= Eu, Gd) and M+(M= Li, Na, K) co-doped alkaline earth nanofluorides obtained by microwave reaction with reactive ionic liquids leading to improved optical properties. Journal of Materials Chemistry C, 2(44), 9439-9450,

Markey, B., McKeever, S., Akselrod, M., Bøtter-Jensen, L., Angersnap Larsen, N., and Colyott, L., 1996. The Temperature Dependence of Optically Stimulated Luminescence From Alpha-Al2O3: C. Radiation Protection Dosimetry, 65(1-4), 185-189,

McKeever, S., Akselrod, M., Colyott, L., Agersnap Larsen, N., Polf, J., and Whitley, V., 1999. Characterisation of Al2O3 for use in thermally and optically stimulated luminescence dosimetry. Radiation Protection Dosimetry, 84(1-4), 163-166,

McKeever, S., and Chen, R., 1997. Luminescence models. Radiation Measurements, 27(5), 625-661,

McKeever, S. W., 1988. Thermoluminescence of solids (Vol. 3): Cambridge University Press.

McKeever, S. W., Moscovitch, M., and Townsend, P. D., 1995. Thermoluminescence dosimetry materials: properties and uses.

Mejdahl, V., 1969. Thermoluminescence dating of ancient Danish ceramics. Archaeometry, 11(1), 99-104,

Milliken, E., Oliveira, L., Denis, G., and Yukihara, E., 2012. Testing a model-guided approach to the development of new thermoluminescent materials using YAG: Ln produced by solution combustion synthesis. Journal of Luminescence, 132(9), 2495-2504,

Moram, M., Kappers, M., Massabuau, F., Oliver, R., and Humphreys, C., 2011. The effects of Si doping on dislocation movement and tensile stress in GaN films. Journal of Applied Physics, 109(7), 073509,

Nakamura, F., Kato, T., Okada, G., Kawaguchi, N., Fukuda, K., and Yanagida, T., 2017. Scintillation and TSL properties of MgF2 transparent ceramics doped with Eu2+ synthesized by spark plasma sintering. Journal of Alloys and Compounds, 726, 67-73,

Nambi, K. (1977). *Thermoluminescence: Its understanding and applications*. Retrieved from

Nanto, H., Murayama, K., Usuda, T., Endo, F., Hirai, Y., Taniguchi, S. i., and Takeuchi, N., 1993a. Laser-stimulable transparent KCl: Eu crystals for erasable and rewritable optical memory utilizing photostimulated luminescence. Journal of Applied Physics, 74(2), 1445-1447,

Nanto, H., Murayama, K., Usuda, Y., Taniguchi, S., and Takeuchi, N., 1993b. Optically stimulated luminescence in KCl: Eu single crystals. Radiation Protection Dosimetry, 47(1-4), 281-284,

Ngamjarurojana, A., Khamman, O., Yimnirun, R., and Ananta, S., 2006. Effect of calcination conditions on phase formation and particle size of zinc niobate powders synthesized by solid-state reaction. Materials Letters, 60(23), 2867-2872,

Norazlina, M. S., Shanmugan, S., and Mutharasu, D., 2013. Structural Analysis of BeO Nanoparticles Synthesized by Polyacrylamide Gel Route. Advanced Science Focus, 1(4), 362-366, 10.1166/asfo.2013.1055.

Ogorodnikov, I., and Kruzhalov, A. (1997). *Defect properties of beryllium oxide.* Paper presented at the Materials Science Forum.

Ogorodnikov, I., Kruzhalov, A., and Kuznetsov, A. Y., 1996. Thermoluminescence, Point Defects and Recombination Processes in BeO and LiB305 Single Crystals. Radiation Protection Dosimetry, 65(1-4), 109-112,

Ogorodnikov, I. N., Ivanov, V. Y., and Kruzhalov, A. V., 1995. Short-wavelenght luminescence and thermostimulated processes in single crystals of BeO. Radiation Measurements, 24(4), 417-421, https://doi.org/10.1016/1350-4487(95)00275-J.

Ogorodnikov, I. N., Petrenko, M. D., and Ivanov, V. Y., 2016. Low-temperature luminescence and thermoluminescence from BeO:Zn single crystals. Optical Materials, 62, 219-226, 10.1016/j.optmat.2016.10.009.

Ogorodnikov, I. N., Petrenko, M. D., and Ivanov, V. Y., 2018. Low-temperature luminescence and thermally stimulated luminescence of BeO: Mg single crystals. Physics of the Solid State, 60(1), 134-146,

Oliveira, L., Yukihara, E., and Baffa, O., 2019. Lanthanide-doped MgO: A case study on how to design new phosphors for dosimetry with tailored luminescent properties. Journal of Luminescence,

Oliveira, L. C., Yukihara, E. G., and Baffa, O., 2016. MgO:Li,Ce,Sm as a high-sensitivity material for Optically Stimulated Luminescence dosimetry. Sci Rep, 6, 24348, 10.1038/srep24348.

Orante-Barrón, V., Oliveira, L., Kelly, J., Milliken, E., Denis, G., Jacobsohn, L., Puckette, J., and Yukihara, E., 2011. Luminescence properties of MgO produced by solution combustion synthesis and doped with lanthanides and Li. Journal of Luminescence, 131(5), 1058-1065,

Ozdemir, A., Altunal, V., Guckan, V., Can, N., Kurt, K., Yegingil, I., and Yegingil, Z., 2018. Characterization and some fundamental features of optically stimulated luminescence measurements of silver activated lithium tetraborate. Journal of Luminescence, 202, 136-146, https://doi.org/10.1016/j.jlumin.2018.05.054.

Ozdemir, A., Yegingil, Z., Nur, N., Kurt, K., Tuken, T., Depci, T., Tansug, G., Altunal, V., Guckan, V., Sigircik, G., Yu, Y., Karatasli, M., and Dolek, Y., 2016. Thermoluminescence study of Mn doped lithium tetraborate powder and pellet samples synthesized by solution combustion synthesis. Journal of Luminescence, 173, 149-158, 10.1016/j.jlumin.2016.01.013.

Pagonis, V., Kitis, G., and Furetta, C., 2006. Numerical and practical exercises in thermoluminescence: Springer Science & Business Media.

Pietkun, A., Polakiewicz, L., and Oczkowski, H., 1992. Measurement system for fractional glow technique. Acta Phys. Pol. A, 81, 687-691,

Prasad, A. K., Kook, M., and Jain, M., 2017. Probing metastable Sm2+ and optically stimulated tunnelling emission in YPO4: Ce, Sm. Radiation Measurements, 106, 61-66,

Purgato, F. L., Montoro, L. A., Ribeiro, J., Kokoh, K. B., and Olivi, P., 2010. The Effect of Heat Treatment on the Preparation of Pt-RuO 2/C Electrocatalysts. Electrocatalysis, 1(2-3), 122-128,

Pushpa, N., and Kokila, M., 2017. Effect of cobalt doping on structural, thermo and photoluminescent properties of ZnO nanopowders. Journal of Luminescence, 190, 100-107,

Rajaeiyan, A., and Bagheri-Mohagheghi, M., 2013. Comparison of sol-gel and co-precipitation methods on the structural properties and phase transformation of γ and α-Al 2 O 3 nanoparticles. Advances in Manufacturing, 1(2), 176-182,

Randall, J. T., and Wilkins, M. H. F., 1945. Phosphorescence and electron traps-I. The study of trap distributions. Proceedings of the Royal Society of London. Series A. Mathematical and Physical Sciences, 184(999), 365-389,

Rane, A. V., Kanny, K., Abitha, V., and Thomas, S. (2018). Methods for synthesis of nanoparticles and fabrication of nanocomposites. In *Synthesis of inorganic nanomaterials* (pp. 121-139): Elsevier.

Rao, R., Gasiot, J., and Fillard, J., 1984. Optically stimulated luminescence and cathodoluminescence of MgS: Eu phosphors. Journal of Luminescence, 31, 213-215,

Rao, R. P., 1986. The preparation and thermoluminescence of alkaline earth sulphide phosphors. Journal of Materials Science, 21(10), 3357-3386,

Rawat, N., Dhabekar, B., Kulkarni, M., Muthe, K., Mishra, D., Soni, A., Gupta, S., and Babu, D., 2014. Optimization of CW-OSL parameters for improved dose detection threshold in Al2O3: C. Radiation Measurements, 71, 212-216,

Reddy, S. S., Chauhan, N., Nagabhushana, K., and Singh, F., 2018. TL/OSL properties of beta irradiated Al2O3: Tm3+ phosphor synthesized by microwave combustion method. Materials Research Bulletin, 104, 236-243,

Rhyner, C. R., and Miller, W. G., 1970. Radiation dosimetry by optically-stimulated luminescence of BeO. Health Physics, 18, 681-684,

Rivera, T., 2011. Synthesis and thermoluminescent characterization of ceramics materials. Advances in ceramics–synthesis and characterization, processing and specific applications. InTech, Rijeka, Croatia, 127-164,

Sabine, T. M., and Hogg, S., 1969. The wurtzite Z parameter for beryllium oxide and zinc oxide. Acta Crystallographica Section B, 25(11), 2254-2256,

Sagar, T. V., Rao, T. S., and Naidu, K. C. B., 2020. Effect of calcination temperature on optical, magnetic and dielectric properties of Sol-Gel synthesized Ni0. 2Mg0. 8-xZnxFe2O4 (x= 0.0–0.8). Ceramics International,

Scarpa, G., 1970. The dosimetric use of beryllium oxide as a thermoluminescent material: A preliminary study. Physics in Medicine and Biology, 15(4), 667,

Simpraditpan, A., Wirunmongkol, T., Pavasupree, S., and Pecharapa, W., 2013. Effect of calcination temperature on structural and photocatalyst properties of nanofibers prepared from low-cost natural ilmenite mineral by simple hydrothermal method. Materials Research Bulletin, 48(9), 3211-3217, https://doi.org/10.1016/j.materresbull.2013.04.083.

Singh, D., Tanwar, V., Samantilleke, A. P., Mari, B., Bhagwan, S., Kadyan, P. S., and Singh, I., 2016a. Preparation and Photoluminescence Properties of SrAl 2 O 4: Eu 2+, RE 3+ Green Nanophosphors for Display Device Applications. Journal of Electronic Materials, 45(6), 2718-2724,

Singh, D., Tanwar, V., Simantilleke, A. P., Bhagwan, S., Mari, B., Kadyan, P. S., Singh, K. C., and Singh, I., 2016b. Synthesis and enhanced luminescent characterization of SrAl 4 O 7: Eu 2+, RE 3+(RE= Nd, Dy) nanophosphors for light emitting applications. Journal of Materials Science: Materials in Electronics, 27(5), 5303-5308,

Singh, S. G., Sen, S., Patra, G. D., Bhattacharya, S., Singh, A. K., Shinde, S., and Gadkari, S. C., 2012. Fabrication, properties and thermo-luminescent dosimetric application of CaF2:Mn transparent ceramic. Nuclear Instruments and Methods in Physics Research Section B: Beam Interactions with Materials and Atoms, 287, 51-55, 10.1016/j.nimb.2012.06.002.

Sommer, M., Freudenberg, R., and Henniger, J., 2007. New aspects of a BeO-based optically stimulated luminescence dosimeter. Radiation Measurements, 42(4-5), 617-620, 10.1016/j.radmeas.2007.01.052.

Sommer, M., and Henniger, J., 2006. Investigation of a BeO-based optically stimulated luminescence dosemeter. Radiat Prot Dosimetry, 119(1-4), 394-397, 10.1093/rpd/nci626.

Sommer, M., Jahn, A., and Henniger, J., 2008. Beryllium oxide as optically stimulated luminescence dosimeter. Radiation Measurements, 43(2-6), 353-356, 10.1016/j.radmeas.2007.11.018.

Sommer, M., Jahn, A., and Henniger, J., 2011. A new personal dosimetry system for HP(10) and HP(0.07) photon dose based on OSL-dosimetry of beryllium oxide. Radiation Measurements, 46(12), 1818-1821, https://doi.org/10.1016/j.radmeas.2011.07.002.

Stoneham, A. M., 2001. Theory of defects in solids: electronic structure of defects in insulators and semiconductors: Oxford University Press.

Strickertsson, K., 1985. The thermoluminescence of potassium feldspars—glow curve characteristics and initial rise measurements. Nuclear Tracks and Radiation Measurements (1982), 10(4-6), 613-617,

Tavernier, S., Gektin, A., Grinyov, B., and Moses, W. W., 2006. Radiation detectors for medical applications: Springer Science & Business Media.

Theivasanthi, T., and Alagar, M., 2011. Electrolytic synthesis and characterizations of silver nanopowder. arXiv preprint arXiv:1111.0260,

Vij, D., 2012. Luminescence of solids: Springer Science & Business Media.

Vij, D. R., and Singh, N., 1997. Thermoluminescence dosimetric properties of beryllium oxide. Journal of Materials Science, 32(11), 2791-2796, Doi 10.1023/A:1018608113663.

Wang, X., Wang, R., Peng, C., Li, T., and Liu, B., 2010. Synthesis and sintering of beryllium oxide nanoparticles. Progress in Natural Science: Materials International, 20, 81-86, 10.1016/s1002-0071(12)60011-2.

Wang, X., Wang, R., Peng, C., Li, T., and Liu, B., 2011. Growth of BeO nanograins synthesized by polyacrylamide Gel route. Journal of Materials Science & Technology, 27(2), 147-152,

Watanabe, S., Gundu Rao, T. K., Page, P. S., and Bhatt, B. C., 2010. TL, OSL and ESR studies on beryllium oxide. Journal of Luminescence, 130(11), 2146-2152, 10.1016/j.jlumin.2010.06.009.

Wdowik, U. D., 2010. Structural stability and thermal properties of BeO from the quasiharmonic approximation. J Phys Condens Matter, 22(4), 045404, 10.1088/0953-8984/22/4/045404.

Wintle, A., and Huntley, D., 1980. Thermoluminescence dating of ocean sediments. Canadian Journal of Earth Sciences, 17(3), 348-360,

Xie, X., Dai, H., Li, T., Gong, G., and Chen, Z., 2018. Effect of calcining temperature on the microstructure and magnetic properties of CuFeO2 multiferroic ceramic. Advances in Applied Ceramics, 117(1), 66-71,

Yamashita, T., Yasuno, Y., and Ikedo, M., 1974. Beryllium oxide doped with lithium or sodium for thermoluminescence dosimetry. Health Physics, 27(2), 201-206,

Yeh, M. Y., Lin, C., Vu, C. T., Hsu, K. F., Lee, S. Y., Li, W. R., and Yen, C.-F., 2017. Post-calcination effects of sodium tantalate synthesized by microwave-assisted hydrothermal method and its photocatalytic performance under UV and visible light. Materials Research Bulletin, 90, 182-187,

Yukihara, E., 2019. Observation of strong thermally transferred optically stimulated luminescence (TT-OSL) in BeO. Radiation Measurements, 121, 103-108,

Yukihara, E. G., 2011. Luminescence properties of BeO optically stimulated luminescence (OSL) detectors. Radiation Measurements, 46(6-7), 580-587, 10.1016/j.radmeas.2011.04.013.

Yukihara, E. G., 2020. A review on the OSL of BeO in light of recent discoveries: The missing piece of the puzzle? Radiation Measurements, 134, 106291, https://doi.org/10.1016/j.radmeas.2020.106291.

Yukihara, E. G., Andrade, A. B., and Eller, S., 2016. BeO optically stimulated luminescence dosimetry using automated research readers. Radiation Measurements, 94, 27-34, 10.1016/j.radmeas.2016.08.008.

Yukihara, E. G., Doull, B. A., Gustafson, T., Oliveira, L. C., Kurt, K., and Milliken, E. D., 2017. Optically stimulated luminescence of MgB4O7:Ce,Li for gamma and neutron dosimetry. Journal of Luminescence, 183, 525-532, https://doi.org/10.1016/j.jlumin.2016.12.001.

Yukihara, E. G., and McKeever, S. W., 2011. Optically stimulated luminescence: fundamentals and applications: John Wiley & Sons.

Yukihara, E. G., Milliken, E. D., and Doull, B. A., 2014. Thermally stimulated and recombination processes in MgB4O7 investigated by systematic lanthanide doping. Journal of Luminescence, 154, 251-259, 10.1016/j.jlumin.2014.04.038.

Yukihara, E. G., Milliken, E. D., Oliveira, L. C., Orante-Barrón, V. R., Jacobsohn, L. G., and Blair, M. W., 2013. Systematic development of new thermoluminescence and optically stimulated luminescence materials. Journal of Luminescence, 133, 203-210, 10.1016/j.jlumin.2011.12.018.

Zahedifar, M., Mehrabi, M., Modarres, M., and Harooni, S., 2011. Thermoluminescece properties of BeO: Mg nanoparticles produced by sol-gel method. Journal of Nanostructures, 1(3), 199-203,

Zeng, X., Yuan, J., and Zhang, L., 2008. Synthesis and photoluminescent properties of rare earth doped ZnO hierarchical microspheres. The Journal of Physical Chemistry C, 112(10), 3503-3508,

Zumdahl, S. S., and DeCoste, D. J., 2012. Chemical principles: Cengage Learning.

CURRICULUM VITAE

Volkan ALTUNAL, Completed his primary, secondary and high school education in Adana. He graduated with the double major degrees of Bachelor of Arts and Sciences in Physics and Mathematics Departments from Cukurova University, Adana, Turkey in 2013. He graduated with MSc in the Physics Department from Cukurova University in 2016. After his MSc graduation, he started to PhD education in the Physics Department at Cukurova University in 2016. He has worked in several research projects supported by the Scientific Research Project Unit of Cukurova University during his PhD. He also worked as a researcher in two international projects supported by NATO during his MSc and PhD. His research areas are radiation energy storage, radiation dosimetry, material synthesis, thermoluminescence, optically stimulated luminescence, radioluminescence, nanotechnology.